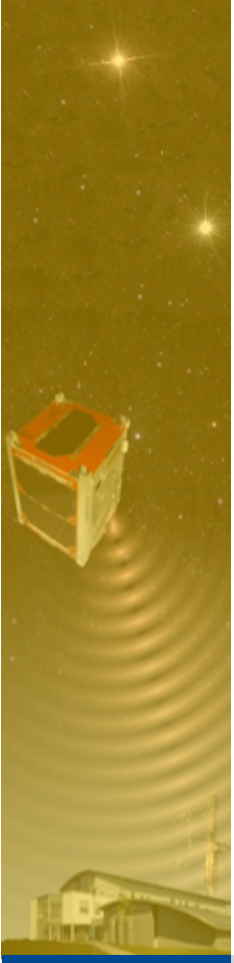

Institut für Informatik
Lehrstuhl für Robotik und Telematik
Prof. Dr. K. Schilling
Prof. Dr. A. Nüchter

Würzburger Forschungsberichte in Robotik und Telematik

Uni Wuerzburg Research Notes in Robotics and Telematics

Julius-Maximilians-
UNIVERSITÄT WÜRZBURG

Band 22

Dissertation an der Graduate School of Science and Technology

Alexander Kramer

Orbit Control of a Very Small Satellite using Electric Propulsion

Julius-Maximilians-Universität Würzburg
Graduate School of Science and Technology

Doctoral thesis / *Dissertation*

for the doctoral degree / *zur Erlangung des Doktorgrads*

Dr. rer. nat.

Orbit control of a very small satellite using electric propulsion

Orbitregelung eines Kleinstsatelliten mithilfe eines elektrischen Antriebssystems

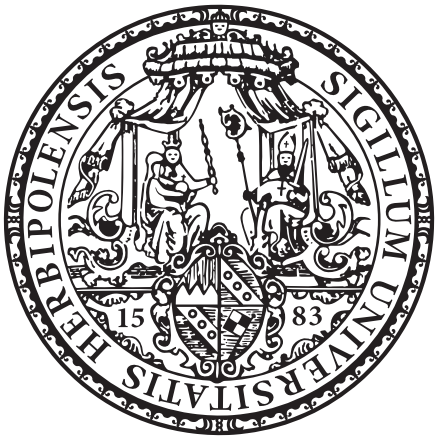

Submitted by / *Vorgelegt von*

Alexander Kramer

from / aus

Kernen im Remstal

Würzburg, 2021

Submitted on / *Eingereicht am*: February 11th, 2021

Members of thesis committee / *Mitglieder des Promotionskomitees*

Chairperson / *Vorsitz*:	Prof. Dr. Sebastian von Mammen
1. Reviewer and Examiner / *1. Gutachter und Prüfer*:	Prof. Dr. Klaus Schilling
2. Reviewer and Examiner / *2. Gutachter und Prüfer*:	Prof. Dr. Sergio Montenegro
3. Reviewer and Examiner / *3. Gutachter und Prüfer*:	Priv.-Doz. Dr.-Ing. Georg Herdrich
4. Examiner / *4. Prüfer*:	Prof. Dr. Martin Tajmar
Day of thesis defense / *Tag des Promotionskolloquiums*:	July 5th, 2021

Abstract

Miniaturized satellites on a nanosatellite scale below 10kg of total mass contribute most to the number of launched satellites into Low Earth Orbit today. This results from the potential to design, integrate and launch these space missions within months at very low costs. In the past decade, the reliability in the fields of system design, communication, and attitude control have matured to allow for competitive applications in Earth observation, communication services, and science missions. The capability of orbit control is an important next step in this development, enabling operators to adjust orbits according to current mission needs and small satellite formation flight, which promotes new measurements in various fields of space science. Moreover, this ability makes missions with altitudes above the ISS comply with planned regulations regarding collision avoidance maneuvering.

This dissertation presents the successful implementation of orbit control capabilities on the pico-satellite class for the first time. This pioneering achievement is demonstrated on the 1U CubeSat UWE–4. A focus is on the integration and operation of an electric propulsion system on miniaturized satellites. Besides limitations in size, mass, and power of a pico-satellite, the choice of a suitable electric propulsion system was driven by electromagnetic cleanliness and the use as a combined attitude and orbit control system. Moreover, the integration of the propulsion system leaves the valuable space at the outer faces of the CubeSat structure unoccupied for future use by payloads. The used NanoFEEP propulsion system consists of four thruster heads, two neutralizers and two Power Processing Units (PPUs).

The thrusters can be used continuously for 50 minutes per orbit after the liquefaction of the propellant by dedicated heaters. The power consumption of a PPU with one activated thruster, its heater and a neutralizer at emitter current levels of 30-60µA or thrust levels of 2.6-5.5µN, respectively, is in the range of 430-1050mW. Two thruster heads were activated within the scope of in-orbit experiments. The thrust direction was determined using a novel algorithm within 15.7° and 13.2° of the mounting direction. Despite limited controllability of the remaining thrusters, thrust vector pointing was achieved using the magnetic actuators of the Attitude and Orbit Control System.

In mid 2020, several orbit control maneuvers changed the altitude of UWE–4, a first for pico-satellites. During the orbit lowering scenario with a duration of ten days, a single thruster head was activated in 78 orbits for 5:40 minutes per orbit. This resulted in a reduction of the orbit altitude by about 98.3m and applied a Δv of 5.4cm/s to UWE–4. The same thruster was activated in another experiment during 44 orbits within five days for an average duration of 7:00 minutes per orbit. The altitude of UWE–4 was increased by about 81.2m and a Δv of 4.4cm/s was applied. Additionally, a collision avoidance maneuver was executed in July 2020, which increased the distance of closest approach to the object by more than 5000m.

Zusammenfassung

Heutzutage werden überwiegend Kleinstsatelliten in niedrige Erdumlaufbahnen befördert, da dies schnell und sehr kostengünstig möglich ist. Von der Planung bis zum Raketenstart vergehen oft nur wenige Monate. Im vergangenen Jahrzehnt haben sich Kleinstsatelliten bezüglich Systemgestaltung, Kommunikation und Lageregelung dahingehend weiterentwickelt, dass diese in den Anwendungsbereichen Erdbeobachtung, Kommunikationsdienstleistungen und wissenschaftlichen Missionen mit herkömmlichen Satelliten konkurrieren können. Ein weiterer wichtiger Entwicklungsschritt für Kleinstsatelliten wäre die Möglichkeit der Orbitkontrolle. Diese würde die Betreiber befähigen, die Flugbahn der Satelliten entsprechend den aktuellen Zielen der Mission anzupassen und Formationsflug von Kleinstsatelliten durchzuführen, um neue wissenschaftliche Erkenntnisse in vielen Bereichen der Weltraumforschung zu fördern. Gleichzeitig würden Kleinstsatelliten den aktuell geplanten Vorschriften Rechnung tragen, nach denen Satelliten mit Flughöhen oberhalb der ISS manövrierfähig sein müssen, um Kollisionen zu vermeiden.

Die vorliegende Dissertation präsentiert die erste erfolgreiche Orbitkontrolle auf einem Piko-Satelliten. Diese Pionierleistung wird auf dem 1U CubeSat UWE–4 demonstriert. Ein Schwerpunkt dieser Arbeit liegt dabei auf der Integration und dem Betrieb eines elektrischen Antriebssystems auf Kleinstsatelliten. Diese Integration des Antriebssystems hält den wertvollen Platz an den Außenflächen des CubeSats für zukünftige Nutzlasten frei und ermöglicht dessen Anwendung als Lage- und Orbitregelungsaktuator. Das verwendete NanoFEEP Antriebssystem beinhaltet vier Triebwerke, zwei Neutralisatoren und zwei Platinen zur Steuerung.

Nach der Verflüssigung des Treibstoffs durch dedizierte Heizer können die Triebwerke pro Erdumrundung für 50 Minuten kontinuierlich genutzt werden. Der Stromverbrauch einer Steuerplatine mit einem aktiven Triebwerk, seinem Heizer und einem Neutralisator bei Emitterströmen von 30-60µA bzw. Schüben von 2.6-5.5µN liegt im Bereich von 430-1050mW. Im Rahmen von In-Orbit Experimenten wurden zwei Triebwerke aktiviert. Die Schubrichtungen der aktiven Triebwerke konnten mit einem neuartigen Algorithmus in einem Winkel von 15.7° bzw. 13.2° bezüglich ihrer Einbaurichtung bestimmt werden. Trotz mangelnder Steuerbarkeit der verbleibenden Triebwerke konnte eine Ausrichtung des Schubvektors unter Zuhilfenahme der magnetischen Aktuatoren des Lageregelungssystems erreicht werden.

Mehrere Orbitregelungsexperimente zur Veränderung der Flughöhe konnten Mitte 2020 zum ersten Mal auf einem Piko-Satelliten gezeigt werden. Um die Flughöhe zu verringern, wurde ein Triebwerk über einen Zeitraum von zehn Tagen während 78 Orbits gefeuert, wobei dieses pro Erdumrundung für durchschnittlich 5:40 Minuten aktiviert wurde. Hierdurch wurde die Flughöhe von UWE–4 um 98m reduziert und seine Geschwindigkeit um ein Δv von $7.2\mathrm{cm/s}$ erhöht. In einem anderen Experiment wurde dasselbe Triebwerk während 44 Orbits in einem Zeitraum von fünf Tagen für

durchschnittlich 7:00 Minuten aktiviert, wodurch die Flughöhe des Kleinstsatelliten um 74.2m angehoben und seine Geschwindigkeit um ein Δv von $4.0 \mathrm{cm}/\mathrm{s}$ verringert wurde. Zudem wurde ein Manöver zur Kollisionsvermeidung durchgeführt, das den Abstand zwschen UWE–4 und dem Objekt auf Kollisionskurs zum Zeitpunkt der kleinsten Annäherung um mehr als 5000m vergrößert hat.

Danksagung

Viele Personen haben mich während dieser Doktorarbeit begleitet und unterstützt - bei diesen möchte ich mich im Folgenden bedanken.
Zunächst möchte ich Prof. Dr. Klaus Schilling für die Möglichkeit danken, meine Dissertation an diesem spannenden Thema im Projekt UWE-4 an seinem Lehrstuhl durchführen zu können. Von dem hohen Maß an Freiheit in der Gestaltung und Durchführung der Aufgaben, die sich während der Arbeit entwickelten, konnte meine selbständige Arbeitsweise stark profitieren. Außerdem danke ich Prof. Dr. Sergio Montenegro und Prof. Dr. Martin Tajmar für die fachliche sowie Dr. Stephan Schröder-Köhne für die administrative Betreuung.
Als zentraler Arbeitskollege und einziges kontinuierliches Mitglied im UWE-Team möchte ich Dieter Ziegler danken für sein Durchhaltevermögen in der Diskussion hardware-technischer Fragestellungen, seine überaus gründliche und weitsichtige Arbeitsweise, sowie viele tiefgehende Gespräche weit über die Arbeit hinaus. Als langjährigem Kollegen, Mentor und Freund möchte ich Dr. Philip Bangert herausstellen, der mich selbst nach seiner Zeit in Würzburg immer wieder mit einem offenen Ohr und neuen Denkansätzen unterstützt hat.
Darüberhinaus möchte ich vielen Kollegen an der Universität Würzburg und dem ZfT meine Wertschätzung aussprechen für ihre unermüdliche Mitarbeit bis spät in die Nacht. Besonderer Dank gilt hier Slavi Dombrovski, der als ständiger Ansprechpartner bei software-technischen Problemstellungen jeder Art einen Lösungsansatz parat hatte und Dr. Stephan Busch, der mich in verschiedenen Bereichen der Promotion mit technischen Ideen versorgte. Neben den Würzburger Kollegen schätze ich auch die gute Kooperation mit der Arbeitsgruppe der TU Dresden im Projekt UWE-4, insbesondere Daniel Bock für die Ausdauer bei der Kommunikation technischer Finessen.
Neben der fachlichen Unterstützung wäre diese Dissertation auch nicht ohne den nötigen Freizeitausgleich möglich gewesen. Hierfür möchte ich mich speziell bei Thea, Jesko, Oli, Philip, Fabi und David bedanken, die meine Fachsimpelei ertragen haben und trotzdem Wege gefunden haben meine Gedanken auf andere Aspekte des Lebens zu leiten.
Außerdem danke ich meinen Eltern dafür, dass sie es mir ermöglicht haben, meinen Wünschen und Träumen zu folgen, die mich zu dieser Dissertation geführt haben.
Nicht zuletzt danke ich dem Menschen an meiner Seite für die Unterstützung und Motivation während der gesamten Dauer meiner Doktorarbeit - du, Kristina, hast die Höhen und Tiefen meiner Doktorarbeit mit mir durch gestanden - ich danke dir dafür! Zudem möchte ich unserem kleinen Sonnenschein Moritz danken - wegen deiner Ankündigung habe ich die letzten Meter dieser Dissertation besonders motiviert gearbeitet!

Acronyms

AOCS	Attitude and Orbit Control System
BeiDou	BeiDou Navigation Satellite System of the People's Republic of China
BP	Backplane
CAD	Computer Aided Design
CDS	CubeSat Design Specification
CNT	Carbon nanotube
COE	Classical Orbital Element
COMM	Radio Communication System
DLR	*Deutsches Zentrum für Luft- und Raumfahrt* [German Aerospace Center]
ECI	Earth Centered Inertial
EMI	Electromagnetic interference
EPS	Electrical Power System
FAB	Front Access Board
FEEP	Field-emission electric propulsion
Galileo	Global Positioning System of the European Union
GEO	Geostationary Orbit
GLONASS	GLObal NAvigation Satellite System of the Russian Federation
GNSS	Global Navigation Satellite System
GPS	Global Positioning System of the United States of America
GTO	GEO Transfer Orbit
HEO	Highly Eccentric Earth Orbit
HV	High voltage
IADC	Inter-Agency Space Debris Coordination Committee
IGRF	International Geomagnetic Reference Field
IKF	Isotropic Kalman Filter
IMU	Inertial Measurement Unit
ISS	International Space Station
LEO	Low Earth Orbit
LMIS	Liquid metal ion source
LMO	LEO-MEO Crossing Orbits
MEMS	Microelectromechanical system
MEO	Medium Earth Orbit

NanoFEEP	Miniaturized Field-emission electric propulsion
NetSat	Networked Pico-Satellite Distributed System Control
NORAD	North American Aerospace Defense Command
OBDH	On-Board Data Handling System
PCB	Printed circuit board
PPT	Pulsed plasma thruster
PPU	Power Processing Unit
PWM	Pulse Width Modulation
SAR	Synthetic Aperture Radar
SGP4	Simplified General Perturbation model 4
TLE	Two-Line Element set
TOM	Telematics Earth Observation Mission
UNISEC	University Space Engineering Consortium
UWE	University Wuerzburg Experimental Satellite
VAT	Vacuum Arc Thruster
ZfT	*Zentrum für Telematik* [Center for Telematics]

Table of Contents

List of publications

[A] Kramer, A., Schilling, K., First demonstration of collision avoidance and orbit control for pico-satellites – UWE–4, Acta Astronautica, 185:244–256, 2021. ISSN 0094-5765. doi: https://doi.org/10.1016/j.actaastro.2021.04.010. URL https://sciencedirect.com/science/article/pii/S0094576521001557.

[B] Kramer, A., Bangert, P., Schilling, K., UWE–4: First Electric Propulsion on a 1U CubeSat - In-Orbit Experiments and Characterization, Aerospace, Vol. 7(7), 2020, 98

[C] Kramer, A., Bangert, P., Schilling, K., Hybrid Attitude Control On-Board UWE–4 Using Magnetorquers and The Electric Propulsion System NanoFEEP, 33rd Annual AIAA/USU Conference on Small Satellites, Logan, USA, August 2019

[D] Bangert, P., Kramer, A., Schilling, K., Hybrid Attitude Control of a Pico-Satellite Using Magnetic Torquers and an Electric Propulsion System, 69th International Astronautical Congress, Bremen, Germany, October 2018

[E] Bangert, P., Kramer, A., Schilling, K., UWE–4: Attitude and Orbit Control on a 1U CubeSat scale using magnetic torquers and an electric propulsion system, 11th Pico- and Nano-Satellite Workshop, Berlin, Germany, 2018

[F] Kramer, A., Azari, P., Bangert, P., Schilling, K., Orbit control on the Pico-Satellite UWE–4 using a NanoFEEP propulsion system and a directive adaptive guidance algorithm, 35th International Electric Propulsion Conference, Atlanta, USA, October 2017

[G] Bangert, P., Kramer, A., Schilling, K., UWE–4: Integration State of the First Electrically Propelled 1U CubeSat, 31st Annual AIAA/USU Conference on Small Satellites, Logan, USA, August 2017

[H] Kramer, A., Bangert, P., Paries, F., Schilling, K., Preparations for Orbit control on the Pico-Satellite UWE–4, 11th IAA Symposium on small satellites for Earth observation, Berlin, 2017

[I] Pietzka, M., Bangert, P., Kramer, A., Lebeda, A., Schilling, K., Schein, J., Propulsion System for CubeSat Formation Flight, IAA Book Series: Small Satellites – Programs, Missions, Technologies and Applications, Volume 1, Number 6, ISBN/EAN IAA : 978-2-917761-49-6, 2016

[J] Bangert, P., Dombrovski, S., Kramer, A., Schilling, K., UWE–4: Orbit Determination and Control on a Pico-Satellite scale, IAA Book Series: Small Satellites – Programs, Missions, Technologies and Applications, Volume 1, Number 6, ISBN/EAN IAA : 978-2-

917761-49-6, 2016

[K] Bangert, P., Busch, S., Kramer, A., Schilling, K., Preparation of Papers for IFAC Conferences & Symposia: Guidance, Navigation, and Control for Future Miniature Satellite Formations: Current Limitations and Impending Advancements, 20th IFAC Symposium on Automatic Control in Aerospace ACA, Sherbrooke, Quebec, Canada, August 2016

[L] Bangert, P., Dombrovski, S., Kramer, A., Schilling, S., UWE–4: Advances in the Attitude and Orbit Control of a Pico-Satellite, The 4S Symposium, Valletta, Malta, May 2016

[M] Bock, D., Kramer, A., Bangert, P., Schilling, S., Tajmar, M., NanoFEEP - Highly miniaturized FEEP propulsion system for attitude and orbit control of CubeSats, Space Propulsion Conference, Rome, Italy, May 2016

[N] Bangert, P., Busch, S., Dombrovski, S., Kramer, A., UWE - Lessons Learned and Future Perspectives, 3rd IAA Conference on University Satellite Missions and CubeSat Workshop, Rome, 2015

[O] Schilling, K., Bangert, P., Busch, S., Dombrovski, S., Freimann, A., Kleinschrodt, A., Kramer, A., Nogueira, T., Ris, D., Scharnagl, J., Tzschichholz, T., Netsat: A Four Pico/Nano-Satellite Mission For Demonstration Of Autonomous Formation Flying, 66th International Astronautical Congress, Jerusalem , Israel, 2015

[P] Bock, D., Kramer, A., Bangert, P., Schilling, K., Tajmar, M., NanoFEEP on UWE platform - Formation Flying of CubeSats using Miniaturized Field Emission Electric Propulsion Thrusters, 34th International Electric Propulsion Conference, Kobe, Japan, 2015

Considerable text fragments and figures from previously listed publications have been used in the dissertation at hand.
Chapter 3 contains text fragments and conceptually similar parts of publications [A], [B], [C], [F], and [G].
Chapter 4 has parts which have been published in [A] and [C].
Chapter 5 contains data and text used beforehand in articles [A], [B] and [C].
Chapter 6 and Chapter 7 are composed of the main contents of publication [B] and [A], respectively. Thus, these chapters contain text parts which were re-used in a one-to-one fashion.
If figures within the dissertation have been published elsewhere, the sources are indicated at the end of the figure captions.

1 Introduction

This thesis describes the path towards enabling orbit control in miniaturized spacecraft. An analysis of state of the art propulsion systems applicable to this satellite class is compared to requirements posed by the small size of pico-satellites and the goal of orbit control. Subsequently, the integration of the Miniaturized Field-emission electric propulsion system (NanoFEEP) into the 1U CubeSat University Wuerzburg Experimental Satellite 4 (UWE–4) and precautions due to the propulsion system will be presented. The thrusters are installed in the satellite structure with a fixed mounting direction. Thus, the attitude control system of the satellite has a special focus, as it needs to rotate the satellite to direct the thrust vector as desired. In order to certify the propulsion system for utilization on pico-satellites, it is characterized based on experimental in-orbit data. A novel thrust direction estimation algorithm constitutes to this qualification and is demonstrated on the basis of measurements conducted with UWE–4. Finally, as a world novelty in pico-satellites, orbit control experiments targeting the lowering and increase of the spacecraft's orbit were demonstrated on UWE–4 and are presented in this thesis. Furthermore, the first collision avoidance maneuver of a small satellite was conducted with UWE–4 in July 2020 regarding a conjunction with an Iridium-33 fragment resulting from the collision with Cosmos 2251 in 2009. These advancements are major breakthroughs in small satellite technology as they open up new fields of applications for both science and economy.

1.1 Motivation

In the year 2000, Heidt et al proposed the CubeSat standard (Heidt et al., 2000). It has become one of the most successful standards in the space industry and is resembled by more than 1200 CubeSats that have been launched since with their number still growing. At the time of the development of the standard, students in space programs could hardly get any hands-on experience in real space projects because of the huge costs associated with them. The introduction of the CubeSat standard aimed at filling this gap by introducing standard sizes and interfaces to a launcher vehicle, thereby reducing the launch costs to about 100 000 $ per CubeSat unit today (Nieto-Peroy and Emami, 2019).

In the following decade, the technology around CubeSats became more mature so that not only educational but also industrial and scientific goals were achieved employing CubeSats. Over the last decade, companies like *Planet* and *Spire* have been monitoring the Earth with a fleet of Flock and Lemur satellites using hundreds of three unit CubeSats

with a physical size of 10x10x30cm^3. Scientific results were achieved in different domains by various missions, among others, the Organism/ORganics Exposure to Orbital Stresses (O/OREOS) nanosatellite (Nicholson et al., 2011) or the Radio Aurora Explorer (RAX)-2 CubeSat (Bahcivan et al., 2014). It is mainly due to the frequent launch opportunities of small satellites at very reasonable prices, compared to those of conventional satellites, that the market of small satellites grew so rapidly. Although the trend in small satellites is tending towards this 3U CubeSat size, some capabilities have not been demonstrated at this size or smaller spacecraft. Technologies demonstrated on smaller platforms often also offer the possibility to be implemented on larger systems by clustering, similar to the multiplication of electronic storage capacities.

A study by the National Academies of Sciences and Medicine (2016) assessed the relevance of pico-satellites in different scientific domains. While many refereed publications were present in solar and space physics and Earth and planetary sciences, already in 2016, it was found that an even larger science impact could be achieved in the aforementioned and other fields by technological advancements in the areas of attitude control, orbit control and propulsion. Millan et al. (2019) emphasize that the application of missions with multiple satellites in different degrees of cooperation among them can enhance scientific findings, impossible to yield with single satellites. However, cooperative missions with conventional spacecraft are often not feasible. Firstly, since several launch vehicles would be necessary for orbit insertion and secondly, because of the disproportional increase of costs associated to large spacecraft. Thus, small satellites remain the only viable option. Many of the proposed mission designs with multiple spacecraft are formulated with orbit control capabilities that are technologically not available yet.

As the application of a propulsion system on these miniaturized spacecraft for attitude and orbit control purposes was defined as an enabling technology by the previously mentioned articles, the most important motivations, from both a technological and a scientific point of view, are pointed out hereafter:

- **Dump momentum from reaction wheels.**
  Precision attitude control is a major field of technological advancements aiming at the application of pico- and nanosatellites for long-time observation in solar or planetary sciences. Usually, reaction wheels are employed as attitude control actuators, as they offer fast response times by momentum storage of the spacecraft. Nonetheless, the stored momentum needs to be reduced if the rotation rate of a reaction wheel reaches its limit, to maintain its use as attitude control actuator. In Low Earth Orbit (LEO), momentum dumping can be achieved using the interaction of magnetorquers with the Earth's magnetic field. However, at orbits with higher altitudes the Earth's magnetic field is too weak and attitude control thrusters are necessary to dump excessive momentum of the reaction wheels.

- **Modify orbit during operations.**
  Spacecraft which do not employ a propulsion system will be placed into their final orbit by the launch vehicle. Nevertheless, a satellite could potentially achieve several mission goals with the same payload, if it had the possibility to adjust its orbit. A potential mission could be an Earth observation satellite in an equatorial orbit

with the mission goal to monitor water vapor, bush fires, or maritime traffic in the coastal areas in the equatorial region. During the operation of the mission, the focus might shift to the subtropical zone as region of interest. If the satellite employs a propulsion system, not only costs for a second satellite but also considerable response time can be saved.

- **De-orbit the satellite at the end of its mission lifetime.**
  Based on a guideline by the Inter-agency space debris coordination committee (2002), a satellite passing through LEO should limit its lifetime to a maximum of 25 years. This limits the orbital altitude of spacecraft in LEO which rely on natural decay due to atmospheric drag to an average altitude of 650km. However, due to the vastly increasing number of satellites originating from missions like Starlink (Williams, 2019), the OneWeb-constellation (de Selding, 2015), or Kuiper (Koziol, 2020), agencies of spacefaring nations are already discussing tightening this rule (Federal Communications Commission, 2020). Satellites employed with a propulsion system could use it to de-orbit faster than their natural decay rate, such that the satellites could leave their orbit earlier and thus limit the risk for collision with other satellites or space debris.

- **Raise the orbit and consequently increase the workspace to higher altitudes than the injection orbit of the launch vehicle.**
  The increasing number of small satellites in the space sector also opened up a new market for launch vehicles dedicated to the launch of small satellites. However, even though the number of operational launch vehicles for small satellites is growing, according to SpaceWorks Enterprises (2020) "[...] the majority of nano/microsatellites in 2019 chose to leverage rideshare alternatives". One possibility for a comparatively cheap launch option is as part of a resupply mission of the ISS; another is to leverage rideshare launch options of other launchers. For both options the orbit altitude of the injection orbit is usually determined by the primary payload of the launch vehicle, or the altitude of the ISS, respectively. If a small satellite is aiming at an orbit altitude above the injection orbit of the launch vehicle, an orbit raising maneuver by the spacecraft itself could enable the satellite to use workspaces at higher altitudes.

- **Compensate atmospheric drag effects on spacecraft.**
  In the past, drag-free satellite missions in LEO were realized in missions like Gravity Probe B (Bencze et al., 2006) and the Gravity field and steady-state Ocean Circulation Explorer (GOCE) (Drinkwater et al., 2003). However, realizing drag-free control in the regime of small satellites qualifies this satellite class for applications in the fields of "[...] navigation, Earth science, fundamental physics, and astrophysics" (Lappas and Kostopoulos, 2020). Future missions like the Drag-Free CubeSat mission (Zanoni et al., 2013) aiming at geodesy measurements are already envisioned for the near future.

- **Prolong missions in very low earth orbit.**
  Orbit altitudes below 400km are interesting for Earth observation missions with high

resolution requirements. Their optical payload would have an increased angular resolution, as the observed object is closer, compared to missions at higher altitudes. Nonetheless, objects below 400km have a very limited lifetime as the atmospheric drag is considerably higher. On the one hand, this reduces the risk for collisions with other objects at this altitude, on the other hand, it also shortens the lifetime of the satellite itself. Orbit control capabilities would enable the spacecraft to use its propulsion system for station-keeping and thus prolong the mission duration.

- **Enable small satellites to avoid collisions by a temporary modification of their orbit.**
  With the increasing number of Earth-orbiting objects, there is a greater risk for collisions among these and their fragments. This collisional cascading is also known as the Kessler effect (Kessler and Cour-Palais, 1978). The North American Aerospace Defense Command (NORAD) monitors earth-orbiting objects and informs the satellite operators about upcoming conjunctions with other objects. Satellites with orbit control capabilities could make use of collision avoidance maneuvers to prevent environmental disasters which could render the altitude of the collision unusable for the next years. One suggested possibility especially focussing on collision avoidance is to "[...] support a propulsion requirement for satellites operating above 400km [...]" (Federal Communications Commission, 2020, Paragraph 62), especially with the focus on collision avoidance maneuvers protecting the ISS.

- **Initialise satellite constellation after deployment.**
  Constellations of satellites, such as the nanosatellite fleet called Flock by *Planet*, are often launched with the same deployer. The deployment procedure from the launch vehicle places all of these satellites in a similar orbit with an arbitrary along-track spacing. So far, a differential drag control scheme in LEO was employed in order to reposition the deployed satellites equally in this orbit (Foster et al., 2018). Nevertheless, with an increase of desired orbit altitude, the atmospheric drag effect vanishes and spacecraft propulsion remains the only viable option.

- **Open up 3D satellite formations as new field of application for small satellites.**
  According to Folta et al. (1996), "[f]ormation flying involves the use of an active control scheme to maintain the relative positions of the spacecraft." Formations thereby enable to distribute the functionality of large satellites to many smaller satellites, which reduces the total involved cost and risk while increasing flexibility and redundancy. So far, missions like the Gravity Recovery and Climate Experiment (GRACE) (Herman et al., 2004) and the Magnetospheric Multiscale Mission (MMS) (Williams et al., 2016) have demonstrated leader-follower and 3D satellite formations on a scale of satellites with more than 500kg. In the considerably smaller regime of satellites at a mass below 20kg, the CanX-4 and 5 (Bonin et al., 2015) and the AeroCube-4 (Gangestad et al., 2013) missions have demonstrated leader-follower formations by the use of a cold gas propulsion system and atmospheric drag, respectively. However, for tasks like observation of the Earth's surface for 3D monitoring with small satellites, a 3D formation is desirable and in order

to ensure long-term operations, the use of electric propulsion is convenient. The Networked Pico-Satellite Distributed System Control (NetSat) mission launched in September 2020 aims at the demonstration of a 3D formation on a 3U CubeSat platform using electric propulsion, a pioneer for small satellite formation flight. The successor mission CloudCT uses the simultaneous observation of clouds from multiple spacecraft to improve our understanding of the formation of clouds and their influence on the climate.

This thesis aims to fill the gap of orbit control capabilities on the smallest scale of spacecraft – namely pico-satellites. In this respect, it will outline guidelines applied in satellite design as well as details about the possibilities of orbit control under the restrictions of mass and power of such a small spacecraft. As the first spacecraft in its class, the satellite designed during this thesis, UWE–4, demonstrated an electric propulsion system in space and its use as orbit control system.

1.2 Thesis Outline

If not mentioned otherwise, all times are given in Coordinated Universal Time (UTC). The phrases ”1 CubeSat unit” and ”1U” are used interchangeably in this dissertation. **Bold** letters are used to indicate vectors and tensors, while derivatives and independent variables, such as the time t and directions x, y, and z, are italicized.

Besides this introduction, this thesis is composed of six technical chapters and a final conclusion of the work presented. A schematic of the structure of this dissertation is shown in Figure 1.1. The single chapters of the thesis comprise of the following content:

Chapter 1: Introduction
The first chapter introduces the main focus of this thesis. It strives to set the presented work in the context of current on-going space research and regulations. It also presents the motivation for this thesis by means of different use-cases of academic and industrial application fields. Furthermore, it outlines the structure of the thesis and shall give the reader the possibility to navigate to the respective chapter of interest.

Chapter 2: State of the art of orbit control
This chapter firstly gives some overview about the historic motivation in spacecraft propulsion since the beginning of space flight. The state of the art analysis describes the operating principles of existing active and passive propulsion devices. Additionally, all successful demonstrations of orbit control devices in nanosatellite missions ($<$10kg of total mass of the satellite) are detailed. Some novel promising developments in this active field of research are given.

Chapter 3: The UWE–4 CubeSat
In this chapter, the UWE–4 mission as well as the design of the associated 1U CubeSat are described. A special focus lies on the AOCS and the NanoFEEP propulsion system. Furthermore, some design guidelines followed by UWE–4 for the integration of an electric

propulsion system are detailed.

Chapter 4: AOCS commissioning
At first, this chapter introduces the physical principles to describe the attitude of a rigid body like a small spacecraft using the Euler equation. Moreover, an estimation of the internal residual magnetic dipole moment using the AOCS sensor suite is given. Finally, some attitude control experiments are shown, as the performance and behavior of attitude control on UWE–4 is playing a vital role during orbit control presented in Chapter 7.

Chapter 5: Propulsion system commissioning
This chapter focuses on the characterization of the NanoFEEP propulsion system developed by TU Dresden for use on UWE–4. It comprises of the single components' measurements, i.e. of the heaters, the neutralizers and the thrusters of the propulsion system in order to verify their operability. The power consumption as well as details of their operation are given. The electrical parameters of the neutralizers and the thrusters, their meaning and their ranges during operation are introduced. The solution strategy for initial issues with single components and the limitations on the application of this propulsion system on UWE–4 are described.

Chapter 6: Thrust direction estimation
This chapter introduces a novel algorithm for the determination of the thrust direction of an attitude control thruster using the AOCS sensor suite. The rotation rate of the satellite as well as a formula employing the electrical characteristics of an electrostatic propulsion system are the basis for this analysis. The results of this chapter will be used during the analysis of the orbit control experiments in Chapter 7.

Chapter 7: Orbit Control
At first, the last technical chapter introduces the basic principles of orbit control for Earth-orbiting spacecraft. Afterwards, the different restrictions for orbit control of the UWE–4 CubeSat, resulting from limitations of the NanoFEEP propulsion system, the attitude control capability of the AOCS and the Electrical Power System (EPS) are discussed in detail. A plan is derived to partially overcome and integrate these limitations in an orbit control strategy with UWE–4. This strategy is applied on UWE–4 and experimental in-orbit data is given and compared to external reference data. One scenario each for orbit lowering and orbit increasing is executed and their results are presented. This experimental data is compared to simulated scenarios in order to define the framework for possible improvements in following small satellite missions. Finally, data of the first in-orbit collision avoidance maneuver ever executed on board of a 1U CubeSat with UWE–4 is shown.

Chapter 8: Conclusion
The conclusion is the final chapter of this thesis. It summarizes the work presented in this dissertation and points out the relevant achievements for the sector of miniaturized satellites. Furthermore, it gives some future perspectives for small satellite missions enabled by the achievements of this work.

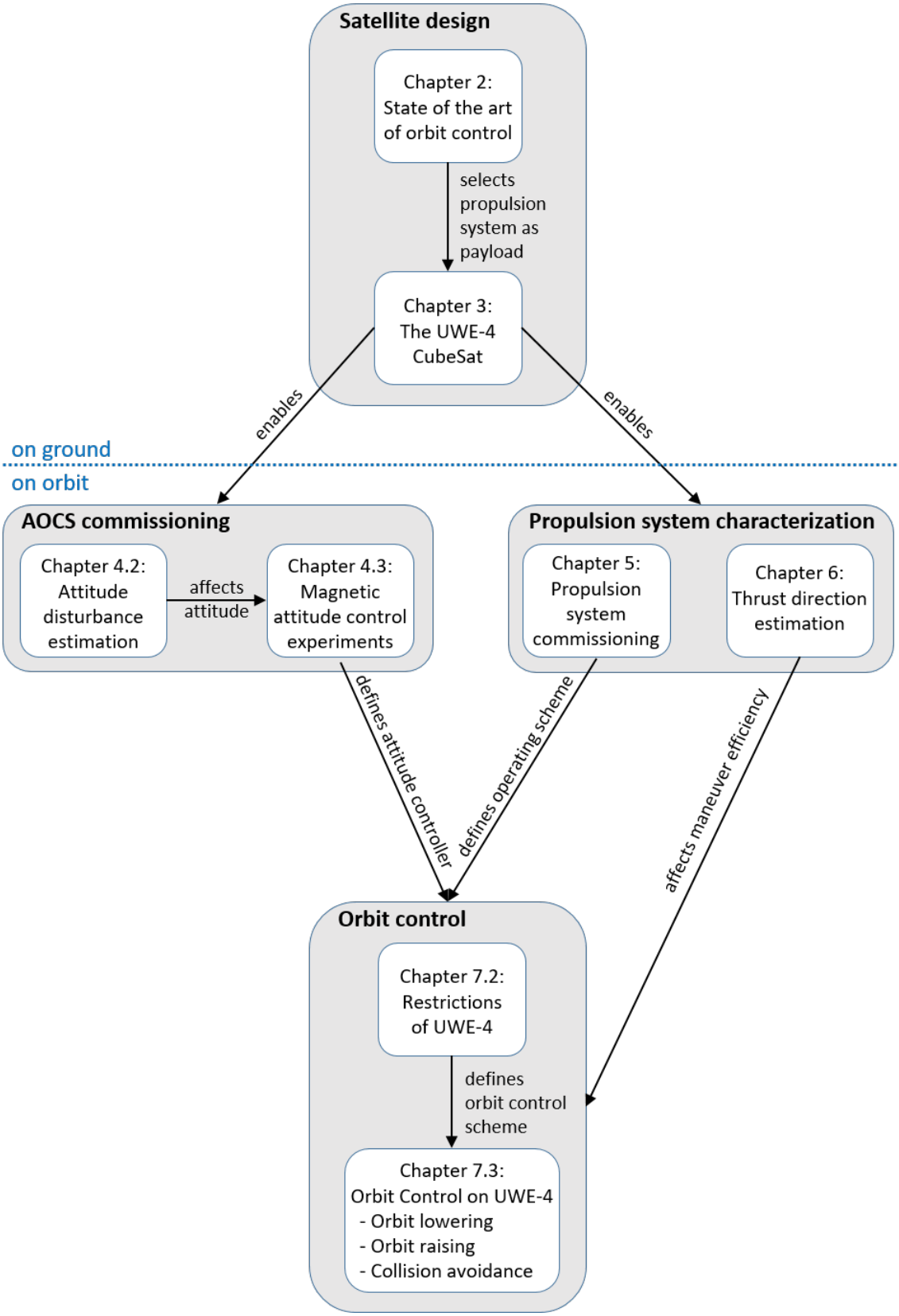

Figure 1.1: Schematic of the outline of the thesis.

2
State of the art of orbit control

The ”Space Race” era in the 1950s and 60s has brought tremendous achievements for the industry of space flight. While the Soviet Union put the first satellite *Sputnik I* into orbit in 1957 and the first man (Yuri Gagarin) into space in 1961, the United States were the first nation to fly to the moon in 1969. Besides these big firsts in space flight history, the competition also stimulated many other developments in the field of orbit control capabilities.

The US *Discoverer 13* mission, which was launched in 1960, is known for being the first mission to bring back a man-made object that was sent to space. For this purpose, the recovery vehicle was spun up in orbit using cold gas thrusters for attitude control prior to deceleration (NASA Space Science Data Coordinated Archive). This marked the first application of a propulsion system on board of a satellite itself instead of the launch vehicle. In 1964, the *Space Electric Rocket Test 1 (SERT 1)* was launched and demonstrated ion engines as the first spacecraft employing an electric propulsion system (Cybulski et al., 1965) on a suborbital flight and was followed by the Soviet *Zond-2* mission employing Pulsed plasma thrusters (PPTs) in the same year (Tajmar, 2003). Further significant milestones in the development of electric propulsion were NASA's *Deep Space 1* mission, which was propelled by the NSTAR[1] ion engine for more than 16000 hours between 1999 and 2001 (Brophy, 2002), and the European *SMART-1*[2] mission, which demonstrated the application of a SNECMA[3] Hall thruster for lunar transfers in 2004 (Racca et al., 2002).

The huge interest in space flight also led to a rising number of Earth-orbiting objects, which are threatening active satellites. The evolution of the total number of objects whose orbits are crossing the LEO region (defined here with an altitude below 2000km) is shown in Figure 2.1. The increase in the yearly object count of this report can be caused by various reasons. Besides additional launch vehicle upper stages, man-made satellites, and improved resolution of monitoring stations, fragmentation of already existing objects can lead to new objects. In Figure 2.1, the Chinese anti-satellite test on January 10$^{\text{th}}$, 2007 as well as the collision between an active Iridium communication satellite and a defunct Russian Cosmos satellite in 2009 can be clearly identified by a large increase in number of objects in 2008 and 2010, respectively (Kennewell and Vo, 2013). While first notes of the topic of space situational awareness can be traced back already to the era of the Space Race (ESA, 2019) and the postulation of the Kessler effect in 1978 (Kessler and

[1] NASA Solar electric propulsion Technology Applications Readiness

[2] Small Mission for Advanced Research in Technology

[3] Société nationale d'études et de construction de moteurs d'aviation; today: Safran Aircraft Engines

Cour-Palais, 1978), only the unexpected collision in 2009 aroused public interest. In 2002, the Space Debris mitigation guidelines were formulated by the Inter-Agency Space Debris Coordination Committee (IADC) and recommend that each satellite shall "[...] ensure that the lifetime after disposal will not exceed 25 years" (Inter-Agency Space Debris Coordination Committee, 2005), in order to limit the number of objects in an Earth orbit. However, no international rules regarding orbit control capabilities for collision avoidance maneuvering or accelerated end-of-life disposal exist yet, but such regulations are to be expected in the next years (Federal Communications Commission, 2020).

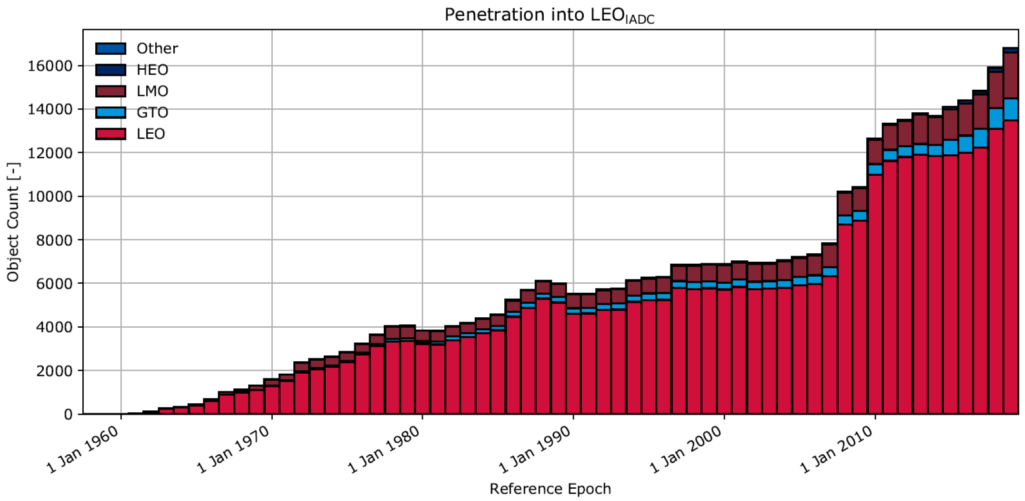

Figure 2.1: Evolution of absolute number of objects, residing in or penetrating LEO. (ESA, 2019)

In the years 2013-2019, the number of satellites with a mass of less than 10kg comprised of more than 40% of all launched satellites worldwide, according to Bryce Space and Technology (2020). Future satellite constellation missions like Starlink, OneWeb, and Kuiper have the potential to increase the number of objects in LEO vastly. Thus, orbit control capabilities for very small satellites are an active field of research aiming, among other goals, at a sustainable use of space.

Changing the orbit of a spacecraft requires a change of the spacecraft's momentum. The satellite can either create the necessary thrust itself by employing a propulsion system or be affected by external forces which change its momentum.

Albeit the huge number of launched spacecraft in the nanosatellite regime, only few implementations of orbit control have been realized in the past. The Canadian mission CanX-4/5 is a key mission regarding formation flying on small satellites. In 2014, it demonstrated different formations at relative distances of up to 1000m by actively controlling the orbit of one spacecraft while the other one remained uncontrolled. The spacecraft have a cubic shape with an edge length of 20cm at a total mass of 15kg each. The cold gas propulsion system CNAPS[4] can produce a total Δv of 18m/s for the CanX-4/5 satellites at a specific impulse of 45s and thrust levels between 12.5mN and 50mN (Bonin et al., 2015).

[4]Canadian Advanced Nanosatellite Propulsion System

Nonetheless, its overall volume of 125x180x70mm^3 (Orr et al., 2008) and its wet mass of more than 1kg according to Eagleson et al. (2006) prevent its consideration for application on pico-satellites.

In the past, scientific returns of space missions were mostly based on single satellite missions. However, scientific space measurements based on single probes lack the time resolution at a single location, as the spacecraft moves at very high velocities. Nevertheless, due to the long development times and the associated high costs, only very few scientific multiple agent missions with conventional large satellites, such as Cluster, Themis[5]/Artemis, MMS[6], and the Van Allen Probes, have been implemented. The aforementioned missions each consist of two to five satellites with masses of the single spacecraft between 128-1500kg and an on-board propulsion system for orbit insertion and formation keeping. While small satellites at the scale of pico- and nanosatellites can not replace conventional satellites, multiple agent missions with hundreds of agents become feasible and may produce, albeit lower resolution, entirely new findings due to the high number of measurement probes. Nevertheless, to acquire a formation, these miniaturized spacecraft necessitate a technology advancement in orbit control, which should preferably keep the valuable space at the center and the outer faces unoccupied for scientific payloads.

This chapter introduces some general physical aspects of propulsion systems and gives an overview of possible orbit control devices applicable to small satellites. In the past decades, many academic and industrial developments led to the creation of numerous devices and it would go beyond the scope of this state of the art analysis to present an in-depth study for all orbit control devices available for all classes of satellites. The orbit control devices presented in more detail will focus on an application in the scope of nano-satellites up to a size of 3U CubeSats as these systems were taken into consideration for the UWE–4 mission and can be compared among each other. However, this chapter will show that most available small satellite propulsion systems have physical dimensions roughly at the size of a CubeSat unit themselves and therefore disqualify for application on UWE–4. Furthermore, none of the presented systems is already well established within the small satellite industry beyond the stage of an initial in-orbit demonstration. For readers interested in systems for larger satellites, the publications by Krejci and Lozano (2018) and Lemmer (2017) or the State of the art for Small Spacecraft Technology report (NASA, 2018) provide a good overview.

Partial content of this chapter was already published in (Kramer et al., 2020).

2.1 General aspects of propulsion systems

For small satellites up to 3U CubeSats, the mass, size and power available for propulsion systems is limited. As the physical size is restricted by the CubeSat form factor, the

[5]Time History of Events and Macroscale Interactions during Substorms
[6]Magnetospheric MultiScale

targeted mass for a propulsion system should amount to a few kgs at most as the spacecraft also needs capacity for the remaining bus and the scientific or industrial payload. The available orbit average power of a 3U CubeSat can be estimated at a range of 15-120W according to (Krejci and Lozano, 2018). Nevertheless, the use of deployable solar panels can change these values considerably.

For the comparison of different propulsion systems some physical magnitudes shall be introduced following (Sutton, 1986). The specific impulse I_{Sp} of a propulsion system is defined as

$$I_{Sp} = \frac{|\mathbf{v}_e|}{g_0} = \frac{|\mathbf{F}|}{g_0 \cdot \dot{m}}. \tag{2.1}$$

In this equation, $\mathbf{v}_e$ denotes the exhaust velocity of the propellant relative to the propulsion system, g_0 represents the standard gravity constant[7], $\mathbf{F}$ is the created thrust and $\dot{m}$ the mass loss of the satellite due to the ejected propellant. The total impulse of a propulsion system describes the possible change of momentum of the spacecraft and calculates as

$$I_t = |\mathbf{F}| \cdot t \tag{2.2}$$

$$\approx m_{Sat} \cdot \Delta v. \tag{2.3}$$

Eq. (2.2) is valid for propulsion systems creating a constant thrust $\mathbf{F}$ over the total active time t until the propellant is depleted. Eq. (2.3) is an approximation of the available Δv for spacecraft with a negligible propellant mass compared to the mass of the spacecraft. This assumption is usually only valid in certain cases of electric propulsion systems.

Eq. (2.1) shows a proportional behaviour of the specific impulse I_{Sp} and the created thrust $\mathbf{F}$. Furthermore, Eq. (2.2) and Eq. (2.3) extend this proportionality to the total available Δv. Thus, the specific impulse can be regarded as a measure for the propellant mass efficiency of a propulsion system.

The purpose of the propulsion system depends on the mission scenario and determines the Δv as well as the thrust level requirements. Systems delivering thrusts at sub-µN levels can be used for precision attitude control, but will hardly impact the orbit of a small spacecraft. While orbit insertion maneuvers and interplanetary missions can require a total Δv in the range of $10^3 m/s$, drag compensation or deorbiting requires only up to $10^2 m/s$, and relative positioning in multi satellite missions may require amounts as small as $1 m/s$ (Krejci and Lozano, 2018).

2.2 Chemical propulsion

The energy source for chemical propulsion systems lies in the molecular bonds of the propellant itself. The operating principle of chemical propulsion systems is to create thrust using the expansion of a hot gas in a nozzle to an exhaust stream of lower density. The acceleration can thereby be created by different means and different propellants:

[7] g_0=9.80665 m/s^2 (Bureau international des poids et mesures, 2019)

- **Cold gas systems**, as shown in Figure 2.2a, expel gases stored in a high-pressure vessel, while

- **Warm gas propulsion systems** heat the gas previous to ejection in order to increase pressure, specific impulse and thrust, as depicted in Figure 2.2b. However, as both of these systems usually have a specific impulse below 100s, a large propellant tank has to be accommodated in order to create a reasonable Δv during mission lifetime.

- **Monopropellant thrusters** typically use the decomposition of a liquid which contains fuel and oxidizer into a hot gas. A schematic of this type of thruster is shown in Figure 2.2c. However, traditional systems use rather toxic propellants such as hydrazine (N_2H_4) or derivatives, which diminishes the launch opportunities for small satellites.

- **Bipropellant systems** combine fuel and oxidizer in a combustion chamber in order to create hot gases, as shown in Figure 2.2d. This system has the highest complexity due to two separate feed systems for oxidizer and fuel, but also offers the highest thrust level. For this reason, it is usually used in missions with significant Δv requirement.

- **Solid propellant** systems are combusting a solid propellant, which creates a hot expanding gas, as depicted in Figure 2.2e. This gas is subsequently expanded in a nozzle similar to the previous systems. Typically, these systems do not allow to vary the thrust and lack restart capability. This makes them rather attractive as end-of-life deorbiting devices.

- **Hybrid propellant** systems separate fuel and oxidizer. Figure 2.2f shows this separation. While the solid fuel is already in the combustion chamber, the liquid oxidizer is fed into the combustion chamber with a dedicated valve system. Thus, restarting capability is possible due to the valve. This increased complexity makes them fairly unattractive for small satellites.

While only a few satellites in the small satellite class have successfully demonstrated propulsion systems in-orbit, almost all of these demonstrations employed cold gas propulsion systems. The chemical propulsion systems with flight heritage are shown in Figure 2.3.

The first in-orbit demonstration of a propulsion system on a 3U CubeSat was conducted on board of the Canadian CanX-2 satellite in 2008. During this mission, the cold gas Nano Propulsion System (NANOPS), which was developed at the *University of Toronto* with an average I_{Sp} of 46s and uses liquid SF_6 as propellant, created a maximum thrust level of 35mN (Sarda et al., 2008). The system has a power consumption of 4W with an overall volume of 50x50x100mm^3 and a total Δv of 2m/s for a standard 3U CubeSat (Mauthe et al., 2005). This mission served as a precursor mission to the formation flying mission of CanX-4 and CanX-5, which utilize the flight heritage of the NANOPS system for the successor Canadian Advanced Nanosatellite Propulsion System (CNAPS).

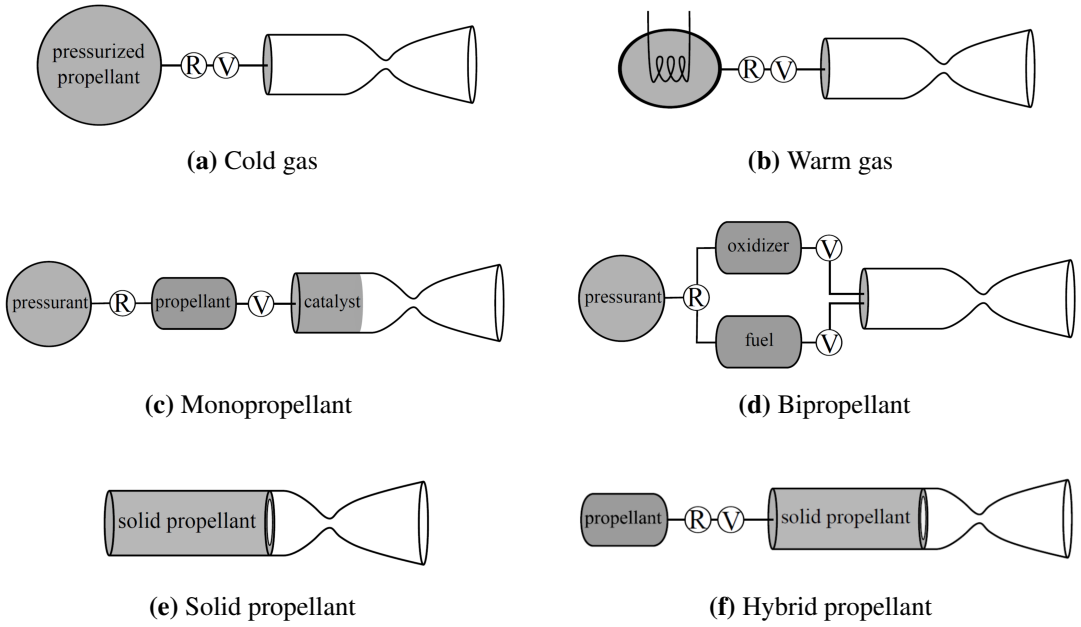

(a) Cold gas

(b) Warm gas

(c) Monopropellant

(d) Bipropellant

(e) Solid propellant

(f) Hybrid propellant

Figure 2.2: Operating principle of chemical propulsion systems (Krejci and Lozano, 2018)

In 2013, the 3U CubeSat mission Delfi-n3Xt of the Delft University of Technology activated the T^3-µPS cool gas propulsion system. This system was developed by *TNO Defence, Security and Safety* and stored nitrogen in a solidified grain as propellant. While ground experimentation resulted in a maximum thrust of 6mN, the in orbit experimentation ended before any thrust could be measured (Guo et al., 2015). The propulsion system has a mass of 120g and a volume of 100x100x35mm^3 (de Jong et al., 2008).

The Singaporean 3U CubeSat "Propulsion Operation Proof SATellite – High Performance 1" (POPSAT-HIP1) demonstrated a cold gas propulsion system by *Microspace* in 2015. It utilizes eight micronozzles of 1mN thrust each. In the demonstrator mission, 2U of the CubeSat structure were occupied by the pressurized tank for the Argon propellant. During the mission, the system was used for attitude control experiments (Manzoni and Brama, 2015).

The Chinese 3U CubeSat STU-2A, also known as TW-1, was launched into orbit in 2015 and demonstrated the Swedish cold gas propulsion system called CubeProp by *NanoSpace*. Although some difficulties with the thrusters arose during operations, in-orbit experimentation raised the altitude of the spacecraft by 600m (Wu et al., 2016).

In 2018, the first interplanetary 6U CubeSat mission "Mars Cube One" (MarCO) with the goal to support the InSight Mars Lander used its cold gas propulsion systems by *VACCO* for trajectory correction maneuvers. A total Δv of more than 9.2m/s was applied to the spacecraft (Klesh et al., 2018). The propulsion system has a total mass of 3490g and a volume of 206x151x83mm^3 (VACCO Industries, a).

The New Zealand company *Dawn Aerospace* developed a bipropellant propulsion module at a volume of 70-97.7x95.4x95.4mm^3 and a mass of 1170-1410g. It consumes 12.5W power during operation and delivers a total of 425-850Ns at a nominal thrust of

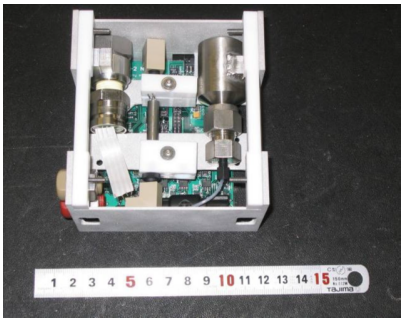

(a) NANOPS, demonstrated on CanX-2 in 2008 (Sarda et al., 2008)

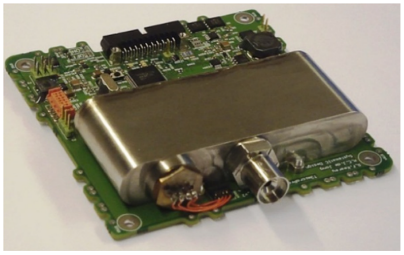

(b) T^3-µPS, demonstrated on Delfi-n3Xt in 2013 (Guo et al., 2015)

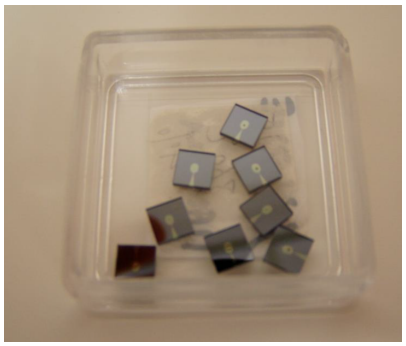

(c) Nozzles of micropropulsion system, demonstrated on POPSAT-HIP1 in 2015 (Manzoni and Brama, 2015)

(d) CubeProp, demonstrated on STU-2A in 2015 (Palmer et al., 2016)

(e) JPL MarCO, demonstrated 2018 on MarCO (VACCO Industries, a)

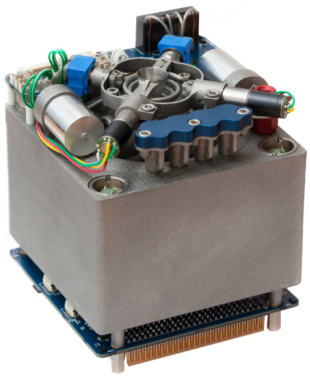

(f) CubeSat Propulsion Module by *Dawn Aerospace*, demonstrated on ION in 2020 (Dawn Aerospace, b)

Figure 2.3: Chemical propulsion systems with flight heritage on small platforms

0.5N (Dawn Aerospace, a). This thruster was launched on September 3rd, 2020 in the *D-Orbit* In Orbit Now (ION) mission (Dawn Aerospace, 2020) and is planned for another *D-Orbit* mission in late 2020. However, no in-orbit data has been presented so far.

Apart from the previously described propulsion systems which were demonstrated already in orbit, numerous chemical propulsion systems were developed in recent years

and were sometimes even launched into orbit, but lack documentation of flight experience. Selected propulsion systems on the rise will be discussed in the following:

The Lithuanian company *NanoAvionics* has developed a chemical propulsion system utilizing the non-toxic monopropellant ammonium dinitramide. The system occupies a volume of 1.3 CubeSat units at a mass of 1.2kg but delivers more than 400Ns of total impulse at a power consumption of about 10W (NanoAvionics). While this system was launched in 2017 on the 3U CubeSat LituanicaSAT-2, unfortunately no documentation about successful in-orbit demonstration could be found.

The Swedish company *ECAPS by Bradford* offers various propulsion solutions employing a green propellant for CubeSats and small satellites. While having flight heritage from the Swedish Prisma mission and the SkySat Earth observation satellites with thrusters in the 1N class, the CubeSat propulsion system in the 100mN class is still waiting for its in-orbit demonstration (Bradford-ECAPS). A CubeSat propulsion system with a size of approximately 1.3 CubeSat units combining the 100mN class thruster with *VACCO*'s Micro Propulsion System shall be demonstrated in the 6U CubeSat ArgoMoon mission in 2021 (VACCO Industries, b).

The US company *Tethers Unlimited, Inc.* developed the propulsion system Hydros-C, which uses water as propellant in a hybrid electrical/chemical operation scheme based on electrolysis. It has a mass of 2.7kg, and a volume of 190x130x92mm^3, and a power consumption of 5-25W at a total impulse of 2151Ns (Tethers Unlimited). It is planned to be demonstrated in orbit on board the Pathfinder Technology Demonstrator (PTD) 1 mission in late 2020 (Messier, 2018).

While this list is not exhaustive, it can be seen that except for the T^3-µPS cool gas propulsion system used in the Delfi-n3Xt satellite, all other presented systems are applicable for nanosatellites with at least 3 CubeSat units size. Even though the T^3-µPS system could be integrated on a smaller bus, the systems' maturity and applicability for orbit control purposes has not been demonstrated yet.

2.3 Electric propulsion

The general difference between chemical and electric propulsion systems is the source of energy for the propellant acceleration. In electric propulsion systems it is converted electrical energy, which is usually harvested using solar cells in small satellites. This comes with the advantage that the propellant of electric propulsion systems itself usually is not explosive. Additionally, these systems generally have a higher specific impulse I_{Sp} than their chemical counterparts, which makes them very attractive for small satellites in terms of mass savings.

While the energy for the acceleration of the propellant is electrical energy, the exact mode of acceleration separates the electric propulsion systems into three groups.

2.3.1 Electrothermal acceleration

Electrothermal thrusters increase the temperature of the liquid propellant by using electric energy in order to augment the exhaust velocity of the propellant after expansion at the

nozzle. Thus, this is a similar operating principle to those in chemical propulsion systems. Figure 2.4a shows the simplest implementation of this operating principle - a resistojet. An electric current heats an ohmic resistor which subsequently heats the propellant. Albeit the simplicity of the implementation, no resistojet implementation has flown on small satellites below a mass of 10kg yet.

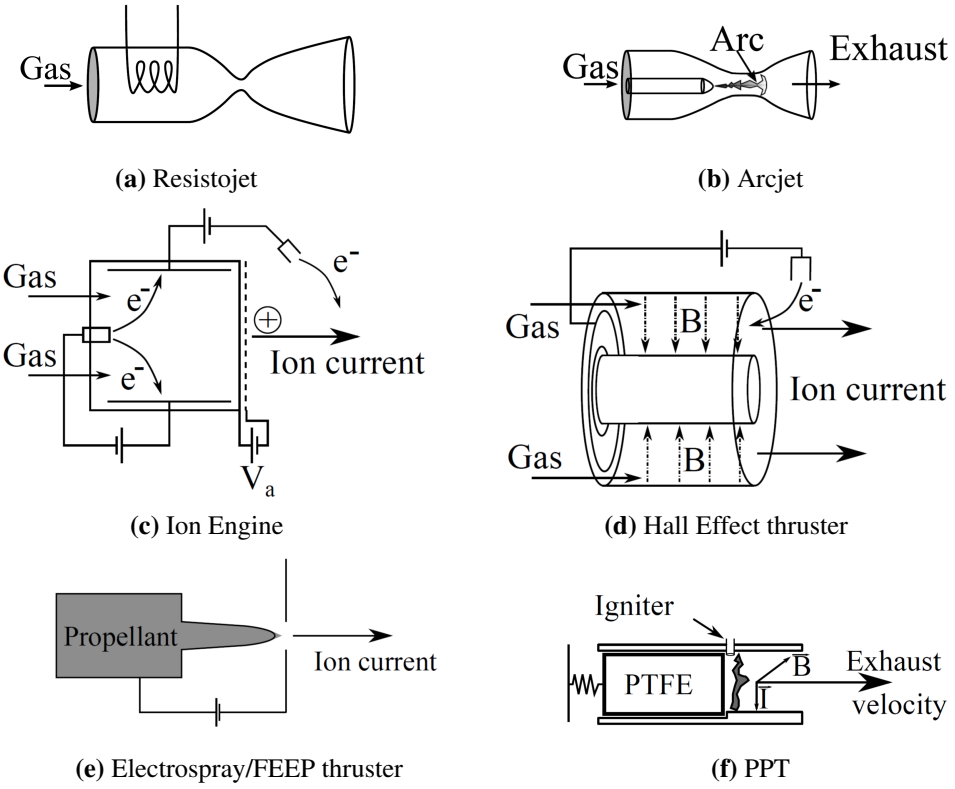

(a) Resistojet **(b)** Arcjet

(c) Ion Engine **(d)** Hall Effect thruster

(e) Electrospray/FEEP thruster **(f)** PPT

Figure 2.4: Operating principle of electric propulsion systems (Krejci and Lozano, 2018)

Arcjets resemble another implementation of electrothermal thrusters. A schematic of this thruster is shown in Figure 2.4b. The propellant is heated when it passes through a plasmic discharge arc. As this necessitates an additional fluidic system and a Power Processing Unit (PPU) for the discharge arc, the increased complexity makes this system unattractive for application in small satellites.

Bradford Space offers an electrothermal propulsion system which uses water as propellant, has a volume of 100x100x260mm^3 and has a mass of 740g. It consumes 25-55W of electrical power and delivers a total impulse of 1155Ns at a thrust of 17mN. However, while versions of this propulsion system have flight heritage from missions like HawkEye360 and BlackSky Global, it was not yet implemented on a nanosatellite scale satellite (Bradford Space).

2.3.2 Electrostatic acceleration

The operating principle of electrostatic propulsion systems is based on the acceleration of charged particles by an electric field. Most of the systems accelerate ions of a gaseous or liquid propellant and therefore need certain means of neutralizing the exhaust plume to ensure charge neutrality.

The processes of ionization of the propellant and its acceleration are usually separated. Following ionization, the propellant is accelerated using the Coulomb force of an electric field and thus has the kinetic energy E_C. If the voltage U_E of the electric field accelerates the singly ionized propellant of mass m_p, the following relationship holds for the kinetic energy E_{kin} of the propellant:

$$\begin{aligned} E_{kin} &= E_C \\ \frac{m_p \cdot |\mathbf{v}_e|^2}{2} &= e \cdot U_E \\ \Rightarrow |\mathbf{v}_e| &= \sqrt{\frac{2 \cdot e}{m_p} \cdot U_E}. \end{aligned} \tag{2.4}$$

The elementary charge is denoted with e.

Assuming that the spacecraft is not exposed to external forces, the momentum of the spacecraft and the propellant has to be conserved. In the following equation of momentum conservation, the spacecraft with instantaneous mass m and velocity $\mathbf{v}$ ejects propellant of mass dm with the previously derived exhaust velocity $\mathbf{v} + \mathbf{v}_e$. Mathematically, this leads to

$$\begin{aligned} \tilde{\mathbf{F}} = \frac{d\mathbf{p}}{dt} &= \frac{d(m\mathbf{v})}{dt} + \left(-\frac{dm}{dt}\right)(\mathbf{v} + \mathbf{v}_e) \\ &= \frac{dm}{dt}\mathbf{v} + m\frac{d\mathbf{v}}{dt} - \frac{dm}{dt}\mathbf{v} - \frac{dm}{dt}\mathbf{v}_e = 0 \\ &\underbrace{m\frac{d\mathbf{v}}{dt}}_{\text{Change of momentum of spacecraft}} = \underbrace{\frac{dm}{dt}\mathbf{v}_e}_{\text{Thrust}}. \end{aligned} \tag{2.5}$$

The exhaust plume of every real propulsion system has a certain divergence which reduces the effectively created thrust and can be accounted for with the divergence efficiency η_{div}. Moreover, some emitted atoms may not be ionized but are ejected in a compound of partially ionized propellant. The ionization efficiency η_{ion} accounts for this effect. Inserting additionally the derived exhaust velocity from Eq. (2.4) into Eq. (2.5), the thrust

of an electrostatic propulsion system can be described by

$$\begin{aligned} |\tilde{\mathbf{F}}| &= \eta_{\text{ion}} \cdot \eta_{\text{div}} \cdot \frac{d\text{m}}{dt} |\mathbf{v}_\text{e}| = \eta_{\text{ion}} \cdot \eta_{\text{div}} \cdot \frac{d(\text{n} \cdot \text{m}_\text{p})}{dt} \cdot \sqrt{\frac{2 \cdot \text{e}}{\text{m}_\text{p}} \cdot \text{U}_\text{E}} \\ &= \eta_{\text{ion}} \cdot \eta_{\text{div}} \cdot \frac{d(\text{n} \cdot \text{e})}{dt} \cdot \sqrt{\frac{2 \cdot \text{m}_\text{p}}{\text{e}} \cdot \text{U}_\text{E}} \\ &= \eta_{\text{ion}} \cdot \eta_{\text{div}} \cdot \text{I}_\text{e} \cdot \sqrt{\frac{2 \cdot \text{m}_\text{p}}{\text{e}} \cdot \text{U}_\text{E}}. \end{aligned} \tag{2.6}$$

In this equation, I_e describes the ion current emitted by an electrostatic thruster.

Several types of electrostatic thrusters can be differentiated mainly based on their means of ionization:

- In **Ion engines**, the gaseous propellant is ionized in an ionization chamber previous to acceleration by electron bombardment (ThrustMe, 2019) or radiation (Busek, a). The ionized propellant is afterwards accelerated by a voltage drop between an extractor and an acceleration grid. This principle is depicted in Figure 2.4c. Ion erosion of the acceleration grid is a lifetime limiting factor for these thrusters. As the ionization efficiency depends on the residence time in the ionization chamber, the ability for miniaturization is limited.

  Even though the technology is mature on larger platforms and was in-orbit demonstrated on board of missions like Deep Space-1 (Brophy, 2002) and the "Gravity field and steady-state Ocean Circulation Explorer satellite" (GOCE) (Canuto and Massotti, 2009), no miniaturized version has been demonstrated yet. However, several development efforts are targeting the application of such propulsion systems on smaller platforms.

  The French company *ThrustMe* developed the NPT30 electric propulsion system with a volume of 1.5-2 CubeSat units and a total power consumption of 30-60W. This thruster uses iodine as propellant and produces 0.4-1.1mN thrust at a specific impulse of 3000N s (ThrustMe, 2019). It is awaiting its demonstration on-board the 6U CubeSat GOMX-5 in 2021 (Jones, 2019).

  The US based company *Busek Co.* developed the BIT-3 radio-frequency ion thruster with a volume of 180x88x102mm^3, a mass of 2.9kg and a power consumption of 56-80W (Busek, a). This iodine fuelled thruster delivers a thrust of 1.2mN with a specific impulse of 2500s. It is expected to perform its in-orbit demonstration in 2021 on board the Lunar IceCube mission (Folta et al., 2016).

- **Hall thrusters** - shown in Figure 2.4d - are the second type of electrostatic propulsion systems. Opposed to ion engines, they do not need an accelerator grid and thus remove this lifetime limiting factor. This system is based on a combined ionization and acceleration chamber, in which the propellant is ionized by collision with electrons produced outside the chamber. The propellant is injected into the chamber through the anode. While the electrons are attracted by the anode, a radial

magnetic field forces the electrons on circular paths inside the chamber, increasing the collision probability with the propellant particles. The charged propellant particles are then repelled by the anode.

While these thrusters are also applied in larger satellite mission, like the SMART-1 (Gonzalez del Amo et al., 2005) moon mission, only a few developments for small satellites can be observed currently and none has been demonstrated in orbit yet.

Current miniaturization efforts of the Halo Hall-Effect Thruster by the US company *ExoTerra* (ExoTerra) and the ExoMG-nano propulsion system by the French company *Exotrail* (Henry, 2020) are targeting 6U CubeSats.

- In **Field-emission electric propulsion (FEEP)** and **electrospray thrusters**, charged particles are produced by a potential difference applied between the liquid propellant and a counter electrode, such that "[...] electrostatic pull is counteracted by surface tension, forming a so-called "Taylor cone" [...]" (Krejci et al., 2015). The operating principle is shown in Figure 2.4e. As soon as the ionization threshold is surpassed, ions are ejected. FEEP thrusters use thin needles or capillaries wetted with metal propellants, which have to be heated to temperatures above the material's liquefaction temperature prior to the ejection of ions. In contrast, electrospray thrusters use ionic liquids or electrolytes as propellants, which do not necessitate liquefaction. As the local field strength at the ion ejection site increases with a sharper propellant tip, miniaturization is very favorable for the operation of this system.

  The Scalable ion Electrospray Propulsion System (S-iEPS) developed at the *Massachusetts Institute of Technology* has a volume of 0.2 CubeSat units, a mass of less than 100g and a power consumption of less than 1.5W and is depicted in Figure 2.5a. It delivered 74µN at a specific impulse of 1150s during laboratory experimentation (Krejci et al., 2015). It was launched into orbit on board of the 1.5U CubeSats of the AeroCube-8 mission in 2015 and 2016 and on board of the 3U CubeSats of the AeroCube-12 mission. Unfortunately, no results of in-orbit experimentation have been presented so far.

  The IFM Nano Thruster by the Austrian company *Enpulsion* is shown in Figure 2.5b and based on the FEEP operating principle, has a size of 100x100x82.5mm^3 with a mass of 900g and a power consumption of 8-40W. It delivers a total impulse of more than 5000N s at the nominal thrust level of 350µN and a specific impulse of 2000-6000s (Enpulsion). It demonstrated orbit control capabilities in early 2018 on board of a 3U CubeSat (Krejci et al., 2018).

  The NanoFEEP propulsion system by the German company *Morpheus Space* is shown in Figure 2.5c and is also based on the FEEP principle. It has a size of 90x25x43mm^3, a mass of 166-200g, a power consumption of 0.2-3W, and delivers a total impulse of up to 3400N s at thrust levels up to 40µN (Morpheus Space). This propulsion system was demonstrated on UWE–4 in 2019 and 2020. The design dedicated to UWE–4 will be detailed throughout this thesis. An upscaled version called multiFEEP is currently in development.

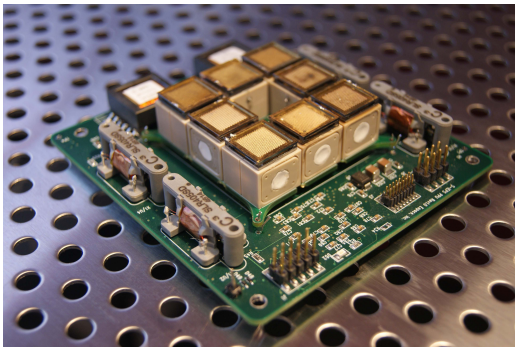

(a) S-iEPS, implemented on several AeroCube missions (Krejci et al., 2015)

(b) IFM Nano Thruster, demonstrated in early 2018 (Krejci et al., 2018)

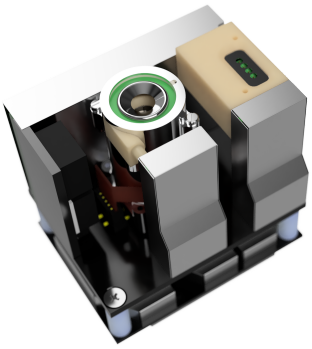

(c) NanoFEEP, demonstrated on UWE–4 with a dedicated setup in 2019 (Etherington, 2019)

Figure 2.5: Electrostatic propulsion systems with flight heritage on small platforms

2.3.3 Electrodynamic acceleration

In electrodynamic propulsion systems, the charged particles are accelerated by their interaction with magnetic fields. Since only propulsion systems with low power consumption are of relevance for small satellites, the analysis focuses on two types of propulsion systems working in a pulsed mode.

- **PPTs** are usually using a solid propellant, typically Teflon. The Teflon bar is ablated by a discharge arc between two electrodes as can be seen in Figure 2.4f. The Lorentz force created by the magnetic field of the discharge arc accelerates the ablated Teflon material.

- A **Vacuum Arc Thruster** or **Cathode Arc Thruster** also creates a discharge arc between two electrodes. However, the cathode is usually made of a soft metal which sublimes locally at the root of the discharge arc and is then accelerated with the same principle as described above.

Both of these systems present themselves favorable for miniaturization due to the solid propellant and scalable power consumption based on the frequency of the discharge arcs. However, the very short and high current of the discharge arc creates considerable

Electromagnetic interference (EMI) effects. While these effects can be mitigated to a certain amount by the design of the electric circuit, the limited spacing of components in small satellites counteracts the EMI mitigation.

The *George Washington University* has developed a Micro-Cathode Arc Thruster (µCAT) propulsion system. A system comprising of four thruster heads demonstrated rotation damping capabilities on board of the United States Naval Academy's 1.5U CubeSat "Ballistic Reinforced Communication Satellite" (BRICSat-P) which was launched in 2015, and is shown in Figure 2.6. It has a total mass of 600g, with a volume of 100x100x60mm^3 (Hurley et al., 2016). It can create impulse bits of 1mNs at a specific impulse of 2000-3000s (Lukas et al., 2014). It was also launched on-board the CubeSat "Astronomy by NASA and Yonsei using Vision ALignment eXperiment" (CANYVAL-X) (Park et al., 2016) and BRICSat2 (Kolbeck and Keidar, 2018) satellites in 2018, but unfortunately no in-orbit results are available.

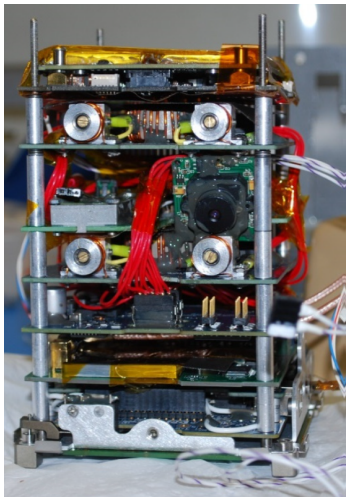

Figure 2.6: µCAT propulsion system, integrated on BRICSAT-P and demonstrated in 2015 (Hurley et al., 2016)

Several development efforts in the recent decades to miniaturize the PPT technology towards an application in the CubeSat scale have led to various systems which are waiting for their demonstration mission.

The UK company *MarsSpace* offers a PPT for CubeSat propulsion called PPTCUP, which has a mass of 280g at a volume of 90x90x25mm^3 and consumes 2W of power at a frequency of 1Hz ((Guarducci et al., 2011), (MarsSpace)). It creates an impulse bit of 34µNs at a specific impulse of approximately 600s.

Busek Co. offers the BmP-220 PPT, whose predecessor system has flight experience from the FalconSat-3 mission in 2007. The BmP-220 consumes less than 3W at a firing frequency of 1Hz, has a mass of 500g and a volume of 70x100x100mm^3. According to laboratory measurements, it provides impulse bits of 20µNs and is aiming at a total impulse of 175Ns (Busek, b).

2.4 Passive devices

Passive orbit control devices are not based on the operating principle of the acceleration of ejected mass (propellant) like the previously presented propulsion systems, but make use of external sources for momentum exchange. As such, they have only limited control capability, for example by being able to modify the orbit's altitude but not the orbital plane. For more details on the representation of a spacecraft's orbit the reader is referred to Chapter 7.

The passive orbit control systems with flight experience are depicted in Figure 2.7. Popular concepts for passive orbit control devices are described hereafter based on their source of momentum:

- **Atmospheric drag** devices are based on the interaction of the satellite with a planet's atmosphere by changing the cross-sectional area of the spacecraft. If the cross-sectional area of a satellite is increased, it will be exposed to more atmospheric drag, thus, the satellite's orbit altitude will decrease. For this reason, these devices are mostly used for end-of-life deorbit scenarios. Possible devices include deployable drag sails like used on the 3U CubeSat mission InflateSail (Taylor et al., 2018) or foldable wings as demonstrated by the AeroCube 4 mission (Gangestad et al., 2013).

- **Solar radiation pressure** is another possible source of external momentum in space. In order to make use of this momentum, a solar sail has to be deployed, which transfers momentum to the spacecraft by reflecting solar photons. After the demonstration on the Earth-Venus interplanetary journey on the Japanese small satellite IKAROS (307kg) (Tsuda et al., 2011), the 3U CubeSat mission LightSail2 changed its apogee altitude in LEO (Spencer et al., 2020).

- **Magnetic fields** of a planet exert the Lorentz force on a conductive electrodynamic tether with a supplied current. This force has the ability to de-/accelerate the spacecraft and thus de-/increase its orbit altitude. The CubeSat based missions Multi-Application Survivable Tether (MAST) (Voronka et al., 2007) and ESTCube-1 (Noorma, 2014) were all designed to demonstrate electrodynamic tether technology but unfortunately none of them can provide sufficient data to support the claim of successful tether deployment.

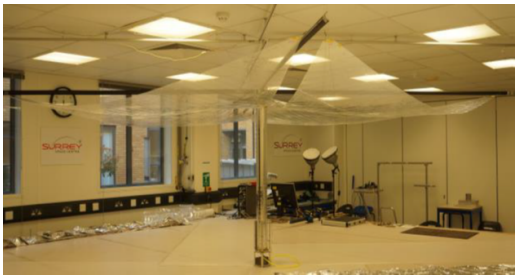

(a) InflateSail, drag sail demonstrated in 2017 (Taylor et al., 2018)

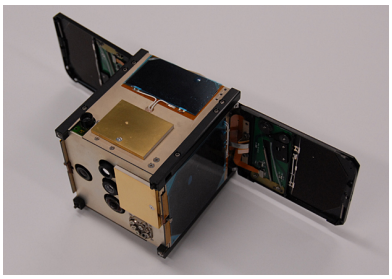

(b) AeroCube 4, demonstrated foldable wings for drag control in 2012 (Cowing, 2013)

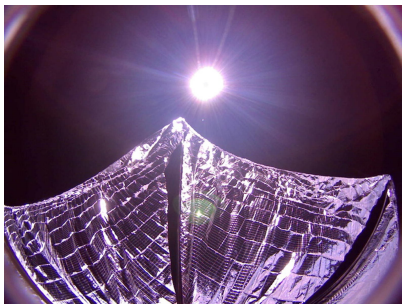

(c) LightSail2, after deployment in 2015 (Spencer et al., 2020)

Figure 2.7: Passive orbit control system with flight heritage

2.5 Summary

This chapter provided an insight into the historic developments of space flight, which lead to the need of orbit control capabilities of small satellites in order to enable novel science measurements and a sustainable industry.

Several different technologies and current developments that can be used as a means for orbit control were described. Passive devices have presented possibilities to use external momentum transfer sources for the reduction of the altitude of small spacecraft. So far, the most in-orbit demonstrated propulsion technologies for CubeSats were cold gas thrusters - most probably due to their simplicity in integration and operation. While cold gas propulsion systems provide high thrusts when compared with electric propulsion systems, the specific impulse is usually at least one order of magnitude lower. Consequently, electric propulsion systems need to be activated for a longer duration to achieve a similar Δv but the necessary propellant will be smaller.

However, as small satellites are limited by size and mass, electric propulsion systems with comparatively high mass efficiencies offer a viable alternative. In the past, three different electric propulsion systems were integrated on 1.5-3U CubeSat missions with different levels of success. Only the IFM Nano Thruster by *Enpulsion* could control the orbit of a 3U CubeSat using an electric propulsion system. Nonetheless, as this system itself consumes almost an entire unit of a CubeSat, a solution applicable also to smaller platforms is still sought-after.

3
The UWE–4 CubeSat

A CubeSat is a satellite built of cubes – so-called units – each having a dimension of 10x10x13.5cm^3. Common designs of CubeSats range from single units to two and three units in a row, up to 2x3 or even 2x2x3 unit assemblies. Standard deployer mechanisms, which can often host three units in a row or twelve units in a 4x3 fashion, are installed on the launch vehicle. These satellites are almost always launched into orbit with a ride-share rocket which has a larger conventional satellite as main payload for which the operator intends to reduce the launch cost by taking CubeSats "piggyback". For this reason, the CubeSats must obey certain design rules so as not to jeopardize the mission of the main payload. These design guidelines are specified in the CubeSat Design Specification (CDS) (California Polytechnic State University, 2014). UWE–4 follows these guidelines with only minor alterations. Its design will be described in this chapter.

The UWE–4 project started as an educational small satellite project in 2015 and was funded under the program *Nationale Weltraumforschung und Weltraumtechnik – Robotik für Raumfahrtsysteme* of the *Deutsches Zentrum für Luft- und Raumfahrt* [German Aerospace Center] (DLR). The primary mission objective of UWE–4 was the technology demonstration and characterization of an electric propulsion system on-board a 1U CubeSat. The secondary objective in the context of the UWE series aimed at the in-orbit demonstration of orbit control capabilities on the way to formation flying missions like NetSat and Telematics Earth Observation Mission (TOM) at the partner institute *Zentrum für Telematik* [Center for Telematics] (ZfT). To achieve this goal, the Julius-Maximilians-University Wuerzburg Chair for Computer Science VII: Robotics and Telematics provided the satellite bus and developed the requirements for a possible CubeSat propulsion system: its electrical supply, isolation, physical size and scope of application as attitude and orbit control actuator. The University of Technology Dresden Chair for Aerospace Engineering: Space Systems developed the NanoFEEP system. The satellite was launched as secondary payload on December 27$^{\text{th}}$, 2018 on-board a Soyuz-2 rocket from Vostochny, Russia into a sun-synchronous LEO at an average altitude of 586km.

The predecessor mission UWE–3 demonstrated attitude control capabilities and a novel satellite electrical interface standard (Busch, 2017), which was published by University Space Engineering Consortium (UNISEC) Europe and inherited by UWE–4. A view into the satellite structure of UWE–4 is depicted in Figure 3.1. The backplane architecture interconnects all subsystems, including the outer panels. The inter-subsystem communication is facilitated using a redundant multi-master I^{2}C bus. The bus features redundant power busses as well as synchronization lines and debug access to every subsystem. Each

subsystem has a standardized interface controller including a hotswap controller which allows to turn the supply of the subsystem off in case of overvoltage, undervoltage, or overcurrent faults autonomously, as well as to monitor, control, and measure the voltages, currents, and power consumption of each single subsystem.

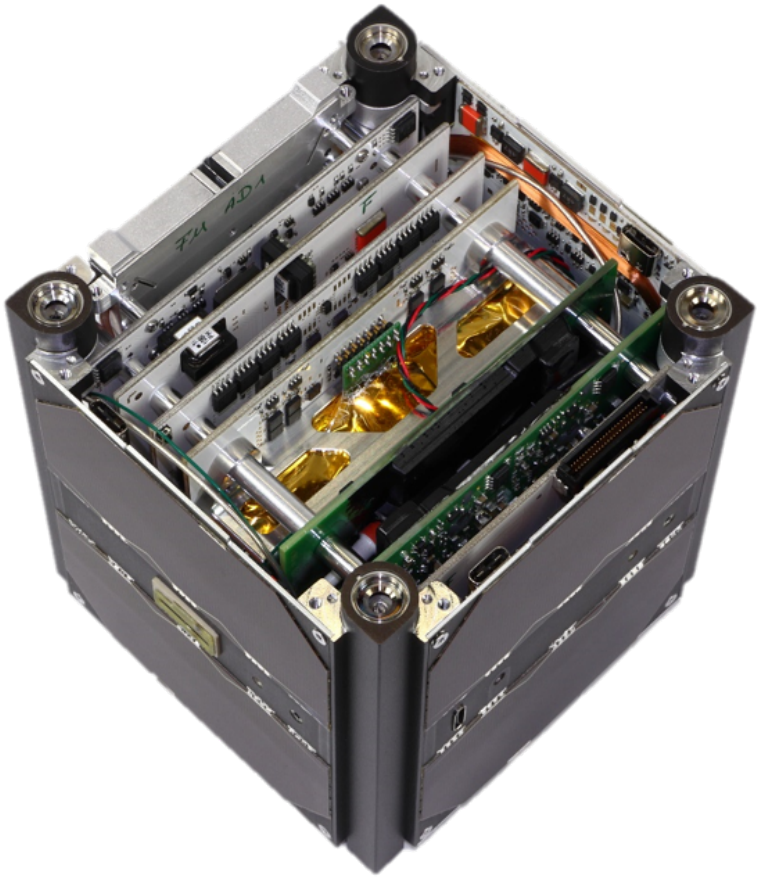

Figure 3.1: A photograph of the UWE–4 CubeSat flight model without the +Z panel (Kramer and Schilling, 2021).

The NanoFEEP system was chosen since it meets the requirements of power and mass of a 1U pico-satellite. Additionally, the physical size of the thruster heads allowed the placement in the rails of the CubeSat structure, which kept the valuable space at the outside panels of the satellite free for solar panels and sun sensors or potential other components in a future mission. Furthermore, this placement of the thruster heads makes it possible to not only use the thrusters collectively as an orbit control device, but also to use them individually as attitude control actuators around body x- and y-axis. This high degree of integration also allows for the interpretation of the propulsion system as part of the bus for future mission objectives. The PPU which is necessary for power conversion was realized by our partners at TU Dresden as a standard UNISEC subsystem. Thus, it was easily integrated into the satellite bus.

The outer dimensions of the CubeSat structure are following the guidelines for a 1U CubeSat with a total satellite mass of 1110g. Figure 3.2 shows the setup with its individual subsystems. It inherits various features from its predecessor mission UWE–3, such as the mechanical structure and the overall design of the Radio Communication System (COMM), the On-Board Data Handling System (OBDH), the AOCS, the EPS and the Front Access Board (FAB). These subsystems have been improved considerably in comparison to their previous version. The Backplane (BP) and the outside panels have been re-designed entirely. All subsystems of the CubeSat follow the UNISEC Europe subsystem interface definition. Except for the NanoFEEP propulsion system from TU Dresden, all subsystems were developed and designed at the University of Wuerzburg.

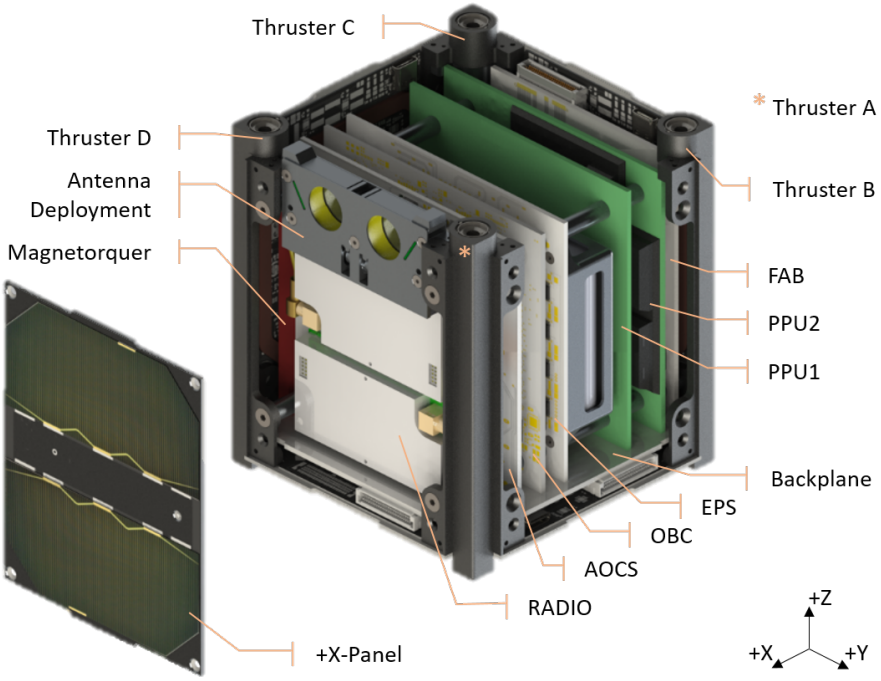

Figure 3.2: A CAD model of the UWE–4 CubeSat. (Kramer et al., 2020)

As the AOCS plays an integral part in both, the thrust direction estimation algorithm in Chapter 6 and in the orbit control described in Chapter 7, its relevant design aspects will be described in this chapter shortly. Furthermore, the used NanoFEEP propulsion system with a special focus on precautions dedicated to its electrical properties is detailed. Chapter 3.2 contains considerable text fragments which were already published in Kramer et al. (2020). Moreover, the overall design of the UWE–4 CubeSat including the placement of the propulsion system was previously published in Kramer and Schilling (2021), Kramer et al. (2019), Kramer et al. (2017a), Bangert et al. (2017).

3.1 Attitude and Orbit Control System

The AOCS of the UWE–4 satellite was designed as a standard UNISEC subsystem with a low-power Texas Instruments MSP430^{TM} micro controller. A photograph of the AOCS

subsystem is shown in Figure 3.3. The software performs sensor fusion of the attitude determination sensors by making use of an Isotropic Kalman Filter (IKF) (Crassidis et al., 1995), as demonstrated in the predecessor mission UWE–3. Furthermore, it can compute the desired torques and thrusts for attitude and orbit control and distribute them to the subsystems housing the respective actuators.

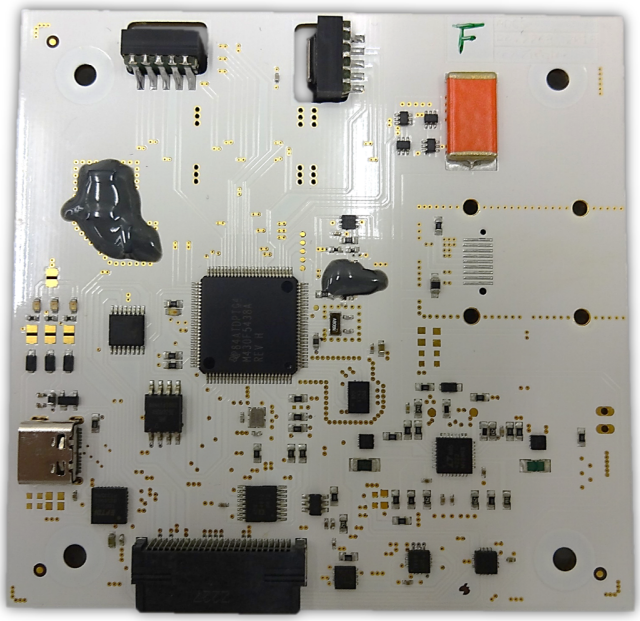

Figure 3.3: Attitude and Orbit Control System of UWE–4.

The AOCS was equipped with novel sensors and stronger actuators than its predecessor UWE–3. However, the magnetometers and gyroscopes of UWE–3 have been kept on the system as a backup. The novel sensor suite comprises of the integrated Microelectromechanical system (MEMS) Inertial Measurement Unit (IMU) BMX055 with a 3-axis gyroscope, magnetometer, and accelerometer each (BMX, 2013). The AOCS and each panel hold an IMU for redundancy.

Additionally, a 250x250 pixel ultra low power CMOS image sensor was fitted with a pinhole aperture with a total physical footprint of 1x1x1.7mm^3 and was integrated into each outside panel as sun sensor. A photograph of this sun sensor is depicted in Figure 3.4. Each of these sun sensors has a field of view of approximately 110° and a nominal power consumption of 4.2mW.

The main attitude control actuators are magnetorquer air coils which are placed on the inside of each panel. During the predecessor mission UWE–3, the attitude control experiments were complicated by a residual internal magnetic dipole moment of a similar magnitude as the total magnetic torque that can be created with its magnetorquers ((Busch et al., 2014), (Busch et al., 2015)). In response to this complication, the magnetorquers of UWE–4 were designed with twice the total magnetic moment of UWE–3 which sums up to 0.1A m^2 per axis.

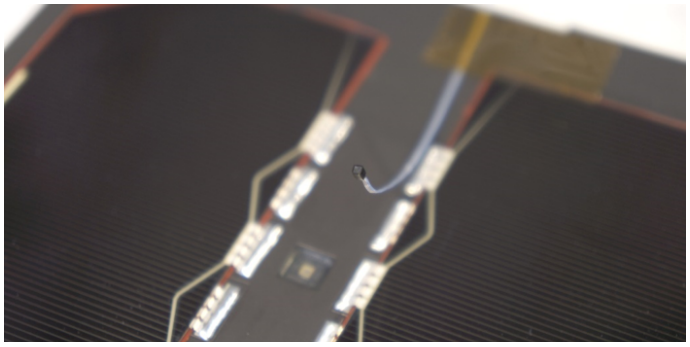

Figure 3.4: Miniature image sensor used as sun sensor on UWE–4 in front of an UWE–3 panel. (Bangert et al., 2017)

3.2 The NanoFEEP system

The propulsion system installed on UWE–4 ((Bock et al., 2014),(Bock et al., 2015), (Bock et al., 2016)) consists of two PPUs, which supply the voltages for two thrusters and one neutralizer each. While the PPUs are placed inside the CubeSat structure as standard UNISEC subsystems, one thruster is placed at the end of each rail in positive z-direction of the body frame (refer to Figure 3.2). One neutralizer each is placed at the center of the panels in positive and negative y-direction. One PPU controls thrusters A and B as well as neutralizer A. Thruster C and D, along with neutralizer B, are controlled by the second PPU. This serves for redundancy in PPUs, neutralizers and thrusters.

The mounting inside the rails ensures a precise thrust vector installation and minimizes the high voltage's and ion emission's impact on the overall satellite system. The CDS encourages to use the end of the rails as contact points for the separation springs of the adjacent CubeSat in the same deployer of the launch vehicle. However, such separation springs of other CubeSats could have harmed the thruster heads and, thus, UWE–4 was launched without another CubeSat in its deployer. Alternatively, UWE–4 could have been placed at both ends of the deployer.

3.2.1 NanoFEEP thruster

The thruster heads of the propulsion system are of electrostatic type. A cutaway view is depicted in Figure 3.5a.

The Liquid metal ion source (LMIS) of this thruster consists of a very sharp needle which reaches into a propellant reservoir. This needle either has a very thin canal in the center (from now on called capillary) or is a porous tungsten needle (refer to Figure 3.5b) - both have the necessary capillary effects to supply liquefied propellant to the needle tip. In order to liquefy the propellant, a heater is integrated into the thruster head. An electric voltage of up to 12kV between the needle and the extractor cathode ionizes and accelerates single ions or small compounds of the thruster by electrostatic force. For this, a thruster needs a certain starting voltage in order to start emission of ions. The starting voltage level depends heavily on the sharpness of the needle tip. Figure 3.5d shows a porous tungsten needle with a tip radius of 0.8µm.

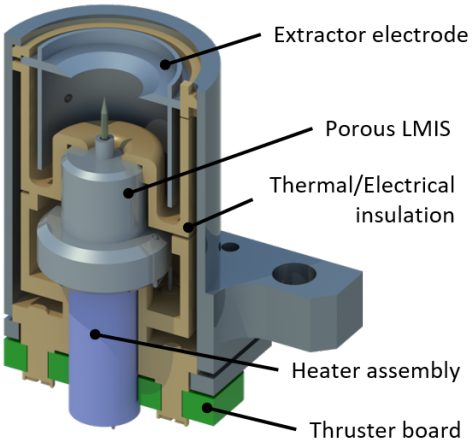

(a) Cut away view of the CAD model of a NanoFEEP thruster. (presentation of (Kramer et al., 2017b))

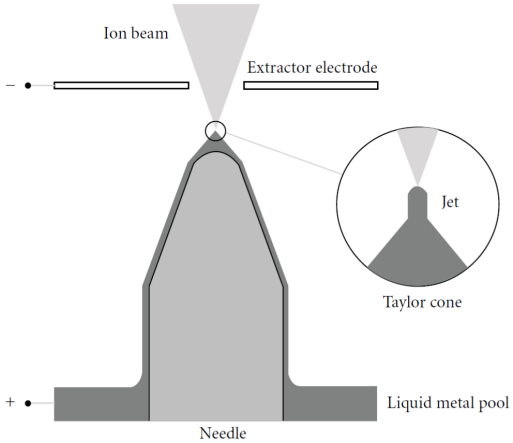

(b) Working principle of the LMIS (Tajmar and Scharlemann, 2011)

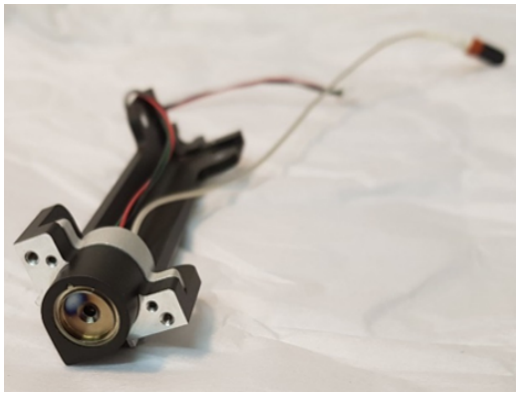

(c) Thruster head integrated into a CubeSat rail. (Kramer et al., 2020)

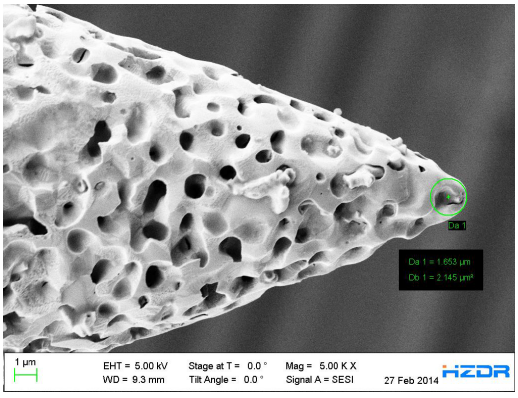

(d) Porous tungsten needle with a tip radius of 0.8 µm (Bock et al., 2014)

Figure 3.5: NanoFEEP thruster assembly

The integrated thrusters use 0.25g gallium each as propellant, which has a melting point of 29.76°C (Haynes, 2014). The needles of thrusters A and C are of porous type - thrusters B and D are capillaries. Each thruster head can realize a specific impulse I_{sp} in the range of 1000-8000s. The maximum possible Δv is about $15 m/s$ for a satellite mass of 1.3kg at thrust levels of up to 20µN per thruster (Bock et al., 2014). The created thrust can be calculated using Eq. (2.6). In the case of NanoFEEP thrusters, the propellant mass equates to the atomic mass of gallium[1], while the divergence efficiency η_{div} (depicted in Figure 3.6b) can be approximated using Malina's formula (Malina, 1940) with ion beam half-angle measurements taken from (Bock et al., 2017a). The ionization efficiency η_{ion} is approximately 1 for small thrusts, where single ions are separated from the needle tip and accelerated by the High voltage (HV). At higher thrust levels, compounds may be released which are only partially ionized. Thus, the ionization efficiency and the electrostatic

[1] $m_{Ga} = 69.723 \cdot 1.6605 \cdot 10^{-27} kg = 1.1577 \cdot 10^{-25} kg$ (Haynes, 2014)

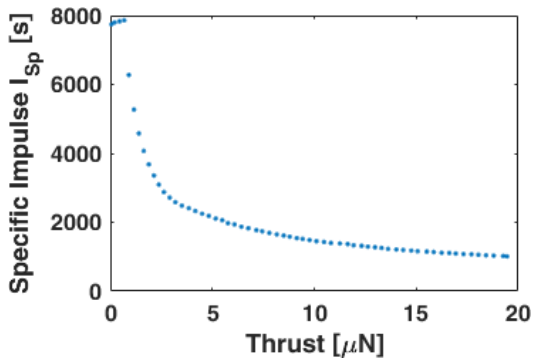

(a) Specific impulse I_{Sp} vs thrust (Bock et al., 2015)

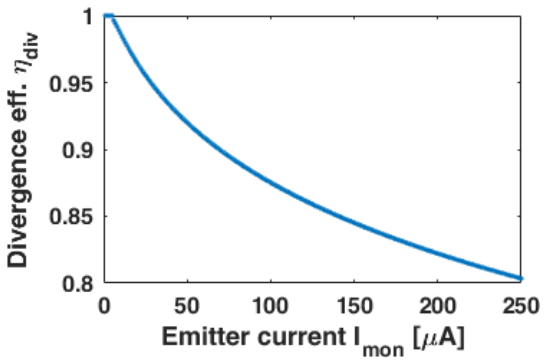

(b) Divergence efficiency η_{div} vs emitter current I_{mon}

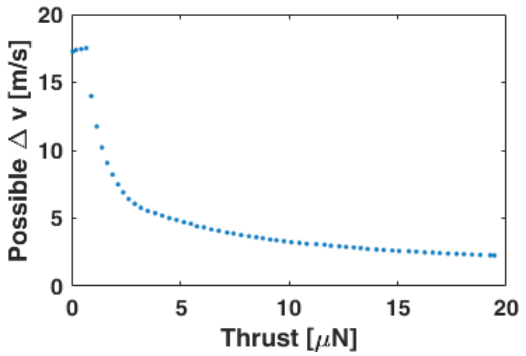

(c) Possible Δv vs thrust

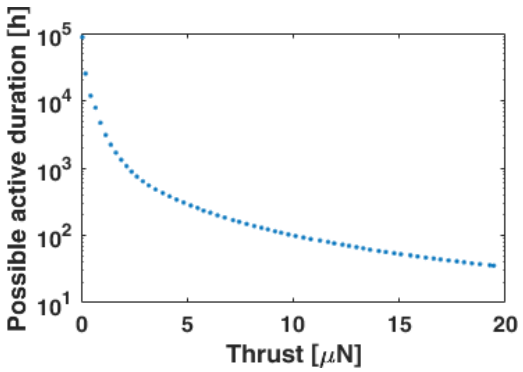

(d) Possible active duration before the propellant is depleted vs thrust

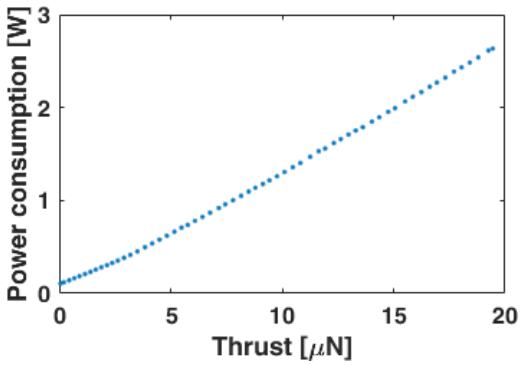

(e) Power consumption of a single thruster head including its heater vs thrust

Figure 3.6: NanoFEEP characteristics of each thruster head known prior to UWE–4.

acceleration force per gallium atom is smaller. This explains the decline of specific impulse of the thruster with increasing thrust level and is depicted in Figure 3.6a. As the specific impulse describes the mass efficiency of a thruster, the maximum possible Δv and firing duration until the propellant is completely depleted scales with the thrust and is shown in Figure 3.6c and Figure 3.6d. The expected power consumption per thruster head including its heater is depicted in Figure 3.6e. Thus, an activation of the propulsion system at low thrust levels below 5µN was envisioned for UWE–4 only during a fraction of an orbit.

As can be seen in Figure 3.5c, the rail itself is the housing of the thruster. Each thruster head has a length of 18.5mm, a diameter of 12mm, and a mass of about 6g.

3.2.2 Neutralizer

Due to the nature of the thrusters to eject only positively ionized gallium, the satellite could charge up negatively relative to the surrounding space plasma (Tribble, 2003). In a best case scenario, this would only affect the efficiency of the thruster heads, but it could also lead to electrostatic discharges and harm the electronics of the satellite. Thus, two neutralizers were installed in order to mitigate spacecraft charging effects. The electron sources on Panels -Y and +Y will from now on also be called neutralizer A and B, respectively.

Like the thrusters, the neutralizers were also developed by TU Dresden and use Carbon nanotubes (CNTs) deposed on a silicon chip (Bock et al., 2016). A schematic of the physical principle of the electron source is depicted in Figure 3.7b. A photograph of the CNTs, taken with a Scanning Electron Microscope, is shown in Figure 3.7d. HV between the silicon chip and an opposite extractor grid accelerates electrons by means of a similar working principle like the thrusters. However, this chip already starts to eject electrons at a voltage just above 1kV.

In order to mount the neutralizer at the outside panel (refer to Figure 3.7c), a protrusion has been attached to the insulating housing as shown in Figure 3.7a, such that it can be glued with epoxy on the inside of the panel. It has a physical size of 18.5x9.5x4.5mm^3 and a mass of 2g.

3.2.3 Power processing unit

The PPU as a subsystem following the UNISEC electrical interface standard also features a very low power Texas Instruments MSP430^{TM} microcontroller in order to command and monitor two thrusters, their respective heaters and one neutralizer. As such, it was able to convert the unregulated bus voltage from approximately 4.2V to up to 12kV for the thrusters and to up to 3kV for the neutralizers. Additionally, it features heating circuits for the thruster heads.

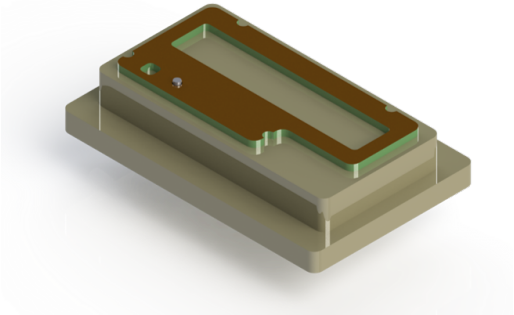

(a) CAD model of a neutralizer with the extractor grid in brown. (Kramer et al., 2020)

(b) Working principle of the neutralizer (Bock and Tajmar, 2016).

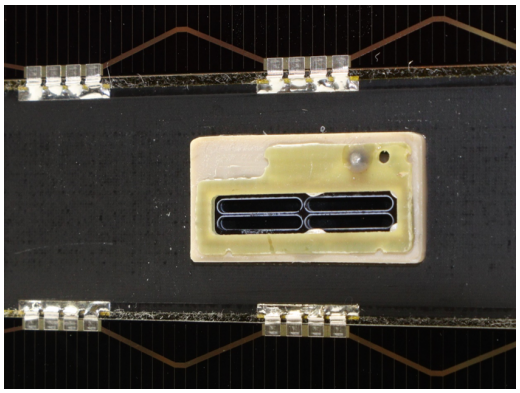

(c) Neutralizer integrated into a side panel of UWE–4. (Kramer et al., 2020)

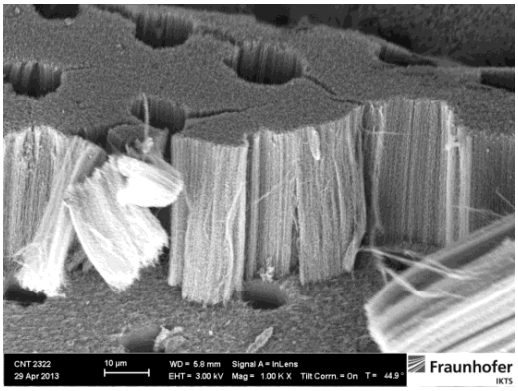

(d) Scanning Electron Microscope image of CNTs deposited on a silicon chip (Tajmar and Stämm, 2014).

Figure 3.7: Neutralizer Assembly

3.2.4 Precautions due to the propulsion system

The operating voltage and working principle of the propulsion system necessitated several precautions during satellite design already:

- Both PPUs face each other with the same side (refer to Figure 3.2), which houses the power conversion stage, since the power conversion may create EMI effects in the satellite. This way, the internal ground layer in the Printed circuit board (PCB) shields the electronics of the rest of the satellite.
- The power conversion stages are potted for improved isolation.
- The thrusters and the neutralizers are connected to the PPU with dedicated HV cables and are not put on the bus with all the other signals and power lines of the satellite, in order to secure the satellite bus from the HV. The heaters are also connected with a dedicated harness.
- The antennas of the radio communication subsystem are partially in the plumes of thrusters A and D. This could lead to charging of the antennas since transceivers are usually equipped with direct current blocking capacitors at the output. Thus, an

antenna bleeder resistor of 50kΩ is installed between antenna and ground potential. This enables the antennas to slowly discharge any static charge, but will not affect the 50Ω impedance. The transmission capability of the antennas as well as the received signal strength indication were experimentally tested during exposition to the thrusters' plasma plume prior to launch. In this test, the design approach of employing an antenna bleeder resistor proved to be effective. Neither the communication system nor any other part of the satellite indicated any harmful effects due to the exposition to the thrusters' plasma plume.

- The plumes of thruster A and D can also partially hit the lids of the antenna deployment system. Thus, the design of the lids was adjusted. On the one side, they need to be conducting for the ion charge hitting the lid to be compensated, on the other side, they need to be insulating to the antennas (refer to Figure 3.8). Consequently, they are produced of aluminium with an additional distance piece to the antenna made of Teflon.

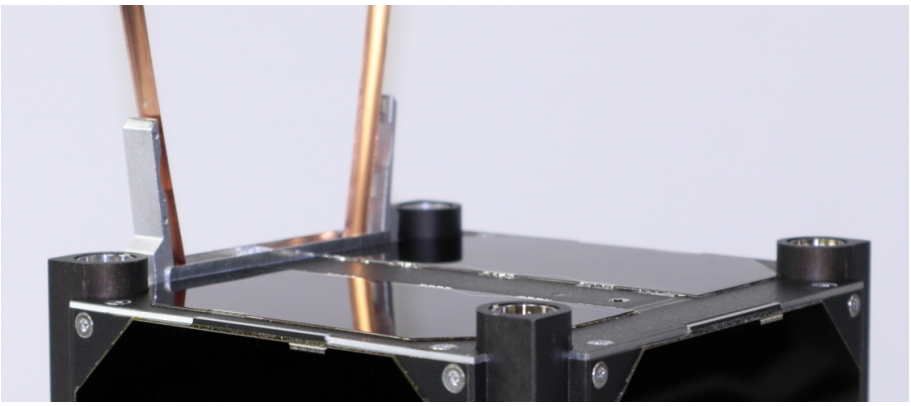

Figure 3.8: A photograph of the UWE–4 CubeSat with deployed antennas in front of two NanoFEEP thrusters. (Kramer et al., 2020)

- Moreover, several software components were implemented in order to detect possible upcoming failures of the power conversion stages, the thrusters or the neutralizers that could lead to spacecraft charging or to damage at any component.

3.3 Summary

This chapter discussed the design guidelines for the integration of a continuous electric propulsion system on-board of a 1U CubeSat at the example of UWE–4. The thruster heads were placed in the rails of the CubeSat structure, while the electron sources for charge neutralization were located on the side panels. Several precautions - taken at design level already - were detailed. Additionally, the CubeSat design itself, with a special focus on the AOCS and the entire NanoFEEP propulsion system, was described. Moreover, the operating principle and characteristics of the NanoFEEP propulsion system and its physical design parameters were given.

4
AOCS commissioning

Any spacecraft mission which is aiming at pointing a scientific or technical payload, like a camera or any other measurement device towards an object (e.g. on the Earth's surface) needs to be able to determine and finally control its attitude with a certain accuracy depending on the mission objective. While spacecraft with optical instruments need to be three-axis stabilized in order to make meaningful measurements, it is sufficient to point the antennas of communication satellites towards Earth or the desired ground station because the rotation around this direction is not important. Similarly, the thrusters of a propulsion system have to be pointed in a certain direction, with an arbitrary rotation around this direction in order to achieve the desired effect on the spacecraft's orbit.

The task of attitude determination is to fuse measurements from several sensors in a filter to minimize the effects of uncertainties of single sensors and to determine the attitude in all three axes. For this purpose, UWE–4 inherits an Isotropic Kalman filter implementation of UWE–3 (Kiefel et al., 2011) which was initially developed in the Tropical Rainfall Measurement Mission (Crassidis et al., 1995). Among the most frequently used attitude sensors are magnetometers - measuring the current magnetic field, sun sensors - determining the direction to sun, star trackers - determining the attitude relative to certain constellations, Earth horizon sensors - determining the direction towards the center of the Earth, and gyroscopes - measuring the angular rate of the spacecraft itself. Gyroscopes, as sensors independent of any outer field, provide only relative rotations and no absolute direction. While star trackers provide attitude information in all three axes, all other absolute sensors mentioned above identify one direction of the attitude, while the rotation around this direction is still unknown.

Actuators, such as magnetorquers, reaction wheels, control moment gyros or attitude control thrusters can be used to control the known attitude of the spacecraft to a desired attitude. However, in the case of actuators several devices have to be used in combination to be able to control the attitude about all axes of the spacecraft. While magnetorquers can only create torques perpendicular to the outer magnetic field, reaction wheels can only create a torque about its rotating axis and attitude control thrusters can only create torques perpendicular to their thrust direction and their position relative to the center of gravity of the satellite.

However, in the case of small satellites, size, mass and power restrictions limit the spectrum of usable sensors and actuators. Thus, UWE–4 was equipped with a 9-axis IMU and ultra-low power sun sensors on each outside panel as sensors and magnetorquers and the NanoFEEP propulsion system as attitude control thrusters.

The following chapter provides the physical background to understand the thrust direction estimation algorithm presented in Chapter 6 as well as attitude control algorithms applied for the purpose of orbit control in Chapter 7. The commissioning of the propulsion system will be described in Chapter 5.

The contents of this chapter have partially been published in Kramer et al. (2019) and Kramer and Schilling (2021).

4.1 The Euler equation

Euler's moment equation describes the attitude of a rigid body in its body frame by

$$\mathbf{T}_{\text{ext}} = \mathbf{I}\dot{\boldsymbol{\omega}} + \boldsymbol{\omega} \times (\mathbf{I}\boldsymbol{\omega}) \tag{4.1}$$

whereby $\boldsymbol{\omega}$ represents the angular rate of the rigid body in body frame with respect to inertial frame and $\mathbf{I}$ the moment of inertia tensor. $\mathbf{T}_{\text{ext}}$ represents all external torques acting on the rigid body. In the case of a satellite in LEO, well-described external torques can act on the body and have to be considered in the Euler equation.

The first class of external torques are desired torques, which are created by attitude control actuators. In the case of UWE–4, magnetorquers and thrusters can create torques. A magnetic torque has to be considered with an additional term of

$$\mathbf{T}_{\text{mag}}(t) = \boldsymbol{\mu}(t) \times \mathbf{B}(t). \tag{4.2}$$

In this equation, $\boldsymbol{\mu}$ describes the internal magnetic dipole moment and $\mathbf{B}$ the external magnetic field. In the case of a spacecraft, this is the desired magnetic moment created by the magnetorquers in the Earth's magnetic field.

A torque created by an attitude control thruster has to be considered in Eq. (4.1) with the following term

$$\mathbf{T}_{\text{thr}}(t) = \mathbf{r} \times \mathbf{F}(t). \tag{4.3}$$

$\mathbf{F}(t)$ describes the instantaneous thrust created by the thruster and $\mathbf{r}$ its position relative to the spacecraft's center of gravity.

The second class of external torques are unwanted attitude disturbance torques. There exist a multitude of sources of attitude disturbance torques. However, the most prominent sources that affect the attitude of a spacecraft in LEO are discussed as follows.

- A **gravity-gradient** within a spacecraft can lead to a torque in the gravity field of a celestial body, like Earth.
- An **aerodynamic** torque can act on a spacecraft moving in the (residual) atmosphere and increases with the distance between the center of mass and the center of pressure of the spacecraft.
- **Solar radiation pressure** can create a disturbance torque when impacting on surfaces of different absorption and reflection coefficients.

- **Static** and **induced magnetic fields** within the spacecraft can create torques according to Eq. (4.2). Magnetized material may be the source of a static magnetic field, while current loops within the satellite constitute a source of an induced magnetic field.

A dedicated estimation for the magnitude of these disturbance torques for 1U CubeSats at an altitude of 700km can be found in (Bangert, 2018). The result of this estimation is shown in Table 4.1.

Type	Typical disturbance
Static magnetic	$4.0 \cdot 10^{-6}$ N m
Induced magnetic	$0.4 \cdot 10^{-6}$ N m
Solar radiation	$5.0 \cdot 10^{-9}$ N m
Aerodynamic	$3.5 \cdot 10^{-9}$ N m
Gravity-Gradient	$1.7 \cdot 10^{-10}$ N m

Table 4.1: Typical contributions of the different disturbance torques on a 1U CubeSat in LEO. (Bangert, 2018)

4.2 Attitude disturbance estimation

As the thrust direction estimation algorithm in Chapter 6 is based on the analysis of the attitude of UWE–4, disturbance torques have to be considered in this analysis and for attitude control. According to Table 4.1, the most prominent disturbance torques are created by static magnetic fields. The predecessor mission UWE–3 had a very strong residual magnetic dipole moment in the order of $\boldsymbol{\mu}_{\text{res}} = [1.3,\ 15.9,\ -52.2]^{\intercal} \cdot 10^{-3} \text{A m}^2$ (Bangert, 2018). Therefore, the residual magnetic dipole moment of UWE–4 will be analysized in this chapter.

To determine the internal residual magnetic dipole moment, the Euler equation described in Chapter 4.1 is used for the analysis of the natural motion of the satellite's attitude. If the satellite's motion is only governed by a residual magnetic dipole moment $\boldsymbol{\mu}_{\text{res}}$, the Euler equation describing this motion looks as follows:

$$0 = \mathbf{I}\dot{\boldsymbol{\omega}}(t) + \boldsymbol{\omega}(t) \times (\mathbf{I}\boldsymbol{\omega}(t)) - \boldsymbol{\mu}_{\text{res}} \times \mathbf{B}(t) \tag{4.4}$$

Since the angular rate $\boldsymbol{\omega}(t)$ and the external magnetic field $\mathbf{B}(t)$ can be measured onboard the satellite and the change of the angular rate $\dot{\boldsymbol{\omega}}(t)$ can be derived numerically, the moment of inertia tensor $\mathbf{I}$ and the dipole moment $\boldsymbol{\mu}_{\text{res}}$ can be found by minimizing the objective function

$$\begin{aligned} E(\boldsymbol{\mu}_{\text{res}}, \mathbf{I}) &= \frac{1}{N} \sum_{i}^{N} \sqrt{\left(\mathbf{T}_{\boldsymbol{\mu}_{\text{res}}}(t_i) - \mathbf{T}_{\text{ext}}(t_i)\right)^2} \\ &= \frac{1}{N} \sum_{i}^{N} \sqrt{\left(\boldsymbol{\mu}_{\text{res}} \times \mathbf{B}(t_i) - \mathbf{I}\dot{\boldsymbol{\omega}}(t_i) - \boldsymbol{\omega}(t_i) \times \mathbf{I}\boldsymbol{\omega}(t_i)\right)^2}. \end{aligned} \tag{4.5}$$

The methodology of this analysis is described in more detail in Bangert (2018).

Several in-orbit measurements performed over the course of the mission of UWE–4 can be used for this analysis. The first measurement of the natural motion of the satellite was conducted on January 31st, 2019 and the last one on May 25th, 2020. The results are depicted in Figure 4.1.

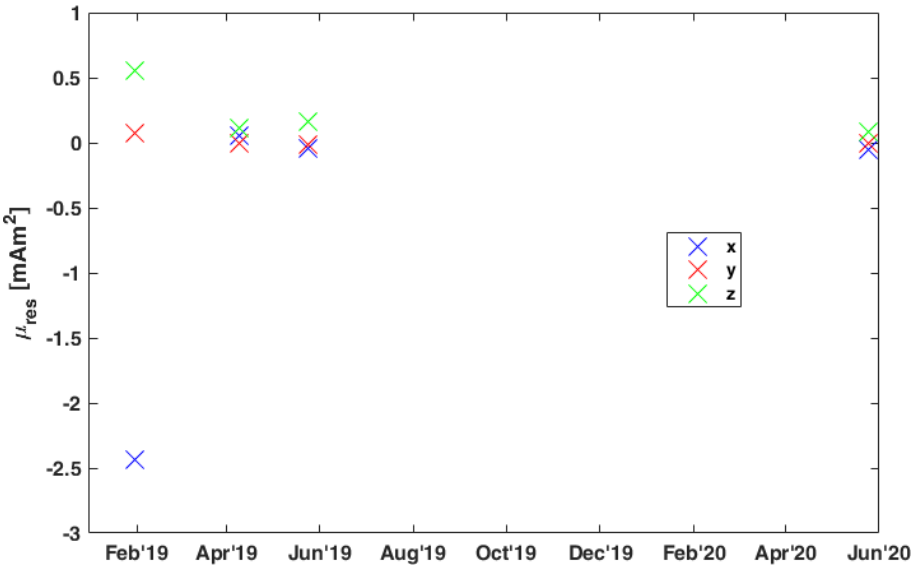

Figure 4.1: Found components of the residual internal magnetic dipole moment of UWE–4.

It can be noted, that the found residual magnetic dipole moments are about two orders of magnitude smaller than those of UWE–3 at an order of magnitude of $1 \cdot 10^{-5}\,\mathrm{A\,m^2}$. Thus, the magnetorquers of UWE–4 which can create magnetic moments up to $1 \cdot 10^{-1}\,\mathrm{A\,m^2}$ about each body axis can easily compensate for the smaller residual magnetic dipole moments of UWE–4. The small magnitude suggests that no residual magnetic dipole moment exists in UWE–4 at all. Nonetheless, Figure 4.2 depicts the normalized autocorrelation of the remaining unexplained torque before and after subtraction of the static magnetic torque, as described in Eq. (4.4), which shows that there is indeed a small residual magnetic dipole moment in the satellite.

A residual dipole moment and a moment of inertia tensor which is in good accordance with all of these measurements could be found as

$$\boldsymbol{\mu}_{\mathrm{res}} = \begin{pmatrix} -56.9 \\ -2.2 \\ 8.2 \end{pmatrix} \cdot 10^{-6}\,\mathrm{A\,m^2} \tag{4.6}$$

$$\mathbf{I} = \begin{pmatrix} 2.1591 \cdot 10^{-3} & -3.7083 \cdot 10^{-6} & -3.7846 \cdot 10^{-5} \\ -3.7083 \cdot 10^{-6} & 2.1861 \cdot 10^{-3} & 5.1167 \cdot 10^{-6} \\ -3.7846 \cdot 10^{-5} & 5.1167 \cdot 10^{-6} & 2.1481 \cdot 10^{-3} \end{pmatrix} \mathrm{kg\,m^2}. \tag{4.7}$$

The inertia tensor in Eq. (4.7) is also in very good accordance with a dedicated Computer Aided Design (CAD) model of UWE–4 which includes every component with at least

1g of mass. These values will be used in Chapter 6 for further analysis of the satellite's attitude motion in order to determine the thrust of the propulsion system.

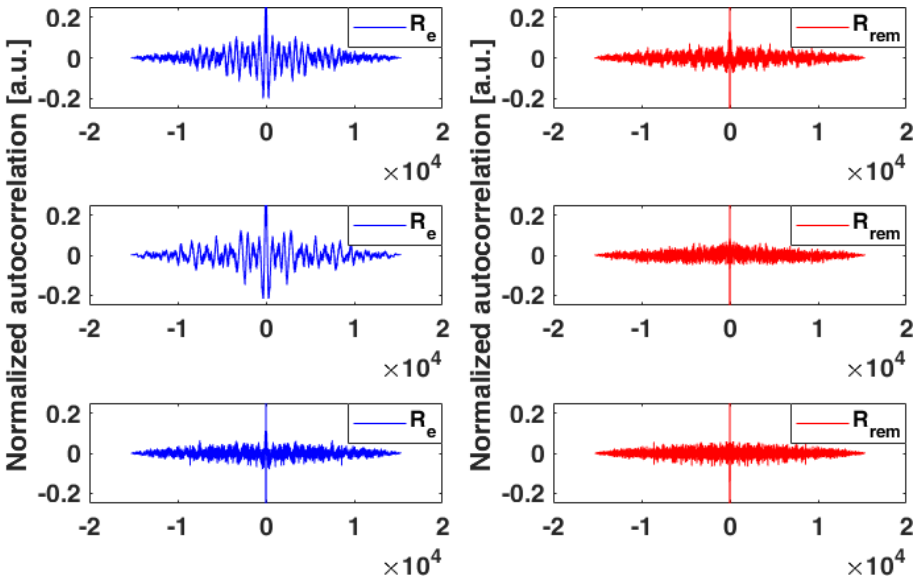

Figure 4.2: Components of the normalized autocorrelation of the external torque $\mathbf{T}_{\text{ext}}$ before (blue) and $\mathbf{T}_{\text{rem}} = \mathbf{T}_{\text{ext}} - \mathbf{T}_{\boldsymbol{\mu}_{\text{res}}}$ after (red) reduction of the static magnetic torque for the experiment on May 25$^{\text{th}}$, 2020.

4.3 Magnetic attitude control experiments

The magnetorquers are the main attitude control actuators of UWE–4. As such, several experiments regarding purely magnetic attitude control have been conducted and will be presented in this chapter as a preview of the attitude controller used during orbit control in Chapter 7.

As published firstly in Bangert et al. (2015) and explained in more detail in Bangert (2018), the attitude control system follows a modular generic architecture which is depicted in Figure 4.3. Usually the operator only has to deal with the high level control objective with a desired change of the rotation rate $\dot{\omega}$ as output. The generic controller translates this input into desired torques of the different actuators and takes the dynamic model of the satellite into account. Thus, the generic control law in this second stage is formulated as follows

$$\mathbf{T}_c = \mathbf{I}\dot{\omega} + \omega \times (\mathbf{I}\omega) - \boldsymbol{\mu}_{\text{res}} \times \mathbf{B} + \mathbf{T}_{\text{man}} + \mathbf{T}_{\text{ECI2Body}}. \tag{4.8}$$

At this stage, the operator has the opportunity to add constant torques in the body frame $\mathbf{T}_{\text{man}}$ or the Earth Centered Inertial (ECI) frame[1] $\mathbf{T}_{\text{ECI2Body}}$.

At the lowest level is a hardware abstraction layer which distributes the desired control torques to the available actuator drivers and translates it into the actuator specific inputs, such as pulse width modulated signals for magnetorquers or thrusts for attitude control

[1] an inertial Cartesian reference frame with the center of mass of the Earth at the origin

thrusters. At this level, the operator can add a constant magnetic moment $\mathbf{M}_{\text{man}}$ [A m^2] to the input of the magnetorquers following

$$\mathbf{M} = \frac{\mathbf{B} \times \mathbf{T}_c}{\mathbf{B}^2} + \mathbf{M}_{\text{man}}. \tag{4.9}$$

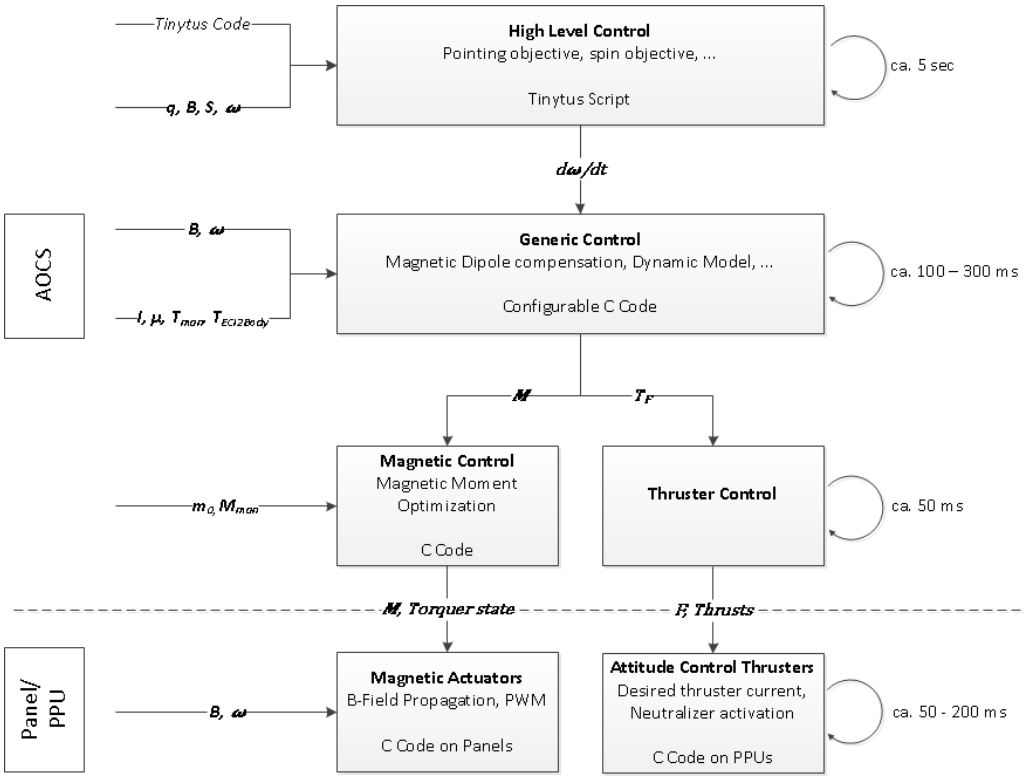

Figure 4.3: Attitude control architecture of UWE–4 as modified version of the UWE–3 control architecture. (Bangert et al., 2015)

4.3.1 Angular rate control

In order to stabilize the attitude of a satellite, the measured angular rate is often reduced using a B-dot control algorithm as described in (Flatley et al., 1997) which aims at minimizing the derivative of the measured magnetic field. However, the same effect can be realized using an angular rate controller which directly adjusts the rotation rate to a desired angular rate ω_{des}.

The high level controller in the control architecture therefore is formulated as

$$\dot{\omega} = -k \cdot (\omega - \omega_{\text{des}}). \tag{4.10}$$

With the top level goal of orbit control in this dissertation, only attitude control experiments with a desired rotation rate of $\omega_{\text{des}} = [0,\ 0,\ 0]^\intercal$ are performed. Several experiments have

been conducted in order to test the controller at different rotation rates and with different gains. The rotation rates for two experiments are depicted in Figure 4.4 and Figure 4.5.

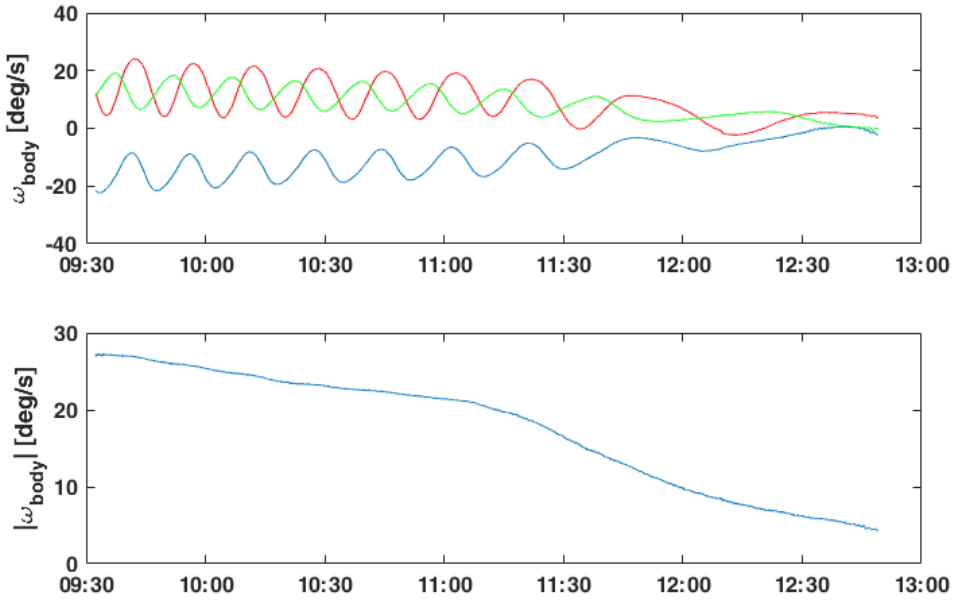

Figure 4.4: Angular rate control experiment on January 31st, 2019. During an overpass over the Groundstation in Wuerzburg, Germany at 11:07:11, the gain k was increased from 0.05 to 0.15.

In the first experiment on January 31st, 2019 the rotation rate was reduced from more than $27°/s$ to below $5°/s$ within 3 hours. The gain of the controller was modified during an overpass over Wuerzburg, Germany at 11:07:11 from $k = 0.05$ to $k = 0.15$, which marks the starting point of the steeper decrease in the absolute value of the rotation rate. The second experiment on March 11th, 2019 showed a stable behaviour of the controller also at low rotation rates below $1°/s$.

4.3.2 Follow-B control

As second purely magnetic attitude control algorithm, a Follow-B controller was implemented and tested in orbit. This algorithm also aims generally at the reduction of the absolute rotation rate of the satellite, but a certain body axis aligns with the Earth's magnetic field $\mathbf{B}$. For this purpose, a constant magnetic moment $\mathbf{M}_{\text{man}}$ was added to the magnetic moment resulting from the desired control torque $\mathbf{T}_c$, as described in Eq. (4.9). This adds a compass-like behaviour of the body axis determined by the direction of the manual magnetic moment to the angular rate controller of Chapter 4.3.1.

On May 13th, 2020 an in-orbit experiment on UWE–4 demonstrated the control algorithm as shown in Figure 4.6 with a manual magnetic moment $\mathbf{M}_{\text{man}} = [0,\ 0,\ -0.07]^{\intercal}\,\text{A}\,\text{m}^2$ and a gain $k = 0.07$. Within 90 minutes, the angular rate of UWE–4 was reduced from $2°/s$ to below $0.7°/s$, as shown in Figure 4.6a. However, in order to align the body -z-axis

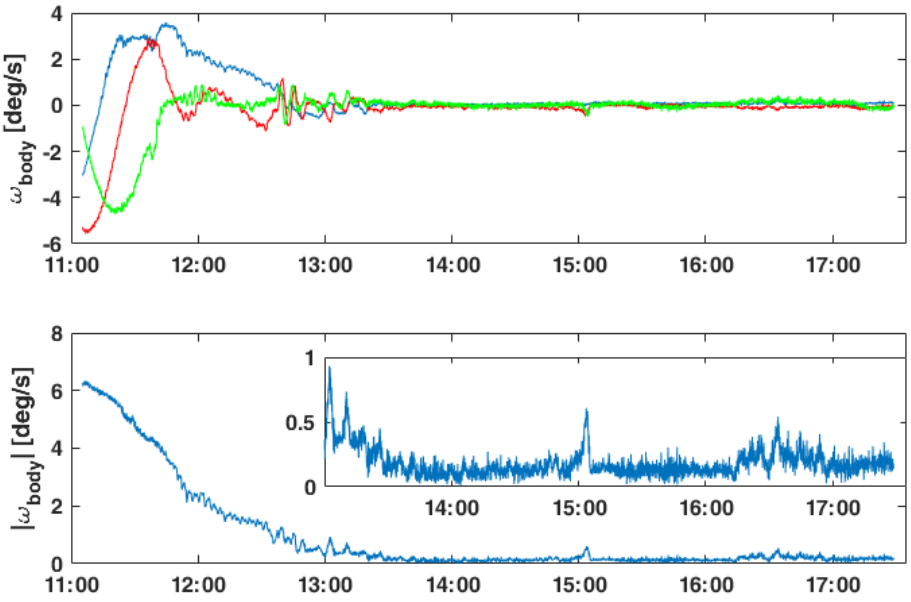

Figure 4.5: Angular rate control experiment on March 11th, 2019 with a gain of $k = 0.15$.

with the Earth's magnetic field, a temporary increase in the rotation rate had to be created, as shown in Figure 4.6b. Subsequently, the angle between the -z-axis of the satellite and the Earth's magnetic field remained below 40° for a duration of at least 3 hours, as depicted in Figure 4.6c.

4.4 Summary

This chapter gave an introduction to the description of the attitude of a rigid body like a spacecraft and the different attitude disturbance torques acting on a spacecraft in LEO. The remaining residual magnetic dipole moment of the UWE–4 spacecraft was determined at a magnitude of $10^{-5}\,\mathrm{A\,m^2}$ which renders the design process of building a magnetically clean satellite a success. Furthermore, the magnetorquers which can create magnetic moments of up to $10^{-1}\,\mathrm{A\,m^2}$ about each body axis can easily compensate this internal magnetic dipole moment.

The performance of selected pure magnetic attitude controllers was demonstrated in orbit on-board UWE–4. While the angular rate control algorithm allows to reduce the rotation rate of the spacecraft, the Follow-B controller additionally enables the satellite to align a random body axis with the Earth's magnetic field after a transient behavior. This algorithm is of utmost importance for the orbit control scheme described in Chapter 7.

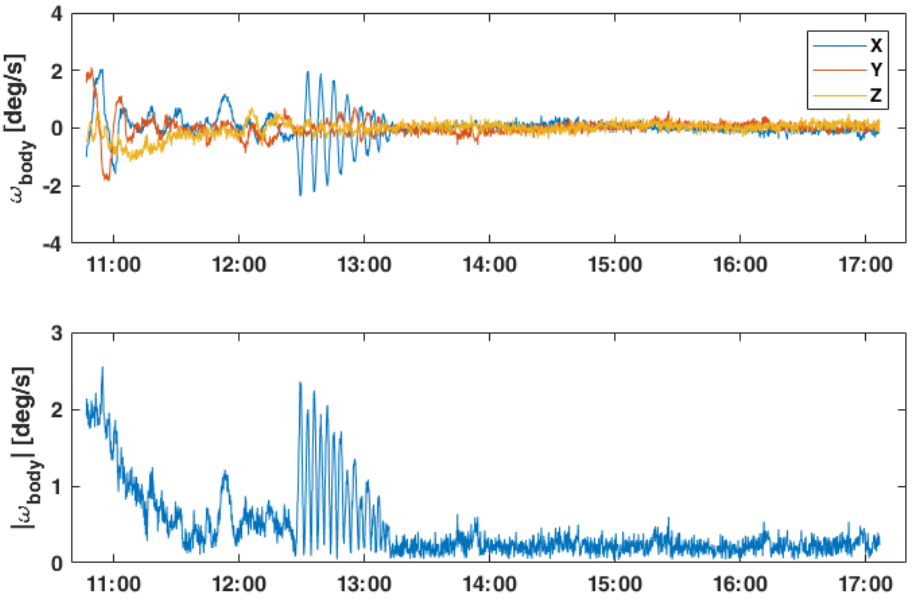

(a) Angular rate in the body frame (top) and absolute value (bottom).

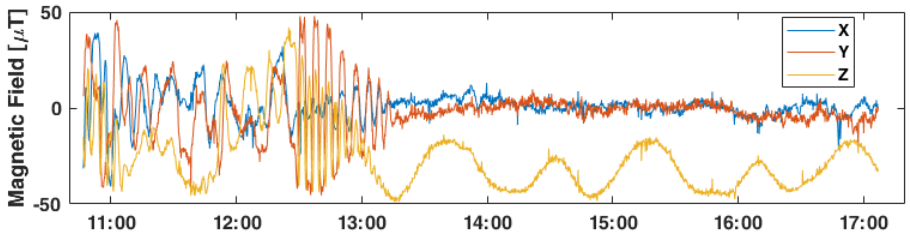

(b) Measured magnetic field in the body frame.

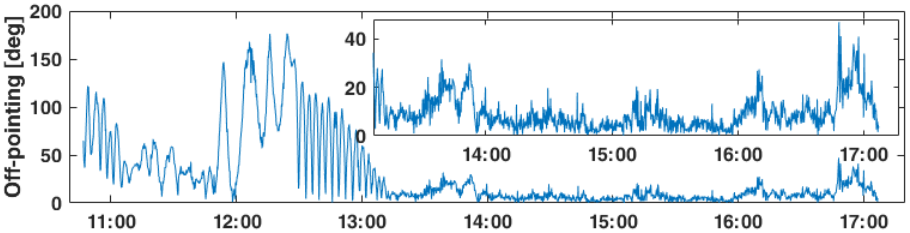

(c) Angle between the satellite's body -z-axis and the measured magnetic field. A magnification of the angle after stabilization of the satellite's attitude is shown in the overlayed image.

Figure 4.6: Follow-B attitude control experiment on May 13th, 2020. (Kramer and Schilling, 2021)

5
Propulsion system commissioning

This chapter will describe experiments and results associated with the NanoFEEP propulsion system as a central component aiming at orbit control. Several experiments were performed already prior to launch in joint test campaigns at a facility at TU Dresden. These were attributed to power consumption of the involved processes, for example, as well as to the activation procedures. For this purpose, the satellite has been partially assembled and installed in a vacuum chamber. A photograph of the setup can be seen in Figure 5.1. The vacuum chamber contained an internal shroud acting as collector for the emitted propellant material and the electrons of the neutralizer. The satellite contained all the internal subsystems. The outside panels were replaced with aluminium plates in order to secure the spacecraft from a contamination by sputter material of the shroud of the vacuum chamber. This way, the low pressure space environment was imitated and the thrusters' as well as the neutralizers' performances were evaluated. These lab tests were confirmed by in-orbit experiments wherever applicable.

In order to characterize the thrusters and the neutralizers, the following magnitudes are monitored and recorded on the PPU:

- U_{mon}: The HV supplied between the emitter of the thruster head or the silicon chip of the neutralizer and the respective extractor.
- I_{des}: The desired current to be ejected by the thruster head or the neutralizer.
- I_{mon}: The electrical current supplied to the needle of the emitter or the silicon chip of the neutralizer respectively. This current is being emitted, but might be intercepted by the extractor before actually leaving the spacecraft.
- $I_{rtn,mon}$: The electrical current intercepted by the extractor of the thruster or the neutralizer and thus returning to the spacecraft.

Additionally, the magnitude of the effective emitter current I_{eff} describes the actual current ejected by the thruster and neutralizer, respectively. For the neutralizer, it describes the process variable in the control loop of the PPU and can be derived from the previous magnitudes as follows:

$$I_{eff} = I_{mon} - I_{rtn,mon} \tag{5.1}$$

Before the propulsion system can be used for attitude and orbit control purposes, the single components have to be tested and evaluated to ensure their proper functionality

in-orbit. With regard to the prevention of spacecraft charging effects, a certain start-up procedure of the components has to be employed:

1. The desired thruster heads are pre-heated to ensure liquefaction of the gallium propellant.
2. The neutralizer is activated to eject at least the desired emitter current of all thrusters.
3. The desired thrusters can ignite and create thrust.

The associated experiments are described in this chapter. The laboratory tests concerning the heating of the propellant were already conducted on November 30th, 2017, while the laboratory experiments dealing with neutralizer and thruster ignition were conducted from October 16th- 18th, 2018. Five weeks after launch at the beginning of February 2019, in-orbit experiments with the propulsion system started already and were on-going until mid 2020. The analysis of the thruster ignition will be presented thruster by thruster. A novel thrust estimation algorithm will be introduced in the subsequent chapter, which makes use of the AOCS sensors.

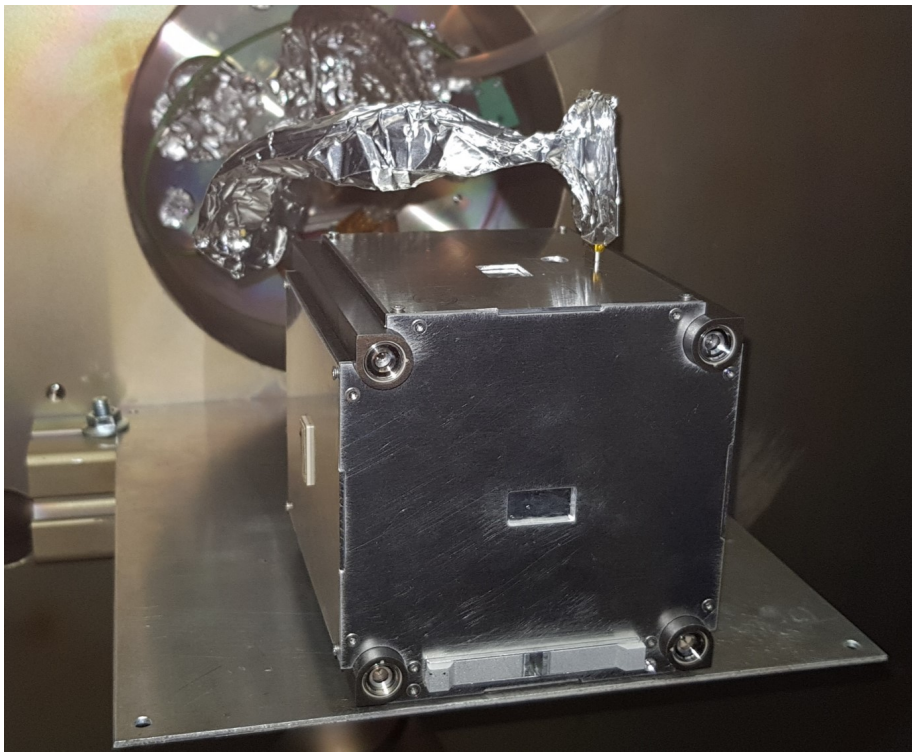

Figure 5.1: Partially assembled flight model of the satellite for laboratory experiments on October 18th, 2018. The thruster heads can be seen at the corners of the satellite and a neutralizer is visible at the left side panel.

The publication Kramer et al. (2020) contains considerable content of this chapter, which was partially taken one-to-one. Furthermore, Kramer et al. (2019) and Kramer and Schilling (2021) also contains first in-orbit results of the propulsion system shown in this chapter.

5.1 Thruster preparation

The propellant of the propulsion system needs to be liquefied before activation of HV of one of the thrusters. Thus, a laboratory measurement was performed in order to confirm the heating circuit, ensure complete liquefaction and quantify the heating duration and power consumption.

Laboratory measurements targeted a heater temperature of 50°C. The thermocouple designated for the measurement of this temperature is part of the heater assembly shown in Figure 3.5a. It is placed opposite to the emitter needle with respect to the propellant reservoir. Consequently, it can only roughly determine the temperature of the needle tip. For this reason, the control temperature was chosen approximately 20°C above the liquefaction temperature of gallium as a security measure so as not to activate a thruster when the propellant is only partially liquefied. Furthermore, a hysteresis of 10°C in the thruster activation has been implemented which deactivates the thruster at temperatures below 40°C.

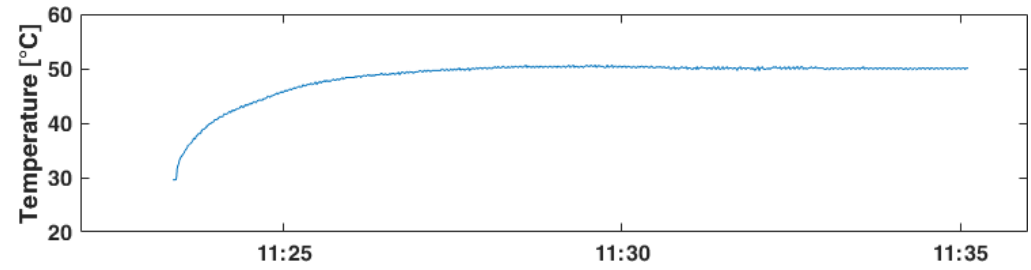

(a) Temperature profile during heating to 50 °C.

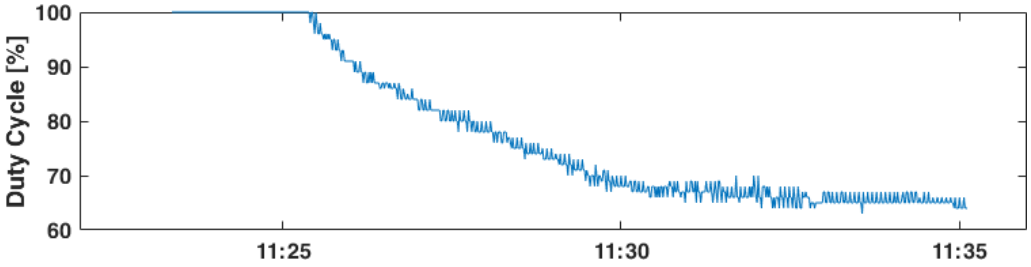

(b) Duty cycle of the heater controller.

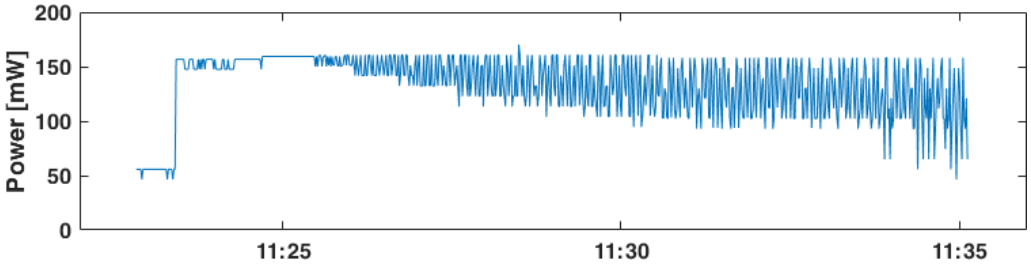

(c) Power consumption of the heating process.

Figure 5.2: Laboratory measurement of heating process on November 30th, 2017.

The results of this experiment are depicted in Figure 5.2. Figure 5.2a and Figure 5.2b show the rising heater temperature and the corresponding duty cycle of the heater controller. Three main power levels can be determined from Figure 5.2c:

1. Prior to the heating process: $\approx 52 \pm 4$mW
2. During the heating process with 100% duty cycle: $\approx 159 \pm 2$mW
3. During the heating process with approximately 65% duty cycle: $\approx 125 \pm 33$mW

Thus, the necessary heating power was expected to be 107 ± 6mW for temperature acquisition. However, after 11:25:30, the heater temperature almost reached the targeted temperature of 50°C and consequently the duty cycle is reduced by the heater controller. The power measurement starts to fluctuate as the duty cycle is reduced, which results from the relative overlap between power sampling interval and Pulse Width Modulation (PWM) signal for heating.

The measured duration of the heating period starting at about 30°C amounted to 260s. Additional laboratory experiments conducted by our partners at TU Dresden compared the on-board temperature measurement of the thermocouple with an external sensor and resulted in an additional increase of the targeted temperature to 60°C (Bock, 2018). It has to be noted that thermal cycling tests with the heaters to confirm its performance at low temperatures were not performed, but the environmental temperature was always approximately 22°C.

In-Orbit measurements on February 6th, 2019 are displayed in Figure 5.3. The graph shows the temperature profile of thrusters A (red) and B (blue) with active heaters at the control parameters defined during laboratory experimentation.

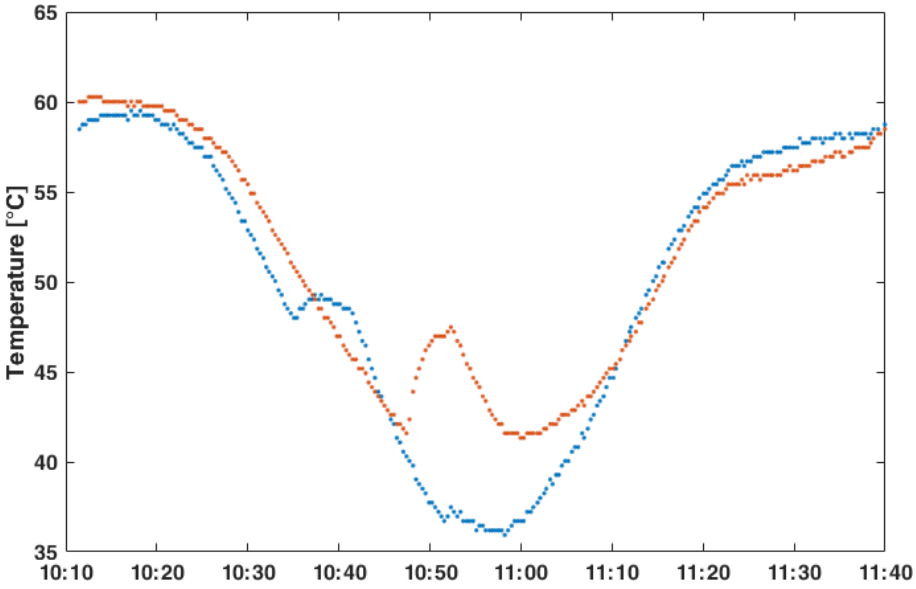

Figure 5.3: Propellant liquefaction and solidification process.

The eclipse phase of the orbit was from 10:19 - 10:54. During this time, the temperature of both sensors went below 42°C, although the heaters were turned on non-stop. The exothermic solidification process of the gallium propellant is visualized by the increase of temperature in the eclipse phase starting 10:47 at thruster A and at 10:35 at thruster B. The flattening of the temperature curve of thruster A at approximately 11:25 appears to be the endothermic liquefaction process. This measurement shows that the temperature of 60°C is not sufficient for a reliable liquefaction of the gallium propellant. Thus, the settings of the heater controller had to be adjusted.

Figure 5.4 shows the temperature profile starting at February 22nd, 2019. For this heating process the targeted temperature was increased to 63°C. Additionally, the sampling frequency of the control loop had been decreased from 1Hz to 0.1Hz.

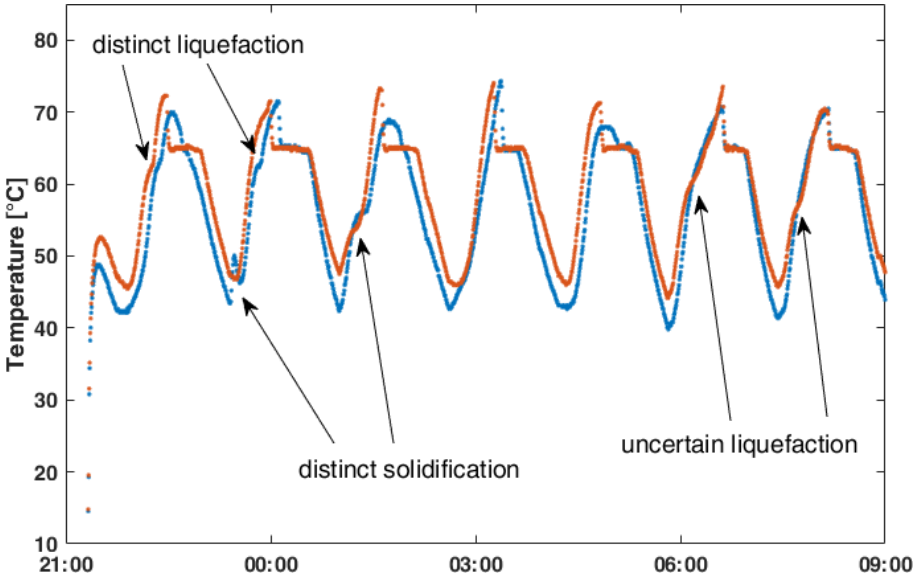

Figure 5.4: Successful liquefaction was achieved above 63°C in a repeatable process on February 22nd, 2019. The temperatures of thruster A and B are depicted in red and blue, respectively. (Kramer and Schilling, 2021)

The solidification process can clearly be identified during the first orbits. However, after the third orbit the solidification of the gallium propellant can merely be suspected due to minor shoulders during liquefaction in the temperature curve on February 23rd, 2019 at 06:11 and 07:42 for thruster A. The temperature profile for thruster B does not show any signs of a liquefaction process after the third orbit. This measurement shows that after heating the propellant for several orbits, the propellant reaches the temperature of assured liquefaction at 63°C approximately 27-35 minutes after leaving the eclipse and the thruster can be activated for a duration of about 50 minutes, before it may solidify again below 53°C. The exact duration after eclipse for a reliable liquefaction of the propellant may depend on the satellite's attitude and correspondingly the sun's illumination and its heating effect on the respective thruster head.

Experimental data of the temperature and associated power consumption measurement is depicted in Figure 5.5. The heating process was started at 23:35 on March 17th, 2020.

After an overshoot in the temperature to more than 70°C, shown in Figure 5.5a, the duty cycle was reduced at 00:22 and the targeted temperature of 65°C maintained. At 00:37, the satellite went into eclipse and the temperature started to decrease, which was associated with an increase in duty cycle, as depicted in Figure 5.5b. The minor spikes in the power measurement can be attributed to single chips on the PPU that were put in energy saving mode when they are not needed. The larger spikes occurred due to the underlying temperature measurement principle, which shortly interrupts the heating process.

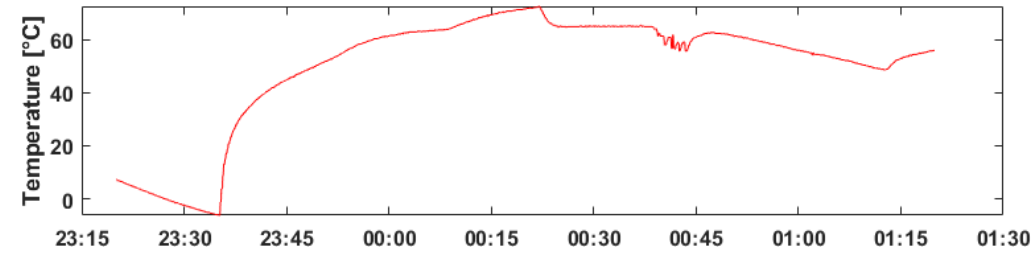

(a) Temperature profile during heating to 63°C.

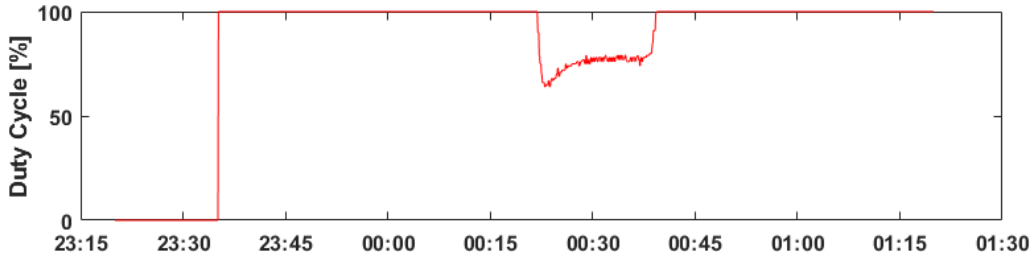

(b) Duty cycle of the heater controller.

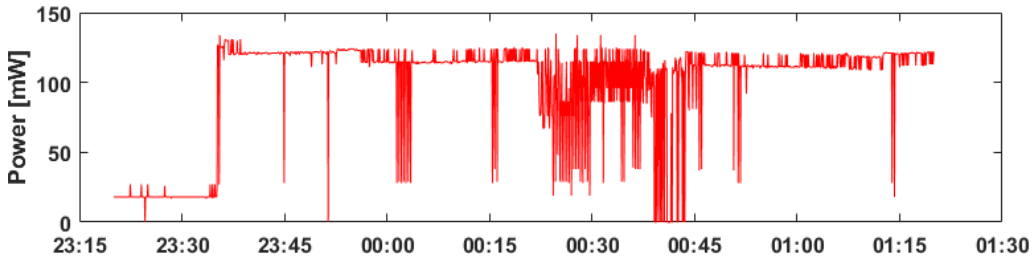

(c) Power consumption of the PPU.

Figure 5.5: In-Orbit measurement of heating process of thruster A on March 17th, 2020.

Two major power levels can be recognized in Figure 5.5c:

1. Before 23:35, without heating: ≈18±1mW
2. After 23:35, with heating at a duty cycle of 100%: ≈121±3mW

This leads to a power consumption of 103±4mW attributed to the heating process, which is in the same range as the laboratory measurements described on page 48.

As a consequence of the previous measurements, we advised our partners at TU Dresden to re-design the PPU with a more powerful heater for future usage in order to assure liquefaction and enable usage of the thruster during the entire orbit.

5.2 Neutralizer activation

The purpose of the neutralizers for this mission is to avoid a space-charge buildup outside of the satellite which could potentially limit the operation of the thruster. In order to fulfill this, some requirements are posed on the software and hardware:

- As the necessary voltage is in the range above 1kV, special care has to be taken for the electrical isolation.
- Each electron source has to be capable to emit a current of the magnitude of the two thrusters of the associated PPU. However, if the neutralizer fails, the associated thrusters will be turned off immediately.
- Some of the emitter current may be incident on the extractor grid of the neutralizer itself. The emitter current has to compensate for it. Nevertheless, if the major part of the emitter current is incident on the extractor grid, the neutralizer and the associated thrusters will shut down autonomously.

The UWE–4 mission is the first in-orbit demonstration of these novel neutralizers. For this reason, two operational modes were implemented. The commissioning mode allows the operator to command desired effective emitter currents I_{des} as set points for the neutralizer without a thruster being active. The automated mode autonomously compensates for the effective emitter currents of the thrusters of the same PPU and the extractor current of the neutralizer itself.

Laboratory measurements, depicted in Figure 5.6, show the characteristics of the electron source during the first commissioning. In this measurement, the intended range of effective emitter currents has been covered.

The following properties of neutralizer B are visible:

- Figure 5.6a shows the range of the voltage U_{mon} between silicon chip and extractor grid between 900-1500V. During power up of the neutralizer, it can have a small peak. However, as the number of CNTs contributing to the emitter current of the neutralizer increases, a lower voltage is sufficient to maintain the desired emitter current.
- The control loop for the neutralizer effective emitter current works well and keeps the measured (light blue) and desired (green) effective emitter currents equal, such that the measured emitter current I_{mon} compensates the current incident on the extractor $I_{rtn,mon}$, as can be seen in Figure 5.6b.
- The power consumption of the PPU rises with increasing emitter current. At very low emitter currents below 20µA, the power consumption becomes unstable, which can be seen in Figure 5.6c around 19:43. This indicates that not all regions of CNTs are active at the same time and thus, the emitter current may fluctuate as well.

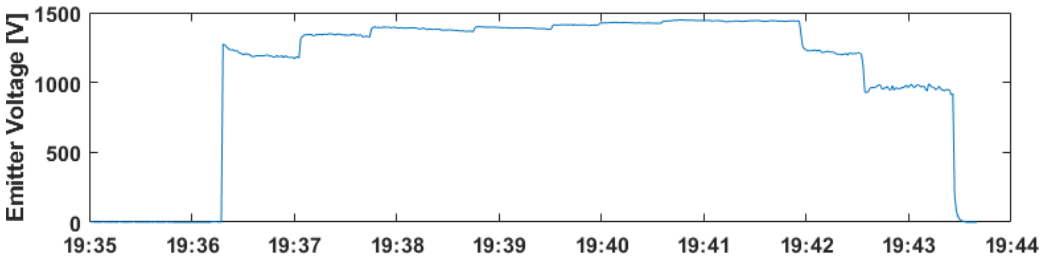

(a) Emitter voltage U_{mon} of the neutralizer chip.

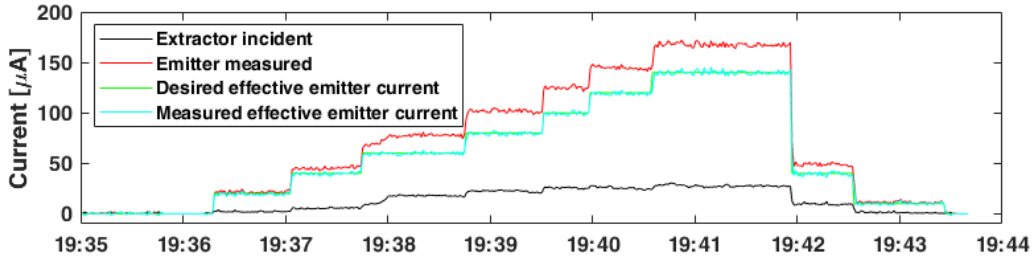

(b) The monitored neutralizer currents of the PPU.

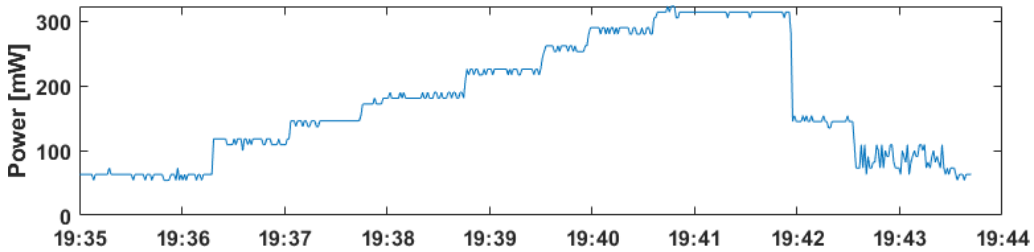

(c) Power consumption of the neutralizer activation.

Figure 5.6: Laboratory experiment of neutralizer B on October 18th, 2018.

In-orbit measurements on February 21st, 2019 were conducted to prove the functionality of the neutralizer in space. Measured electrical parameters are shown in Figure 5.7.

This was the first time a neutralizer of this kind was activated in space on board a 1U CubeSat. During this experiment, neutralizer A was commanded to emit an effective electron current of $I_{eff} = 60\mu A$. The control algorithm is implemented such that the neutralizer will increase its emitter current by the electron current hitting the extractor grid in order to ensure the commanded electron current is effectively emitted by the spacecraft. Thus, the measured neutralizer emitter current I_{mon} is about 70µA.

For the purpose of an in-orbit characterization of the electron sources, they were both activated at several set points. The experiments of both neutralizers were conducted on March 27th, 2020 and March 28th, 2020. The measured electrical data is depicted in Figure 5.8 and Figure A.4. At this time, both neutralizers had already been active on-board UWE–4 for several hours total.

The following properties are apparent:

- The voltage U_{mon} of neutralizer B is in the range of 2000-2500V, while the operating range for neutralizer A is between 1300-1800V.

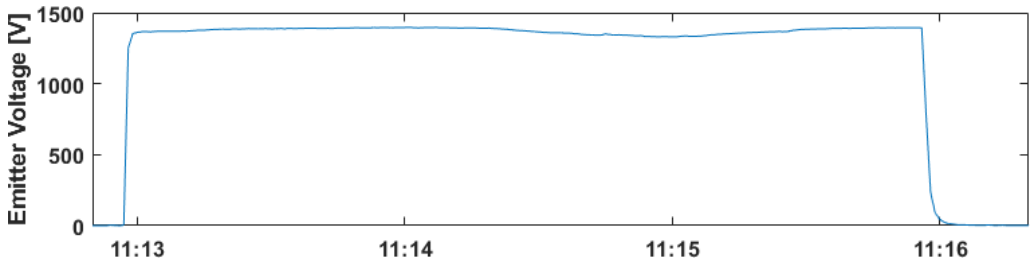

(a) Emitter voltage U_{mon} of neutralizer A.

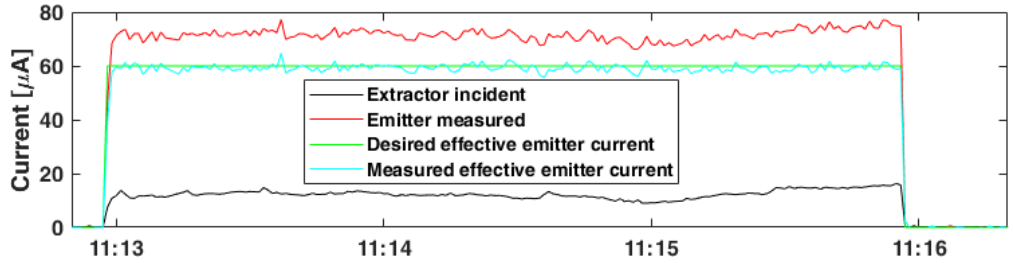

(b) The monitored currents of neutralizer A.

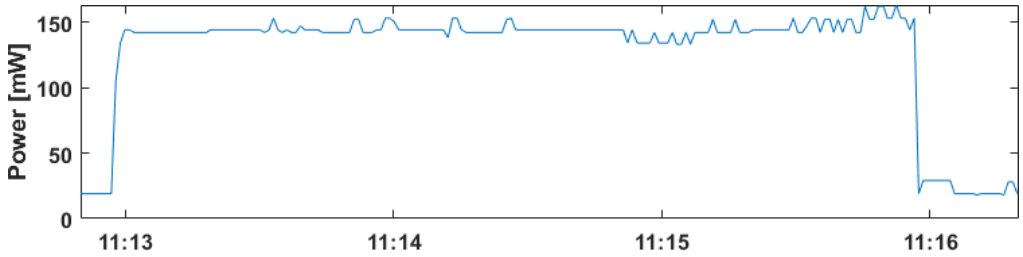

(c) Power consumption of the neutralizer activation.

Figure 5.7: First in-orbit experiment of this CNT based electron source using neutralizer A on February 21st, 2019. (Kramer et al., 2020)

- The current incident on the extractor $I_{rtn,mon}$ is below 30µA for neutralizer B, while the extractor current for neutralizer A can rise to more than 100µA in the same range of effective emitter current.

- The power consumption of neutralizer B is very stable during the whole operating range. Neutralizer A shows some fluctuations at emitter currents I_{mon} above 160µA.

- Each PPU has a small power consumption without any active heater, neutralizer or thruster. This basic power consumption of the PPUs can be seen at the beginning of the experiments with 19mW for the PPU attached to neutralizer A and 27mW for the PPU attached to neutralizer B.

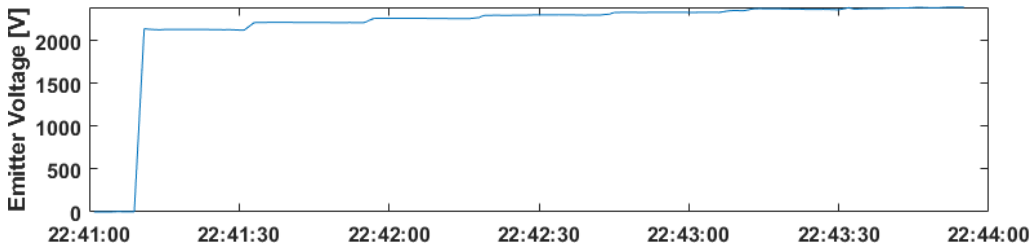

(a) Emitter voltage U_{mon} of neutralizer B.

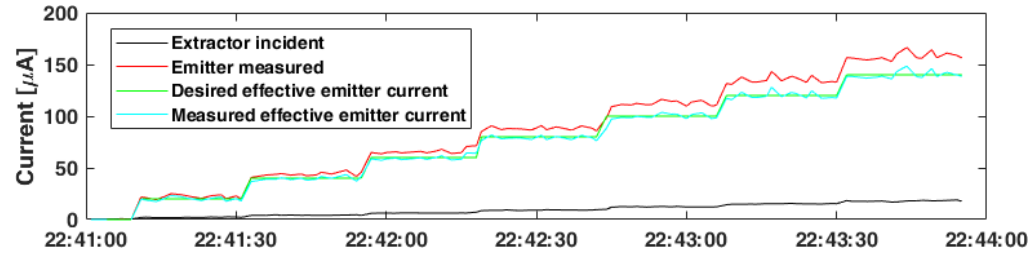

(b) The monitored currents of neutralizer B.

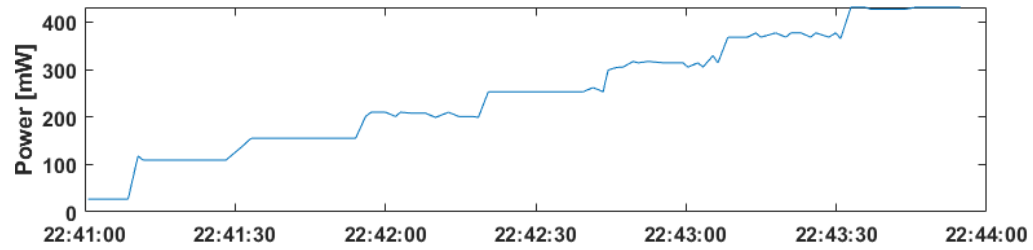

(c) Power consumption of the PPU during neutralizer B activation.

Figure 5.8: In-orbit characterization of neutralizer B on March 28th, 2020. (Kramer et al., 2020)

The neutralizer transmissivity describes the percentage of emitter current effectively passing through the extractor grid and is thus defined mathematically as

$$\eta_{\text{curr}} = \frac{\text{I}_{\text{mon}} - \text{I}_{\text{rtn,mon}}}{\text{I}_{\text{mon}}} \, . \tag{5.2}$$

Figure 5.9 shows that the transmissivity of neutralizer B did fluctuate considerably during laboratory testing at emitter currents below 70µA, but increased for higher currents. At low emitter currents, only few CNTs were effectively contributing. Additionally, these were not fully stretched out between silicon chip and extractor grid. However, with increasing emitter current an increasing number of CNTs were stretched out and carried an electron current.

The in-orbit transmissivity of neutralizer B is shown in green and remained rather constant at $\eta_{\text{n,curr}} = 88 - 92\%$. This efficiency was also valid for low emitter currents at 20µA. The most probable cause for this performance discrepancy is a reflection of electrons from vacuum chamber walls during laboratory testing, which returned to the extractor and decreased the emitter efficiency. This justifies an improved transmissivity during in-orbit testing. Neutralizer A had a lower emitter efficiency between 50-60%, due to the high current intercepted by the extractor. The reason for the performance difference

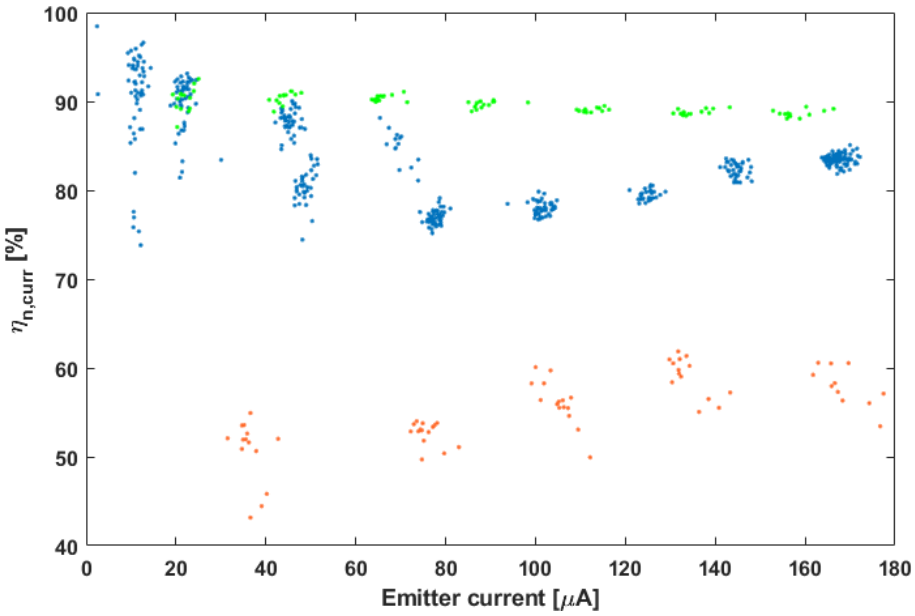

Figure 5.9: Neutralizer B transmissivity according to laboratory experiment on October 18th, 2018 in blue. In-orbit data of neutralizer B from March 28th, 2020 and of neutralizer A from March 27th, 2020 in green and orange, respectively. The depicted data was already partially published in Kramer et al. (2020).

between both neutralizers is unknown.

In Figure 5.10, the power consumptions of both neutralizers are depicted in dependency of the emitter current. The laboratory measurement of neutralizer B in blue can be compared to its in-orbit measurement in green and to those of neutralizer A in orange. Both trend lines resemble a certain activation voltage by their y-intercept. The in-orbit trendlines follow these equations:

$$\text{Neutralizer A}: \quad P_{N_A}\,[\text{mW}] = (2.36 \pm 0.07) \cdot I_{\text{mon}}\,[\mu\text{A}] + (23.35 \pm 7.47) \quad (5.3)$$

$$\text{Neutralizer B}: \quad P_{N_B}\,[\text{mW}] = (1.68 \pm 0.08) \cdot I_{\text{mon}}\,[\mu\text{A}] + (14.50 \pm 12.55) \quad (5.4)$$

However, the laboratory experiment of neutralizer A had a lower power consumption per emitted current with $1.43 \pm 0.01\text{mW}/\mu\text{A}$.

A long term analysis of the neutralizer performance is conducted with the main focus on the neutralizer transmissivity η_{curr}. In order to estimate the neutralizer's power consumption in a joint experiment with active thrusters, the emitter current I_{mon} of the neutralizer has to be known. This emitter current is necessary to create the effective emitter current I_{eff} of the electron source in order to compensate for both thrusters' emitter currents.

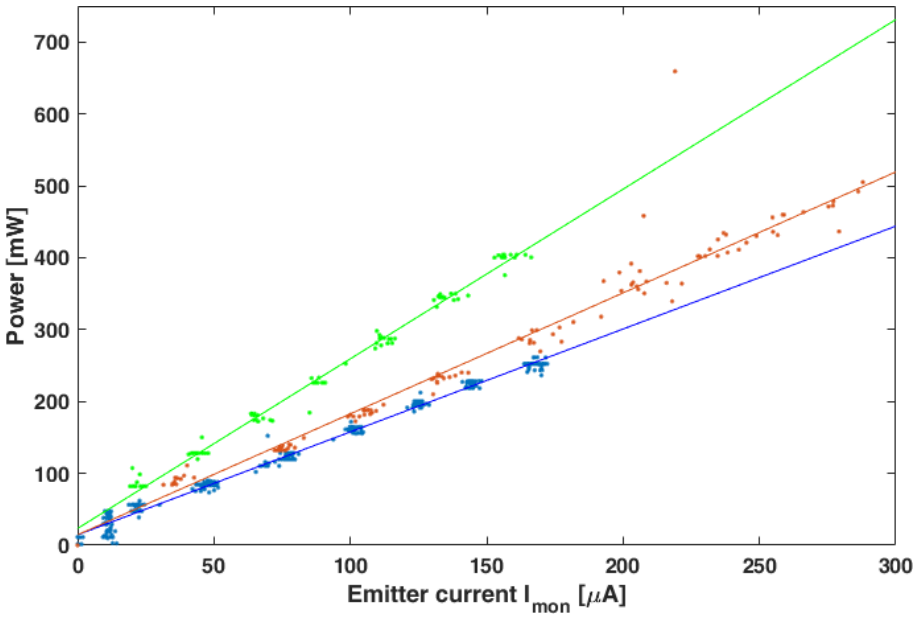

Figure 5.10: Emitter current vs power consumption. Laboratory measurements of neutralizer B from October 18th, 2018 are shown in blue. In-orbit measurements of neutralizer B from March 28th, 2020 and of neutralizer A on March 27th, 2020 are shown in green and orange, respectively.

Figure 5.11 relates the desired effective emitter current I_{eff} with its necessary emitter current I_{mon} for neutralizer A. The active orbit time is encoded in the color. For comparison purposes, the laboratory measurement of neutralizer A is added in black. It is directly apparent that the slope of the different colors is increasing over time. While the first in orbit measurements in blue have a similar gradient like the laboratory measurement, the later measurements in green and red are following a steeper inclination. It has to be pointed out that these two hours of total in-orbit operation were conducted within the first 16 months after launch, i.e. the three different colors correspond to experimental campaigns within the first six, after 12 and after 16 months in orbit.

Ohkawa et al. (2019) has measured much steeper decreases in CNT based field-emission cathode emitter performances at an altitude of approximately 370km. However, the decrease in this publication is attributed to the direct impact of atomic oxygen, whose flux is several orders of magnitude higher at these low altitudes. An alternative reason for the performance decrease over time may be impacting dust particles which could already have harmed the fragile structure of CNTs.

The characteristics of the linear trend lines are summarized in Table 5.1.

Color	Equation	η_{curr} [%]	Valid months
blue	$I_{mon} = (1.21 \pm 0.01) \cdot I_{eff} - (1.86 \pm 0.73)$	$82,6 \pm 0,7$	1 – 6
green	$I_{mon} = (1.67 \pm 0.02) \cdot I_{eff} + (3.69 \pm 1.32)$	$59,9 \pm 0,7$	11 – 12
red	$I_{mon} = (2.37 \pm 0.54) \cdot I_{eff} + (10.39 \pm 20.25)$	$42,2 \pm 9,6$	15 – 16

Table 5.1: The different trend lines of Figure 5.11 and their valid time ranges.

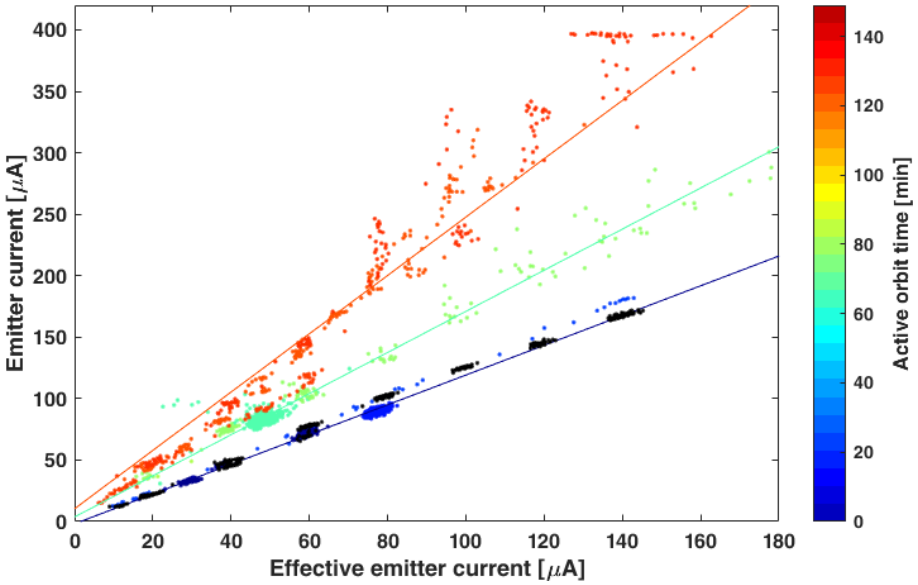

Figure 5.11: Effective emitter current I_{eff} vs emitter current I_{mon} of neutralizer A during the first 2.5 hours of in-orbit usage. The color indicates the total time of in-orbit activation. The laboratory measurement of Figure 5.6 is added in black.

For the gradient m of the linear fits it holds:

$$m = \frac{dI_{mon}}{dI_{eff}} = \frac{I_{mon}}{I_{mon} - I_{rtn,mon}} = \frac{1}{\eta_{curr}} \tag{5.5}$$

As a conclusion, a steeper gradient m directly converts to a lower transmissivity η_{curr} and to a higher power consumption per µA effectively emitted current.

Some further consequences can directly be deduced:

- In order to compensate a thruster emitter current of 40µA with neutralizer A, the emitter current I_{mon} had to be 50µA at the beginning of its lifetime and about 100µA after approximately two hours of in-orbit operation or 16 months in orbit.
- The red colored measurement has a maximum emitter current of 400µA for different effective emitter currents I_{eff}. Firstly, while the set point was 160µA target current I_t, the effective emitter current rose from 130µA to 160µA due to a declining incident extractor current $I_{rtn,mon}$. Secondly, this also means that the PPU's maximum emitter current is $I_{mon,max} \approx 400$µA. Otherwise the control loop had increased the emitter current $I_{mon}$to achieve the 160µA set point faster.

5.3 Thruster activation

The UWE–4 mission was the first 1U CubeSat mission to demonstrate an electric propulsion system in orbit. The measurement of the first activation is presented in this chapter.

Prior to orbit control, the power consumption of a PPU with an active thruster and its associated heater and neutralizer needs to be characterized and the activation procedure as well as the emitter current compensation by the neutralizers must be ensured. The operating mode of the thrusters was realized such that a desired emitter current I_{des} can be commanded as set point for the control loop. In contrast to the neutralizer operating mode, the extractor current $I_{rtn,mon}$ of the thruster was not to be compensated by increasing the emitter current I_{des}. This was decided for as a safety measure for the first in-orbit demonstration of the propulsion system to prevent an uncontrolled increase of the emitter current I_{des} due to an increasing extractor current $I_{rtn,mon}$ of a thruster.

The thrusters can only be activated in-orbit if the liquefaction temperature of the propellant is met and a neutralizer compensates for the charge loss. However, during laboratory experimentation the spacecraft can compensate for the charge loss also by surface contact to the side walls of the vacuum chamber. Thus, the presented laboratory measurements were conducted without an active neutralizer.

To provide a means for a more intuitive classification of the thruster's performance, a rough estimation of the thrust magnitude based on the electrical values shall be derived shortly by taking a closer look at Eq. (2.6). The thrust magnitude increases linearly with the ejected current and with the square root of the voltage of the electric field. As will be shown in measurements presented in this chapter, the voltage of the thrusters varies only by about 10% in the operating range. The voltage of both thruster types is at values between 5-8kV, thus the square root in Eq. (2.6) reduces to values in the range of 0.09-0.11 with singly ionized gallium propellant. Assuming perfect ionization and neglecting the effect of divergence in the plasma plume and the extractor current $I_{rtn,mon}$, the thrust magnitude can be estimated to be

$$|\tilde{\mathbf{F}}|_{\text{rough}}[\mu\text{N}] \approx 0.1 \cdot I_{\text{mon}}[\mu\text{A}]. \tag{5.6}$$

This chapter will firstly discuss the activation of thrusters A and B and their electrical characteristics. The compensation of the neutralizer and the characterization of the power consumption of thrusters A and B will be shown using in-orbit data of an active thruster and the associated neutralizer. Unfortunately, thrusters C and D could not be activated in-orbit, as their activation resulted in a security shut-down of the associated power path by the hotswap circuit of the PPU. The results of laboratory measurements of thrusters C and D will be discussed briefly. The associated Figures can be found in the appendix.

5.3.1 Thruster A

This porous type NanoFEEP thruster is installed in the +X+Y+Z corner of the satellite, as depicted in Figure 3.2. Thus, its plasma plume will partially hit an antenna of UWE–4 as well as the lid of the antenna deployment system. However, as mentioned in Chapter 3.2.4, no harm is to be expected to the antennas or the lid due to the incident current.

Laboratory measurements showed that thruster A had an activation voltage of approximately 5300V, while the operating voltage reached 8200V for high emitter currents of 160µA. Figure 5.12 shows the electrical characteristics of the experiment. In Figure 5.12b, a comparably high extractor current $I_{rtn,mon}$ during the first half of the experiment showed

that a fraction of the plasma current is hitting the extractor electrode. This indicates that the needle emitter is either contaminated with oxidized gallium propellant on the surface or has a small undissolved droplet of propellant somewhere close to the needle tip. This causes the plasma to be partially deflected towards the extractor electrode.

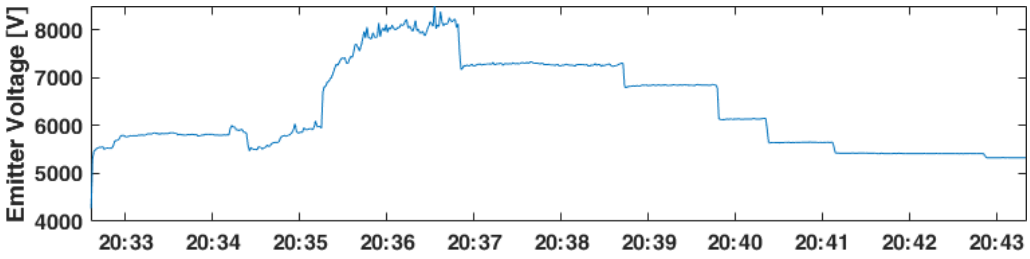

(a) Emitter voltage U_{mon} of thruster A.

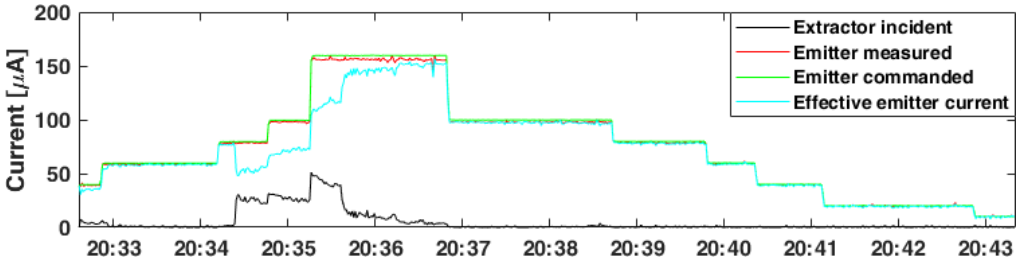

(b) The monitored currents of thruster A.

Figure 5.12: Laboratory measurement of thruster A on October 18th, 2018.

A cleaning mechanism can sometimes resolve this situation. This procedure was initiated with the increase of the desired emitter current I_{des} at 20:35:15. The cleaning mechanism is based on the idea that the contaminated material can be carried away with a high current. Thus, it can be compared to cleaning a pipe with high pressure. During the phase of the highest current of 160µA, the incident extractor current $I_{rtn,mon}$ decreased and finally vanished.

The transmissivity of thruster A, as defined in Eq. (5.2), is depicted in Figure 5.13. The transmissivity during the contamination of the emitter is colored red in order to contrast it to normal operation of the thruster. Except for very low emitter currents below 20µA, it lies above 92%.

In-orbit measurements were initiated with the first in-orbit activation of thruster A on February 26th, 2019 at 09:59:00. As a first test, the thruster was activated with a desired emitter current of $I_{des} = 40\mu A$ for only 30s. The electrical characteristics of this activation are depicted in Figure 5.14. Several observations can be made:

- The necessary emitter voltage U_{mon} depicted in Figure 5.14a for an emitter current of 40µA rose from 4.7kV to 5.5kV.
- Figure 5.14a shows that the extractor current $I_{rtn,mon}$ of thruster A is negligible, such that the measured emitter current I_{mon} and the effective emitter current I_{eff} are matching.

- The neutralizer voltage and currents in Figure 5.14b stayed almost constant. The transmissivity η_{curr} of the neutralizer varies within the range of 78-85% and thus fits to the early experimental range in Table 5.1.

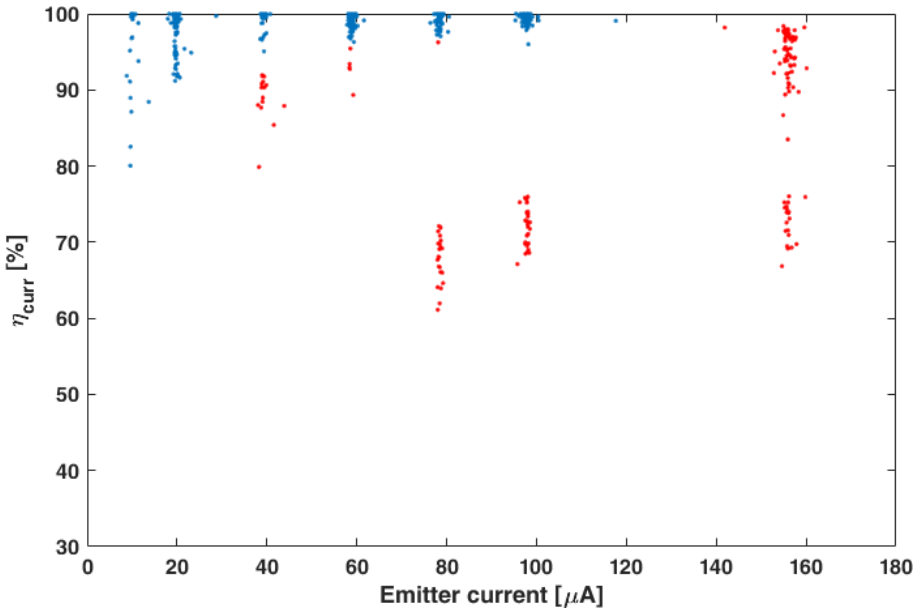

Figure 5.13: Thruster A current efficiency according to laboratory experiment on October 18th, 2018 in blue. The transmissivity during the contamination of the emitter is colored red.

The different regions in Figure 5.14c correspond to three different operational modes of the PPU, which are specified in Table 5.2. With the intention to deduce the power consumption of thruster A, the composition of the measured power consumption of the PPU has to be examined. The following equation holds for the measured power consumption:

$$P_{\text{total}} = P_{\text{base}} + P_{\text{n}} + (P_{\text{heater}} + P_{\text{thr}}) \tag{5.7}$$

Time Range	Active components	Total power consumption [mW]
09:58:50 – 09:58:55	Heater A & B	215 ± 4
09:58:56 – 09:58:59	Heater A	117 ± 4
09:59:00 – 09:59:30	Heater A Thruster A Neutralizer A	412–459
09:59:31 – 09:59:39	Heater A	117 ± 4

Table 5.2: The power consumption of the different operational modes in Figure 5.14c.

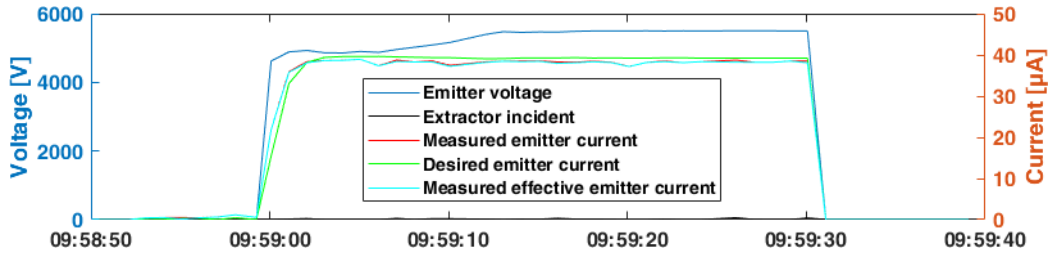

(a) The electrical characteristics of thruster A.

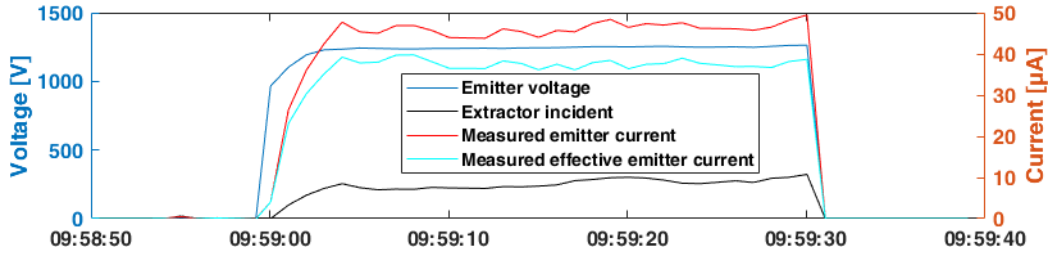

(b) The electrical characteristics of neutralizer A.

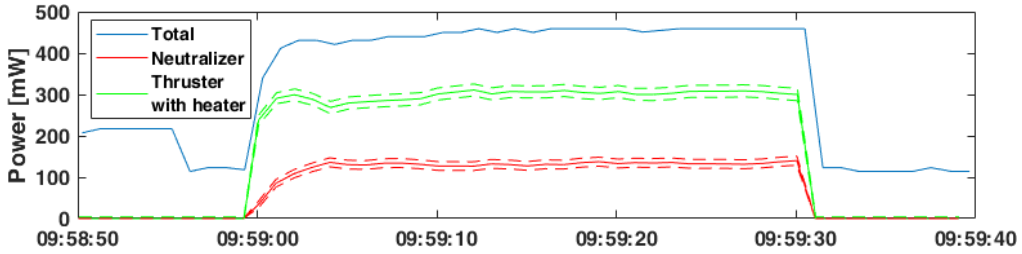

(c) The power consumption of the PPU, the neutralizer, and the thruster with its associated heater within their uncertainties.

Figure 5.14: First in-orbit activation of thruster A on February 26th, 2019. The depicted data was already partially published in Kramer et al. (2020).

P_{base} and P_{heater} describe the basic power consumption of the PPU of 18 ± 1mW and the fraction associated with the heater of thruster A, respectively (refer to Chapter 5.1). P_n represents the fraction of the neutralizer (refer to Eq. (5.3)) and P_{thr} the fraction of the thruster itself. The result is also depicted in Figure 5.14c. Due to the focus on the necessary power for the thruster including its own heater and the power consumption of the neutralizer, the fraction of the basic power consumption of the PPU was omitted.

Applying this analysis to all in-orbit measurements of thruster A enables to define a power consumption depending on the emitter current or the created thrust of thruster A using Eq. (5.6). The measurements are depicted in Figure 5.15. For an emitter current I_{mon} larger than 80µA, a steep increase in power consumption can be observed. The most probable cause for this is a loss in the conversion efficiency of the PPU. Linear trend lines for a value range of the emitter current I_{mon} of 18–80µA are shown in the same figure. Thus, the total power consumption of the PPU in this range follows the equation

$$P_{tot,Th\ A}\ [\mathrm{mW}] = (8.5 \pm 0.1)[\mathrm{mW/\mu A}] \cdot I_{mon}\ [\mu\mathrm{A}] + (184.0 \pm 8.5)[\mathrm{mW}] \quad (5.8)$$

$$\approx (85.2 \pm 0.8)[\mathrm{mW/\mu N}] \cdot |\tilde{\mathbf{F}}|_{rough}[\mu\mathrm{N}] + (184.0 \pm 8.5)[\mathrm{mW}]. \quad (5.9)$$

While the power consumption of thruster A with its associated heater follows the equation

$$P_{\text{Th A}}\,[\text{mW}] = (7.9 \pm 0.1)[\text{mW}/\mu\text{A}] \cdot I_{\text{mon}}\,[\mu\text{A}] + (34.3 \pm 7.1)[\text{mW}] \quad (5.10)$$

$$\approx (78.9 \pm 0.7)[\text{mW}/\mu\text{N}] \cdot |\tilde{\mathbf{F}}|_{\text{rough}}[\mu\text{N}] + (34.3 \pm 7.1)[\text{mW}]. \quad (5.11)$$

It has to be noted that the evolution of the transmissivity $\eta_{\text{curr,N}_\text{A}}$ of the used neutralizer A over time led to an increase in total power consumption.

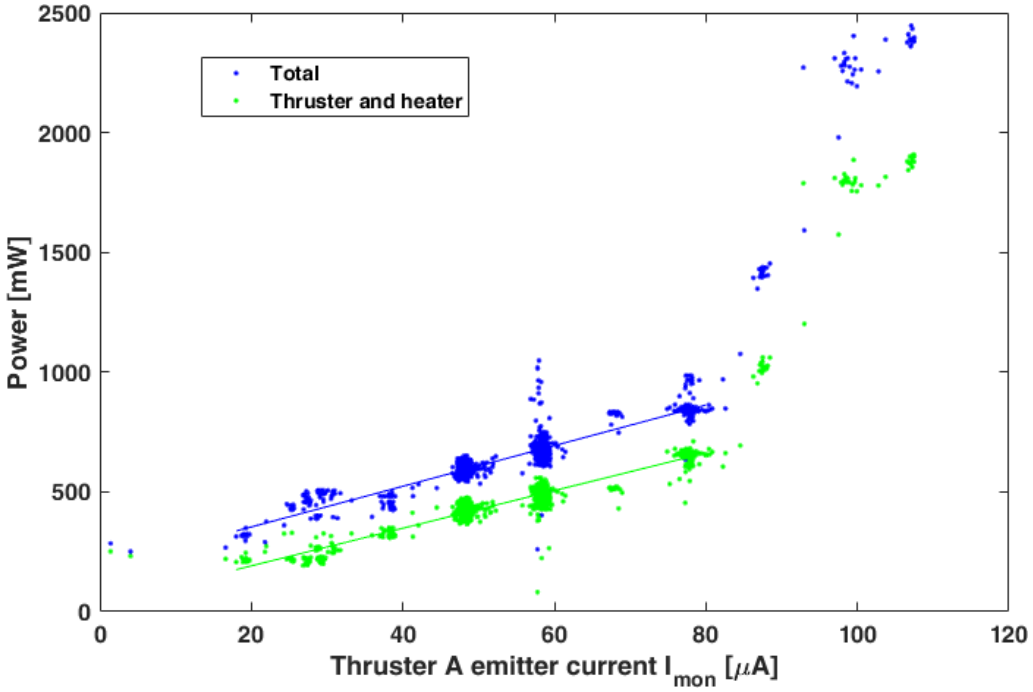

Figure 5.15: Power consumption vs emitter current of thruster A. The total power consumption is depicted in blue, the power consumption of thruster A and its heater in green. (Kramer et al., 2020)

A long term analysis of the thruster A emitter efficiency η_{curr} is shown in Figure 5.16. Almost all measurements follow the linear trend in Figure 5.16c. Figure 5.16a and Figure 5.16b also show a transmissivity η_{curr} of almost 100% during the entire active in-orbit time. The few outliers in light blue in Figure 5.16a and Figure 5.16c result from one measurement with an increase in extractor current $I_{\text{rtn,mon}}$ for the duration of less than two minutes. It was most probably associated with an undissolved propellant particle which deflected the plasma beam. The depicted linear trend line follows the equation

$$I_{\text{mon}} = (1.0 \pm 0.0) \cdot I_{\text{eff}} + (0.3 \pm 0.1). \quad (5.12)$$

The equation clearly shows that the thruster did not degrade in terms of transmissivity η_{curr} during its in-orbit lifetime.

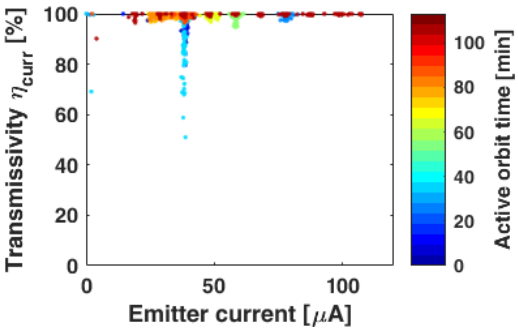

(a) The transmissivity η_{curr} of thruster A.

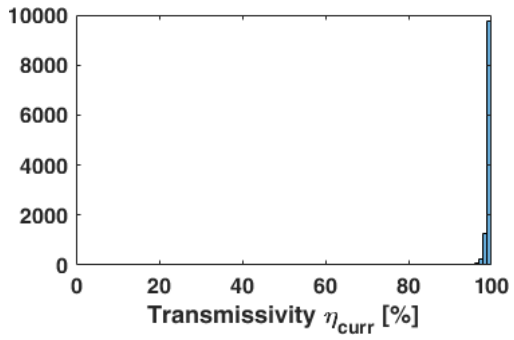

(b) Histogram of the transmissivity η_{curr} of the in-orbit operations of thruster A.

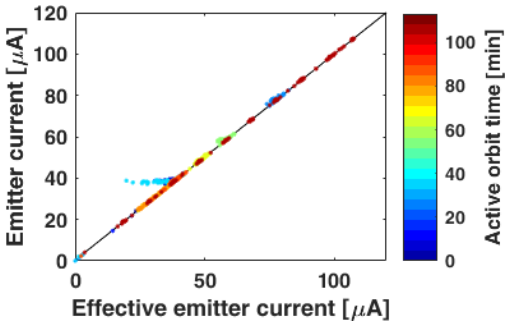

(c) Effective emitter current vs emitter current of thruster A. (Kramer et al., 2020)

Figure 5.16: The long term behavior of the transmissivity of thruster A.

5.3.2 Thruster B

This capillary type NanoFEEP thruster is installed in the -X+Y+Z corner of the CubeSat and is controlled by the same PPU like thruster A.

Laboratory measurements are depicted in Figure 5.17 and show that this thruster has a higher activation voltage than thruster A of approximately 8000V which raises only slightly to about 8150V for the highest emitter current of $I_{des} = 160\mu A$.

However, the voltage U_{mon} is not stable at emitter currents of $I_{mon} = 20\mu A$ and most probably lower, which can be seen in the minutes preceding 21:38. At these low emitter currents, the thruster may not emit continuously which also leads to a deflection of ions and an increase in extractor current $I_{rtn,mon}$. Thus, the thruster should be operated predominantly at a higher emitter current to prevent the contamination of the thruster's inner side. A contamination may lead eventually to a conducting path between needle and extractor and might consequently result in a short-cut and the end of operation for this thruster head.

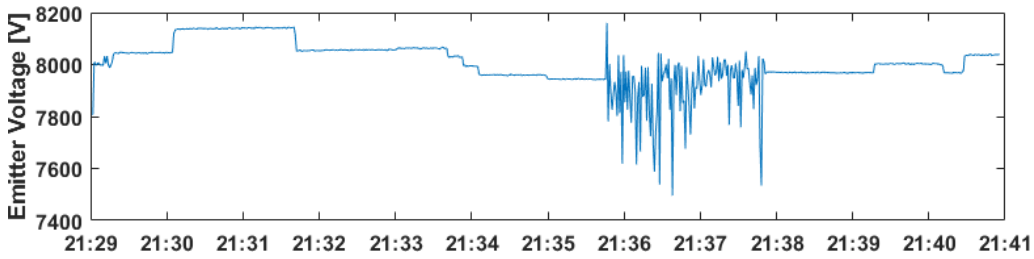

(a) Emitter voltage U_{mon} of thruster B.

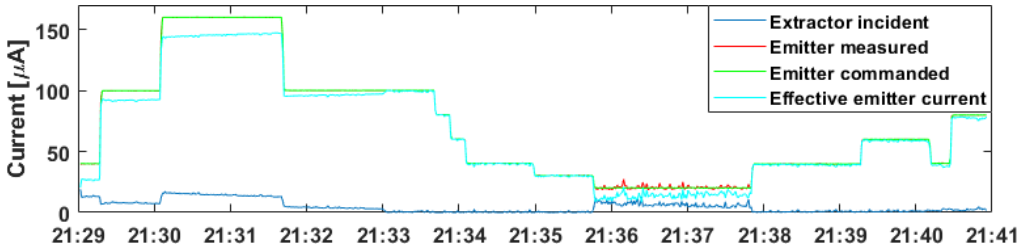

(b) The monitored currents of thruster B.

Figure 5.17: Laboratory measurement of thruster B on October 18th, 2018.

Figure 5.18 shows the transmissivity η_{curr} of this laboratory experiment. The data corresponding to the beginning of the experiment is colored red. At the beginning of the experiment in Figure 5.17, a rather high extractor current $I_{rtn,mon}$ similar to the behaviour of thruster A can be seen. Thus, a cleaning process was done with this thruster which led to a decline and finally to a vanishing extractor current. The transmissivity after the cleaning process, colored blue in Figure 5.18, stayed above 92%, similar to thruster A.

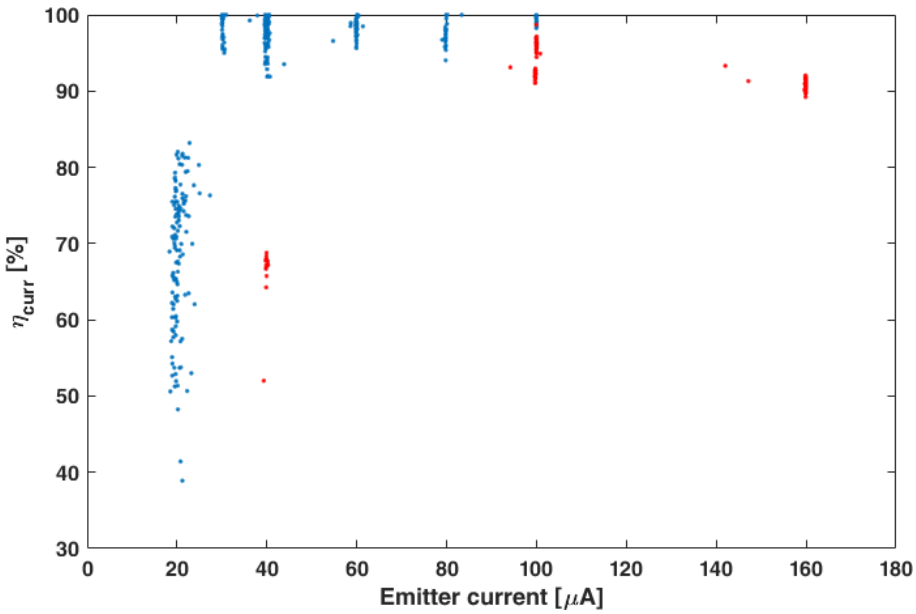

Figure 5.18: Transmissivity of Thruster B during laboratory experiment on October 18th, 2018 (blue); transmissivity during the contamination of the emitter (red).

In-orbit measurements with thruster B were initiated on November 30th, 2019. An exemplary thruster firing from May 23rd, 2020 is depicted in Figure 5.19.

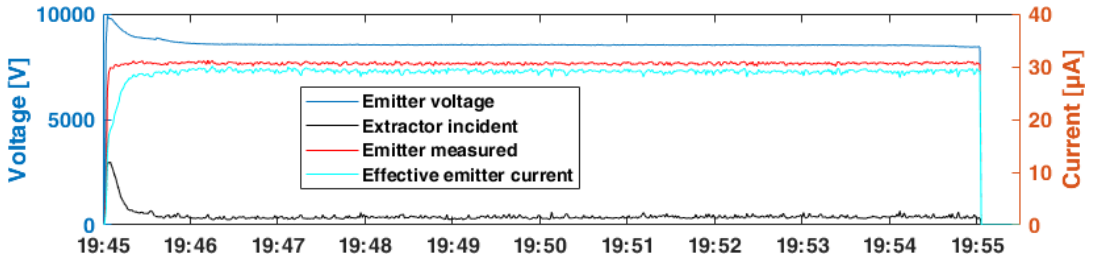

(a) Thruster B electrical characteristics (Kramer et al., 2020)

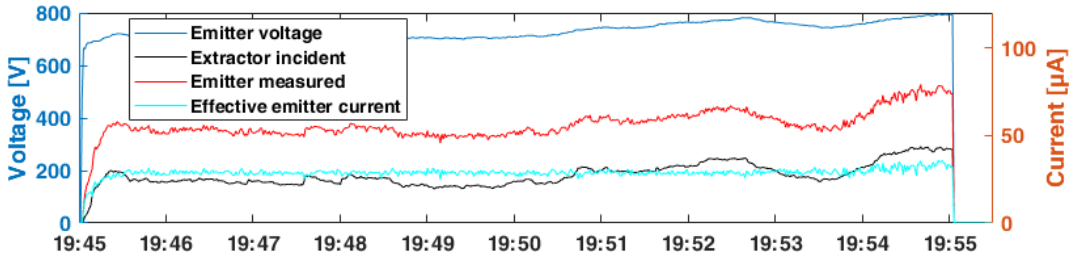

(b) Neutralizer A electrical characteristics

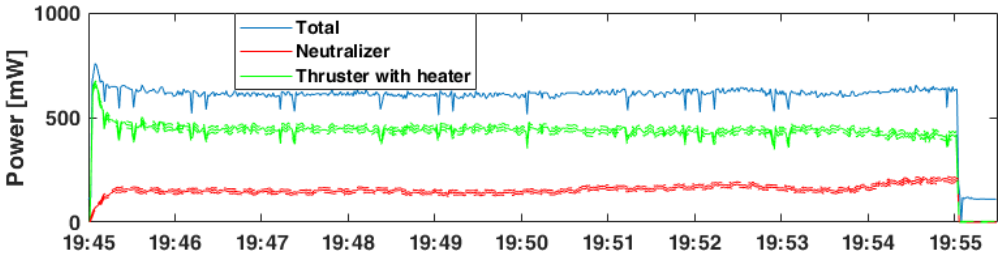

(c) The power consumption of the PPU, the neutralizer, and thruster B with its associated heater within their uncertainties. (Kramer et al., 2020)

Figure 5.19: In-orbit measurement of thruster B on May 23rd, 2020.

During this activation, thruster B was commanded to apply a desired emitter current I_{des} of 30µA. In comparison to thruster A, thruster B has a higher operating voltage of approximately 8400–8600V. The reason for this property is the emitter, as it is a capillary instead of a needle. Additionally, a slight increase in emitter voltage U_{mon} can be seen after activation of the thruster. Thus, the power consumption of thruster B is also at a higher level of about 460mW at an emitter current of 30µA. Furthermore, a considerable extractor current $I_{rtn,mon}$ was registered at activation of the thruster which remained at a measureable level during the entire experiment. The neutralizer characteristics in Figure 5.19b show a steadily increased extractor current $I_{rtn,mon}$ compared to the thruster A experiment shown in Figure 5.14b. However, the thruster A experiment was conducted during early operations already two months after the launch.

To determine the power consumption of thruster B, the analysis described for thruster A in Figure 5.15 was repeated for thruster B. The result of this analysis is shown in Figure 5.20.

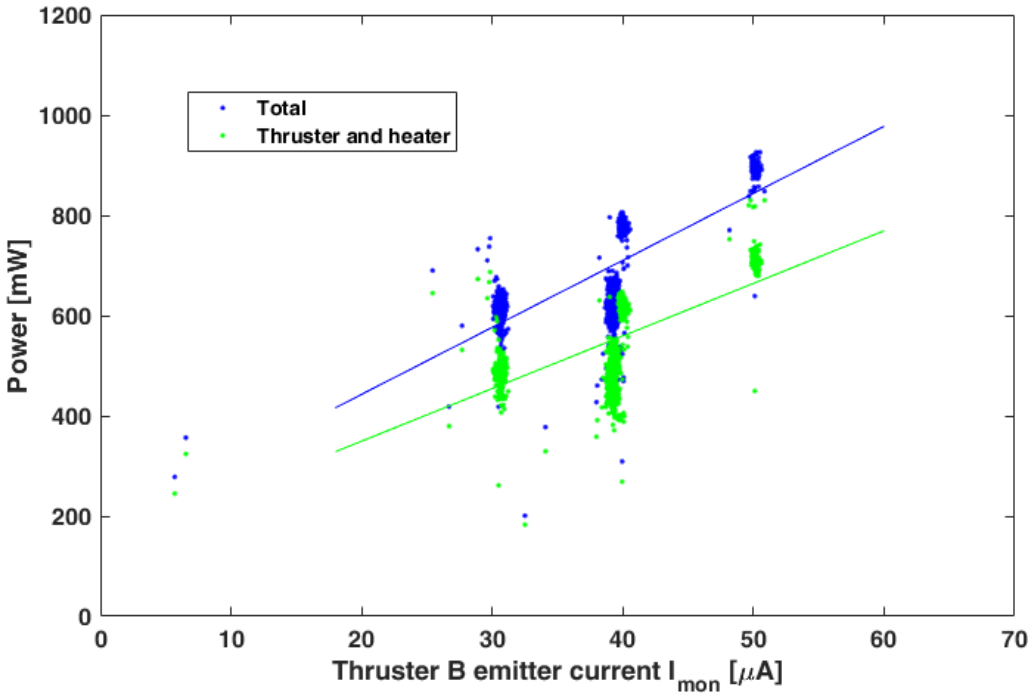

Figure 5.20: Power consumption vs emitter current of thruster B. The total power consumption is depicted in blue, the power consumption of thruster B and its heater in green.

The power consumption of the PPU was only measured at thruster B emitter currents I_{mon} and thrusts $|\tilde{\mathbf{F}}|_{rough}$ in the range of 30–50µA or 3.0–5.0µN, respectively. For these ranges, linear trend lines can be computed which are depicted in Figure 5.20. The total power consumption of the PPU for the thruster B activation follows the equation

$$P_{tot,Th\ B}\ [mW] = (13.4 \pm 0.5)[mW/\mu A] \cdot I_{mon}[\mu A] + (175.5 \pm 18.5)[mW] \quad (5.13)$$

$$\approx (133.7 \pm 4.8)[mW/\mu N] \cdot |\tilde{\mathbf{F}}|_{rough}[\mu N] + (175.5 \pm 18.5)[mW]. \quad (5.14)$$

Reducing the total PPU power consumption by the fraction of the neutralizer and the basic PPU power consumption, yields

$$P_{Th\ B}\ [mW] = (10.5 \pm 0.4)[mW/\mu A] \cdot I_{mon}[\mu A] + (139.6 \pm 16.7)[mW] \quad (5.15)$$

$$\approx (105.0 \pm 4.3)[mW/\mu N] \cdot |\tilde{\mathbf{F}}|_{rough}[\mu N] + (139.6 \pm 16.7)[mW]. \quad (5.16)$$

Thus, the power consumption of thruster B is higher than of thruster A. However, a wider range of operating points for thruster B might have an influence on this observation.

A long term analysis of thruster B is shown in Figure 5.21. The electrical characteristics of thruster B were not consistent during the whole duration of operation, but can be divided in three phases. At the beginning of the operations of thruster B, it was very difficult to activate as the extractor current $I_{rtn,mon}$ indicated an electrical short. This lead to an emergency shut-down of thruster B after 30 seconds of each activation. This behavior

of reduced transmissivity η_{curr} of thruster B during the first 12 minutes of operation is depicted in Figure 5.21a and Figure 5.21b. However, after several attempts of reactivation, the extractor current was reduced and the thruster was activated for further operation, as can be seen in Figure 5.21c and Figure 5.21d. The latter shows a very stable emission with a constant high transmissivity at 94%, when compared to early operations in Figure 5.21b.

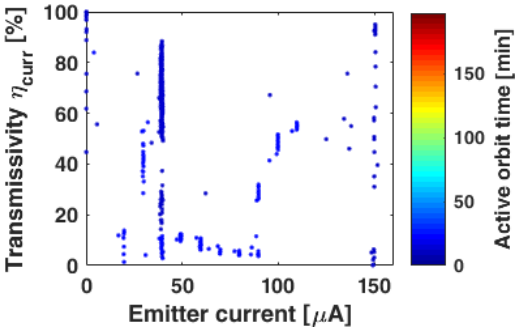

(a) Unstable behavior during first 12 minutes of early operations. (Kramer et al., 2020)

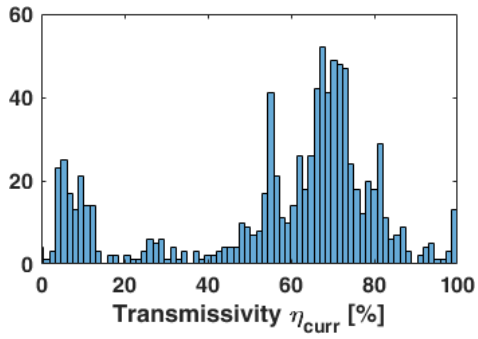

(b) Histogram of the transmissivity η_{curr} during the first 12 minutes of operations.

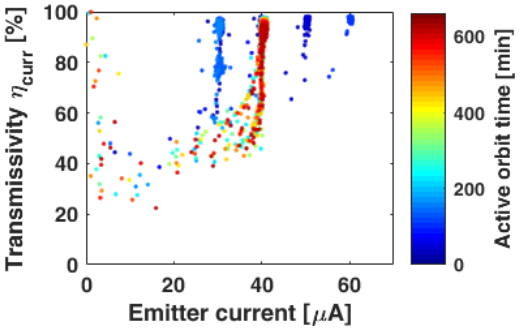

(c) Operations for thruster characterizations and orbit control experiments until total time of operation of 650 minutes.

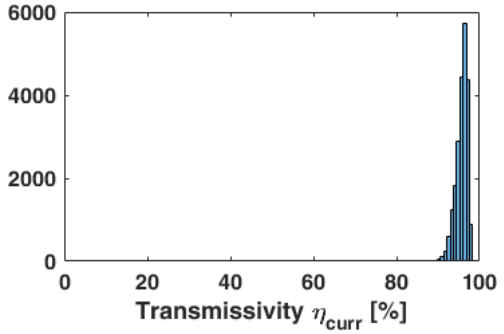

(d) Histogram of the transmissivity η_{curr} during the same phase as in Figure 5.21c.

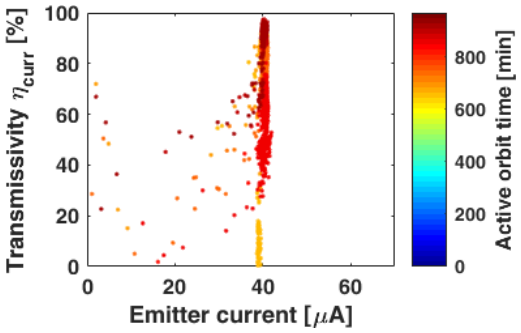

(e) During the late orbit control experiments, the transmissivity of thruster B changed to an unstable behavior.

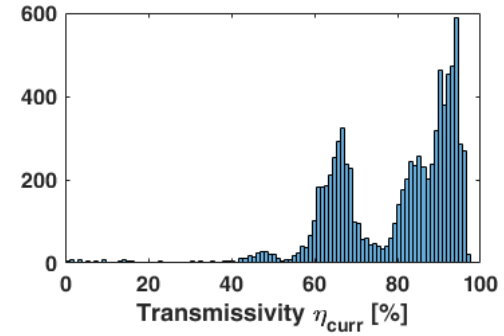

(f) Histogram of the transmissivity η_{curr} during late orbit control experiments. A second peak is built up at 67% transmissivity.

Figure 5.21: Transmissivity progress of thruster B during in-orbit experiments between November 30$^{\text{th}}$, 2019 and July 25$^{\text{th}}$, 2020.

The experiments serving as basis for the power consumption analysis in Figure 5.20 were conducted during this second phase of stable transmissivity. After approximately 200 minutes of operation for the characterization of the thruster head itself, it was activated for orbit control experiments (refer to Chapter 7). After a total of 650 minutes of in-orbit operation of thruster B, the transmissivity of the thruster decreased again, as shown in Figure 5.21e and Figure 5.21f. During the orbit control experiments, thruster B was always commanded to an emitter current I_{des} of 40µA. Nonetheless, it can be seen that a second maximum is built up in Figure 5.21f at a value of about 67%, which corresponds to very late measurements in Figure 5.21e, as indicated by the dark red color. Unfortunately, the orbit control experiments with thruster B were stopped by a malfunction, which put an end to 954 minutes of successful operation. It was not possible to reactivate the thruster again because of reoccurring overcurrent faults at the PPU.

5.3.3 Thruster C

This porous type NanoFEEP thruster is mounted in the -X-Y+Z corner of the CubeSat structure of UWE–4. It is controlled by the same PPU as thruster D and neutralizer B. While the thruster performed as desired during laboratory experimentation, the in-orbit activation was not successful.

Laboratory measurements on October 18th, 2018 have shown a similar behaviour like thruster A - the other mounted porous type NanoFEEP thruster on UWE–4, as can be seen in Figure A.5. The operating voltage U_{mon} covered a range of 6000-8200V for emitter currents I_{mon} between 2–140µA. The extractor current $I_{rtn,mon}$ did only increase over the noise floor for emitter currents larger than 100µA. However, as this effect only arises at high emitter currents, this can rather be attributed to the beam divergence than to an unexpected behaviour of the emitter.

The transmissivity of thruster C, which is shown in Figure A.6, shows a similar performance like thruster A with values above 95% for emitter currents larger than 20µA and varying efficiencies at lower emitter currents.

Figure A.7 shows the power consumption of thruster C. For effective emitter currents I_{eff} below 80µA or thrusts $|\tilde{\mathbf{F}}|_{rough}$ below 8.0µN a linear trend line following the equation

$$\begin{aligned} P_{tot,Th\ C}\ [mW] &= (9.0 \pm 0.4)[mW/\mu A] \cdot I_{mon}[\mu A] + (114.6 \pm 14.1)[mW] && (5.17) \\ &\approx (90.2 \pm 3.8)[mW/\mu N] \cdot |\tilde{\mathbf{F}}|_{rough}[\mu N] + (114.6 \pm 14.1)[mW] && (5.18) \end{aligned}$$

can be inserted. While the slope is similar to the gradient of thruster A in Eq. (5.8), the ordinate of this laboratory experiment does not comprise of the power consumption of the neutralizer and can thus not be compared.

5.3.4 Thruster D

Thruster D is a needle type NanoFEEP emitter and mounted in the +X-Y+Z corner of UWE–4. Like thruster C of the same PPU, it performed well during laboratory experimentation but could not be activated in-orbit.

Laboratory measurements on October 16th, 2018 are depicted in Figure A.8. The operating voltage U_{mon} is in the range between 6700–7000V in an emitter current range I_{mon} of 40–200µA. In this regime, the extractor current stays at the noise floor. Similar to thruster B, the operating voltage is not stable at low emitter currents and the extractor current $I_{rtn,mon}$ is fluctuating accordingly. However, the comparable thruster B has shown a similar behaviour for low emitter currents.

Figure A.9 correspondingly shows an emitter transmissivity above 95% for currents larger than 40 µA and a strong fluctuation at lower emitter currents.

5.4 Summary

The preceding chapter introduced to the operation and the relevant electrical characteristics of the NanoFEEP propulsion system. It comprises of the three main components, namely the heater circuit for the liquefaction of the propellant, the thruster heads themselves which create thrust by ejecting positively charged gallium ions, and the neutralizers for the compensation of the charge loss due to the emission of positive ions by the thruster heads.

While the heater circuit reliably liquefied the propellant during laboratory experimentation, it was not powerful enough to liquefy the propellant during the entire orbital duration. However, with some adjustments of the heater controller, it was possible to activate the thrusters during roughly 50 minutes of the sun-synchronous orbit of UWE–4, starting approximately 27–35 minutes after leaving the eclipse interval of the orbit. The power consumption of the heater circuit of each thruster head was found to be at 103±4mW. A suggestion for the improvement of the heater circuit by increasing the used voltage was forwarded to the NanoFEEP propulsion system manufacturer from TU Dresden.

The CNT based neutralizers of the PPUs were always able to compensate for the charge loss of their associated thruster heads. Their performances differed generally in two main criteria. The power consumption of neutralizer A was 2.36mW/µA, while neutralizer B only consumed 1.68mW/µA. Additionally, after more than one year in-orbit, the transmissivity of neutralizer A was in the range of 50–60%, in contrast to 88–92% of neutralizer B. It was observed that the transmissivity of neutralizer A decreased considerably from a value of 82% to 42% during the time in orbit, which may be attributed to the impact of atomic oxygen according to Ohkawa et al. (2019).

It was observed that a stable compensation of the ejected ion current of the thrusters was possible by using the neutralizers. At the time of writing this thesis, thruster A was activated for about 120 minutes in total and has not shown any signs of performance loss, yet. Additionally, no interaction with the antenna of the radio communication system was observed. The power consumption of thruster A including its associated heater circuit is at a value of 7.9mW/µA or 78.9mW/µN, respectively. The transmissivity η_{curr} stayed at almost 100% during the entire in-orbit duration.

The in-orbit operation of thruster B was possible intermittently. The initialisation of the operations was difficult due to a high extractor current $I_{rtn,mon}$ which indicated an electrical short. However, stable operation was achieved after several reactivations of the thruster head. During this second phase of stable operations, the power consumption of the thruster head and its associated heater circuit was 10.5mW/µA or 105.0mW/µN, respectively. The

transmissivity was at about 94%. After about 650 minutes of operations, the transmissivity was reduced again to 67% until the thruster operation was stopped by an overcurrent fault after 954 minutes of operation. No further activation of thruster B was possible afterwards.

Thrusters C and D could not be activated in-orbit on board UWE–4. However, laboratory experiments have shown a similar performance like thrusters A and B. As thrusters C and D are associated with the same PPU, an electrical hardware issue is the most probable cause for the emergency shut-down of the corresponding hotswap circuit.

6
Thrust direction estimation

As UWE–4 uses the newly developed NanoFEEP propulsion system for its orbit control purposes, the uncertainties of this novel propulsion system relevant for orbit control shall be clarified. While the magnitude of the created thrust can be calculated from the electrical characteristics of the thrusters using Eq. (2.6), the thrust direction is only determined by the mounting direction. Bock et al. (2017b) describe plume characterization measurements conducted with the NanoFEEP propulsion system. As the measured current distributions do not center about the thruster's vertical axis but with a few degrees offset, the publication states that "[t]his may either be caused by a not straight emission of the tested thruster or by an angular misalignment of the thruster" relative to the current measuring probe. In order to estimate the amount of thrust produced in the desired direction, the average thrust direction of each thruster head has to be determined. Assuming that the center direction of the current distribution of the plume is directly opposite to the thrust direction, measuring the thrust direction should also give the possibility to validate the conclusion of the aforementioned publication of an angular misalignment.

For the purpose of determining the angular stability of the created thrust, a novel algorithm in order to estimate the thrust direction has been developed. The algorithm as well as the results of the NanoFEEP propulsion system on-board UWE–4 will be presented in this chapter. The starting point of this algorithm was inspired by work presented by Bangert (2018) concerning the estimation of the thrust magnitude. As the algorithm and the results were the key content of Kramer et al. (2020), considerable parts of this chapter were already published in the aforementioned article.

The created torque of the NanoFEEP propulsion system thrusters can be estimated numerically by making use of the AOCS sensors and the euler equation described in Chapter 4.1. If a thruster at position $\mathbf{r}_{\text{thr}}$ (measured from the center of gravity of the satellite) creates a thrust $\mathbf{F}_{\text{thr}}$, the following euler equation describes the attitude motion:

$$\begin{aligned} \mathbf{T}_{\text{ext}}(t) &= \mathbf{T}_{\text{thr}}(t) + \mathbf{T}_{\mu}(t) \\ \mathbf{r}_{\text{thr}} \times \mathbf{F}_{\text{thr}}(t) &= \mathbf{I}\dot{\boldsymbol{\omega}}(t) + \boldsymbol{\omega}(t) \times (\mathbf{I}\boldsymbol{\omega}(t)) - \boldsymbol{\mu}_{\text{res}} \times \mathbf{B}(t) \end{aligned} \tag{6.1}$$

The moment of inertia tensor $\mathbf{I}$ is determined alongside the residual magnetic dipole moment $\boldsymbol{\mu}_{\text{res}}$ in Chapter 4.2 and is in very good agreement with the moment of inertia tensor retrieved from the CAD model. Thus, it is justified to use the position vector $\mathbf{r}_{\text{thr}}$ of the respective thruster head from the CAD model for this computation as well with an assumed uncertainty of $\delta \mathrm{r}_{\text{thr},i} = 5 \cdot 10^{-3}\mathrm{m}$ in every direction. For the purpose of thrust

estimation, the respective thruster will be commanded to emit continuously at the same desired emitter current I_{des}. As shown in Chapter 5.3, the emitter current of a NanoFEEP thruster has a very low noise amplitude. Therefore, the created thrust of a commanded emitter can be assumed to be constant if only experiments with very low extractor currents are considered. Thus, the time dependency of the thrust $\mathbf{F}_{thr}$ in Eq. (6.1) can be neglected. An example of the calculated thrust magnitude is depicted in Figure 6.1. Additionally, the created torque is expected to be constant in contrast to the torque created by a residual magnetic dipole moment, which depends on the attitude relative to the Earth's magnetic field.

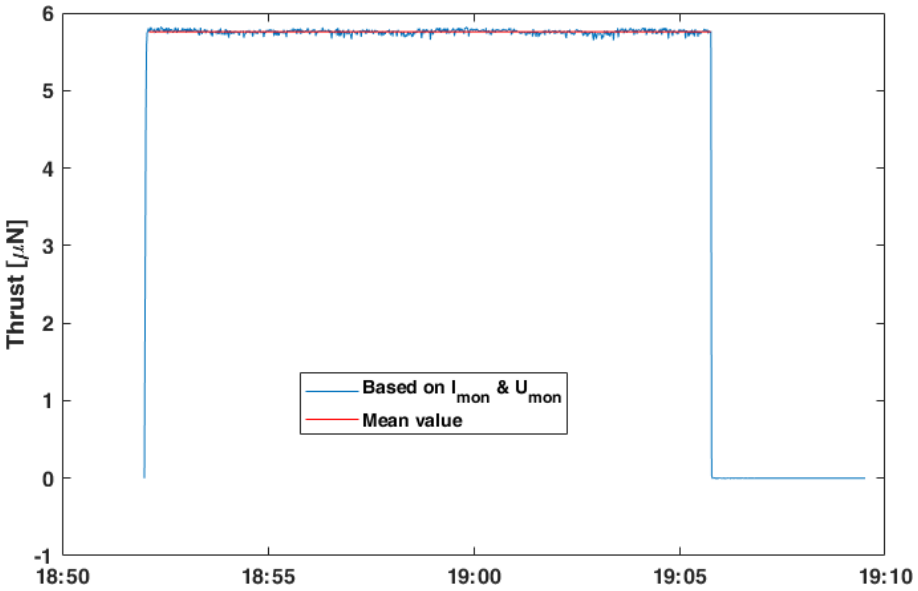

Figure 6.1: Thrust magnitude of thruster B during experiment on May 31st, 2020 according to Eq. (2.6) in blue. The mean value is depicted in red. (Kramer et al., 2020)

While the angular rate $\omega(t)$ and the Earth's magnetic field $\mathbf{B}(t)$ can be measured onboard the satellite, special care has to be taken in the numeric differentiation of $\dot{\omega}(t)$. Eq. (6.1) can be solved for every time instant t_i if the magnetic field $\mathbf{B}(t_i)$ and the angular rate are available.

6.1 Preparation of measurement data

The measured data of magnetic field $\mathbf{B}$ and angular rate ω has to be prepared for this analysis with several steps.

The first step of data preparation of both the magnetic field $\mathbf{B}$ and the angular rate ω is smoothing the data using a local weighted regression model with a linear polynomial (Cleveland, 1979). As the created thruster torque was constant, the only frequency consideration in the configuration of the smoothing process was for the (de-)activation processes of the thruster. An experiment for thrust estimation was always executed with a constant

thrust for a duration between 8–15 minutes. As a trade-off between smoothing noise in the angular rate and retaining rather sharp edges in the change of the angular rate $\dot{\omega}$ during the (de-)activation process of the thruster, a 20 second window around the time instant t_i was chosen for the smoothing. Afterwards, the data was re-sampled using a spline interpolation algorithm to equidistant times. An example of smoothed and re-sampled data is depicted in Figure 6.2 which shows the angular rate measurement during an activation of thruster B with a desired emitter current of 60µA for 15 minutes on May 31st, 2020.

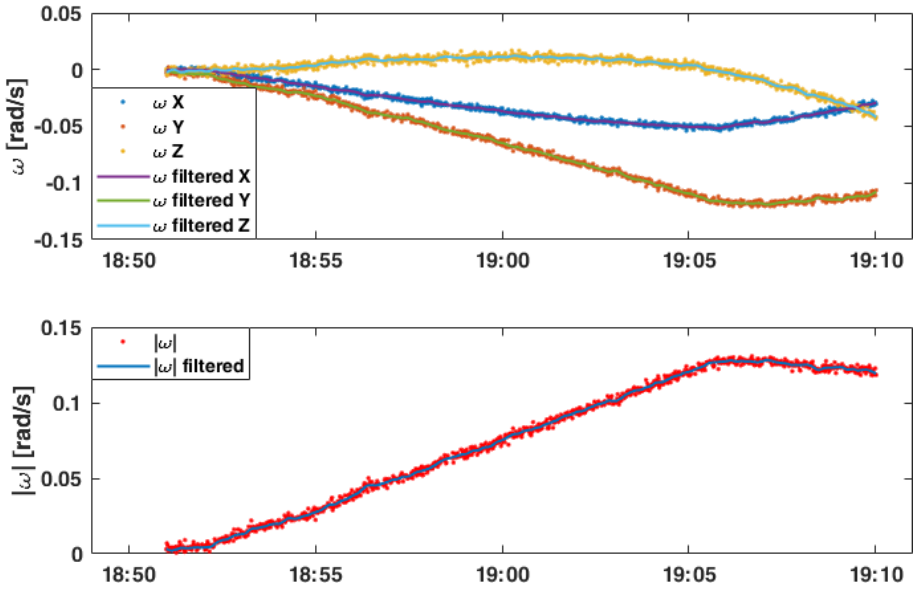

Figure 6.2: Smoothing of angular rate data as preparation for thrust estimation. Raw (dots) vs smoothed (line) angular rate data during thruster B firing on May 31st, 2020. (Kramer et al., 2020)

In order to compute the change of the angular rate $\dot{\omega}(t)$ numerically to a rather smooth signal, the measured quantity ω has to be differentiated numerically in a robust way which suppresses high frequency components of the noise. For this purpose, also a local weighted differentiation is used which assigns lower weight to more distant data points (Holoborodko). The three neighbouring points $t_{i-3} - t_{i+3}$ for each data point t_i are used to this effect.

6.2 Objective Function

If the measured data were not noisy and it was assumed that the thruster always created thrust in exactly the same direction, the direction of the created torque would always be the same and the negative of the mean value of the external torque $\mathbf{T}_{\text{ext}}(t_i)$ would be a good choice for the torque created by the thruster. However, these assumptions shall not be made here in order to be able to determine the thrust direction and its empirical repeatability.

To determine the torque created by the NanoFEEP propulsion system, which explains

the attitude motion of the spacecraft best, a quadratic error function was defined as

$$\begin{aligned} \mathrm{E}(\mathbf{F}_{\mathrm{thr},\perp}) &= \frac{1}{\mathrm{N}}\sum_{i}^{N}\sqrt{\left(\mathbf{T}_{\mathrm{thr}}-\mathbf{T}_{\mathrm{ext}}(t_i)+\mathbf{T}_{\mu}(t_i)\right)^2} \\ &= \frac{1}{\mathrm{N}}\sum_{i}^{N}\sqrt{\left(\mathbf{r}_{\mathrm{thr}}\times\mathbf{F}_{\mathrm{thr},\perp}-(\mathbf{I}\dot{\omega}(t_i)+\omega(t_i)\times(\mathbf{I}\omega(t_i)))+\boldsymbol{\mu}_{\mathrm{res}}\times\mathbf{B}(t_i)\right)^2} \end{aligned} \quad (6.2)$$

The MATLAB™ function *fminsearch* optimizes the three independent components of the thrust $\mathbf{F}_{\mathrm{thr},\perp}$ using a Nelder-Mead simplex algorithm (Lagarias et al., 1998).

This objective function is only capable to determine a part of the created thrust $\mathbf{F}_{\mathrm{thr}}$ for which holds $\mathbf{F}_{\mathrm{thr},\perp} \perp \mathbf{r}_{\mathrm{thr}}$, since the part of the thrust $\mathbf{F}_{\mathrm{thr},\parallel}$ which is parallel to the position vector $\mathbf{r}_{\mathrm{thr}}$ does not contribute to the created torque $\mathbf{T}_{\mathrm{thr}}$. While the thrusters are mounted at the end of the rails in +Z - direction, the position vector $\mathbf{r}_{\mathrm{thr}}$ is rather a diagonal in 3D-space, as can be seen in Figure 3.2. Thus, the thrust $\mathbf{F}_{\mathrm{thr},\perp}$ derived with Eq. (6.2) can only be a part of the total thrust $\mathbf{F}_{\mathrm{thr}}$.

After the application of the objective function, the torque created by the thruster can be computed already. For this purpose, Eq. (4.3) can be employed with the thrust $\mathbf{F}_{\mathrm{thr},\perp}$ which is computed by using Eq. (6.2). The external torque $\mathbf{T}_{\mathrm{ext}}$ and the thruster torque $\mathbf{T}_{\mathrm{thr}}$ are depicted for two experiments with different thrust magnitudes in Figure 6.3. It shows that the constant torque created by the thruster shifts the measured external torques in each axes.

The measured external torques $\mathbf{T}_{\mathrm{ext},i}$ depicted in Figure 6.4 resemble a normal distribution. Furthermore, the subtraction of the thruster torque $\mathbf{T}_{\mathrm{thr}}$ does not change the width of the distribution like the subtraction of a torque created by a static magnetic dipole would. The standard deviation $\sigma(\mathbf{T}_{\mathrm{ext},i}) = \delta\mathbf{T}_{\mathrm{ext},i} = \delta\mathbf{T}_{\mathrm{thr},i}$ contains the measurement inaccuracies of the angular rate ω, the Earth's magnetic field $\mathbf{B}$, the residual magnetic dipole moment $\boldsymbol{\mu}_{\mathrm{res}}$ and the moment of inertia tensor $\mathbf{I}$ and is a good choice for error propagation to the found thrust. Since Eq. (4.3) holds, the equation can be solved for $\mathbf{F}_{\mathrm{thr},\perp}$ as

$$\mathbf{F}_{\mathrm{thr},\perp} = \mathbf{T}_{\mathrm{thr}} \times \mathbf{r}_{\mathrm{thr}}. \quad (6.3)$$

The uncertainty of the found thrust component $\delta\mathrm{F}_{\mathrm{thr},\perp,i}$ thus calculates as

$$\delta\mathrm{F}_{\mathrm{thr},\perp,i} = \sqrt{\sum_{j,k=x,y,z}\left((\mathrm{r}_{\mathrm{thr},j}\cdot\delta\mathrm{T}_{\mathrm{ext},k})^2+(\mathrm{T}_{\mathrm{ext},j}\cdot\delta\mathrm{r}_{\mathrm{thr},k})^2\right)} \quad | \, i \neq j \neq k. \quad (6.4)$$

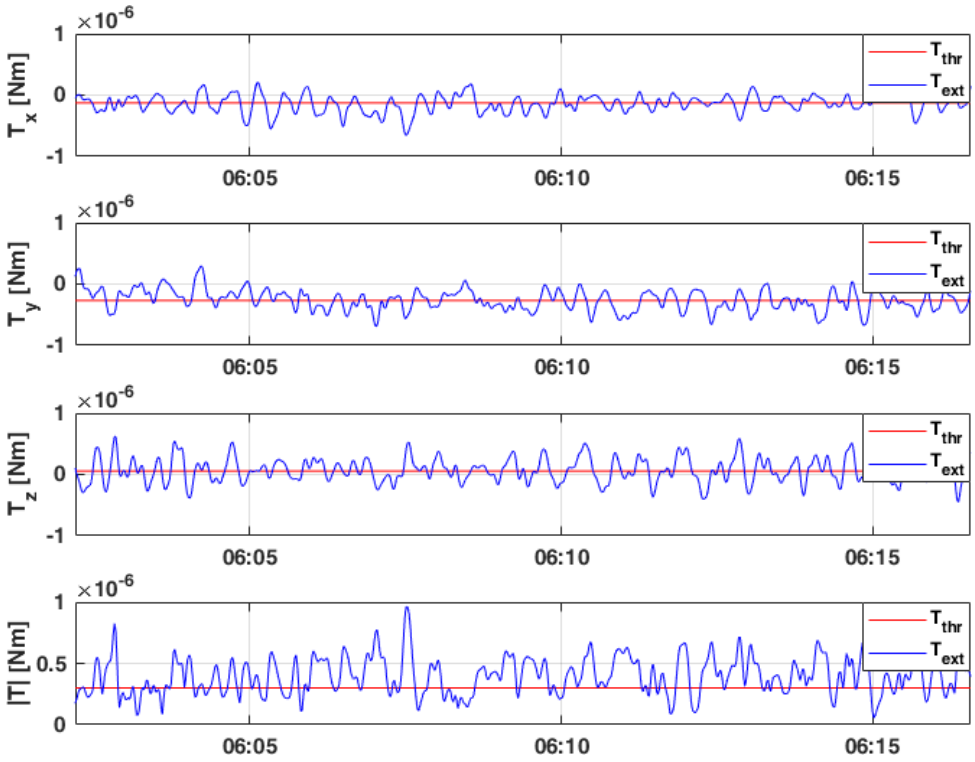

(a) Activation on May 31st, 2020 with 5.8 µN thrust.

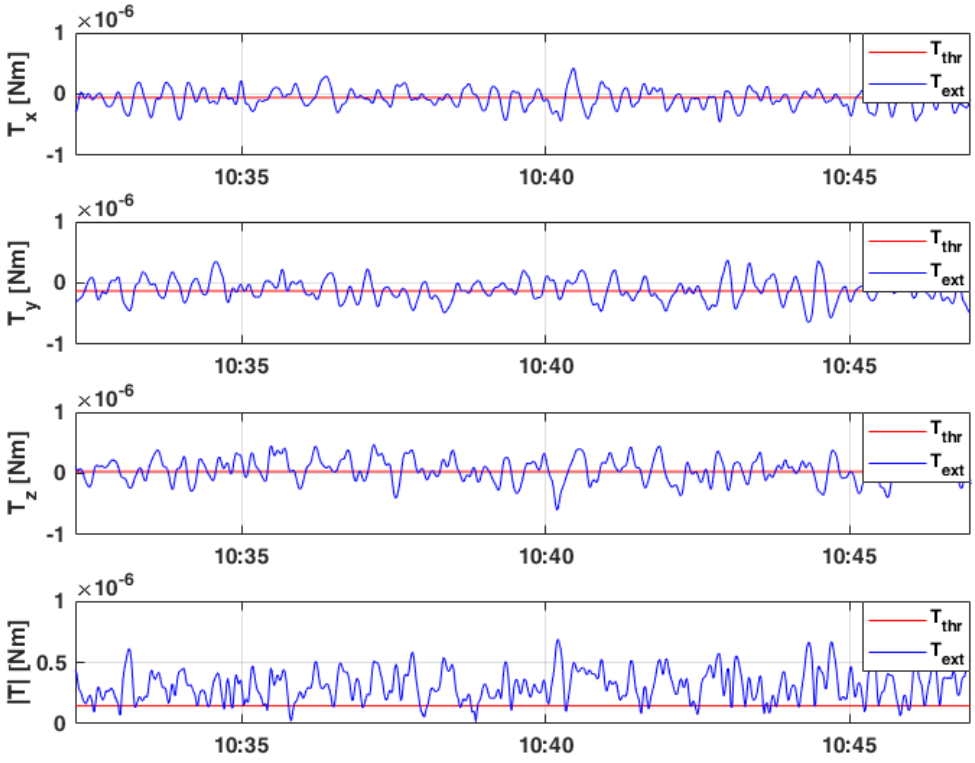

(b) Activation on June 18th, 2020 with 3.0 µN thrust.

Figure 6.3: External torque $\mathbf{T}_{ext}$ (blue) and derived thruster torque $\mathbf{T}_{thr}$ (red) created by thruster B during different experiments.

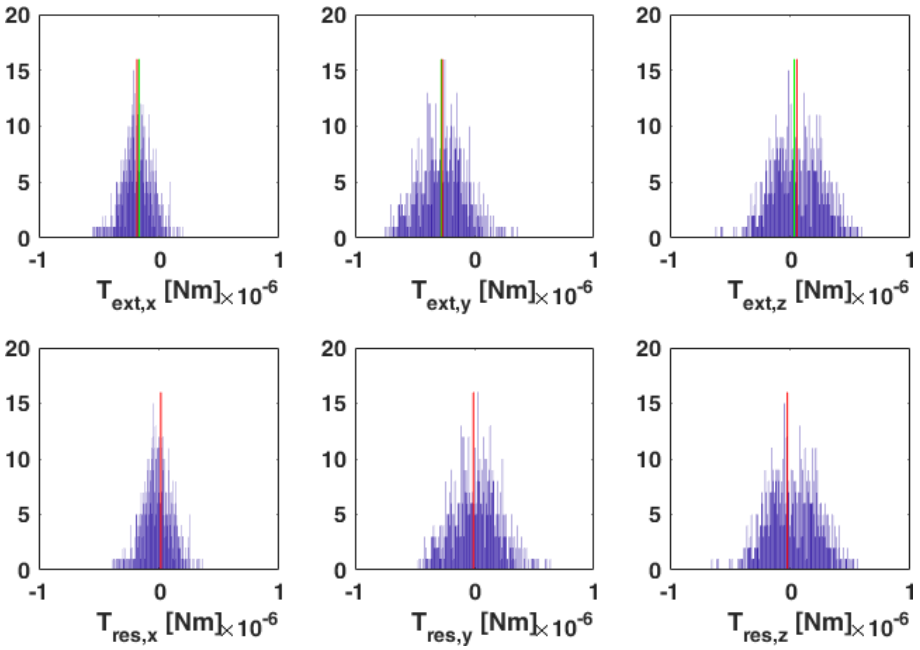

Figure 6.4: The external torque $\mathbf{T}_{\text{ext}}$ in the top row vs the remaining torque $\mathbf{T}_{\text{rem}} = \mathbf{T}_{\text{ext}} - \mathbf{T}_{\text{thr}}$ in the bottom row for the thruster B experiment on May 31$^{\text{st}}$, 2020. The mean value of $\mathbf{T}_{\text{ext}}$ and $\mathbf{T}_{\text{rem}}$ is shown in red and the torque following Eq. (4.3) with the thrust determined using Eq. (6.2) in green. (Kramer et al., 2020)

6.3 Total thrust estimate

As already mentioned in the previous section, the component $\mathbf{F}_{\text{thr},\parallel}$ of the thrust which is parallel to the position vector of the respective thruster $\mathbf{r}_{\text{thr}}$ does not affect the spacecraft's attitude behaviour. Thus, the total thrust can be written as

$$\begin{aligned} \mathbf{F}_{\text{thr}} &= \mathbf{F}_{\text{thr},\perp} + \mathbf{F}_{\text{thr},\parallel} \\ &= \mathbf{F}_{\text{thr},\perp} + \alpha \cdot \mathbf{r}_{\text{thr}}. \end{aligned} \tag{6.5}$$

The thrust magnitude $|\tilde{\mathbf{F}}|$ of a NanoFEEP thruster can be calculated using Eq. (2.6). A study by Bock et al. (2017a) has proven the equation experimentally using a thrust measuring probe. However, the emitted ion current I_e has to be replaced with (I_{mon} - $I_{\text{rtn,mon}}$) and the voltage of the electric field with U_{mon}. In this paper, the calculated thrust magnitude deviates from the measured thrust by maximal 5%. Consequently, it holds

$$|\tilde{\mathbf{F}}| = ||\mathbf{F}_{\text{thr},\perp} + \alpha \cdot \mathbf{r}_{\text{thr}}||_2 \tag{6.6}$$

which can be solved for α as

$$\alpha_{1,2} = \frac{-\mathbf{F}_{\text{thr},\perp} \cdot \mathbf{r}_{\text{thr}}}{\mathbf{r}_{\text{thr}}^2} \cdots$$
$$\frac{\pm\sqrt{|\tilde{\mathrm{F}}|^2 \mathbf{r}_{\text{thr}}^2 - \left(\mathrm{F}_{\perp,x}\mathrm{r}_y - \mathrm{F}_{\perp,y}\mathrm{r}_x\right)^2 - \left(\mathrm{F}_{\perp,x}\mathrm{r}_z - \mathrm{F}_{\perp,z}\mathrm{r}_x\right)^2 - \left(\mathrm{F}_{\perp,y}\mathrm{r}_z - \mathrm{F}_{\perp,z}\mathrm{r}_y\right)^2}}{\mathbf{r}_{\text{thr}}^2}. \quad (6.7)$$

In Eq. (6.6), the sign $||\mathbf{x}||_2$ represents the 2-norm and thus the length of the vector $\mathbf{x}$. Mathematically, two solutions for α exist. However, only the solution for α_1 with the plus sign in Eq. (6.7) leads to a total thrust vector $\mathbf{F}_{\text{thr}}$ pointing in the half space of the -Z - direction. Due to the mounting of the NanoFEEP thrusters, the other mathematical solution is not feasible. The error propagation of the uncertainties in Eq. (6.7) can be found in the appendix in Chapter B.

With the found α the total thrust $\mathbf{F}_{\text{thr}}$ can be calculated as described in Eq. (6.5). The error propagation for $\delta\mathbf{F}_{\text{thr}}$ thereby follows

$$\begin{aligned}\delta\mathrm{F}_{\text{thr},i} &= \sqrt{\left(\frac{\partial \mathrm{F}_{\text{thr},i}}{\partial \mathrm{F}_{\text{thr},\perp,i}} \cdot \delta\mathrm{F}_{\text{thr},\perp,i}\right)^2 + \left(\frac{\partial \mathrm{F}_{\text{thr},i}}{\partial \mathrm{r}_{\text{thr},i}} \cdot \delta\mathrm{r}_{\text{thr},i}\right)^2 + \left(\frac{\partial \mathrm{F}_{\text{thr},i}}{\partial \alpha} \cdot \delta\alpha\right)^2} \\ &= \sqrt{\delta\mathrm{F}_{\text{thr},\perp,i}^2 + \left(\alpha \cdot \delta\mathrm{r}_{\text{thr},i}\right)^2 + \left(\mathrm{r}_{\text{thr},i} \cdot \delta\alpha\right)^2}. \quad (6.8)\end{aligned}$$

6.4 Angular stability

While the thrust magnitude has been fixed using Eq. (2.6), the direction of the created thrust can be calculated. For this purpose, spherical coordinates are introduced. The representation of spherical coordinates in a Cartesian reference frame is shown in Figure 6.5. The transformation from Cartesian to spherical coordinates as well as the error propagation in the representation of a vector in spherical coordinates is described in the appendix in Chapter C.

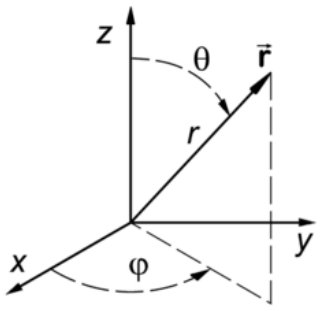

Figure 6.5: Representation of spherical coordinates in a Cartesian reference frame.

In total, 15 experiments with the purpose of thrust estimation have been conducted - 5 experiments with thruster A and 10 experiments with thruster B. The detailed results of

these measurements as well as the variation of the parameters thrust magnitude $|\tilde{\mathbf{F}}|$ and activation duration are shown in Table 6.1.

Thruster	Thrust [µN]	Activation time [mm:ss]	φ [deg]	Θ [deg]
A	3.3	09:57	101.2 ± 67.4	175.0 ± 5.1
A	4.9	09:57	177.2 ± 19.9	163.8 ± 6.6
A	4.1	10:01	178.8 ± 12.5	153.8 ± 7.1
A	2.4	10:00	139.7 ± 18.3	162.6 ± 6.0
A	4.1	09:58	132.6 ± 23.3	166.3 ± 5.7
B	4.9	08:34	-89.8 ± 14.2	157.8 ± 5.1
B	4.9	08:46	59.0 ± 22.3	166.9 ± 4.8
B	3.9	09:52	89.5 ± 32.1	169.9 ± 4.9
B	3.9	09:50	-78.2 ± 17.4	161.3 ± 5.2
B	3.9	14:54	-84.6 ± 16.8	161.0 ± 5.1
B	5.8	14:27	77.7 ± 29.6	169.2 ± 5.0
B	5.8	13:39	56.3 ± 50.8	173.8 ± 5.3
B	3.0	14:52	-51.5 ± 23.5	166.2 ± 5.6
B	3.0	14:56	-40.6 ± 61.5	174.9 ± 5.6
B	3.0	14:45	86.4 ± 23.9	166.8 ± 4.8

Table 6.1: Parameters and results of the thrust estimation experiments.

While the thrust varied in the range of 2.4–5.8µN, the activation time of the experiments was in the range of 08:34–14:56 minutes. The angle Θ was determined with an uncertainty in the range of 4.8–7.1° in each experiment, opposed to the rather large uncertainty in φ at up to 67.4°. The averaged results are shown in Table 6.2.

	Θ [deg]	φ [deg]
Thruster A	164.3±7.6	145.9±32.7
Thruster B	166.8±5.5	2.4±77.3

Table 6.2: Average thrust direction in spherical coordinates.

The results show a slight off-pointing of the analysed thrust direction from the mounting direction of the thrusters, as indicated by the angle Θ in Table 6.2. Consequently, the determined thrust vectors always point predominantly in negative z-direction in the body-fixed coordinate system. However, the large uncertainty in φ does not allow to fully define whether the direction is inclined towards positive or negative x- or y- direction. Due to the conversion to spherical coordinates, small variations in the thrust contributions in the x-y-plane result in a large uncertainty, as can be seen in the values of the angle φ in Table 6.2.

The thrust magnitude pointing in negative z-direction in the body-fixed coordinate frame is reduced due to the misalignment of the thrust direction relative to the body-fixed coordinate frame and can be calculated as follows

$$|\tilde{\mathbf{F}}|_{-z} = |\tilde{\mathbf{F}}| \cdot \cos(180° - \Theta). \tag{6.9}$$

Thus, the percentage of thrust applied by the two active thrusters A and B in the negative z-direction is in the range of 92–99% and 95–99%, respectively.

6.5 Summary

This chapter presented a novel algorithm to determine the thrust direction by analysing the created torque of the thrust using the attitude determination sensors. In a first step, a necessary torque created by the thruster is determined, which explains the rotation rate of the spacecraft. However, the determined torque does not include the entirely created thrust, as the thrust vector is not perpendicular to the position vector of the thruster relative to the center of gravity of the satellite. As the thrust magnitude can be calculated from the electrical characteristics of the used NanoFEEP propulsion, the final thrust direction can be found making use of the absolute thrust value.

Both thruster heads have shown a slight off-pointing of $15.7 \pm 7.6°$ for thruster A and $13.2 \pm 5.5°$ for thruster B from their mounting direction. The corresponding reduction of thrust in the desired negative z-direction will be considered in the following chapter.

Furthermore, the laboratory measurements presented by Bock et al. (2017b), which indicate a slight off-pointing of the emission, can be confirmed.

7
Orbit Control

Small satellites in the pico- or nanosatellite regime are usually launched with a ride-share rocket, which delivers them into their final orbit. Most small satellite manufacturers have little to no influence on the exact insertion orbit, but can only choose the rocket, which is targeting an altitude and inclination which suits the mission needs. The vast majority of these satellites are inserted into LEO and therefore their altitude will decrease during their lifetime due to friction with the residual atmosphere of the Earth. At the end of their life, they burn out upon re-entry at an altitude of approximately 100km above the Earth's surface. Extending or reducing the lifetime constitute just two of many applications of orbit control for small satellites in LEO (refer to Chapter 1.1).

To fully describe the orbit of a satellite, six parameters are necessary. In an inertial reference frame, these six parameters can be intuitively assigned as three parameters for the position and three parameters for the velocity of the satellite. However, as the Earth is rotating around its polar axis, a description of the orbit of an earthbound satellite which takes this property into account can be understood more intuitively. The most popular formulation uses the so-called Classical Orbital Elements (COEs), which are described in Table 7.1. The shape of the orbit of earth-orbiting spacecraft is always elliptical. The parameters i, ω, and Ω of the COEs describe the relative attitude between the orbital plane and the equatorial plane of the Earth, while the remaining three parameters a, e, and M describe the shape of the ellipse and the position of the satellite within this ellipse.

Symbol	Name
a	the semimajor axis
e	eccentricity
i	inclination
ω	argument of perigee
Ω	right ascension of the ascending node
M	mean anomaly

Table 7.1: Classical orbital elements definition (Sidi, 1997)

UWE–4 is on a circular, sun-synchronous, noon/midnight Low Earth Orbit with an inclination of i $= 97.7°$ at an altitude above the Earth's surface of approximately 585km.

Orbit determination is a task covered either by the spacecraft itself or externally by other means. Larger spacecraft often employ Global Navigation Satellite System (GNSS) receivers, which enable to determine the orbit based on satellite systems, like the Global

Positioning System of the United States of America (GPS), the GLObal NAvigation Satellite System of the Russian Federation (GLONASS), the Global Positioning System of the European Union (Galileo), and the BeiDou Navigation Satellite System of the People's Republic of China (BeiDou). Today, positioning accuracies in the application of GNSS receivers can be better than 1m (Montenbruck et al., 2018). Using a numerical propagator with time steps of about 60s to compute the position in a LEO orbit, errors below 10m can be achieved in a 7 day period without new measurement inputs (Shuster, 2017). However, for the regime of pico- and nanosatellites such receivers are often too expensive in terms of power and require a certain autonomy in attitude control in order to direct the respective antenna towards the GNSS satellites, which may not be available. Thus, this class of very small satellites generally makes use of an external source for orbit determination. The so-called Two-Line Element sets (TLEs) can be converted to a set of COEs and are provided free of charge at least on a daily basis by NORAD. The position and velocity vector can be calculated with reasonable computing power using a Simplified General Perturbation model 4 (SGP4) propagator. However, the position error is on the order of 1000m (Shuster, 2017). UWE–4 uses TLEs alongside the SGP4 propagator for orbit determination.

This dissertation and the project UWE–4 successfully demonstrate orbit control onboard a miniaturized satellite. The change of the altitude of UWE–4 - as a part of the semimajor axis a - was targeted for this demonstration. This strategy allows to use the TLE as an external measurement source to prove the maneuverability of UWE–4. Several limiting factors arose during the design and operational phase of the project. Their source and the strategy to overcome these limitations will be discussed in the following.

This chapter will at first shed light on the mathematical description of efficient orbital maneuvers for Earth-orbiting spacecraft in Chapter 7.1 in order to lead to an understanding of the optimal thrust direction for maneuvers aiming at a change of the altitude of a spacecraft. Afterwards, the technical limits of UWE–4 for these maneuvers will be discussed in more detail and the orbit control strategy will be developed. The results of the orbit control experiments on UWE–4 are presented subsequently and are compared to the measurements of NORAD provided by the TLEs.

Considerable parts of this chapter were already published in Kramer and Schilling (2021), as this publication presents the orbit control results of UWE–4. Text fragments were re-used partially in a one-to-one fashion.

7.1 Theory of spacecraft maneuvers in Earth orbit

Maneuvering a spacecraft in order to modify a single or multiple COEs at a time is usually described as single or multiple impulsive maneuvers - which means a high acceleration for a short duration at distinct locations in the orbit. However, some of the COEs can also be modified by long duration maneuvers in the vicinity of these locations.

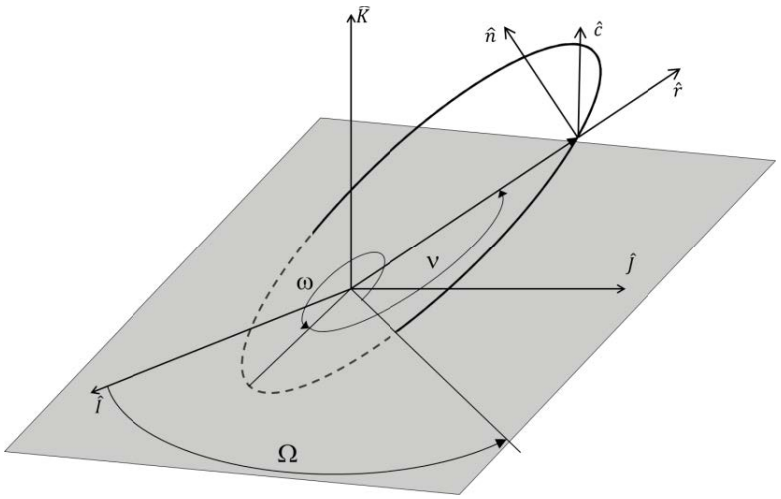

Figure 7.1: Radial-circumferential-normal reference frame in the ECI reference frame (IJK).(Ruggiero et al., 2011)

Taking a closer look at the change of the COEs, the Gauss Variational Equations (Battin, 1999) describe the effect of an acceleration **A** on the respective COE in the **r**adial-**c**ircumferential-**n**ormal body frame, which is shown in Figure 7.1:

$$\frac{da}{dt} = \frac{2a}{nb}\left(e\sin(\nu)A_r + \frac{b^2}{ar}A_c\right) \tag{7.1}$$

$$\frac{de}{dt} = \frac{1}{nab}\left(\frac{b^2}{a}\sin(\nu)A_r + \left(\left(\frac{b^2}{a}+r\right)\cos(\nu)+re\right)A_c\right) \tag{7.2}$$

$$\frac{di}{dt} = \frac{r\cos(\omega+\nu)}{nab}A_n \tag{7.3}$$

$$\frac{d\omega}{dt} = \frac{1}{nabe}\left(-\frac{b^2}{a}\cos(\nu)A_r + \left(\frac{b^2}{a}+r\right)\sin(\nu)A_c\right) - \frac{r\sin(\omega+\nu)\cos(i)}{nab\sin(i)}A_n \tag{7.4}$$

$$\frac{d\Omega}{dt} = \frac{r\sin(\omega+\nu)}{nab\sin(i)}A_n \tag{7.5}$$

$$\frac{dM}{dt} = n + \frac{1}{na^2e}\left(\left(\frac{b^2}{a}\cos(\nu)-2re\right)A_r - \left(\frac{b^2}{a}+r\right)\sin(\nu)A_c\right) \tag{7.6}$$

In these equations, n describes the so-called mean motion which is the number of spacecraft revolutions around Earth per day, b the semiminor axis of the elliptical orbit, r the distance to the focal point of the ellipse, and the index of A_i the component of the acceleration **A** in the **r**adial-**c**ircumferential-**n**ormal body frame. Moreover, ν denotes the true anomaly which can be calculated from the mean anomaly using M = E - e sin E and $\tan(\nu/2) = \sqrt{\frac{1+e}{1-e}}\tan(E/2)$. The remaining variables describe COEs.

According to Eq. (7.3), maneuvers to modify the inclination i are most efficient if $\omega+\nu = 0°$ or 180° and without any effect if $\omega+\nu = \pm 90°$. This relation is exactly inverted for a change of the right ascension of ascending node (refer to Eq. (7.5)). As a direct conclusion of Eq. (7.1), there is no position restriction for maneuvers aiming at a

change of the semimajor axis. In the limit of a circular orbit, the eccentricity e vanishes and a = b = r. Hence, the optimal direction for a maneuver targeting a change in the semimajor axis a points (anti-)parallel to the circumferential direction, which coincides with the (anti-)velocity direction. A change in the semimajor axis of Earth-orbiting satellites can always be achieved by pointing the thrust vector (anti-)parallel to the velocity direction.

As the atmospheric drag can be understood as a perturbing force which reduces the velocity and the altitude of a spacecraft, the necessary Δv maneuver in order to maintain the altitude points in velocity direction. Thus, the exact opposite maneuver in anti-velocity direction reduces the velocity and consequently the altitude of the spacecraft.

Simulations regarding the orbit control possibilities on UWE–4 employing the low-thrust propulsion system NanoFEEP have shown that it is possible to change the semi-major axis a in a reasonable time. However, the capabilities of the propulsion system regarding the change of the eccentricity e and the inclination i are exceeded by the natural oscillations, due the effects of the non-spherical gravitational field of the Earth. Maneuvers with UWE–4 in order to change the argument of perigee ω or the right ascension of the ascending node Ω have shown no measurable effect to the orbit (Azari, 2016). These results have been published in Kramer et al. (2017a).

7.2 Restrictions of UWE–4

UWE–4 as a miniaturized satellite posed restrictions on the selection of a suitable propulsion system and other components during the design phase. Furthermore, during the operational phase, several additional limitations on the possible application of the propulsion system arose. These restrictions partially emerged already in previous chapters, but their consequences for orbit control will be discussed in the following pages. A strategy for orbit control with the focus on changing the altitude which integrates the limitations of UWE–4 is developed during this chapter.

7.2.1 Heater restriction

Chapter 5.1 has shown that the propellant of a thruster head is only reliably liquefied approximately 27–35 minutes after leaving the eclipse. At this moment, the thruster temperature reaches 63°C. About 50 minutes later, the propellant may solidify again in the eclipse of the orbit at a temperature below 53°C. This poses a localized limitation on the activation of the propulsion system and thus the maneuverability of UWE–4.

The Earth is inclined by 23.5° with respect to the ecliptic plane. For the different locations on Earth, this results in the change of seasons with their climatic characteristics as the Earth moves around sun. For a satellite in a sun synchronous noon/midnight orbit - like UWE–4 - this has a distinct consequence. The location of the satellite over the Earth's surface where it exits the eclipse phase, i.e. the latitude, changes in the course of the year. A shift of the possible activation region of the propulsion system due to the liquefaction of the propellant follows from this.

Figure 7.2 and Figure 7.3 show temperature measurements of thruster A with active heating in the four different seasons over their respective locations above the Earth.

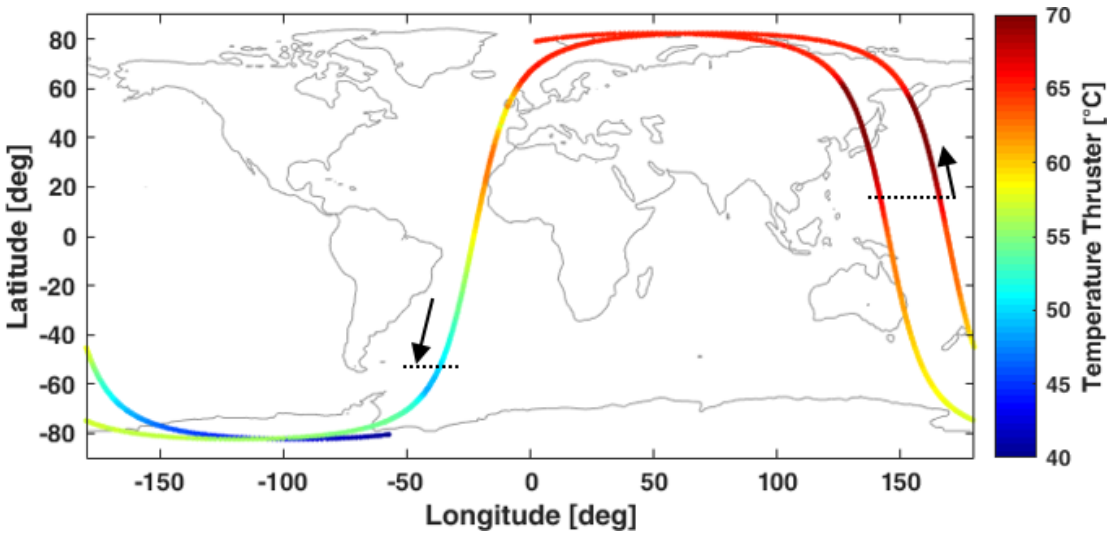

(a) Thruster A temperature during heating on March 17th, 2020.

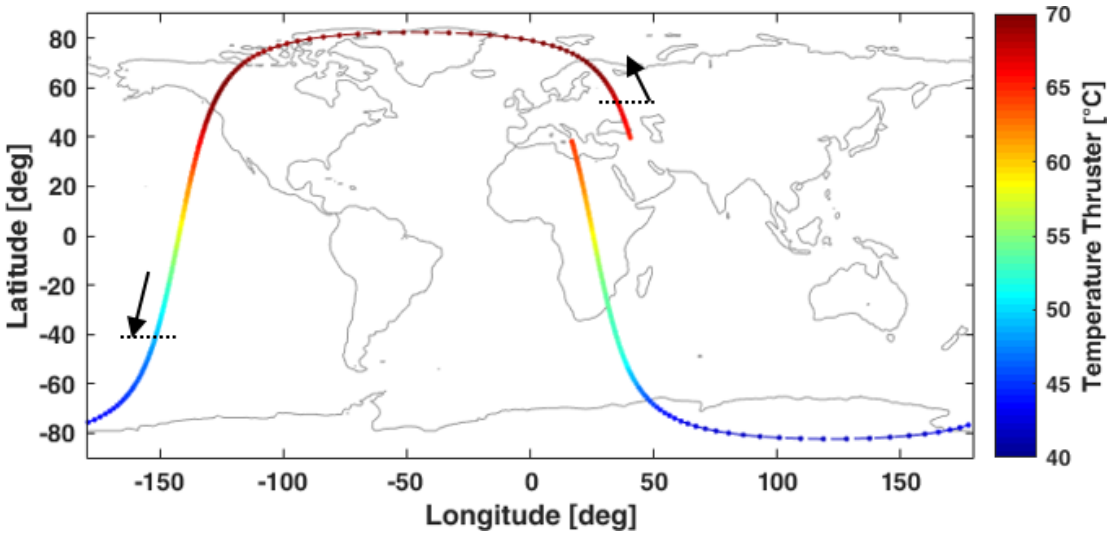

(b) Thruster A temperature during heating on May 23rd, 2020.

Figure 7.2: Temperature behavior of thruster A during active heating. Regions of liquefied propellant during the first half of the year are indicated with dotted lines and arrows. (Kramer and Schilling, 2021)

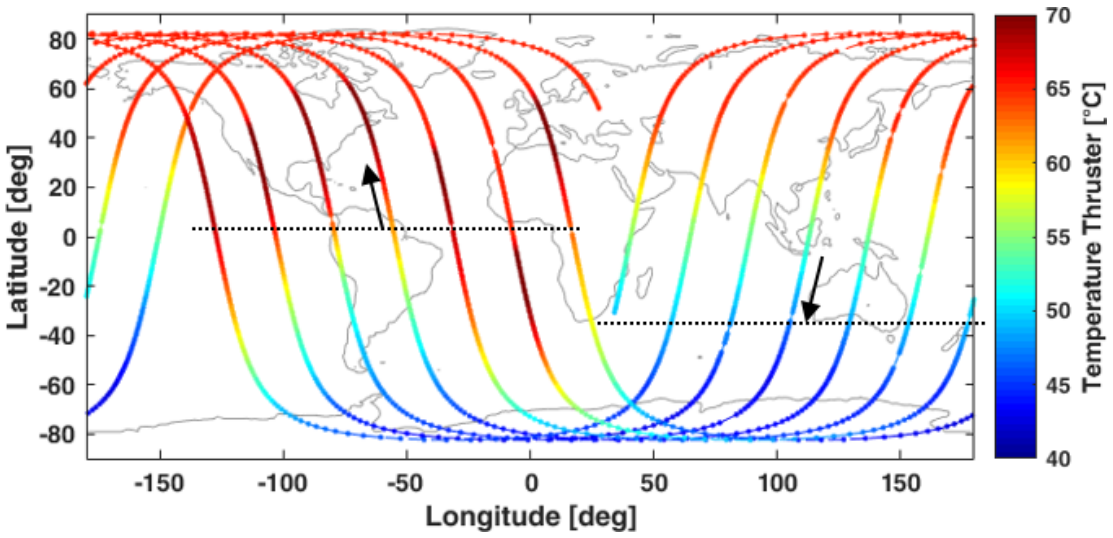

(a) Thruster A temperature during heating on October 2nd, 2019.

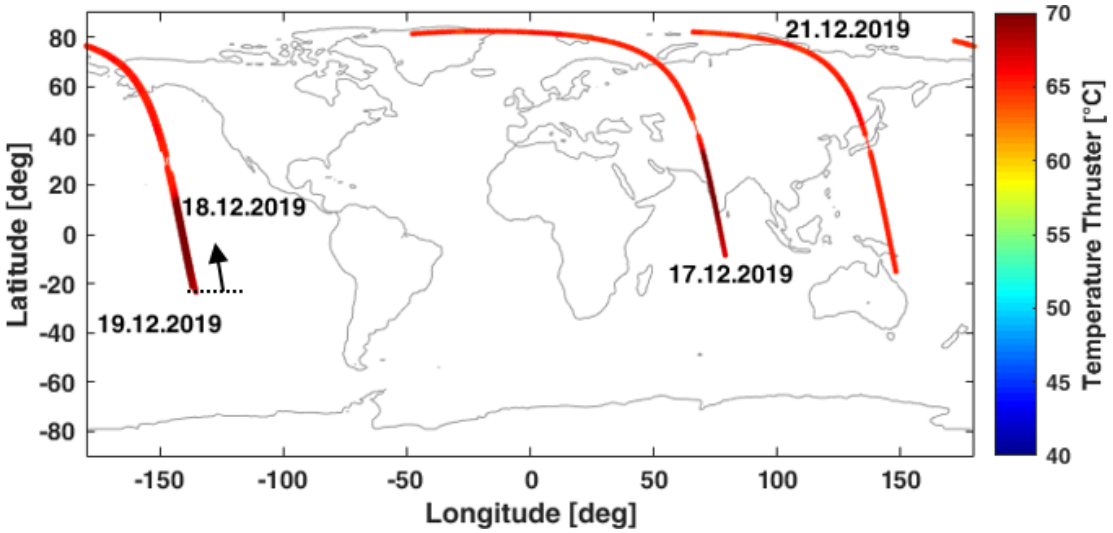

(b) Thruster A temperature during heating in winter of the northern hemisphere. Unfortunately, the temperature was not recorded for a complete orbit. However, it can be observed that the propellant is liquefied already at a latitude of approximately $-20°$.

Figure 7.3: Temperature behavior of thruster A during active heating (continued). Regions of liquefied propellant during the second half of the year are indicated with dotted lines and arrows. (Kramer and Schilling, 2021)

UWE–4 progresses in these Figures as indicated by the arrows - from right to left. As UWE–4 is in a polar orbit with a local time of the ascending node around noon, it moves from north to south on the eclipse side of the Earth and vice versa on the sunlit side of the Earth during the entire year.

Reliable liquefaction of the propellant at approximately 63°C is reached at a latitude below -10° during winter of the northern hemisphere, as can be seen in Figure 7.3b, and above 50° during summer, as depicted in Figure 7.2b.

While the region around the geographic north pole can be used for maneuvers throughout the whole year, the region around the south pole can not be used at any time. Liquefaction of the propellant over the equatorial region is reached on the eclipse side of the Earth during the whole year. However, the thrusters can be used over the equatorial region of the sunlit side of the Earth only during winter of the northern hemisphere.

7.2.2 AOCS restriction

In Chapter 7.1, the pointing requirement of the thrust vector in (anti-)velocity direction to change the altitude of the satellite was derived. In a general case, this requires the satellite to have the capability to control its attitude, i.e. the thrust vector, freely around each axis in 3D space. The design concept for UWE–4 foresaw a 2D attitude control capability in the plane perpendicular to the Earth's magnetic field direction using the magnetorquers. The placement of the propulsion system thrusters should allow for an additional 2D attitude control around body x- and y-axis. These two sets of actuators were intended to be used in combination in order to achieve three axis attitude control. As only two thruster heads could be activated which do not have an opposing effect on the attitude (refer to Chapter 5.3), UWE–4 can control its attitude only relative to the magnetic field vector of the Earth using the magnetorquers.

However, this restriction does not prohibit orbit control maneuvers to change the altitude. Besides the misalignment angle Θ determined in Chapter 6, the concept to overcome this limitation involves two angles which will be defined as follows:

1. Chapter 4.3.2 has introduced a Follow-B attitude controller, which reduces the angular rate of the satellite while aligning a selected direction in the body frame with the Earth's magnetic field. During the experiment shown in Figure 4.6a and Figure 4.6b, the body -z-axis of UWE–4 was aligned with the Earth's magnetic field. The off-pointing angle α shown in Figure 4.6c is the angle between the body -z-axis and the measured magnetic field on-board UWE–4.

2. As the satellite progresses along its orbit, the angle β between the velocity direction and the Earth's magnetic field changes. The velocity vector can be computed using the SGP4 propagator, whereas the International Geomagnetic Reference Field (IGRF) model provides the Earth's magnetic field vector. Both of these models are implemented on-board UWE–4. The angle β for the experiment on May 13th, 2020 is depicted in Figure 7.4. Figure 7.4b shows the angle β for the respective location over the Earth. It is close to 180° (red) during equatorial passage on the eclipse side of the orbit, which indicates an almost anti-parallel alignment of the velocity direction of UWE–4 and the Earth's magnetic field.

Both of these angles can be calculated using the scalar product of the corresponding vectors.

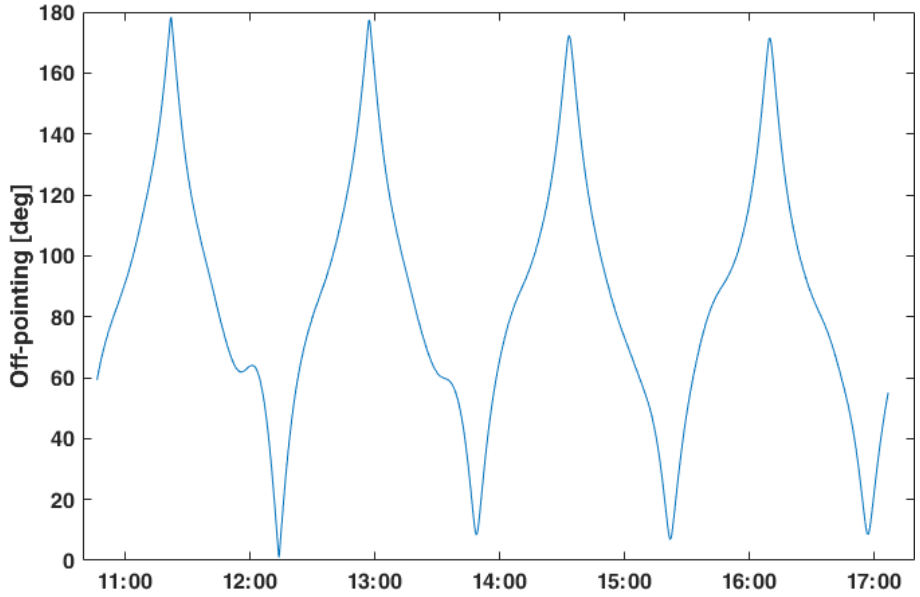

(a) Timeline of the angle β

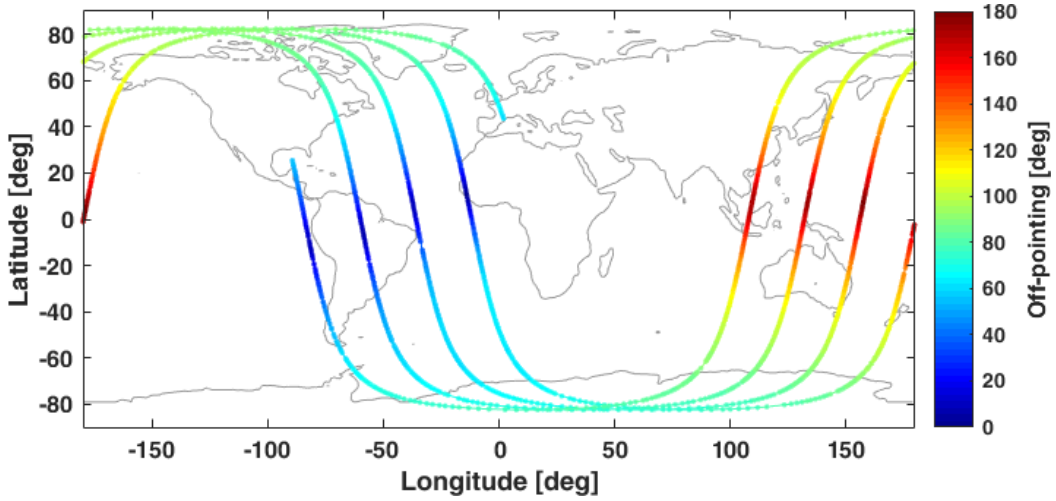

(b) The angle β is color-encoded at its respective location over the Earth. (Kramer and Schilling, 2021)

Figure 7.4: Progression of the angle β between velocity direction of UWE–4 and the Earth's magnetic field during Follow-B attitude control experiment on May 13th, 2020.

If the propulsion system had been activated on May 13th, 2020 for a certain duration during equatorial passage on the eclipse side of the Earth, it would have resulted in a Δv maneuver almost anti-parallel to the velocity direction and thus would have lowered the altitude of UWE–4.

The relevant angle γ in order to estimate the thrust contribution for an altitude change is the angle between thrust direction and (anti-)velocity direction. However, as the rotation of UWE–4 around the magnetic field direction can not be controlled, only an estimate can

be given at this point:

Aiming at lowering the altitude of a spacecraft the two angles α and $180° - \beta$ are directly opposite to each other, in a best case scenario. Additionally, the rotation of the spacecraft around the magnetic field direction further reduces the off-pointing angle γ, such that $\gamma_{\text{best,low}} = ||(180° - \beta) - \alpha| - (180° - \Theta)|$. In a worst case scenario, all angles are parallel, such that $\gamma_{\text{worst,low}} = |(180° - \beta) + \alpha + (180° - \Theta)|$. Figure 7.5 shows these possible angle combinations.

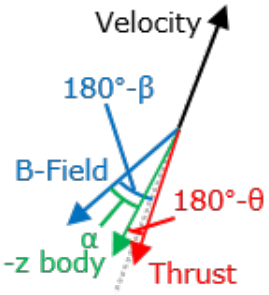

(a) Best case:
$\gamma_{\text{best,low}} = ||(180° - \beta) - \alpha| - (180° - \Theta)|$

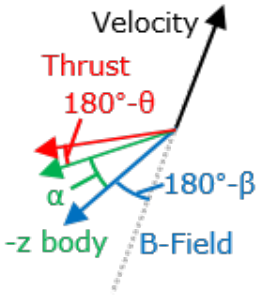

(b) Worst case:
$\gamma_{\text{worst,low}} = |(180° - \beta) + \alpha + (180° - \Theta)|$

Figure 7.5: Possible combination of the angles α, $(180° - \beta)$, and $(180° - \Theta)$ for an orbit lowering scenario. (Kramer and Schilling, 2021)

If the orbit shall be raised, the angles α and β are parallel in a worst case scenario and opposite to each other in a best case scenario, such that $\gamma_{\text{best,raise}} = ||\beta - \alpha| - (180° - \Theta)|$ and $\gamma_{\text{worst,raise}} = ||\beta + \alpha - 360°| + (180° - \Theta)|$. The possible combinations of these angles are shown in Figure 7.6. The manual magnetic moment $\mathbf{M}_{\text{man}}$ in Eq. (4.9) has to be chosen positively to align the body -z-axis with the velocity direction of the satellite.

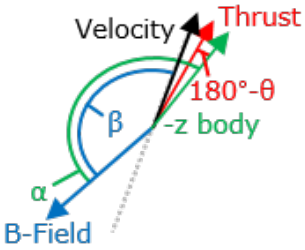

(a) Best case:
$\gamma_{\text{best,raise}} = ||\beta - \alpha| - (180° - \Theta)|$

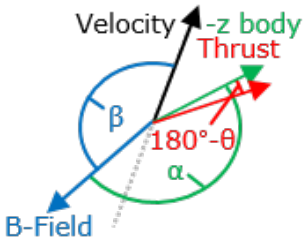

(b) Worst case:
$\gamma_{\text{worst,raise}} = ||\beta + \alpha - 360°| + (180° - \Theta)|$

Figure 7.6: Possible combination of the angles α, β, and $(180° - \Theta)$ for an orbit raising scenario. (Kramer and Schilling, 2021)

Combining the restrictions presented in Chapter 7.2.1 and Chapter 7.2.2, the thruster can be activated having liquefied propellant over the equatorial region on the eclipse side of the Earth and the angle β between velocity direction of UWE–4 and the Earth's magnetic field is suitable. Consequently, the orbit control maneuvers focus on this region over the Earth.

While the time to produce thrust can be narrowed down to equatorial passage, the Follow-B attitude controller is always active during the remainder of the orbit.

7.2.3 Supply voltage restriction

Each subsystem features its own subsystem interface controller which monitors the supply lines and is capable of shutting the supply lines down in case of over-/undervoltage or overcurrent faults. Unfortunately, fault shut-downs of the hotswap of the PPU were traced back to situations, in which a second actuator was activated while a thruster was already active. This second actuator can be a thruster or a magnetorquer. All actuators are supplied by the same unregulated power bus. Since an actuator electrically acts as a load on the unregulated supply line, the inrush current of the second actuator has the capability to lead to a short collapse of the supply voltage, which in turn leads to an undervoltage condition at the hotswap circuit of the PPU. As the hotswap circuitry is a security feature for the health of the complete satellite, it can not be changed in orbit of UWE–4.

This poses a limitation on the combined application of several actuators, as a thruster can not be active while another thruster or a magnetorquer is active. The concept to resolve this issue was to perform either orbit control with a single thruster or attitude control with the magnetorquers of UWE–4, but to refrain from combined attitude and orbit control.

The scenario described in Chapter 7.2.2 was adjusted, such that no other actuator can be activated as long as thrust is applied. Specifically two situations are distinguished:

1. $\alpha > 50°$ for altitude lowering and $\alpha < 130°$ for orbit raising scenario: This resembles an off-pointing between the axis (anti-)parallel to the Earth's magnetic field **B** and the -z-axis of more than 50°. At first, the used thruster head is deactivated. Afterwards, the Follow-B attitude controller is activated employing the magnetorquers to re-align the thrust vector (anti-)parallel to the Earth's magnetic field **B**.

2. $\alpha < 35°$ for altitude lowering and $\alpha > 145°$ for orbit raising scenario: The thrust vector is aligned sufficiently (anti-)parallel to the external magnetic field direction. The Follow-B attitude controller is deactivated and all magnetorquers are safely shut-down. Afterwards, thrust is applied.

An orbit control strategy can be derived by the integration of the previously presented restrictions of UWE–4. This strategy is shown schematically in Figure 7.7 for the duration of a single orbit. While the heater is active during the entire orbit (orange), the propellant of the used thruster is liquefied only during a fraction of the orbit (red), which depends slightly on the time of the year (dotted red). The Follow-B attitude controller is active during a large phase of the orbit (green), but alternates with periods of orbit control during equator passage (blue). Whether the orbit altitude increases or decreases, depends on the manual magnetic moment in the Follow-B attitude controller.

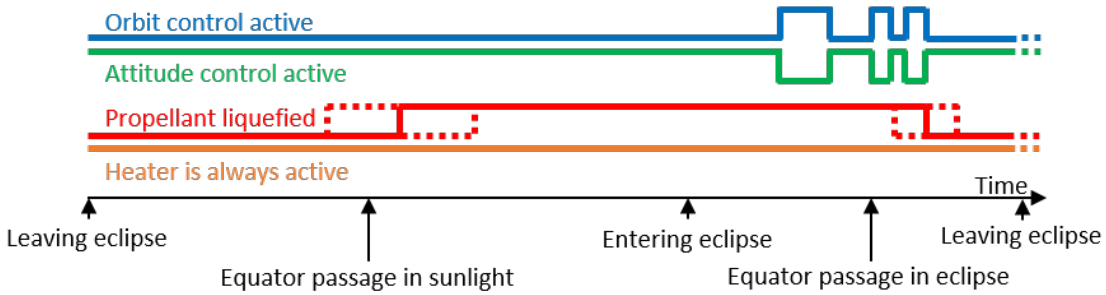

Figure 7.7: This schematic shows the (in-)active components of the AOCS and the PPU during a single orbit of the orbit control scenario. (Kramer and Schilling, 2021)

7.3 Orbit Control on UWE–4

The orbit control experiments focus on the change of the altitude of UWE–4 above the Earth's surface and at the same time on the semi major axis a. Chapter 7.2 gives details about the restrictions of the UWE–4 mission that limit the efficiency to achieve this goal and derives a strategy to overcome these restrictions and nevertheless enable UWE–4 to change its altitude. Thruster B was used as the only orbit control actuator during the experiments presented in this chapter. The first experiment presented in this chapter targets altitude lowering and will be followed by an experiment targeting the raising of the orbit of UWE–4.

7.3.1 Orbit lowering maneuver

As described in Chapter 7.1, it is necessary to direct the thrust vector anti-parallel to the velocity direction to reduce the satellite's orbital energy and its altitude.

This chapter shows data of the NanoFEEP propulsion system and the AOCS in order to estimate the created Δv that led to a decrease in altitude during an experiment from June 22nd, 2020 to July 3rd, 2020. TLEs of UWE–4 are analysed as a source of external reference and simulation data regarding the altitude progression is presented.

7.3.1.1 Experimental data

The analysis of the experimental data will be described using an exemplary subset of the entire maneuver on June 23rd, 2020 from 14:08:11 to 14:23:00. The maneuver during this orbit was activated at 14:08:33, when the satellite was located at 42.72°N, 146.08°E – just east of the Japanese island Hokkaido, flying south on the eclipse side of the Earth. The angular rate and the measured magnetic field of the AOCS are shown in Figure 7.8.

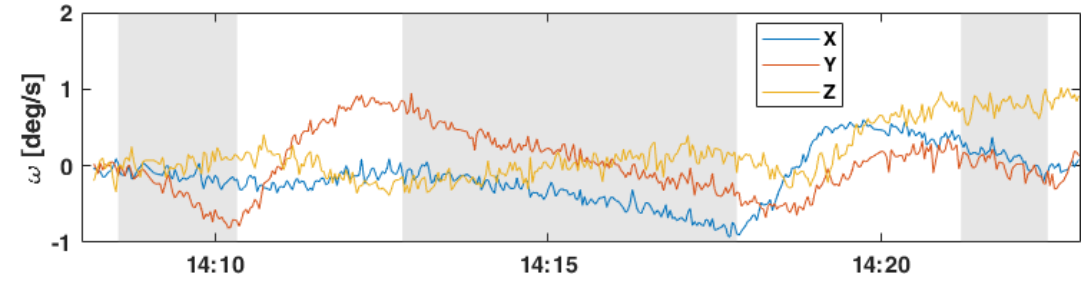

(a) Angular rate in the individual axes

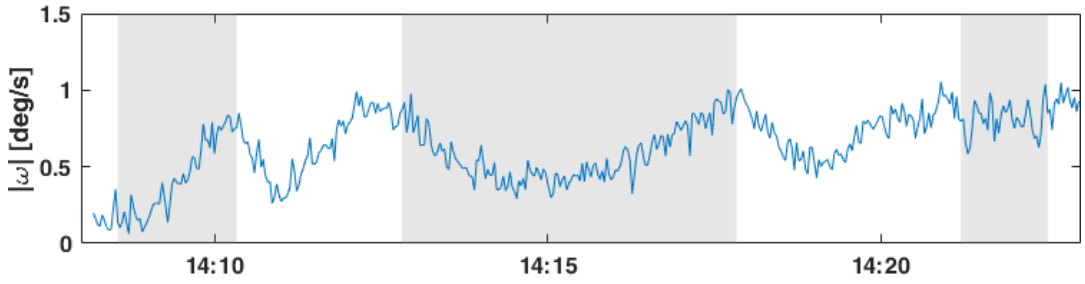

(b) Absolute value of the angular rate

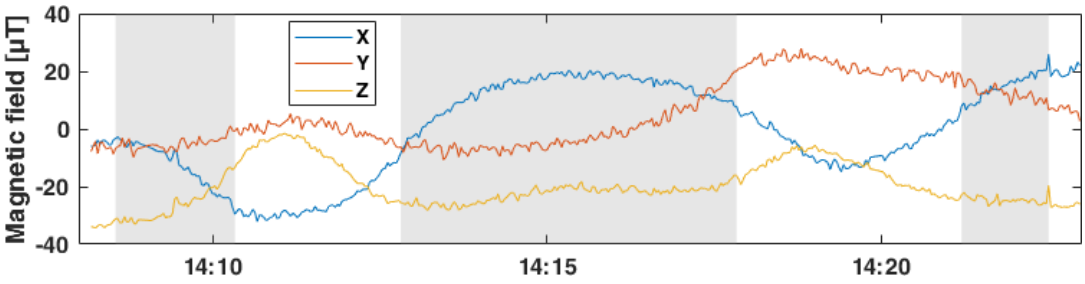

(c) Magnetic field measured in the individual axes

Figure 7.8: Measurements of the AOCS during altitude lowering maneuver from June 23rd, 2020. Time ranges of active orbit control are shaded. (Kramer and Schilling, 2021)

Before 14:08:33, the Follow-B algorithm was active for more than 60 minutes. At the beginning of the maneuver, the satellite's -z-axis was aligned with the Earth's magnetic field, as the highest magnitude of magnetic field was measured along the -z-axis. Furthermore, UWE–4 was hardly rotating, as can be seen in Figure 7.8a and Figure 7.8b.

The measured data of the PPU is depicted in Figure 7.9. The three periods of thruster B activation and neutralizer compensation can be identified. The thruster was active for a total time of 484 seconds in this orbit. During the first active phase of the propulsion system, the satellite started to rotate as shown in Figure 7.8a and the alignment of the -z-axis with the external magnetic field was lost.

The angle α, shown in Figure 7.10a, between the Earth's magnetic field and the body -z-axis was below 20° at the beginning of the maneuver, but increased due to the rotation created by the torque of thruster B. At 14:10:20, the thruster turned off. However, the angle α increased already to more than 60°, while the switching condition should have already triggered at 50°. As the algorithm on board of UWE–4 computes the angle α

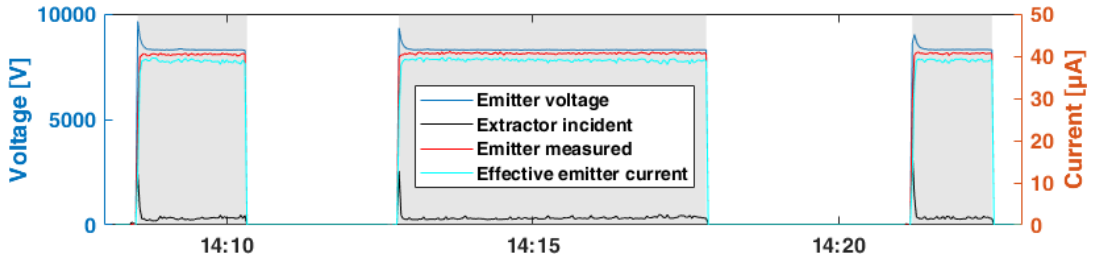

(a) Thruster B electrical characteristics

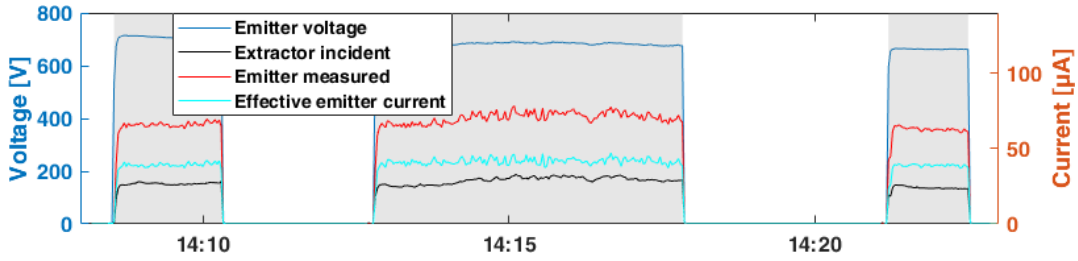

(b) Neutralizer electrical characteristics

Figure 7.9: Measurements of the PPU during altitude lowering maneuver from June 23rd, 2020. Time ranges of active orbit control are shaded. (Kramer and Schilling, 2021)

asynchronous to checking the switching condition between attitude and orbit control, a short time delay may occur. During the subsequent phase of attitude control, the Follow-B controller could restore the alignment of the body -z-axis with the Earth's magnetic field, as can be seen in Figure 7.8c and Figure 7.10a. At 14:12:30, the angle α went below 35°, so the attitude controller was turned off and thruster B was activated again. This process was repeated three times during this orbit.

Figure 7.10b shows the timeline of the angle β between the Earth's magnetic field and the velocity direction according to SGP4 and IGRF model. The absolute off-pointing angle γ is estimated as described in Chapter 7.2.2 and is depicted in Figure 7.10c. In the best case assumption, the angle γ is always below 50°, so the created thrust always contributes to a reduction of the velocity of UWE–4. However, in the worst case scenario, the angle γ may become larger than 90°, which occurred exemplary at the center of the first firing at 14:09:28. This would contribute to an increase of the velocity of UWE–4. The reader has to be aware that the thruster was only active during periods indicated by the shadows in the corresponding Figures.

Nonetheless, the average thrust contribution of the maneuver during this single orbit - even in the worst case scenario - has a positive contribution to the reduction of the velocity of the spacecraft. The thrust magnitude created by thruster B can be computed by the electrical characteristics of the thruster and Eq. (2.6) to an average value of $|\tilde{\mathbf{F}}| = 3.85\mu\text{N}$. The fraction of this thrust which contributes to the reduction of the satellite's velocity depends on the pointing accuracy. Thus, two cases can be distinguished:

$$\text{Best case:} \qquad |\mathbf{F}_{\text{best}}| = |\tilde{\mathbf{F}}| \cdot \cos(||(180° - \beta) - \alpha| - (180° - \Theta)|) \tag{7.7}$$

$$\text{Worst case:} \qquad |\mathbf{F}_{\text{worst}}| = |\tilde{\mathbf{F}}| \cdot \cos(|\ (180° - \beta) + \alpha\ + (180° - \Theta)|) \tag{7.8}$$

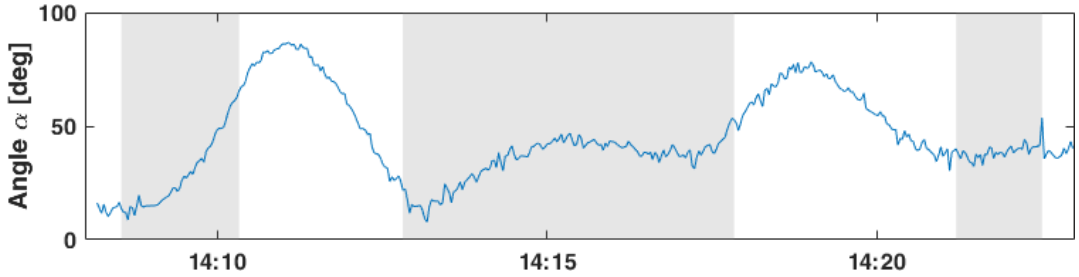

(a) The progression of the angle α between the Earth's magnetic field and the body -z-axis.

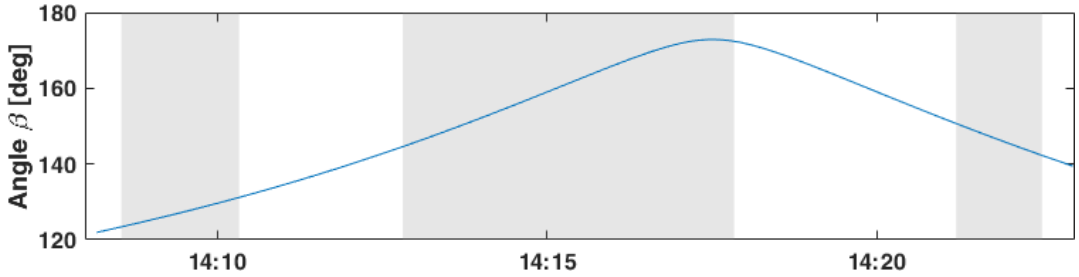

(b) The progression of the angle β between the Earth's magnetic field and the velocity direction.

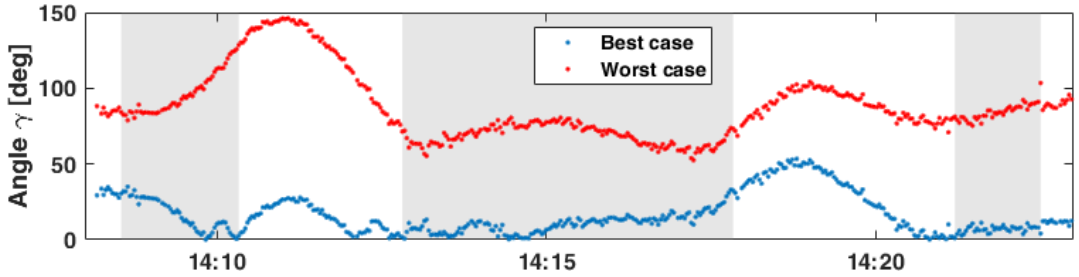

(c) The angle γ between thrust and anti-velocity direction can be estimated between $||(180° - \beta) - \alpha| - (180° - \Theta)|$ (best case) and $|(180° - \beta) + \alpha + (180° - \Theta)|$ (worst case).

Figure 7.10: Pointing accuracy during altitude lowering experiment on June 23rd, 2020. Time ranges of active orbit control are shaded. (Kramer and Schilling, 2021)

A histogram of the thrust contribution in anti-velocity direction is shown in Figure 7.11. The mean value of the thrust contribution of the maneuver during this orbit in anti-velocity direction is $|\mathbf{F}_{\text{best}}| = 3.71\mu\text{N}$ in the best case scenario. In the worst case scenario this mean value is $|\mathbf{F}_{\text{worst}}| = 0.50\mu\text{N}$.

Using the data from Figure 3.6a with Eq. (2.1), the propellant loss in this orbit can be computed to $\Delta m = 0.11\text{mg}$.

The Δv contribution to reduce the velocity can be calculated with the following relation

$$\Delta v = \frac{|\tilde{\mathbf{F}}|}{m_{\text{Sat}}} \cdot \Delta t. \tag{7.9}$$

In this formula, m_{Sat} is the satellite mass of UWE–4 and Δt is the duration of the maneuver. As the consumed propellant during the maneuver is seven orders of magnitude below the mass of UWE–4, the reduction in accelerated mass is neglected. Thus, the created Δv in anti-velocity direction is in the range of $\Delta v = (0.28 - 1.88) \cdot 10^{-3}\text{m/s}$, depending on the

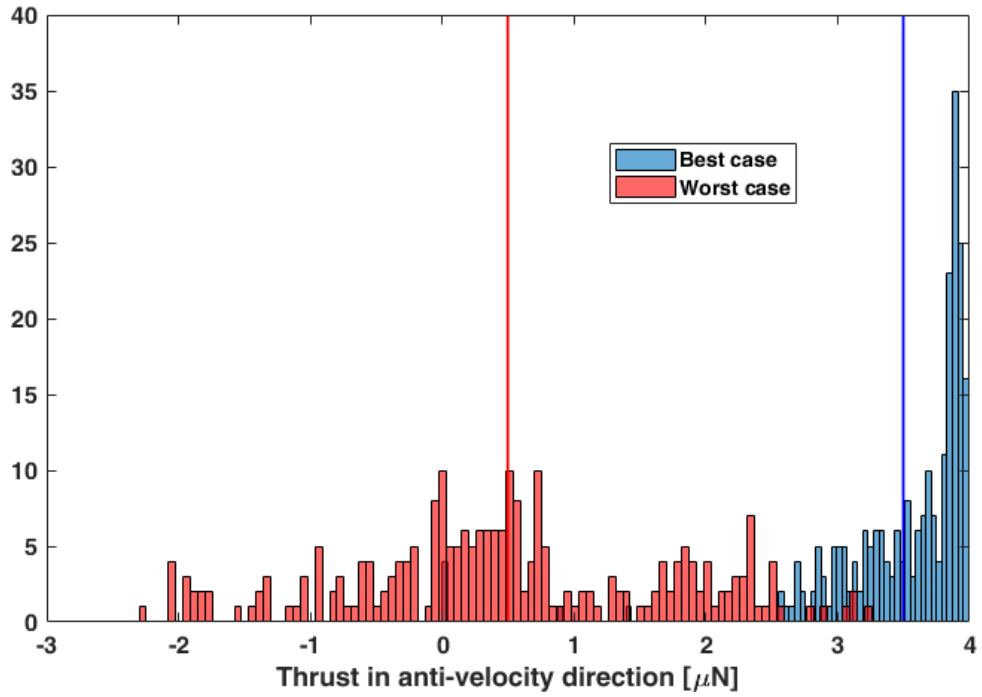

Figure 7.11: Histogram of the thrust contribution of the maneuver during the single orbit from June 23rd, 2020 in anti-velocity direction of UWE–4. The mean best (blue) and worst (red) case contributions are added as vertical lines. (Kramer and Schilling, 2021)

worst or best case estimation of the thrust contribution in anti-velocity direction.

The entire maneuver from June 23rd, 2020 to July 3rd, 2020 was activated during 78 orbits with a two day break from June 27th, 2020 to June 28th, 2020 and is analysed following the scheme outlined in this chapter. During the maneuver, thruster B was active for a total time of approximately 442 minutes, which corresponds on average to 5:40 minutes per orbit. The average off-pointing angle γ between thrust and anti-velocity direction of UWE–4 is shown in Figure 7.12. The mean value of γ for all active thruster B times is $\gamma_{\text{avg}} = 43.61°$.

A histogram of the thrust contribution of the complete maneuver is depicted in Figure 7.13. Thruster B created a mean thrust magnitude of $|\tilde{\mathbf{F}}| = 3.90\mu\text{N}$ during the complete maneuver.

The mean value of the best case scenario for a thrust contribution in anti-velocity direction is $|\mathbf{F}_{\text{best}}| = 3.73\mu\text{N}$, while the mean value for the worst case scenario is $|\mathbf{F}_{\text{worst}}| = 0.73\mu\text{N}$. Thus, the midpoint between both cases is at a thrust of $|\mathbf{F}_{\text{avg}}| = 2.23\mu\text{N}$ and was directed in the desired direction anti-parallel to the velocity vector of UWE–4. This corresponds to 57.1% of the created thrust of thruster B.

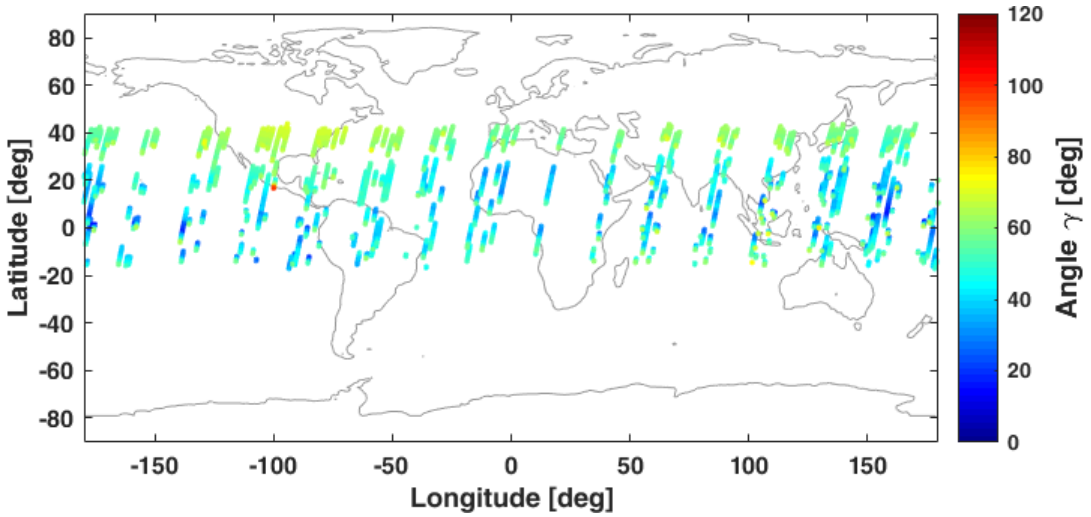

Figure 7.12: Average angle γ for all active thruster B times at their respective location over the Earth. (Kramer and Schilling, 2021)

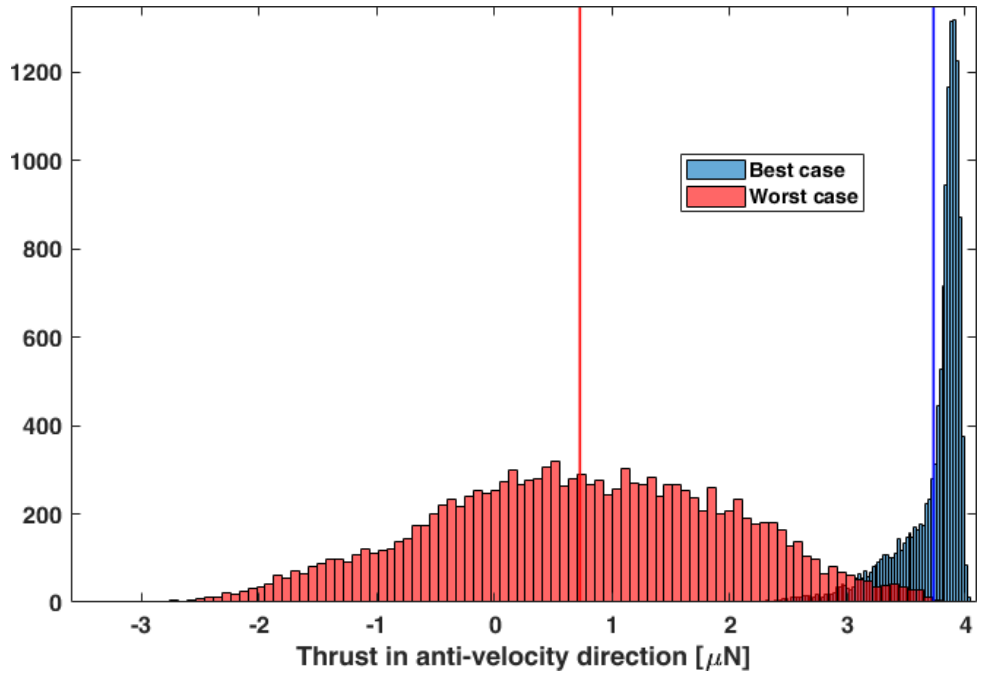

Figure 7.13: Histogram of the thrust contribution of the complete maneuver from June 23rd, 2020 to July 3rd, 2020 in anti-velocity direction of UWE–4. The mean best (blue) and worst (red) case contributions are added as vertical lines. (Kramer and Schilling, 2021)

The created Δv of the individual days is depicted in Figure 7.14. The total Δv in anti-velocity direction during ten active days lies in the range of $\Delta v = (1.75 - 8.99) \cdot 10^{-2} \mathrm{m/s}$. For this entire maneuver $\Delta m = 4.81 \mathrm{mg}$ gallium of thruster B was consumed.

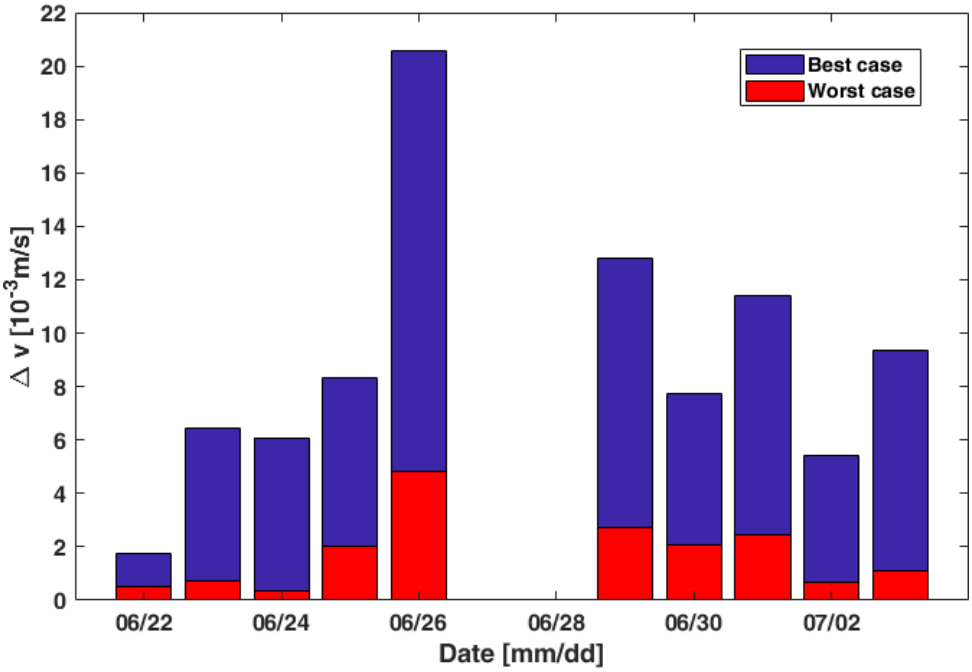

Figure 7.14: The created Δv contribution of the entire orbit lowering maneuver between June 23rd, 2020 and July 3rd, 2020. (Kramer and Schilling, 2021)

The power consumption of the PPU can be calculated using the measurement data from Chapter 5 to

$$\begin{aligned} P_{PPU}[mW] &= P_{base} + P_{N_A} + P_{Th\,B}(\text{incl. heater}) \\ &= 19 + (117.75 \pm 10.27) + (559.6 \pm 32.7) \\ &= 696.35 \pm 42.97. \end{aligned} \tag{7.10}$$

This orbit lowering maneuver is the first orbit control maneuver ever demonstrated on board of a satellite platform below the size of a 3U CubeSat.

7.3.1.2 External measurement data

The orbital parameters of UWE–4 are monitored by NORAD since launch on December 27th, 2018 and published online[1] as TLEs with NORAD ID 43880. The TLE describing the orbit of UWE–4 prior to the orbit lowering maneuver on June 22nd, 2020 is as follows:

```
UWE-4
1 43880U 18111E   20174.69422425 +.00000927 +00000-0 +86666-4 0  9997
2 43880 097.7037 082.3122 0011028 221.7673 138.2707 14.96478573081276
```

[1] possible sources are www.celestrak.com for current data and www.space-track.org for historical data

The TLE describing the orbit of UWE–4 after the maneuver on July 3rd, 2020 is:

```
UWE-4
1 43880U 18111E   20185.72680577 -.00000321  00000-0 -23129-4 0  9992
2 43880  97.7028  93.1734 0011867 185.1652 174.9449 14.96518032 80922
```

The interested reader is referred to Vallado and Cefola (2012) for the exact description of each digit of a TLE.

The semi major axis a_{Sat} of a spacecraft can be calculated using the mean motion n (**bold** in TLE), given in $\frac{\text{revolutions}}{\text{day}}$ in the second line of each TLE in digit 53-63 as

$$a_{Sat}[m] = \sqrt[3]{G_0 \cdot \frac{\left(\frac{86400}{n}\right)^2}{4\pi^2}}. \tag{7.11}$$

In this equation, G_0 describes the geocentric gravitational constant[2]. The mean altitude h_{Sat} of a spacecraft over the Earth's surface can be calculated subsequently via

$$h_{Sat} = a_{Sat} - r_{Earth}. \tag{7.12}$$

r_{Earth} describes the mean radius of the Earth[3]. The altitude progress of UWE–4 is shown in Figure 7.15 using its TLE history. The orbit lowering maneuver is clearly shown at the end of the timeline. The history of the COEs of UWE–4 during its orbital lifetime is shown in Figure A.10.

The eccentricity of a satellite is given in digits 27-33 of the second line of a TLE, with an assumed decimal point. The orbit of UWE–4 has an eccentricity about 10^{-3} and thus the orbit is considered circular for the following analysis. The velocity for circular keplerian orbits in vicinity of the Earth can be calculated as

$$v = \sqrt{\frac{G_0}{a_{Sat}}}. \qquad \text{(Sidi, 1997)} \tag{7.13}$$

This way, the daily Δv resulting from atmospheric drag can be calculated using the semi major axis a_{Sat} on

- December 29th, 2018: $6.9570976 \cdot 10^6$m and
- June 9th, 2020: $6.9559510 \cdot 10^6$m

to $\Delta v_{Drag} \approx 1.2 \cdot 10^{-3}$m/s. Furthermore, the daily natural decay rate can be calculated to $\Delta h_{Drag} = 2.18$m/d. Consequently, the altitude lowering effect Δh of the maneuver due to

[2] $G_0 = 3.986005 \cdot 10^{14} \frac{m^3}{s^2}$ (Moritz, 1980)
[3] $r_{Earth} = 6.371 \cdot 10^6$m (Moritz, 1980)

thrusting can be calculated using Eq. (7.11) to

$$\begin{aligned} \Delta h[\mathrm{m}] &= |a_{\mathrm{Sat}}(\text{July } 3^{\mathrm{rd}}, 2020) - a_{\mathrm{Sat}}(\text{June } 22^{\mathrm{nd}}, 2020)| - \Delta h_{\mathrm{Drag}} \cdot 11\mathrm{d} \\ &= |6.9558022 \cdot 10^6 - 6.9559245 \cdot 10^6| - 23.96 \\ &= 98.3 \end{aligned} \tag{7.14}$$

and a Δv of UWE–4 during the orbit lowering maneuver can be computed using Eq. (7.13) to

$$\begin{aligned} \Delta v[\mathrm{m/s}] &= |v(\text{July } 3^{\mathrm{rd}}, 2020) - v(\text{June } 22^{\mathrm{nd}}, 2020)| - \Delta v_{\mathrm{Drag}} \cdot 11\mathrm{d} \\ &= |7569.9900 - 7569.9234| - 0.0130 \\ &= 5.35 \cdot 10^{-2}. \end{aligned} \tag{7.15}$$

According to the TLEs, the created Δv is in very good agreement with the experimental data in Chapter 7.3.1.2, which results in a range of $\Delta v = (1.75 - 8.99) \cdot 10^{-2}\mathrm{m/s}$.

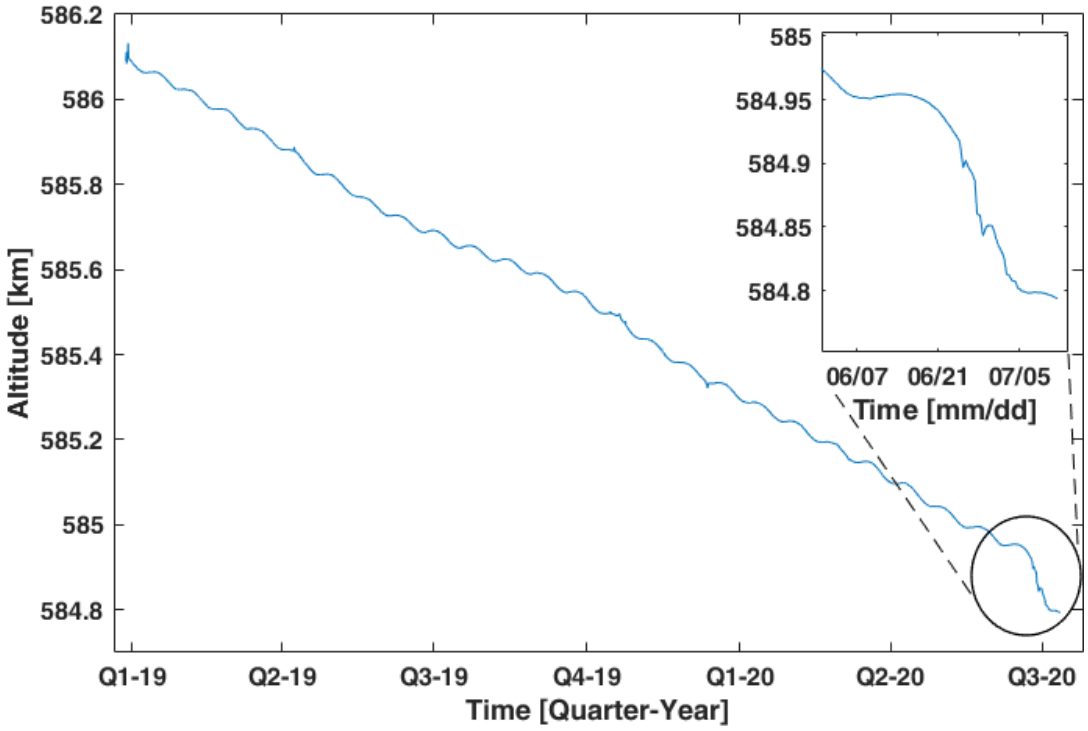

Figure 7.15: The progress of the altitude of UWE–4 between launch on December 27th, 2018 and July 11th, 2020 according to the TLEs provided by NORAD. The inner window shows a zoom into the orbit lowering maneuver. (Kramer and Schilling, 2021)

7.3.1.3 Simulation

The orbit lowering scenario is simulated using the Orekit library (Maisonobe et al., 2010) with a classical Runge-Kutta integrator with a step-size of 10 seconds, employing the

following force models:

- 10^{th} degree gravitational Holmes-Featherstone attraction model (Holmes and Featherstone, 2002)
- Modified Harris-Priester atmosphere model (Montenbruck and Gill, 2005)
- Third body attraction models for sun and moon

As initial state the COEs of UWE–4 on June 22^{nd}, 2020 23:22 is chosen:

- Semimajor axis a: 6951809m
- Eccentricity e: 0.001872
- Inclination i: 97.818°
- Argument of perigee ω: 202.176°
- Right ascension of ascending node Ω: 82.32°
- True anomaly ν: 221.96°

The scenarios of the simulation start at the same time the real execution of the orbit lowering maneuver in orbit on UWE–4 was executed. The simulation is stopped at June 28^{th}, 2020 04:36, which is equivalent to 78 orbits of UWE–4 and thus corresponds to the number of active orbits of the altitude lowering scenario described in Chapter 7.3.1.1.

Several scenarios are simulated as reference and in order to estimate the possibilities of the NanoFEEP propulsion system, if the restrictions were not or only partially present. The altitude progress of the scenarios is shown in Figure 7.16. The common feature of all simulations is that only one thruster head is active, which creates thrust perfectly anti-parallel to the velocity direction of UWE–4. The simulated scenarios are configured as follows:

1. No restriction (light blue): Active altitude control during the complete orbit with 3.90µN thrust.
2. Heater restriction (red): Active altitude control during 50 minutes of each orbit with 3.90µN thrust.
3. Heater and AOCS restriction (green): Active altitude control during 18 minutes of each orbit with 2.23µN thrust. The reduced thrust corresponds to the average thrust in anti-velocity direction in Chapter 7.3.1.1. During the real maneuver, the controller was given 18 minutes for orbit control each orbit.
4. Heater, AOCS, and power restriction (black): Active altitude control during 5 minutes and 40 seconds of each orbit with 2.23µN thrust. This duration corresponds to the average active thruster duration per orbit in Chapter 7.3.1.1.

5. Natural Decay (dark blue): No thrust is applied as reference.

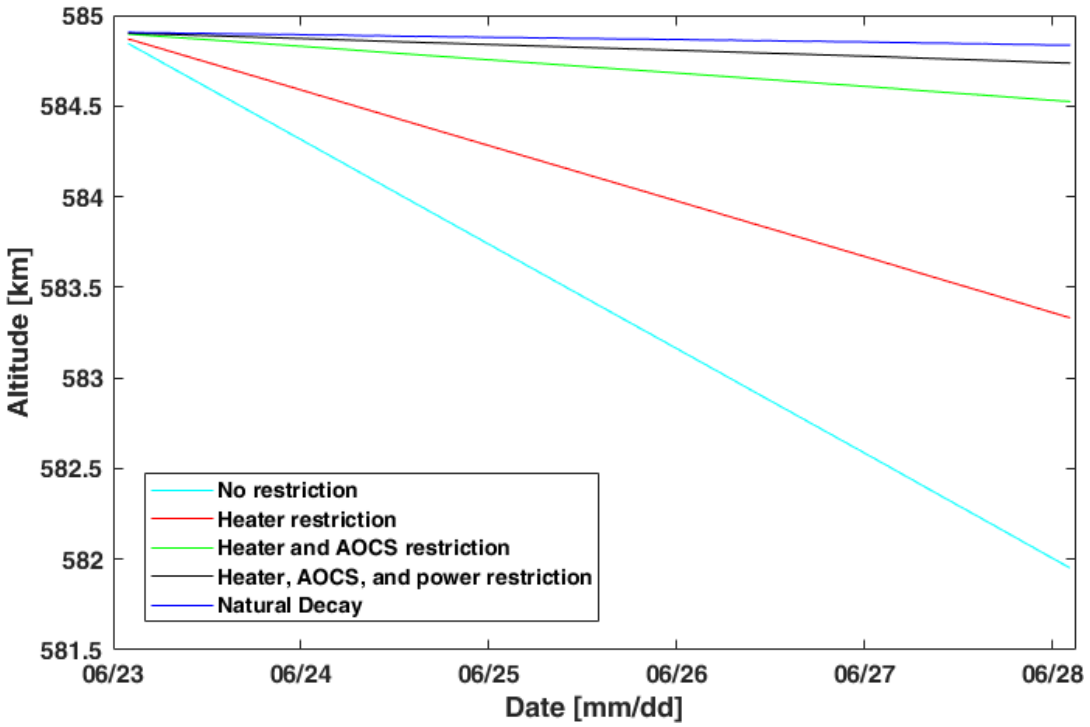

Figure 7.16: The simulated progress of the altitude of UWE–4 at different levels of restrictions. The natural decay and perfect altitude control without any restrictions are depicted as reference.

The black line in Figure 7.16 can be compared to the experimental results, as it implements all present restrictions of UWE–4. Thus, it becomes clear that there is still a lot of potential for improvement. However, the restrictions can unfortunately only be overcome in a future spacecraft mission as they all result from hardware issues.

Additionally, the activation of several thruster heads at the same time would enable to use them for attitude control purposes with a different attitude control strategy. Moreover, each thruster would create a lower thrust, so the point of operation of each thruster would shift to a much better specific impulse and thus better mass efficiency. This way the achievable total Δv and therefore the altitude decrease would be improved.

As the atmospheric drag depends heavily on solar activity, a model for a simulation may not exactly imitate the real atmospheric drag. In the simulation, the natural decay of UWE–4 was approximately $13.5\mathrm{m/d}$. However, as described in Chapter 7.3.1.2, the daily natural decay of UWE–4 according to the TLE history is only $2.18\mathrm{m/d}$. For this reason, relative altitude changes of the simulations and the experimental scenario have been corrected from the natural decay effect, in order to be able to compare the results.

Table 7.2 shows the results of the simulation and the experimental maneuver. Inaccuracies of the environment models may influence the result.

	Altitude decrease [m] (drag corrected)	Propellant consumption [10^{-3}g]
Natural decay (dark blue)	0	0.0
No restriction (light blue)	2822.71	80.06
Heater restriction (red)	1468.00	41.56
Heater and AOCS restriction (green)	302.05	14.96
Heater, AOCS, and power restriction (black)	94.88	4.71
Experimental maneuver from June 23rd, 2020 to July 3rd, 2020	98.3	4.81

Table 7.2: Comparison of the results of the altitude decreasing scenario and the experimental maneuver. The decay due to atmospheric drag was already subtracted.

7.3.2 Orbit raising maneuver

Between July 21st, 2020 and July 25th, 2020, an experimental scenario in order to increase the altitude of UWE–4 was conducted. For this purpose, the thrust vector of the NanoFEEP propulsion system should optimally be directed parallel to the velocity vector of the spacecraft, as derived in Chapter 7.1. The Follow-B algorithm presented in Chapter 4.3.2 was employed with a manual magnetic moment $\mathbf{M}_{\text{man}} = 0.07\text{A}\,\text{m}^2$.

After the presentation of the experimental data, analysis of TLEs of UWE–4 will be presented for external reference.

7.3.2.1 Experimental data

The analysis of the in-orbit data of the AOCS and the PPU of UWE–4 is done following the scheme presented in the analysis of the altitude lowering scenario in Chapter 7.3.1.1. For the sake of conciseness, only the differences in the analysis scheme and the results of the maneuver will be presented here.

During the orbit raising maneuver, UWE–4 aligned its body +z-axis with the Earth's magnetic field in phases of attitude control, as can be seen in Figure 7.17c for an exemplary orbit on July 21st, 2020. While the satellite's rotation rate was damped almost completely prior to activation of the maneuver, it was rising intermittently to a maximum rotation rate of almost $3°/\text{s}$, as shown in Figure 7.17b. Thruster B and the corresponding neutralizer were activated five times with intermediary phases of attitude control in this orbit, as shown in Figure 7.18.

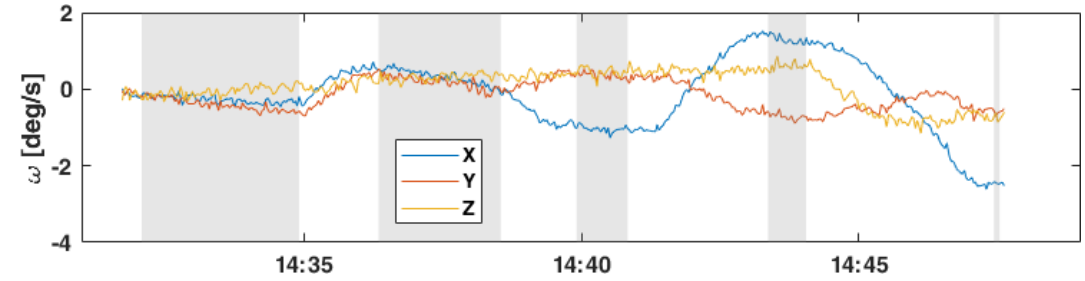

(a) Measured angular rate

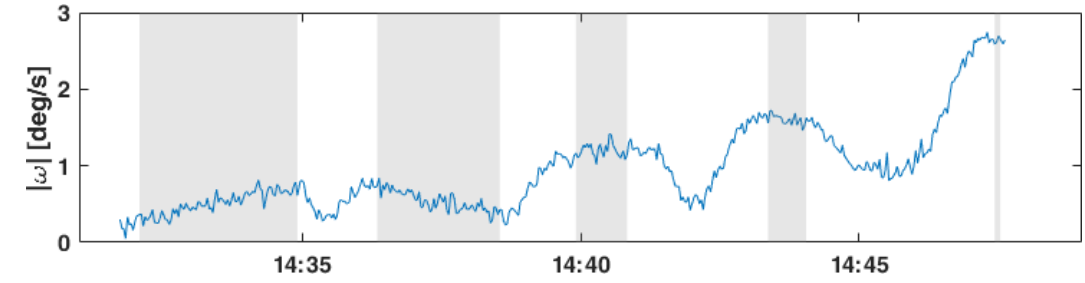

(b) Absolute value of the angular rate

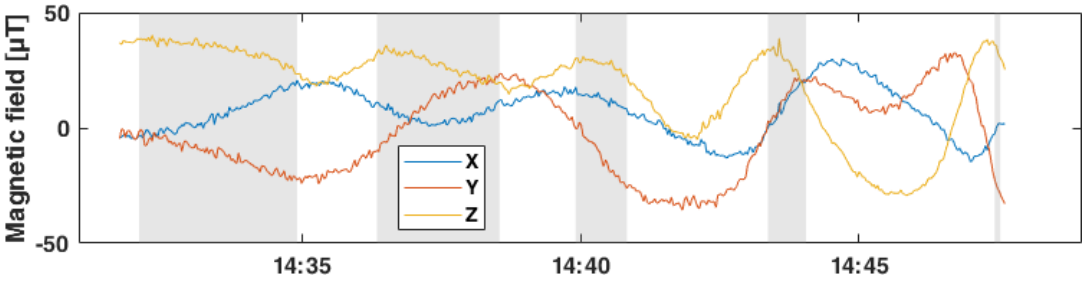

(c) Measured magnetic field

Figure 7.17: Measurements of the AOCS during the orbit raising maneuver from July 21st, 2020. Time ranges of active orbit control are shaded. (Kramer and Schilling, 2021)

The involved angles α, β, and γ are shown in Figure 7.19 for this experiment. As α describes the angle between the Earth's magnetic field and the body -z-axis, which coincides with the thrusters mounting direction, it is desired to attain the value of 180° in order to point opposite to the Earth's magnetic field during equatorial passage while the spacecraft is in the shadow of the Earth. As the angle α decreases below 130°, thruster B is turned off and the Follow-B attitude controller realigns the body +z-axis with the Earth's magnetic field direction. When the angle α increases to 145°, the Follow-B attitude controller is shut off and the thruster is reactivated. Thus, the switching angles between attitude and orbit control are at $\alpha = 130°$ and $\alpha = 145°$ for this maneuver.

The part of the thrust of thruster B contributing to an increase of the velocity of UWE–4 and thus increasing the orbits altitude is calculated with the following equations:

$$\text{Best case:} \quad |\mathbf{F}_{\text{best}}| = |\tilde{\mathbf{F}}| \cdot \cos(|| \quad \beta \quad - \quad \alpha \quad | - (180° - \Theta)|) \tag{7.16}$$

$$\text{Worst case:} \quad |\mathbf{F}_{\text{worst}}| = |\tilde{\mathbf{F}}| \cdot \cos(||\beta + \alpha - 360°| + (180° - \Theta)|) \tag{7.17}$$

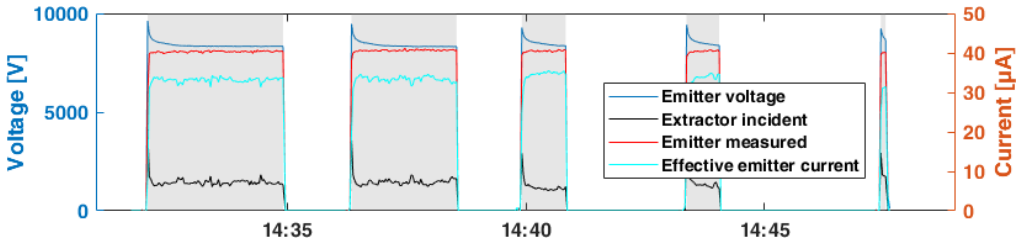

(a) Thruster B electrical characteristics

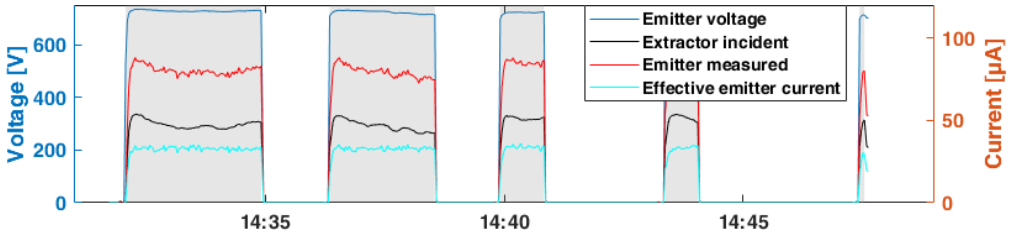

(b) Neutralizer electrical characteristics

Figure 7.18: PPU measurements during orbit raising maneuver from July 21st, 2020. Time ranges of active orbit control are shaded. (Kramer and Schilling, 2021)

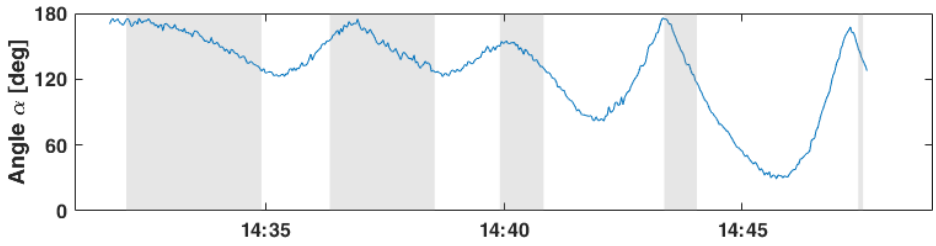

(a) The progression of the angle α between the Earth's magnetic field and the body -z-axis.

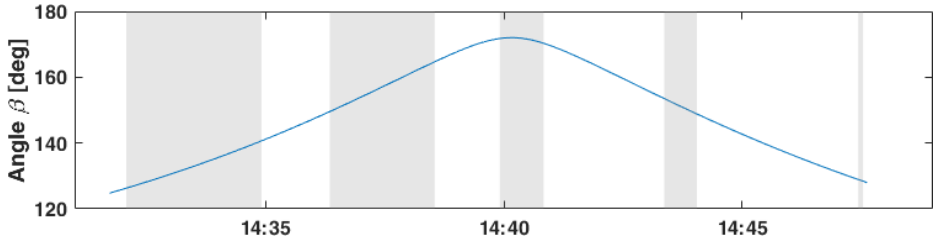

(b) The progression of the angle β between the Earth's magnetic field and the velocity direction.

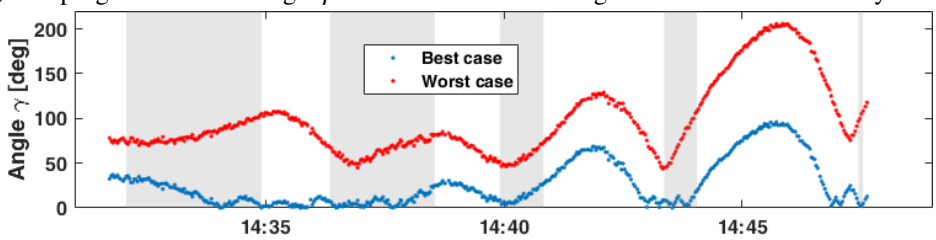

(c) The angle γ between thrust and velocity direction is estimated between $||\beta - \alpha| - (180° - \Theta)|$ (blue) and $||\beta + \alpha - 360°| + (180° - \Theta)|$ (red).

Figure 7.19: Pointing accuracy during orbit raising experiment on July 21st, 2020. Time ranges of active orbit control are shaded. (Kramer and Schilling, 2021)

In the complete scenario between July 21st, 2020 and July 25th, 2020, orbit control was active during 44 orbits. Thruster B was active for a total of 300 minutes, which corresponds to 7 minutes per orbit on average. The average thrust created was 3.39µN, even though thruster B was commanded to create the same thrust as during the orbit lowering maneuver. However, during the orbit raising scenario, the extractor current of thruster B increased and reduced the ejected net ion current and the created thrust, as depicted in Figure 5.21f. Furthermore, it was not possible to activate thruster B after the orbit increasing maneuver any more due to overcurrent faults at the hotswap circuit of the PPU.

The histogram of best and worst case thrust contribution according to Eq. (7.16) and Eq. (7.17) is depicted in Figure 7.20. The average thrust in the best case scenario is $|\mathbf{F}_{\text{best}}|$ = 3.24µN and in the worst case scenario $|\mathbf{F}_{\text{worst}}|$ = 0.81µN. This results on average in a thrust of $|\mathbf{F}_{\text{avg}}|$ = 2.02µN in velocity direction, which corresponds to 59.8% of the created thrust of thruster B.

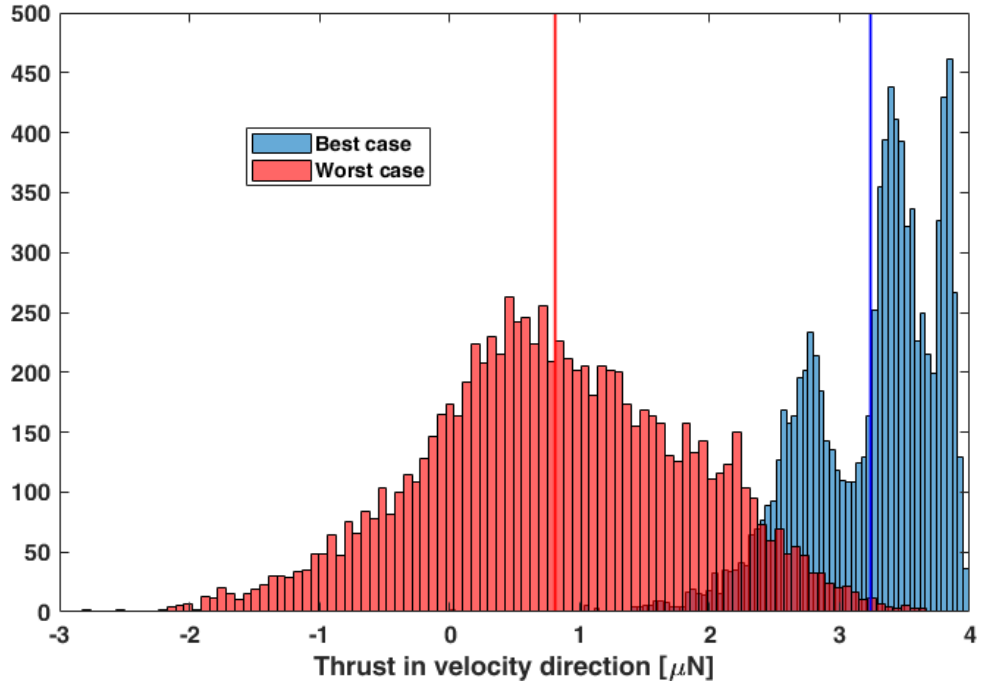

Figure 7.20: Histogram of the thrust contribution of the complete maneuver from July 21st, 2020 to July 25th, 2020 in velocity direction of UWE–4. The mean best (blue) and worst (red) case contributions are added as vertical lines. (Kramer and Schilling, 2021)

Following Eq. (7.9), the created Δv in velocity direction of UWE–4 lies in a range of $\Delta v = (1.33 - 5.30) \cdot 10^{-2} \text{m/s}$. In total, 3.27mg of gallium propellant were consumed during this scenario.

As the same emitter current of 40µA was commanded to thruster B, a power consumption of the PPU as during the orbit lowering scenario in Chapter 7.3.1.1 is expected. However, thruster B was operated during this orbit control experiment with reduced transmissivity η_{curr}, as indicated in Figure 5.21f. Consequently, the emitted current and thus the power consumption attributed to the neutralizer may have been reduced by up to 20mW.

7.3.2.2 External measurement data

The orbit of UWE–4 is monitored by NORAD and published online. Following the scheme outlined in Chapter 7.3.1.2, the TLEs can be analysed in a similar fashion. The basis for this analysis is the TLE prior to the orbit raising maneuver of late July 20th, 2020

```
UWE-4
1 43880U 18111E   20202.97748778  .00000031  00000-0  77847-5 0  9990
2 43880  97.7016 110.1539 0013339 127.7827 232.4604 14.96536014 83504
```

and as representation of the satellite's orbit after the scenario, the TLE of late July 25th, 2020:

```
UWE-4
1 43880U 18111E   20207.85849402 -.00000282 +00000-0 -19724-4 0  9997
2 43880 097.7005 114.9583 0013521 113.9224 246.3416 14.96513341086230.
```

Employing Eq. (7.11) and Eq. (7.12), the altitude progression of UWE–4 can be calculated and is shown in Figure 7.21.

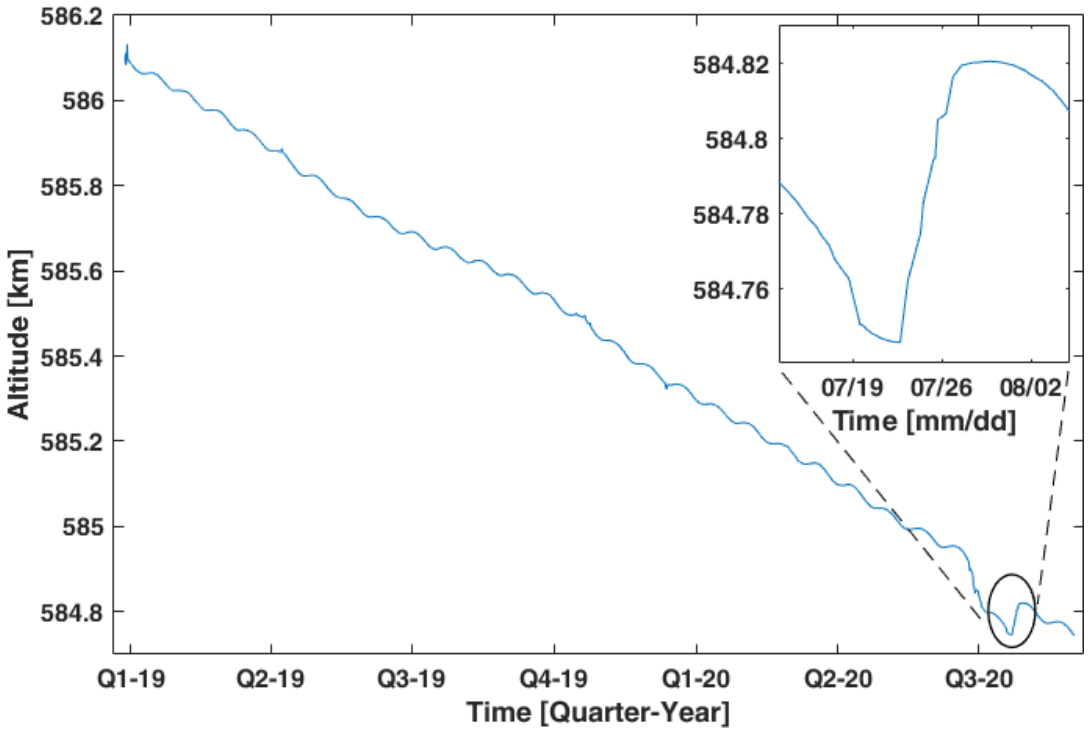

Figure 7.21: The progress of the altitude of UWE–4 since launch on December 27th, 2018 according to the TLEs provided by NORAD. The inner window shows a zoom into the orbit raising maneuver. (Kramer and Schilling, 2021)

Following Eq. (7.14) the altitude change due to the orbit raising maneuver can be calculated as

$$\begin{aligned} \Delta h[\mathrm{m}] &= |a_{\mathrm{Sat}}(\text{July } 25^{\text{th}}, 2020) - a_{\mathrm{Sat}}(\text{July } 20^{\text{th}}, 2020)| + \Delta h_{\mathrm{Drag}} \cdot 5\mathrm{d} \\ &= |6.9558168 \cdot 10^6 - 6.9557465 \cdot 10^6| + 10.89 \\ &= 81.20. \end{aligned} \tag{7.18}$$

Subsequently, the velocity of UWE–4 can be computed using Eq. (7.13) and a similar approach as in Eq. (7.15). So the created Δv of the orbit raising maneuver follows as

$$\begin{aligned} \Delta v[\mathrm{m/s}] &= |v(\text{July } 25^{\text{th}}, 2020) - v(\text{July } 20^{\text{th}}, 2020)| + \Delta v_{\mathrm{Drag}} \cdot 5\mathrm{d} \\ &= |7569.9821 - 7570.0203| + 0.006 \\ &= 4.42 \cdot 10^{-2}. \end{aligned} \tag{7.19}$$

The Δv contribution derived from the TLEs of UWE–4 is in very good accordance with the estimation of $\Delta v = (1.33 - 5.30) \cdot 10^{-2}\mathrm{m/s}$ based on the experimental data.

7.3.2.3 Simulation

The orbit raising scenario has been simulated using the Orekit library in the same configuration as described in Chapter 7.3.1.3. As initial state, the COEs of UWE–4 on July 20$^{\text{th}}$, 2020 23:50 is chosen:

- Semimajor axis a: 6943631m
- Eccentricity e: 0.001164
- Inclination i: 97.813°
- Argument of perigee ω: 159.833°
- Right ascension of ascending node Ω: 109.91°
- True anomaly ν: 284.15°

In this scenario the simulation stopped at July 23$^{\text{rd}}$, 2020 22:30, which corresponds to 44 orbits of UWE–4. This is equivalent to the duration of the experimental scenario described in Chapter 7.3.2.1. Additionally, the thrust in this scenario is directed parallel to the velocity direction of UWE–4. The simulation results of the orbit raising maneuver are shown in Figure 7.22.

The simulated scenarios are as follows:

1. No restriction (light blue): Active altitude control during the complete orbit with 3.39µN thrust.
2. Heater restriction (red): Active altitude control during 50 minutes of each orbit with 3.39µN thrust.

3. Heater and AOCS restriction (green): Active altitude control during 18 minutes of each orbit with 2.02µN thrust. The reduced thrust corresponds to the average thrust in velocity direction in Chapter 7.3.2.1. During the real maneuver, the controller was given 18 minutes for orbit control each orbit.

4. Heater, AOCS, and power restriction (black): Active altitude control during 7 minutes of each orbit with 2.02µN thrust. This duration corresponds to the average active thruster duration per orbit in Chapter 7.3.2.1.

5. Natural Decay (dark blue): No thrust is applied for reference.

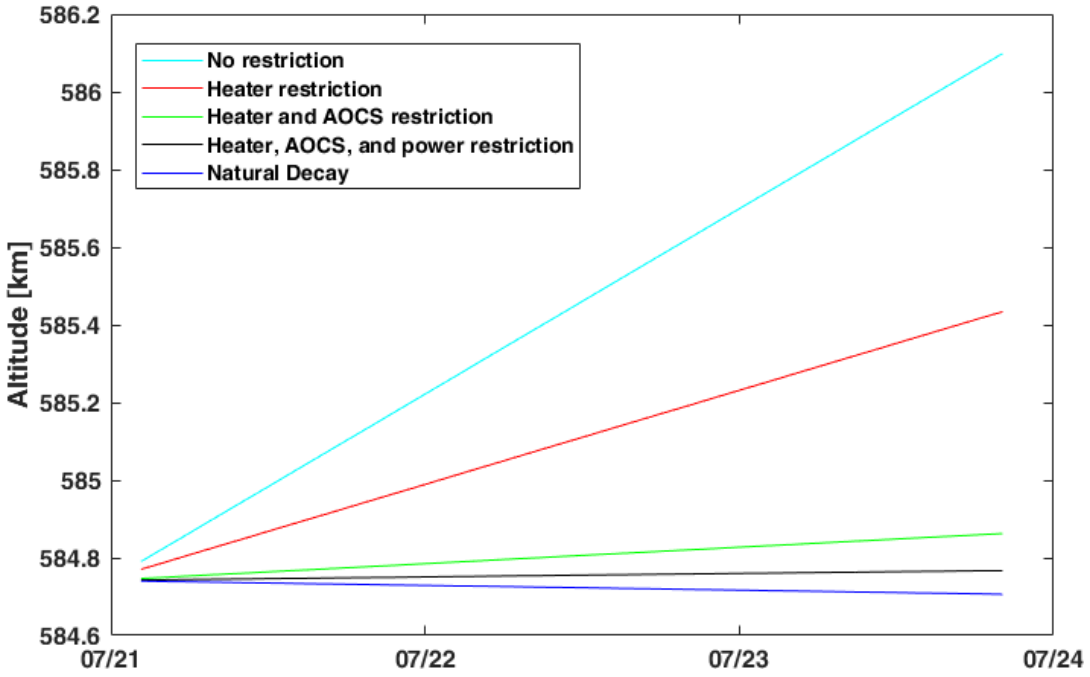

Figure 7.22: The simulated progress of the altitude of UWE–4 at different levels of restrictions. The natural decay and perfect altitude control without any restrictions are depicted as reference.

Table 7.3 shows the simulation results and the experimental results for comparison. As described in Chapter 7.3.1.3, the atmospheric drag model differs from the experimental results in its effect on the altitude change. This is a very likely cause for the difference between the altitude increase of the experimental scenario and the simulated scenario of heater, AOCS and power restriction. Furthermore, the accuracy of the used TLEs and a differing actual average thrust also influence the results of experimental and simulated altitude increase.

	Altitude increase [m] (drag corrected)	Propellant consumption [10^{-3}g]
Natural decay (dark blue)	0	0.0
No restriction (light blue)	1342.48	45.33
Heater restriction (red)	697.58	23.52
Heater and AOCS restriction (green)	149.94	8.47
Heater, AOCS, and power restriction (black)	58.24	3.29
Experimental maneuver from July 21st, 2020 to July 25th, 2020	81.20	3.27

Table 7.3: Comparison of the results of the simulated orbit raising scenario and the experimental maneuver. The decay due to atmospheric drag was already subtracted.

7.3.3 Collision avoidance maneuver

In the morning of July 2nd, 2020, a conjunction data message was issued by the United Air Force's 18th Space Control Squadron about a conjunction of UWE–4 with a fragment that was part of the Iridium-33 payload that fragmented due to a collision with Cosmos 2251 in 2009 (NORAD ID 34147). This conjunction occurred in the morning of July 5th, 2020. According to the analysis of the 18th Space Control Squadron, the objects were supposed to have a closest approach of about 822m. An analysis of the orbits using the Systems Tool Kit™ by AGI[4] has shown that UWE–4 would be already at a slightly lower altitude during the closest approach. Thus, it was decided to continue with the on-going orbit lowering maneuver in order to increase the relative distance of the two objects. After July 5th, 2020, an analysis of the relative distance for the time of closest approach has shown that the relative distance was enlarged to more than 6000m, which rendered a collision impossible.

The orbit lowering maneuver of UWE–4 after the conjunction data message is the first collision avoidance maneuver of a CubeSat.

7.4 Summary

The Gauss Variational Equations present a very clear picture of necessary thrust directions in order to change the COEs of a spacecraft efficiently. However, reality may pose additional restrictions to the efficiency.

In the case of UWE–4, the orbit control capabilities are limited by several factors. The heater of the NanoFEEP propulsion system only allows to use the available thrusters during 50 minutes of each orbit, as the propellant is not completely liquefied during the entire orbit. Additionally, only two of the implemented four thruster heads could be activated.

[4]Analytical Graphics, Inc., Exton, Pennsylvania, US

This limits the attitude control capabilities, as the available magnetorquers can not control the satellite's rotation about the Earth's magnetic field direction but only perpendicular to it. The third strongly limiting hardware issue of UWE–4 is an electrical restriction, which does not allow to activate a second actuator besides an already active thruster head. Thus, combined attitude and orbit control at the same time were impossible.

Nevertheless, an orbit control strategy could be derived, which allowed to control the altitude on a 1U CubeSat for the first time. For the purpose of altitude control, the thrust axis of the satellite is aligned parallel or anti-parallel along the Earth's magnetic field using the magnetorquers. Thruster B is then activated during positions where the Earth's magnetic field direction and the velocity direction of UWE–4 are only separated by a small angle. As attitude and orbit control are not possible at the same time, it was switched between those two functionalities, depending on the alignment with the Earth's magnetic field.

With this strategy, the satellite's altitude could be lowered by almost 100m on top of the decay due to atmospheric drag during 78 orbits. If this maneuver were continued with similar efficiency with one of the thruster heads on UWE–4, the satellite's altitude could be reduced by more than 5.1km in total. Additionally, the altitude could be raised by more than 81m during 44 orbits. The altitude de- or increase changes accordingly with the number of activated thruster heads.

On July 5th, 2020, a collision with a fragment of an Iridium 33 satellite threatened the safety of UWE–4. However, a collision avoidance maneuver by lowering the altitude of UWE–4 increased the minimal distance of the two spacecraft from 822m to more than 6000m, such that a collision became virtually impossible.

8
Conclusion

In the past decade, the absolute number of objects in LEO almost doubled compared to the preceding 50 years of space flight, resulting in a total of more than 20000 objects (ESA, 2019). Furthermore, the current evolution in LEO missions is governed by the huge amount of more than 63000 satellites to be launched in the upcoming years as part of satellite constellations of *SpaceX*, *OneWeb* and *Amazon* for a global provision of internet access (Witze, 2020). While companies like *Planet* and *Spire* started their nanosatellite constellation for Earth observation in 2013 already, hundreds of nanosatellites are to come with applications in Earth observation and communications (Camps, 2019). In consequence, the probability for collisions on orbit will increase for all objects in LEO. Hence, orbit control capabilities for positioning, de-orbiting and collision avoidance maneuvering will be one of the key capabilities of future small satellite missions.

Moreover, past implementations of cooperative multi satellite missions have produced entirely new science data of spatial and timely resolved measurements which could not be retrieved with single spacecraft. However, these projects were implemented exclusively on large satellite platforms, as miniaturized satellites lacked several crucial technologies. To counteract differential orbit disturbances between many spacecraft or to reposition satellites in a new formation was beyond the capabilities of current pico-satellite technology (National Academies of Sciences and Medicine, 2016). Nevertheless, on the one hand this would make these miniaturized spacecraft very attractive for use as passive sensor networks supporting larger spacecraft, but on the other, it could enable envisioned mission scenarios using hundreds of sensor nodes which are not feasible on conventional platforms.

While the trend in nanosatellite missions is leaning towards multiple unit structures, ongoing miniaturization of sensors and the provision of enabling technologies on pico-satellite platforms, combined with the lower launch and development costs, still render this smallest satellite class an attractive alternative for many mission scenarios. One of these enabling technologies was demonstrated for the first time as part of this thesis on board of the 1U CubeSat UWE–4 which was launched on December 27th, 2018 from Vostochny Cosmodrome into a sun-synchronous orbit at an average altitude of 586km.

8.1 Achievements presented in this thesis

This thesis provides a solution for the need of orbit control capabilities on board of 1-3U CubeSats. The solution presented in this dissertation was demonstrated on a 1U CubeSat

platform but can be easily adapted to larger platforms. For this purpose, the dissertation comprises of the following main contributions:

The first demonstration of an electric propulsion system on a 1U CubeSat platform.
During the UWE–4 mission design phase, several miniaturized propulsion systems were examined for their applicability to a pico-satellite platform. The NanoFEEP propulsion system was chosen due to its electromagnetic cleanliness and flexibility in positioning its components inside the CubeSat structure and in operation during the mission. Four miniaturized thruster heads could be integrated in the CubeSat rails and two CNT based neutralizers were placed in the side panels. These components were controlled by two dedicated PPUs.
About eight weeks after launch of UWE–4, the first neutralizer of this kind could be demonstrated in-orbit, which was followed by the first in-orbit demonstration of an electric propulsion thruster head five days later on February 26th, 2019. The actuation of the thruster heads and the neutralizers required voltages of up to 11kV, which was converted from the CubeSat bus voltage of 4.2V. This also marks the first time in pico-satellite history to create such a high voltage. The emitted ion current was at maximum 110µA. The created thrust level was up to 10µN.
While one thruster head is still functional after 120 minutes of operation, another thruster head ceased operation after more than 950 minutes active usage and more than 20 months in orbit. Unfortunately, the two remaining thruster heads could never be activated. The most probable cause for this is an electrical fault on the respective PPU.

The development of a novel thrust direction estimation algorithm, demonstrated with in-orbit data of UWE–4 using common attitude determination sensors.
A propulsion system can be used on spacecraft for attitude and orbit control purposes. If the center of gravity of the spacecraft does not coincide with the thrust axis of the thruster head, the created thrust will also exert a torque on the satellite. For a precise application of the thrust for attitude or orbit control purposes, the thrust magnitude and direction need to be known. For electrostatic propulsion systems, the thrust magnitude can be computed based on the electrical characteristics of the thruster heads following Eq. (2.6). However, the thrust direction is still unknown.
In this thesis, an analytical method is developed to determine the thrust direction of an attitude control thruster by analysing its effect on the satellite's attitude. This algorithm was demonstrated with in-orbit measurements conducted with the NanoFEEP propulsion system of UWE–4. It was found that the thrust direction of the two thruster heads divert by 15.7$\pm$7.6° and 13.2$\pm$ 5.5° from their mounting direction. Additionally, the uncertainty of this direction can be used after several experiments as a measure for the angular stability of the thrust direction.

The first successful implementation of orbit control on a pico-satellite.
Until UWE–4 proved differently, orbit control capability was reserved for larger satellite structures. Only limited success could be shown on 3U CubeSats and none so far for smaller platforms.

At the end of June 2020, UWE–4 executed an orbit lowering scenario, which reduced the altitude by more than 98m, corresponding to a total Δv of 5.35cm/s. For this purpose, UWE–4 activated one of the thruster heads during 78 orbits for an average duration of five minutes and 40 seconds per orbit with a thrust magnitude of 3.90µN.
About one month later, a scenario to increase the altitude of UWE–4 was executed. Within 44 orbits, one thruster head was activated for an average of seven minutes per orbit at an average thrust of 3.39µN. This raised the altitude of UWE–4 by more than 81m which corresponds to a total Δv of 4.42cm/s.
In early July 2020, a possible collision with a fragment that was part of the Iridium-33 payload that fragmented due to a collision with Cosmos 2251 in 2009 threatened UWE–4. Using the new orbit control capabilities of UWE–4, its altitude was lowered as a collision avoidance maneuver. This maneuver changed the distance of the two spacecraft at closest approach from a value of 822m to more than 6000m.

8.2 Future perspectives

Further capabilities of single and multi satellite missions arising from orbit control or other applications of propulsion systems are given in the following analysis.

In view of thousands of new satellites in LEO within the next years, the focus of **sustainability in space flight** is shifting towards the preservation of available orbit altitudes. A collision of two satellites in LEO endangers all other spacecraft on similar orbits and potentially renders this altitude useless for the following decades to centuries due to uncontrollable space debris. For this reason, a requirement of maneuverability for **collision avoidance** is about to be imposed on spacecraft aiming at altitudes above 400km (Federal Communications Commission, 2020).

8.2.1 Single satellite missions

Besides enabling miniaturized spacecraft to conform to upcoming regulations, the ability to perform orbit control maneuvers opens the field of applications to a whole new set of missions with small satellites. Single satellites can **prolong the mission duration** by compensating the atmospheric drag. This is especially attractive for the large number of CubeSats deployed from the ISS whose mission duration is up to several months at best with natural decay. While they do not endanger the ISS by maintaining a lower orbit, they can potentially double their lifetime at very low Earth orbits using an active propulsion system.

Today, all satellites have to de-orbit within 25 years after end of mission (Inter-agency space debris coordination committee, 2002). As most of the spacecraft launched nowadays do not employ a propulsion system, launch vehicles are usually targeting orbits below 650km altitude to comply with this regulation by natural decay. The possibility to increase the orbit of a spacecraft independent of the launch vehicle allows small satellites to **operate at higher altitudes**.

Furthermore, an **accelerated decay** of small satellites after mission finalization reduces the risk of in orbit collisions with decommissioned satellites. For this purpose spacecraft

can lower their orbit altitude using an on-board propulsion system and thus ensure earlier re-entry into the Earth's atmosphere than with natural decay.

In the field of planetary exploration, maneuverable miniaturized spacecraft can not replace conventional satellites but could make **complementary science** measurements or provide **differential measurements** using a small relative distance to the main spacecraft. Furthermore, miniaturized instrumentation could be integrated on pico- and nanosatellites for persistent observation of stellar objects at high-resolution. However, this requires precise pointing with reaction wheels using a propulsion system for **momentum dumping** beyond LEO.

8.2.2 Multi satellite missions

Further applications lie in the field of fractionated spacecraft. In LEO, this allows for novel science missions based on multi-point measurements of the Earth's environment. A possible implementation is the mission ANDESITE, which aims to measure the distributed electrical currents causing aurora (Parham et al., 2019). The pico-satellites, which build the fractionated sensor network, will be deployed from the main spacecraft at an altitude below 400km. A propulsion system could increase their lifetime and **maintain the desired spatial relative distance** for observation over a longer duration.

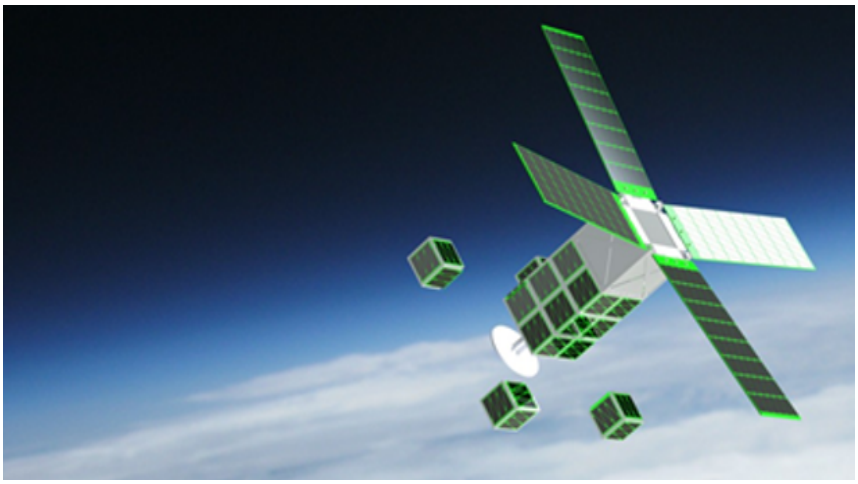

Figure 8.1: ANDESITE: Exploring aurora with a distributed sensor network. (Boston University)

Additionally, small satellite constellation operators gain a certain degree of freedom in their choice of launch vehicle for **replenishment of single satellites** as they can re-position their satellites from a larger variety of insertion orbits. The distribution of the single satellites after deployment from the launch vehicle is achieved today in a long duration process employing differential atmospheric drag. As the atmosphere gets thinner with increasing altitude, the application of differential drag is not feasible any more. The distribution for **constellation establishment is accelerated** by the use of a propulsion system and thus it increases the active time during which it supports the mission

with **station-keeping**. Furthermore, this allows for **faster technology updates** of the constellation by replacement of outdated or failed satellites.

According to the National Academies of Sciences and Medicine (2016), the implementation of constellations in the field of space science enables to achieve the decadal science goal of understanding the "[...] dynamics and coupling of Earth's magnetosphere, ionosphere and atmosphere[...]". For this purpose, a cooperative satellite constellation mission aiming at discoveries about how the magnetosphere stores, processes and releases energy is envisioned. Albeit this mission is not feasible with large satellites due to the complexity and the associated risk of failure, miniaturized maneuverable spacecraft could retrieve lower resolution long-term measurement data and thus **contribute to this scientific discipline** with an increased number of sensor nodes.

However, the most significant novelty perhaps lies in the field of small satellite formation missions that initialize and maintain a certain topology using high-tech attitude and orbit control capabilities. In different space science disciplines the simultaneous observation of targets **improves the science return** by increased resolution or 3D reconstruction of the images. The first mission to demonstrate 3D formation flight on 3U CubeSats called NetSat was launched in September 2020. Formation flight missions are the focus of active research for applications in the field of Earth observation. The upcoming mission CloudCT employing a CubeSat formation aims at computer tomography measurements of clouds to provide a better understanding of the influence of clouds on the climate (Schilling and Aumann, 2020). In this mission, many orbit control maneuvers are necessary to allow for the different formation topologies.

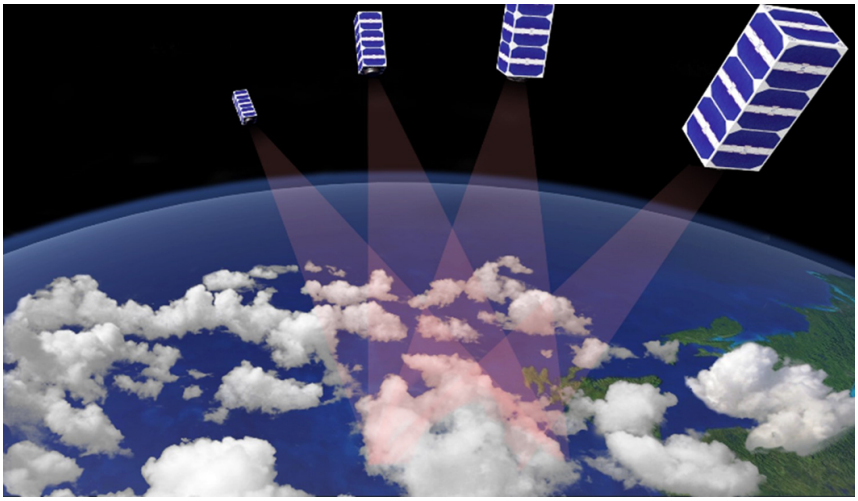

Figure 8.2: CloudCT: Computer tomography of clouds enabled by nanosaellite formation flight. (Schilling et al., 2019)

In the field of astrophysics, **interferometric applications that are located in space** can achieve significantly higher spatial resolution compared to ground based systems. The necessary high precision relative attitude and orbit maintenance requires highly accurate propulsion systems.

Multi-static Synthetic Aperture Radars (SARs) employing a single active radar on a larger satellite platform with additional passive radar receivers has attracted interest in Earth observation for the past decades ((Krieger and Moreira, 2005), (Gutierrez-Nava et al., 2012), (Guccione et al., 2020)). Its advantages compared to monostatic SAR are, among others, efficient interference suppression and resolution enhancement. While small satellites can not fulfill the requirements of the active spacecraft, they can be passive radar receivers. With the newly attained ability of orbit control, small satellites can be employed as **passive receivers of a multi-static SAR**.

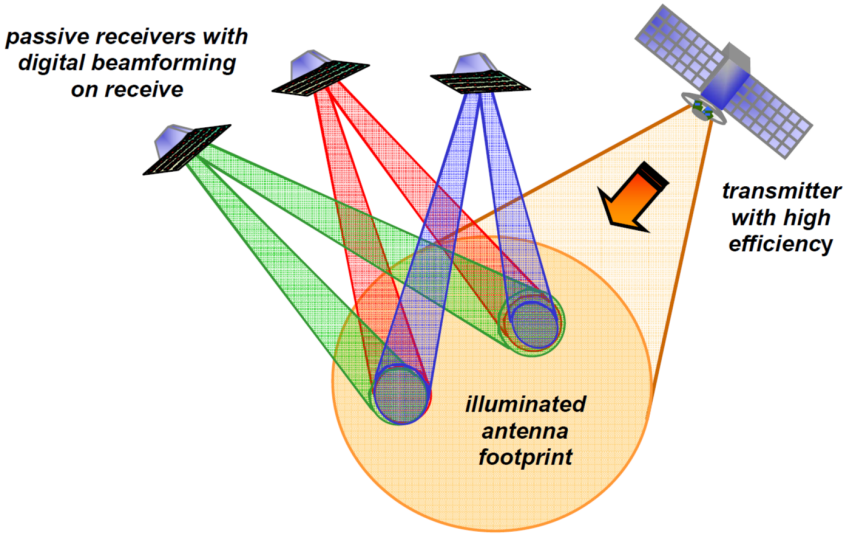

Figure 8.3: Principle of multi-static SAR. (Krieger and Moreira, 2005)

Many space flight missions require power levels, communication or computing capabilities or other mission specific needs which can not be fulfilled by small satellites. Nonetheless, the introduction of orbit control capabilities at the smallest scale of spacecraft has the potential to enable missions which can only be met with a distributed sensor network that is out of scope to be implemented on larger satellite platforms. Furthermore, it can preserve sustainability within the LEO environment by making collision avoidance maneuvers and targeted de-orbiting of decommissioned miniaturized satellites possible.

Appendix

A Figures

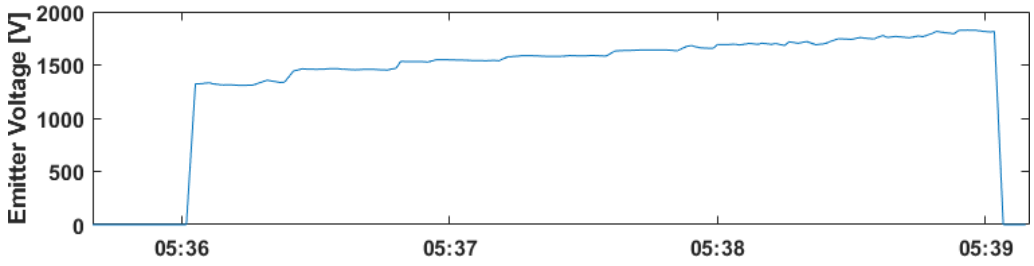

(a) Emitter voltage of neutralizer A.

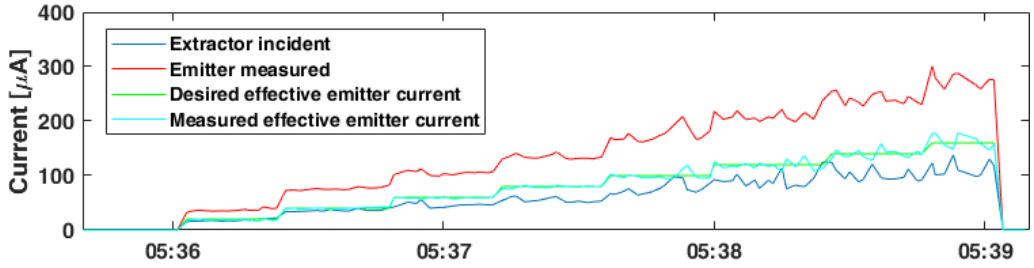

(b) Monitored currents of neutralizer A.

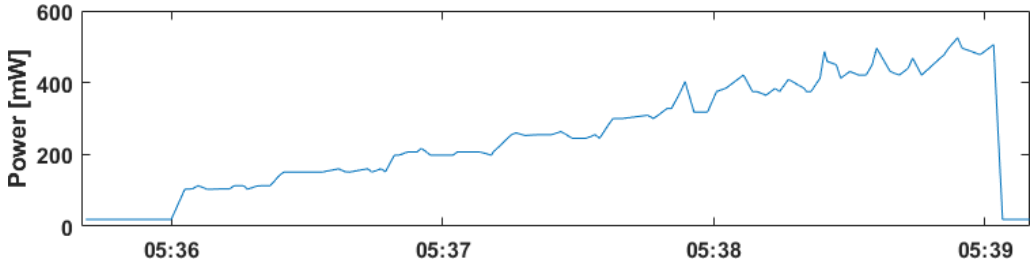

(c) Power consumption of the PPU during neutralizer A activation.

Figure A.4: In-orbit characterization of neutralizer A on March 27th, 2020.

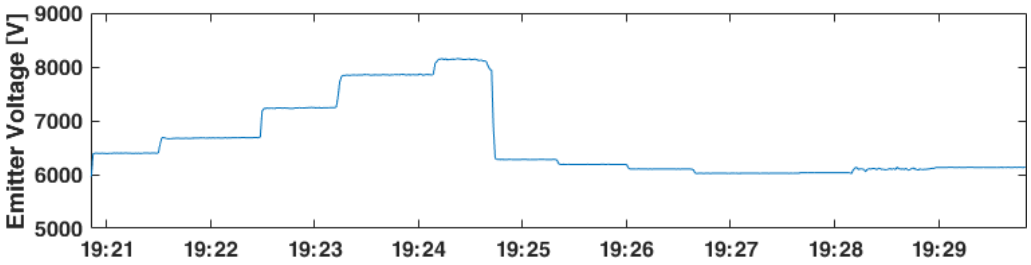

(a) Emitter voltage U_{mon} of thruster C.

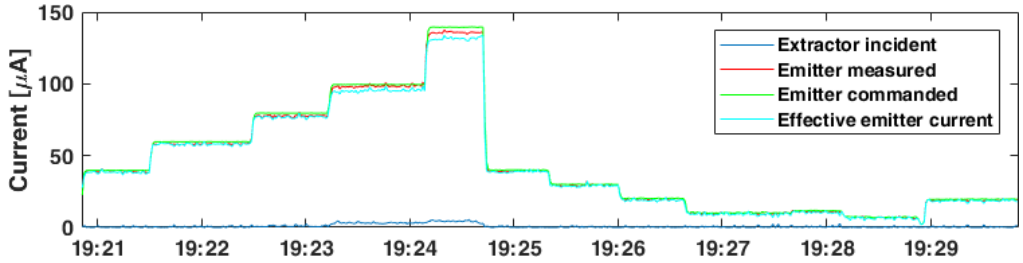

(b) Monitored currents of thruster C.

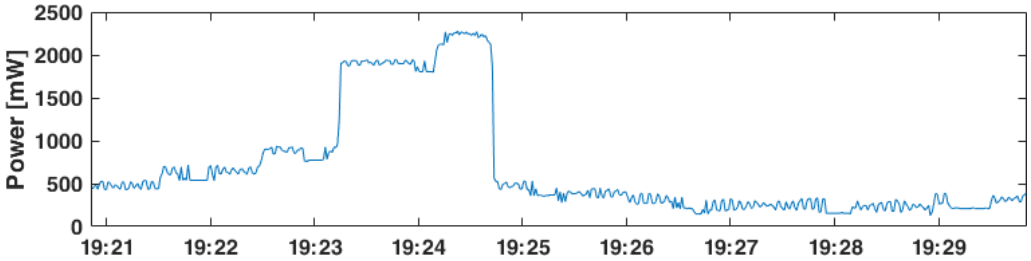

(c) Power consumption of the PPU.

Figure A.5: Laboratory experiment with thruster C on October 18th, 2018.

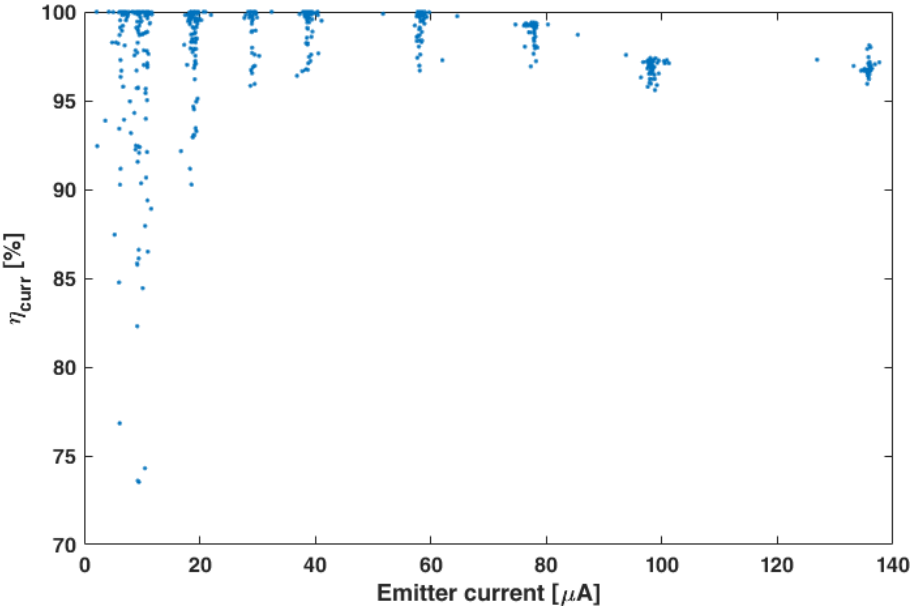

Figure A.6: Thruster C current efficiency according to laboratory experiment on October 18th, 2018.

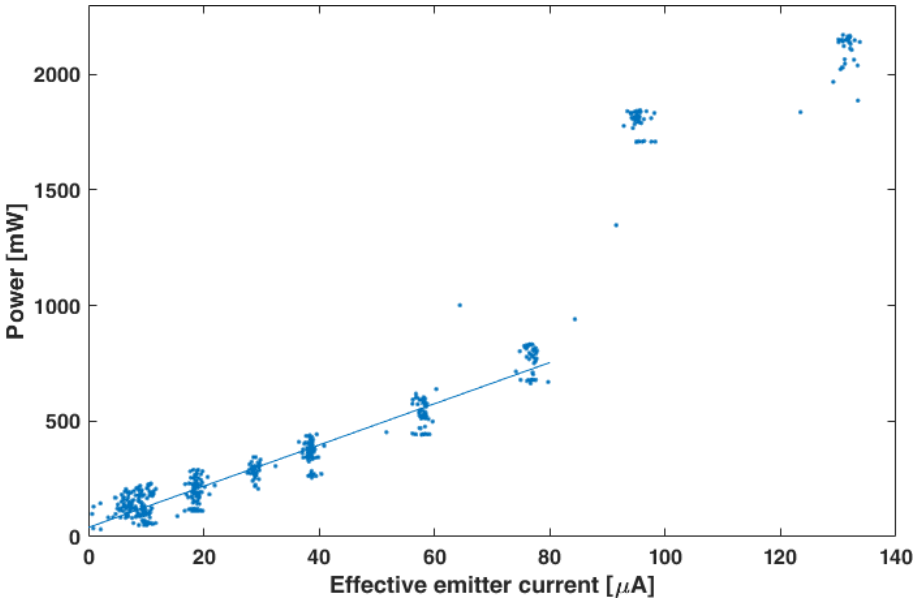

Figure A.7: Power consumption of the PPU vs emitter current of thruster C. The neutralizer was not active during this experiment.

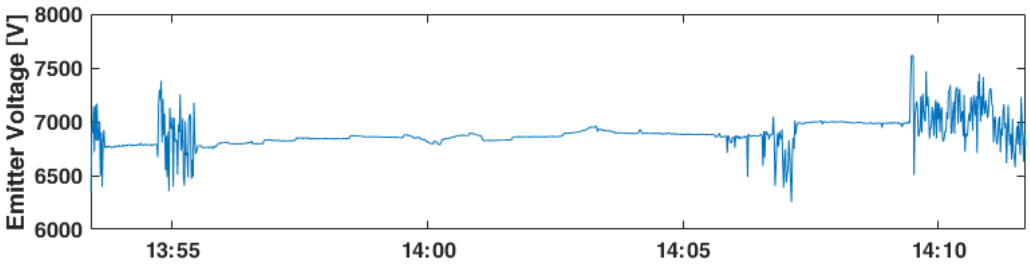

(a) Emitter voltage U_{mon} of thruster D.

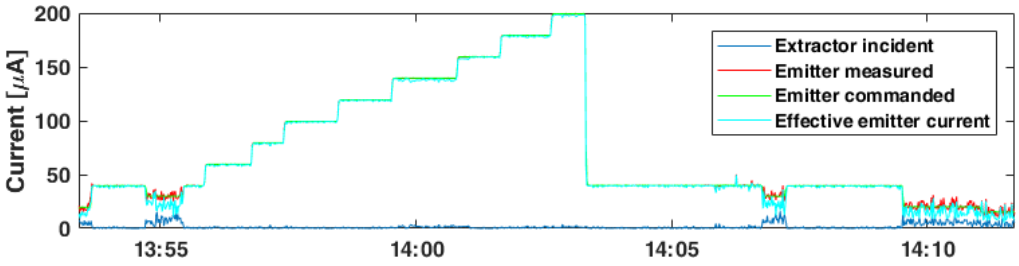

(b) Monitored currents of thruster D.

Figure A.8: Laboratory experiment with thruster D on October 16th, 2018.

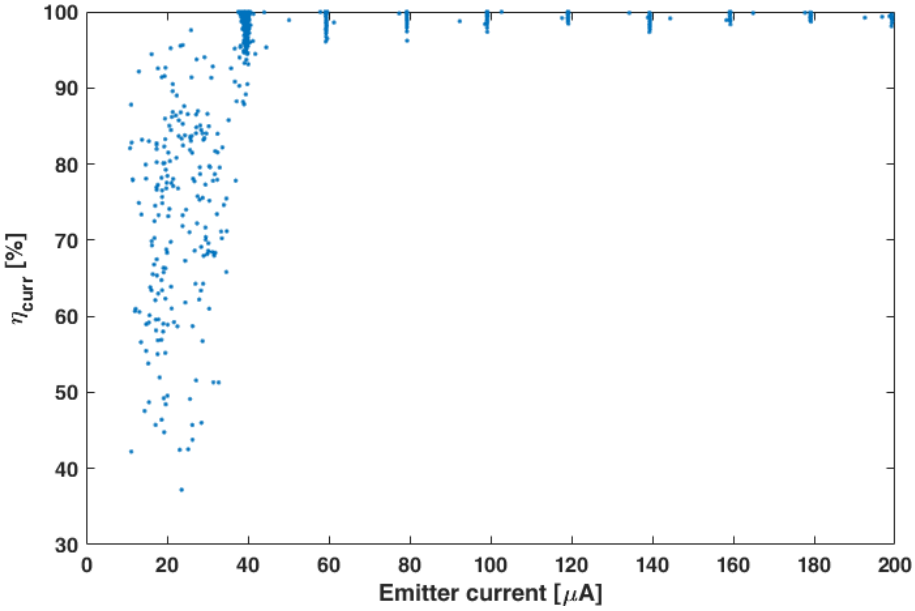

Figure A.9: Thruster D current efficiency according to laboratory experiment on October 16th, 2018.

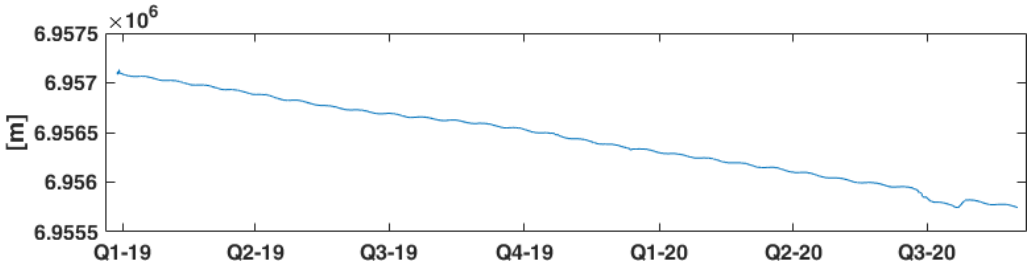

(a) Semimajor axis a.

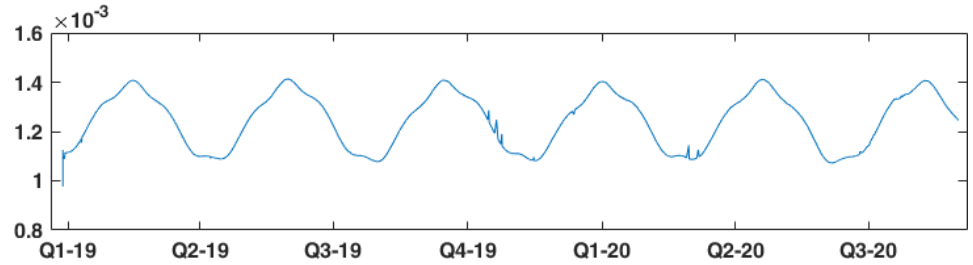

(b) Eccentricity e.

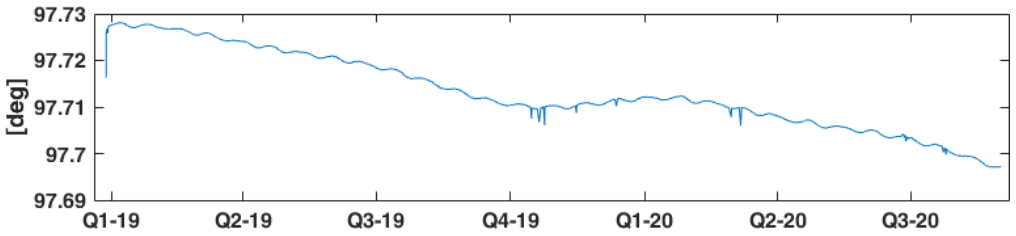

(c) Inclination i.

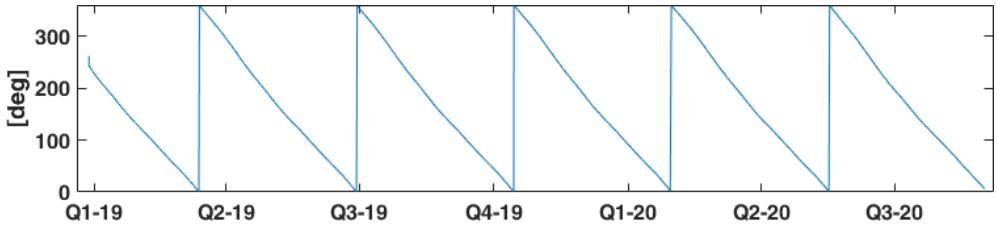

(d) Argument of perigee ω.

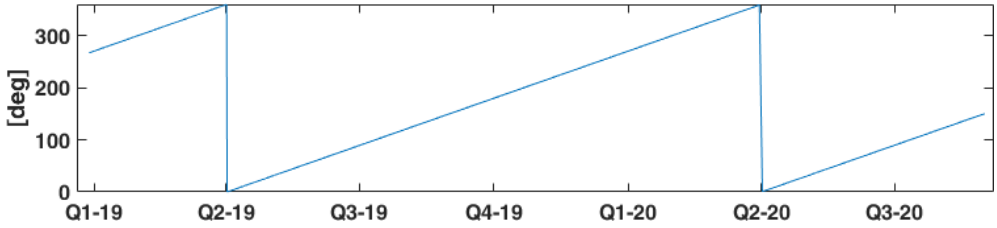

(e) Right ascension of ascending node Ω.

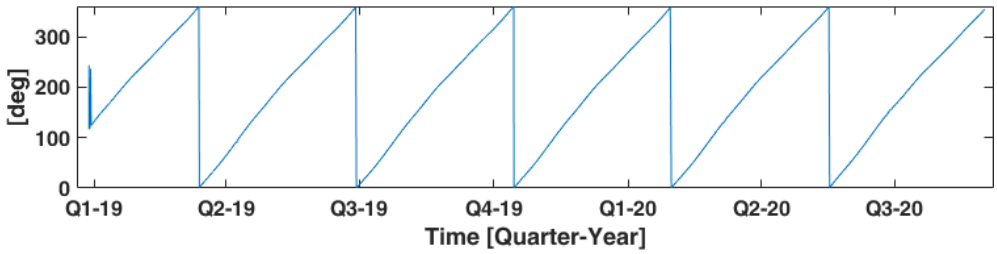

(f) Mean anomaly M.

Figure A.10: COE history of UWE–4.

B Error propagation in Eq. (6.7)

For reasons of readability, the following variable is introduced:

$$\gamma = 2 \cdot \sqrt{-(\mathrm{F}_{\perp,x}\mathrm{r}_y - \mathrm{F}_{\perp,y}\mathrm{r}_\mathrm{x})^2 - (\mathrm{F}_{\perp,x}\mathrm{r}_z - \mathrm{F}_{\perp,z}\mathrm{r}_\mathrm{x})^2 - (\mathrm{F}_{\perp,y}\mathrm{r}_z - \mathrm{F}_{\perp,z}\mathrm{r}_\mathrm{y})^2 + |\tilde{\mathrm{F}}|^2|\mathrm{r}|^2} \tag{B.1}$$

For the error propagation holds

$$\delta\alpha_1 = \sqrt{\sum_{i=x,y,z}\left(\left(\frac{\partial\alpha_1}{\partial \mathrm{F}_{\perp,i}} \cdot \delta \mathrm{F}_{\perp,i}\right)^2 + \left(\frac{\partial\alpha_1}{\partial \mathrm{r}_i} \cdot \delta \mathrm{r}_i\right)^2\right) + \left(\frac{\partial\alpha_1}{\partial|\tilde{\mathrm{F}}|} \cdot \delta|\tilde{\mathrm{F}}|\right)^2} \tag{B.2}$$

with

$$\frac{\partial\alpha_1}{\partial \mathrm{F}_{\perp,x}} = \frac{\frac{-2\mathrm{r}_y(\mathrm{F}_{\perp,x}\mathrm{r}_y - \mathrm{F}_{\perp,y}\mathrm{r}_x) - 2\mathrm{r}_z(\mathrm{F}_{\perp,x}\mathrm{r}_z - \mathrm{F}_{\perp,z}\mathrm{r}_x)}{\gamma} - \mathrm{r}_x}{|\mathrm{r}|^2} \tag{B.3}$$

$$\frac{\partial\alpha_1}{\partial \mathrm{F}_{\perp,y}} = \frac{\frac{2\mathrm{r}_x(\mathrm{F}_{\perp,x}\mathrm{r}_y - \mathrm{F}_{\perp,y}\mathrm{r}_x) - 2\mathrm{r}_z(\mathrm{F}_{\perp,y}\mathrm{r}_z - \mathrm{F}_{\perp,z}\mathrm{r}_y)}{\gamma} - \mathrm{r}_y}{|\mathrm{r}|^2} \tag{B.4}$$

$$\frac{\partial\alpha_1}{\partial \mathrm{F}_{\perp,z}} = \frac{\frac{2\mathrm{r}_x(\mathrm{F}_{\perp,x}\mathrm{r}_z - \mathrm{F}_{\perp,z}\mathrm{r}_x) + 2\mathrm{r}_y(\mathrm{F}_{\perp,y}\mathrm{r}_z - \mathrm{F}_{\perp,z}\mathrm{r}_y)}{\gamma} - \mathrm{r}_z}{|\mathrm{r}|^2} \tag{B.5}$$

$$\begin{aligned}\frac{\partial\alpha_1}{\partial \mathrm{r}_x} = &\frac{\frac{2\mathrm{F}_{\perp,y}(\mathrm{F}_{\perp,x}\mathrm{r}_y - \mathrm{F}_{\perp,y}\mathrm{r}_x) + 2\mathrm{F}_{\perp,z}(\mathrm{F}_{\perp,x}\mathrm{r}_z - \mathrm{F}_{\perp,z}\mathrm{r}_x) + 2|\tilde{\mathrm{F}}|^2\mathrm{r}_x}{\gamma} - \mathrm{F}_{\perp,x}}{|\mathrm{r}|^2} \cdots \\ &- \frac{2\mathrm{r}_x(\gamma - \mathrm{F}_{\perp,x}\mathrm{r}_x - \mathrm{F}_{\perp,y}\mathrm{r}_y - \mathrm{F}_{\perp,z}\mathrm{r}_z)}{|\mathrm{r}|^4}\end{aligned} \tag{B.6}$$

$$\begin{aligned}\frac{\partial\alpha_1}{\partial \mathrm{r}_y} = &\frac{\frac{-2\mathrm{F}_{\perp,x}(\mathrm{F}_{\perp,x}\mathrm{r}_y - \mathrm{F}_{\perp,y}\mathrm{r}_x) + 2\mathrm{F}_{\perp,z}(\mathrm{F}_{\perp,y}\mathrm{r}_z - \mathrm{F}_{\perp,z}\mathrm{r}_y) + 2|\tilde{\mathrm{F}}|^2\mathrm{r}_y}{\gamma} - \mathrm{F}_{\perp,y}}{|\mathrm{r}|^2} \cdots \\ &- \frac{2\mathrm{r}_y(\gamma - \mathrm{F}_{\perp,x}\mathrm{r}_x - \mathrm{F}_{\perp,y}\mathrm{r}_y - \mathrm{F}_{\perp,z}\mathrm{r}_z)}{|\mathrm{r}|^4}\end{aligned} \tag{B.7}$$

$$\begin{aligned}\frac{\partial\alpha_1}{\partial \mathrm{r}_z} = &\frac{\frac{-2\mathrm{F}_{\perp,x}(\mathrm{F}_{\perp,x}\mathrm{r}_z - \mathrm{F}_{\perp,z}\mathrm{r}_x) - 2\mathrm{F}_{\perp,y}(\mathrm{F}_{\perp,y}\mathrm{r}_z - \mathrm{F}_{\perp,z}\mathrm{r}_y) + 2|\tilde{\mathrm{F}}|^2\mathrm{r}_z}{\gamma} - \mathrm{F}_{\perp,z}}{|\mathrm{r}|^2} \cdots \\ &- \frac{2\mathrm{r}_z(\gamma - \mathrm{F}_{\perp,x}\mathrm{r}_x - \mathrm{F}_{\perp,y}\mathrm{r}_y - \mathrm{F}_{\perp,z}\mathrm{r}_z)}{|\mathrm{r}|^4}\end{aligned} \tag{B.8}$$

$$\frac{\partial\alpha_1}{\partial|\tilde{\mathrm{F}}|} = \frac{|\tilde{\mathrm{F}}|}{\gamma} \tag{B.9}$$

C Spherical coordinates

A random vector $\mathbf{A} = [\mathrm{x}, \mathrm{y}, \mathrm{z}]^\intercal$ is transformed into spherical coordinates using

$$\mathbf{A} = \begin{pmatrix} \rho \\ \theta \\ \varphi \end{pmatrix} = \begin{pmatrix} \sqrt{x^2+y^2+z^2} \\ \frac{180}{\pi} \cdot \arctan\left(\frac{y}{x}\right) \\ \frac{180}{\pi} \cdot \arccos\left(\frac{z}{\sqrt{x^2+y^2+z^2}}\right) \end{pmatrix}. \tag{C.1}$$

The error propagation of a vector $\mathbf{A}$ follows

$$\begin{aligned} \delta\theta(\mathbf{A}) &= \sqrt{\left(\frac{\partial \mathbf{A}}{\partial \mathrm{A}_x} \cdot \delta \mathrm{A}_x\right)^2 + \left(\frac{\partial \mathbf{A}}{\partial \mathrm{A}_y} \cdot \delta \mathrm{A}_y\right)^2} \\ &= \frac{180}{\pi} \cdot \sqrt{\left(-\frac{\mathrm{A}_y}{\mathrm{A}_x^2+\mathrm{A}_y^2} \cdot \delta \mathrm{A}_x\right)^2 + \left(\frac{\mathrm{A}_x}{\mathrm{A}_x^2+\mathrm{A}_y^2} \cdot \delta \mathrm{A}_y\right)^2} \end{aligned} \tag{C.2}$$

$$\begin{aligned} \delta\varphi(\mathbf{A}) &= \sqrt{\left(\frac{\partial \mathbf{A}}{\partial \mathrm{A}_x} \cdot \delta \mathrm{A}_x\right)^2 + \left(\frac{\partial \mathbf{A}}{\partial \mathrm{A}_y} \cdot \delta \mathrm{A}_y\right)^2 + \left(\frac{\partial \mathbf{A}}{\partial \mathrm{A}_z} \cdot \delta \mathrm{A}_z\right)^2} \\ &= \frac{180}{\pi} \cdot \sqrt{\sum_{i=x,y} \left(\frac{\mathrm{A}_i \mathrm{A}_z}{|\mathbf{A}|^3 \cdot \sqrt{1-\frac{\mathrm{A}_z^2}{|\mathbf{A}|^2}}} \cdot \delta \mathrm{A}_i\right)^2 + \left(\frac{\frac{1}{|\mathbf{A}|} - \frac{\mathrm{A}_z^2}{|\mathbf{A}|^3}}{\sqrt{1-\frac{\mathrm{A}_z^2}{|\mathbf{A}|^2}}} \cdot \delta \mathrm{A}_z\right)^2}. \end{aligned} \tag{C.3}$$

It is refrained from the error propagation for the component ρ, since it is not necessary in this thesis.

List of Tables

List of Figures

References

Bmx055 - small, versatile 9-axis sensor module. October 2013.

Esa's annual space environment report. resreport, European Space Operations Centre, July 2019. URL https://www.sdo.esoc.esa.int/environment_report/Space_Environment_Report_latest.pdf. Retrieved September 23rd, 2020.

Azari, P. An orbit control system for UWE–4 using the high fidelity simulation toolkit orekit. Master's thesis, Julius-Maximilians University of Wuerzburg, Chair of Robotics and Telematics, November 2016.

Bahcivan, H., Cutler, J., Springmann, J., Doe, R., and Nicolls, M. Magnetic aspect sensitivity of high-latitude e region irregularities measured by the rax-2 cubesat. *Journal of Geophysical Research*, 119:1233–1249, February 2014. doi: 10.1002/2013JA019547.

Bangert, P., Busch, S., and Schilling, K. In-Orbit Performance of the Pico-Satellite UWE-3. In *10th IAA Symposium on Small Satellites for Earth Observation*, Berlin Germany, 2015.

Bangert, P. *Magnetic Attitude Control of Miniature Satellites and its Extension towards Orbit Control using an Electric Propulsion System*. PhD thesis, Julius-Maximilians-University Wuerzburg, 2018.

Bangert, P., Kramer, A., and Schilling, K. Uwe-4: Integration state of the first electrically propelled 1u cubesat. *31st Annual AIAA/USU Conference on Small Satellites*, 2017.

Battin, R. H. *An Introduction to the Mathematics and Methods of Astrodynamics*. American Institute of Aeronautics and Astronautics, Inc., 1999.

Bencze, W., Debra, D., Herman, L., Holmes, T., Adams, M., Keiser, G., and Everitt, C. On-orbit performance of the gravity probe b drag-free translation control system. *Advances in the Astronautical Sciences*, 125, January 2006.

Bock, D. and Tajmar, M. Highly miniaturized feep propulsion system (nanofeep) for attitude and orbit control of cubesats. In *67th International Astronautical Congress*, Guadalajara, Mexico, September 2016.

Bock, D., Bethge, M., and Tajmar, M. Highly miniaturized FEEP thrusters for CubeSat applications. In *4th Spacecraft Propulsion Conference*, Cologne, Germany, 2014.

Bock, D., Kramer, A., Bangert, P., Schilling, K., and Tajmar, M. NanoFEEP on UWE platform – Formation Flying of CubeSats using Miniaturized Field Emission Electric Propulsion Thrusters. *Joint Conference of 30th International Symposium on Space Technology and Science, 34th International Electric Propulsion Conference and 6th Nano-satellite Symposium*, 2015.

Bock, D., Kramer, A., Bangert, P., Schilling, K., and Tajmar, M. NanoFEEP - Highly Miniaturized FEEP Propulsion System for Attitude and Orbit Control of CubeSats. In *Proceedings of the 5th Spacecraft Propulsion Conference*, 2016.

Bock, D., Spethmann, A., Trottenberg, T., Kersten, H., and Tajmar, M. In-plume thrust measurement of nanofeep thruster with a force measuring probe using laser interferometry. *Proceedings of the 35th International Electric Propulsion Conference*, October 2017a.

Bock, D. NanoFEEP heater specification, September 2018. Personal Communication.

Bock, D., Laufer, P., Paries, F., Kopnarski, M., and Tajmar, M. Plume characterization of nanofeep thrusters with a plasma diagnostics facility using carbon-velvet probes. *Proceedings of the 35th International Electric Propulsion Conference*, October 2017b.

Bonin, G., Roth, N., Armitage, S., Newman, J., Risi, B., and Zoe, R. E. Canx-4 and canx-5 precision formation flight: Mission accomplished! *29th Annual AIAA/USU Conference on Small Satellites*, August 2015.

Boston University. Andesite, a cubesat running android. Online. URL http://www.bu.edu/csp/hall_display/ANDESITE.html. Retrieved September 27th, 2020.

Bradford-ECAPS. Flight-proven- high perfomance green propulsion. Online. URL https://www.ecaps.space/assets/pdf/Bradford_ECAPS_Folder_2017.pdf. Retrieved September 16th, 2020.

Bradford Space. Comet - water-based smallsat propulsion. Online. URL https://www.bradford-space.com/assets/pdf/be_datasheet_comet_2019oct.pdf. Retrieved September 16th, 2020.

Brophy, J. Nasa's deep space 1 ion engine (plenary). *Review of Scientific Instruments*, 73: 1071–1078, 02 2002. doi: 10.1063/1.1432470.

Bryce Space and Technology. Smallsats by the numbers. Online, 2020. URL https://brycetech.com/reports/report-documents/Bryce_Smallsats_2020.pdf. Retrieved September 22nd, 2020.

Bureau international des poids et mesures. Le système international d'unités (si). Online, 2019. URL https://www.bipm.org/utils/common/pdf/si-brochure/SI-Brochure-9-FR.pdf. Retrieved September 21st, 2020.

Busch, S. CubeSat Subsystem Interface Definition. UNISEC Europe, 2017.

Busch, S., Bangert, P., Dombrovski, S., and Schilling, K. In-Orbit Performance and Lessons Learned of a Modular and Flexible Satellite Bus for Future Picosatellite Formations. In *Proceedings of the 65. IAC Congress, Toronto, Canada*, 2014.

Busch, S., Bangert, P., Dombrovski, S., and Schilling, K. Uwe-3, in-orbit performance and lessons learned of a modular and flexible satellite bus for future picosatellite formations. *Acta Astronautica*, 117:73 – 89, 2015. ISSN 0094-5765. doi:

http://dx.doi.org/10.1016/j.actaastro.2015.08.002. URL http://www.sciencedirect.com/science/article/pii/S0094576515003185.

Busek. Bit-3 rf ion thruster. Online, a. URL http://www.busek.com/index_htm_files/70010819F.pdf. Retrieved September 17th, 2020.

Busek. Bmp-220 micro-pulsed plasma thruster. Online, b. URL http://busek.com/index_htm_files/70008502G.pdf. Retrieved September 18th, 2020.

California Polytechnic State University. CubeSat Design Specification Rev. 13, The CubeSat Program. https://static1.squarespace.com/static/5418c831e4b0fa4ecac1bacd/t/56e9b62337013b6c063a655a/1458157095454/cds_rev13_final2.pdf, February 2014.

Camps, A. *Satellites Missions and Technologies for Geosciences*, chapter Nanosatellites and Applications to Commercial and Scientific Missions. IntechOpen, November 2019. ISBN 978-1-78985-995-9.

Canuto, E. and Massotti, L. All-propulsion design of the drag-free and attitude control of the european satellite goce. *Acta Astronautica*, 64(2):325 – 344, 2009. ISSN 0094-5765. doi: https://doi.org/10.1016/j.actaastro.2008.07.017. URL http://www.sciencedirect.com/science/article/pii/S0094576508002683.

Cleveland, W. S. Robust locally weighted regression and smoothing scatterplots. *Journal of the American Statistical Association*, 74(368):829–836, 1979. doi: 10.1080/01621459.1979.10481038. URL https://www.tandfonline.com/doi/abs/10.1080/01621459.1979.10481038.

Cowing, K. Aerocube-4 captures images of the moon's shadow. *SpaceRef*, November 2013. URL http://spaceref.com/nasa-hack-space/aerocube-4-captures-images-of-the-moons-shadow.html. Retrieved September 20th, 2020.

Crassidis, J. L., Andrews, S. F., Landis, F., and Ha, K. Contingency designs for attitude determination of trmm. 1995.

Cybulski, R. J., Shellhammer, D. M., Lovell, R. R., Domino, E. J., and Kotnik, J. T. Results of the sert 1 ion rocket flight test. Technical report, National Aeronautics and Space Administration, 1965.

Dawn Aerospace. Cubesat propulsion module. Online, a. URL https://www.dawnaerospace.com/products/p/cubesat-propulsion-module. Retrieved September 19th, 2020.

Dawn Aerospace. Cubesat propulsion module imagery. Online, b. URL https://www.dawnaerospace.com/press-kit/cubesat-propulsion. Retrieved September 20th, 2020.

Dawn Aerospace. D-orbit's first ion satellite carrier mission has launched on vv16! Online, September 2020. URL https://www.dawnaerospace.com/blog/ionscvlucas. Retrieved September 19th, 2020.

de Jong, S., Maddox, E., Vollmuller, G., Schuurbiers, C., van Swaaij, R., Ubbels, W., and Hamann, R. The delfi-n3xt nanosatellite: Space weather research and qualification of microtechnology. In *Proceedings of the 59th International Astronautical Congress, Glasgow, Scotland, UK*, 2008.

de Selding, P. B. Oneweb taps airbus to build 900 internet smallsats. *SpaceNews*, June 2015. URL https://spacenews.com/airbus-wins-oneweb-contract/. Retrieved September 15th, 2020.

Drinkwater, M. R., Floberghagen, R., Haagmans, R., Muzi, D., and Popescu, A. *GOCE: ESA's First Earth Explorer Core Mission*, pages 419–432. Springer Netherlands, Dordrecht, 2003. ISBN 978-94-017-1333-7. doi: 10.1007/978-94-017-1333-7_36. URL https://doi.org/10.1007/978-94-017-1333-7_36.

Eagleson, S., Sarda, K., Mauthe, S., Tuli, T., and Zee, R. Adaptable, multi-mission design of canx nanosatellites. *20th Annual AIAA/USU Conference on Small Satellites*, 2006.

Enpulsion. Ifm nano thruster. Online. URL https://www.enpulsion.com/wp-content/uploads/ENP2018-001.F-IFM-Nano-Thruster-Product-Overview.pdf. Retrieved September 17th, 2020.

Etherington, D. Morpheus space's modular, scalable satellite propulsion could be a game-changer for orbital industry. *Techcrunch*, October 2019. URL https://techcrunch.com/2019/10/28/morpheus-spaces-modular-scalable-satellite-propulsion-could-be-a-game-changer-for-orbital-industry/. Retrieved October 11th, 2020.

ExoTerra. Halo hall-effect thruster. Online. URL https://exoterracorp.com/wp-content/uploads/2020/08/NEWBrochureHaloThruster_Web-1.pdf. Retrieved September 17th, 2020.

Federal Communications Commission. In the Matters of Mitigation of Orbital Debris in the New Space Age, April 2020. URL https://docs.fcc.gov/public/attachments/DOC-363486A1.pdf. FCC-CIRC2004-03.

Flatley, T., Morgenstern, W., Reth, A., and Bauer, F. A B-Dot Acquisition Controller for the RADARSAT Spacecraft. In *Flight Mechanics Symposium, NASA Conference Publication*, pages 79–90, 1997.

Folta, D., Newman, L., and Gardner, T. *Foundations of formation flying for Mission to Planet Earth and New Millennium*, pages pp. 656–666. American Institute of Aeronautics and Astronautics, Inc., 1996. doi: 10.2514/6.1996-3645. URL https://arc.aiaa.org/doi/abs/10.2514/6.1996-3645.

Folta, D., Bosanac, N., Cox, A., and Howell, K. The lunar icecube mission design: Construction of feasible transfer trajectories with a constrained departure. February 2016.

Foster, C., Mason, J., Vittaldev, V., Leung, L., Beukelaers, V., Stepan, L., and Zimmerman, R. Differential drag control scheme for large constellation of planet satellites and on-orbit

results. In *Proceedings of the 9th International Workshop on Satellite Constellations and Formation Flying*, June 2018.

Gangestad, J., Hardy, B., and Hinkley, D. Operations, orbit determination, and formation control of the aerocube-4 cubesats. *27th Annual AIAA/USU Conference on Small Satellites*, 2013.

Gonzalez del Amo, J., Estublier, D., Capacci, M., Tajmar, M., Biagioni, L., and Passaro, A. Flight experience from the smart-1 electric propulsion system. October 2005.

Guarducci, F., Coletti, M., and Gabriel, S. Design and testing of a micro pulsed plasma thruster for cubesat application. *Proceedings of the 32nd International Electric Propulsion Conference*, September 2011.

Guccione, P., Guarnieri, A. M., Rocca, F., Giudici, D., and Gebert, N. Along-track multistatic synthetic aperture radar formations of minisatellites. *Remote Sensing*, 12(1), 2020.

Guo, J., Bouwmeester, J., and Gill, E. In-orbit results of delfi-n3xt: Lessons learned and move forward. *Acta Astronautica*, 121, December 2015. doi: 10.1016/j.actaastro.2015.12.003.

Gutierrez-Nava, A., Ponce, O., Lopez-Dekker, P., Patyuchenco, A., Younis, M., Krieger, G., Reigber, A., Moreira, A., Vicente-Vivas, E., Ocampo-Torres, F. J., and Pacheco, E. Topmex-9 distributed sar mission employing nanosatellite cluster. *63rd International Astronautical Congress*, 2012.

Haynes, W. M., editor. *Handbook of Chemistry and Physics*. CRC Press, 95 edition, 2014.

Heidt, H., Puig-Suari, J., Moore, A., Nakasuka, S., and Twiggs, R. CubeSat: A new Generation of Picosatellite for Education and Industry Low-Cost Space Experimentation. *14th Annual AIAA/USU Small Satellite Conference, Logan, UT*, August 2000.

Henry, C. French startup exotrail raises $13 million for propulsion, space software and on-orbit transport systems. *SpaceNews*, July 2020. URL https://spacenews.com/french-startup-exotrail-raises-13-million-for-propulsion-on-orbit-transport-systems/. Retrieved September 17th, 2020.

Herman, J., Presti, D., Codazzi, A., and Belle, C. Attitude control for grace the first low-flying satellite formation. *Proceedings of the 18th International Symposium on Space Flight Dynamics*, 548, January 2004.

Holmes, S. and Featherstone, W. A unified approach to the clenshaw summation and the recursive computation of very high degree and order normalised associated legendre functions. *Journal of Geodesy*, 76:279–299, May 2002. doi: 10.1007/s00190-002-0216-2.

Holoborodko, P. Smooth noise-robust differentiators. Website. URL http://www.holoborodko.com/pavel/numerical-methods/numerical-derivative/smooth-low-noise-differentiators/. Retrieved June 15th, 2020.

Hurley, S., Teel, G., Lukas, J., Haque, S., Keidar, M., Dinelli, C., and Kang, J. Thruster subsystem for the united states naval academy's (usna) ballistically reinforced communication satellite (bricsat-p). *Transactions of the Japan Society for Aeronautical and Space Sciences, Aerospace Technology Japan*, 14:pp. 157–163, December 2016. doi: 10.2322/tastj.14.Pb_157.

Inter-agency space debris coordination committee. Iadc space debris mitigation guidelines. Technical report, Steering Group and Working Group 4, 2002.

Inter-Agency Space Debris Coordination Committee. Report of the inter-agency space debris coordination committee activities on iadc space debris mitigation guidelines & supporting document. Technical report, Inter-Agency Space Debris Coordination Committee, 2005. URL https://www.iadc-home.org/documents_public/file_down/id/4112.

Jones, A. French startup thrustme found fast route to orbit through china's spacety. *SpaceNews*, November 2019. URL https://spacenews.com/french-startup-thrustme-found-fast-route-to-orbit-through-chinas-spacety/. Retrieved September 17th, 2020.

Kennewell, J. A. and Vo, B.-N. An overview of space situational awareness. *Proceedings of the 16th International Conference on Information Fusion*, July 2013.

Kessler, D. J. and Cour-Palais, B. G. Collision frequency of artificial satellites: The creation of a debris belt. *Journal of Geophysical Research: Space Physics*, 83(A6):2637–2646, 1978. doi: 10.1029/JA083iA06p02637. URL https://agupubs.onlinelibrary.wiley.com/doi/abs/10.1029/JA083iA06p02637.

Kiefel, P., Busch, S., Dröge, W., and Schilling, K. Implementation, Calibration and Verification of a Kalman Filter based Attitude Determination System for the Picosatellite UWE-3. In *Proceedings of the 8th International ESA Conference on Guidance & Navigation Control Systems*, June 2011.

Klesh, A., Clement, B., Colley, C., Essmiller, J., Forgette, D., Krajewski, J., Marinan, A., Martin-Mur, T., Steinkraus, J., Sternberg, D., Werne, T., and Young, B. Marco: Early operations of the first cubesats to mars. *32nd Annual AIAA/USU Conference on Small Satellites*, 2018.

Kolbeck, J. and Keidar, M. Gw-sat: Gw's first satellite with propulsive 3-axis-stabilization. *32nd Annual AIAA/USU Conference on Small Satellites*, 2018.

Koziol, M. Amazon's project kuiper is more than the company's response to spacex. *IEEE Spectrum*, August 2020. URL https://spectrum.ieee.org/tech-talk/aerospace/satellites/amazons-project-kuiper-is-more-than-the-companys-response-to-spacex.

Kramer, A., Bangert, P., and Schilling, K. Uwe-4: First electric propulsion on a 1u cubesat - in-orbit experiments and characterization. *Aerospace*, 7(98), July 2020.

Kramer, A. and Schilling, K. First demonstration of collision avoidance and orbit control for pico-satellites — uwe-4. *Acta Astronautica*, 185:244–256, 2021. ISSN 0094-5765.

doi: https://doi.org/10.1016/j.actaastro.2021.04.010. URL https://www.sciencedirect.com/science/article/pii/S0094576521001557.

Kramer, A., Azari, P., Bangert, P., and Schilling, K. Orbit control on the pico-satellite uwe 4 using a nanofeep propulsion system and a directive adaptive guidance algorithm. *Proceedings of the 35th International Electric Propulsion Conference*, 2017a.

Kramer, A., Bangert, P., Paries, F., and Schilling, K. Preparations for Orbit control on the Pico-Satellite UWE-4. *11th IAA Symposium on Small Satellites for Earth Observation*, 2017b.

Kramer, A., Bangert, P., and Schilling, K. Hybrid attitude control on-board uwe-4 using magnetorquers and the electric propulsion system nanofeep. *33rd Annual AIAA/USU Conference on Small Satellites*, 2019.

Krejci, D. and Lozano, P. Space propulsion technology for small spacecraft. *Proceedings of the IEEE*, PP:1–17, January 2018. doi: 10.1109/JPROC.2017.2778747.

Krejci, D., Mier-Hicks, F., Fucetola, C., Lozano, P., Hsu, A., and Martel, F. Design and characterization of a scalable ion electrospray propulsion system. July 2015.

Krejci, D., Reissner, A., Seifert, B., Jelem, D., Hörbe, T., Friedhoff, P., and Lai, S. Demonstration of the ifm nano feep thruster in low earth orbit. In *4S Symposium*, May 2018.

Krieger, G. and Moreira, A. Multistatic sar satellite formations: Potentials and challenges. *IEEE International Geoscience and Remote Sensing Symposium*, 2005.

Lagarias, J., Reeds, J., Wright, M., and Wright, P. Convergence properties of the nelder–mead simplex method in low dimensions. *SIAM Journal on Optimization*, 9:112–147, December 1998. doi: 10.1137/S1052623496303470.

Lappas, V. and Kostopoulos, V. *Satellites Missions and Technologies for Geosciences*, chapter A Survey on Small Satellite Technologies and Space Missions for Geodetic Applications. IntechOpen, July 2020. ISBN 978-1-78985-995-9.

Lemmer, K. Propulsion for cubesats. *Acta Astronautica*, 134, February 2017. doi: 10.1016/j.actaastro.2017.01.048.

Lukas, J., Teel, G., Haque, S., Shashurin, A., and Keidar, M. Thruster subsystem design for the ballistic reinforced communication satellite (bricsat-p). *28th Annual AIAA/USU Conference on Small Satellites*, 2014.

Maisonobe, L., Pommier, V., and Parraud, P. Orekit: An open source library for operational flight dynamics applications. In *Proceedings of the 4th International Conference on Astrodynamic Tools and Techniques (ICATT)*, April 2010.

Malina, F. J. Characteristics of the rocket motor unit based on the theory of perfect gases. *Journal of the Franklin Institute*, 230(4):433 – 454, 1940. ISSN 0016-0032. doi: https://doi.org/10.1016/S0016-0032(40)91348-5. URL http://www.sciencedirect.com/science/article/pii/S0016003240913485.

Manzoni, G. and Brama, Y. L. Cubesat micropropulsion characterization in low earth orbit. *29th Annual AIAA/USU Conference on Small Satellites*, 2015.

MarsSpace. Pulsed plasma thruster (ppt) projects. Online. URL https://mars-space.co.uk/ppt. Retrieved September 18th, 2020.

Mauthe, S., Pranajaya, F., and Zee, D. R. E. The design and test of a compact propulsion system for canx nanosatellite formation flying. *19th Annual AIAA/USU Conference on Small Satellites*, 2005.

Messier, D. Nasa selects tethers unlimited's hydros-c thruster for first ptd cubesat mission. *Parabolic Arc*, June 2018. URL http://www.parabolicarc.com/2018/06/30/nasa-selects-tuis-hydrosc-thruster-ptd-cubesat-mission/. Retrieved September 16th, 2020.

Millan, R. M., von Steiger, R., Ariel, M., Bartalev, S., Borgeaud, M., Campagnola, S., Castillo-Rogez, J. C., Fléron, R., Gass, V., Gregorio, A., Klumpar, D. M., Lal, B., Macdonald, M., Park, J. U., Sambasiva Rao, V., Schilling, K., Stephens, G., Title, A. M., and Wu, J. Small satellites for space science: A cospar scientific roadmap. *Advances in Space Research*, 64(8):1466 – 1517, 2019. ISSN 0273-1177. doi: https://doi.org/10.1016/j.asr.2019.07.035. URL http://www.sciencedirect.com/science/article/pii/S0273117719305411.

Montenbruck, O. and Gill, E. *Satellite Orbits: Models, Methods and Applications*. Springer, 2005. doi: 10.1007/978-3-642-58351-3.

Montenbruck, O., Steigenberger, P., and Hauschild, A. Multi-gnss signal-in-space range error assessment – methodology and results. *Advances in Space Research*, 61(12):3020 – 3038, 2018. ISSN 0273-1177. doi: https://doi.org/10.1016/j.asr.2018.03.041. URL http://www.sciencedirect.com/science/article/pii/S0273117718302813.

Moritz, H. Geodetic reference system 1980. *Bulletin géodésique*, 54:395–405, September 1980.

Morpheus Space. Designed to outperform. Online. URL https://www.morpheus-space.com/static/MSWeb/documents/M-SpaceProducts.pdf. Retrieved October 11th, 2020.

NanoAvionics. Cubesat propulsion system epss. Online. URL https://nanoavionics.com/cubesat-components/cubesat-propulsion-system-epss/. Retrieved September 16th, 2020.

NASA, A. R. C. State of the art - small spacecraft technology, December 2018. URL https://www.nasa.gov/sites/default/files/atoms/files/soa2018_final_doc-6.pdf. Retrieved September 15th, 2020.

NASA Space Science Data Coordinated Archive. Discoverer 13. Online. URL https://nssdc.gsfc.nasa.gov/nmc/spacecraft/display.action?id=1960-008A. Retrieved September 22nd, 2020.

National Academies of Sciences, E. and Medicine. *Achieving Science with CubeSats: Thinking Inside the Box*. The National Academies Press, Washington, DC, 2016. ISBN 978-0-309-44263-3. doi: 10.17226/23503. URL https://www.nap.edu/catalog/23503/achieving-science-with-cubesats-thinking-inside-the-box.

Nicholson, W., Ricco, A., Agasid, E., Beasley, C., Diaz-Aguado, M., Ehrenfreund, P., Friedericks, C., Ghassemieh, S., Henschke, M., Hines, J., Kitts, C., Luzzi, E., Ly, D., Mai, N., Mancinelli, R., McIntyre, M., Minelli, G., Neumann, M., Parra, M., and Young, A. The o/oreos mission: first science data from the space environment survivability of living organisms (seslo) payload. *Astrobiology*, 11:951–8, November 2011. doi: 10.1089/ast.2011.0714.

Nieto-Peroy, C. and Emami, M. R. Cubesat mission: From design to operation. *Applied Sciences*, 9(15), 2019. ISSN 2076-3417. doi: 10.3390/app9153110. URL https://www.mdpi.com/2076-3417/9/15/3110.

Noorma, M. Estcube-1 mission results: Status on september 23, 2014. Online, 2014. URL http://tstc2014.to.ee/download/m5425c58f2bf52. Retrieved September 18th, 2020.

Ohkawa, Y., Okumura, T., Iki, K., Okamoto, H., and Kawamoto, S. Operation of a carbon nanotube field-emission cathode in low earth orbit. *Journal of Vacuum Science & Technology B*, 37(2):022203, 2019. doi: 10.1116/1.5067299. URL https://doi.org/10.1116/1.5067299.

Orr, N. G., Eyer, J. K., Larouche, B. P., and Zee, R. E. Precision Formation Flight: The Can X-4 and Can X -5 Dual Nanosatellite Mission. In Conroy, L., editor, *4S Symposium Small Satellites Systems and Services*, volume 660 of *ESA Special Publication*, page 6, August 2008.

Palmer, K., Li, Z., and Wu, S. In-orbit demonstration of a mems-based micropropulsion system for cubesats. *30th Annual AIAA/USU Conference on Small Satellites*, 2016. URL https://digitalcommons.usu.edu/cgi/viewcontent.cgi?article=3467&context=smallsat. Retrieved September 19th, 2020.

Parham, J. B., Kromis, M., Einhorn, D., Teng, P., Posnov, S., Levin, H., Dessel, O. V., Zosuls, A., Walsh, B., and Semeter, J. Networked small satellite magnetometers for auroral plasma science. *Journal of Small Satelites*, 8(1):801–814, 2019. URL https://jossonline.com/wp-content/uploads/2019/05/Final-Parham-Networked-Small-Satellite-Magnetometers-for-Auroral-Plasma-Science-PayloadScienceMissions.pdf. Retrieved September 26th, 2020.

Park, J.-P., Park, S.-y., Lee, K., Oh, H., Choi, K. Y., Song, Y., Yim, J.-C., Lee, E., Hwang, S.-H., Kim, S., Kang, S., Kim, M.-S., Jin, S., Lee, S., Kwon, S., Lee, D., Cho, W.-H., Park, J.-H., Yeo, S.-W., and Kim, T.-H. Mission analysis and cubesat design for

canyval-x mission. In *14th International Conference on Space Operations*, May 2016. doi: 10.2514/6.2016-2493.

Racca, G., Marini, A., Stagnaro, L., van Dooren, J., di Napoli, L., Foing, B., Lumb, R., Volp, J., Brinkmann, J., Grünagel, R., Estublier, D., Tremolizzo, E., McKay, M., Camino, O., Schoemaekers, J., Hechler, M., Khan, M., Rathsman, P., Andersson, G., Anflo, K., Berge, S., Bodin, P., Edfors, A., Hussain, A., Kugelberg, J., Larsson, N., Ljung, B., Meijer, L., Mörtsell, A., Nordebäck, T., Persson, S., and Sjöberg, F. Smart-1 mission description and development status. *Planetary and Space Science*, 50(14):1323 – 1337, 2002. ISSN 0032-0633. doi: https://doi.org/10.1016/S0032-0633(02)00123-X. URL http://www.sciencedirect.com/science/article/pii/S003206330200123X. Lunar Exploration.

Ruggiero, A., Pergola, P., Marcuccio, S., and Andrenucci, M. Low-thrust maneuvers for the efficient correction of orbital elements. *Proceedings of the 32nd International Electric Propulsion Conference*, September 2011.

Sarda, K., Grant, C., Eagleson, S., Kekez, D., and Zee, R. Canadian advanced nanospace experiment 2: On-orbit experiences with a three-kilogram satellite. *22nd Annual AIAA/USU Conference on Small Satellites*, September 2008.

Schilling, K. and Aumann, A. Cloudct: Design challenges for a formation of 10 nanosatellites. *5th IAA Conference on University Satellite Missions and CubeSats Workshop*, 2020.

Schilling, K., Schechner, Y. Y., and Koren, I. Cloudct – computed tomography of clouds by a small satellite formation. *12th IAA symposium on Small Satellites for Earth Observation*, 2019. IAA-B12-1502.

Shuster, S. P. A survey and performance analysis of orbit propagators for leo, geo and highly elliptical orbits. Master's thesis, Utah State University, 2017.

Sidi, M. J. *Spacecraft Dynamics & Control: A Practical Engineering Approach*. Cambridge University Press, 1997.

SpaceWorks Enterprises, I. Nano/microsatellite market forecast, 10th edition. Technical report, February 2020. URL https://www.spaceworks.aero/wp-content/uploads/Nano-Microsatellite-Market-Forecast-10th-Edition-2020.pdf. Retrieved September 24th, 2020.

Spencer, D. A., Betts, B., Bellardo, J. M., Diaz, A., Plante, B., and Mansell, J. R. The lightsail 2 solar sailing technology demonstration. *Advances in Space Research*, 2020. ISSN 0273-1177. doi: https://doi.org/10.1016/j.asr.2020.06.029. URL http://www.sciencedirect.com/science/article/pii/S027311772030449X.

Sutton, G. *Rocket Propulsion Elements: An Introduction to the Engineering of Rockets*. Wiley-Interscience publication. Wiley, 1986. ISBN 9780471800279. URL https://books.google.de/books?id=jIFTAAAAMAAJ.

Tajmar, M. and Scharlemann, C. Development of electric and chemical microthrusters. *International Journal of Aerospace Engineering*, 2011. doi: 10.1155/2011/361215.

Tajmar, M. and Stämm, S. Mems-based gas-field-ion-source for micro thruster and gas sensor application. In *4th Space Propulsion Conference*, Cologne, Germany, May 2014.

Tajmar, M. *Advanced Space Propulsion Technologies*. Springer, 2003. ISBN 978-3-211-83862-4.

Taylor, B., Underwood, C., Viquerat, A., Fellowes, S., Duke, R., Stewart, B., Aglietti, G., Bridges, C., Schenk, M., Massimiani, C., Masutti, D., and Denis, A. Flight results of the inflatesail spacecraft and future applications of dragsails. *32nd Annual AIAA/USU Conference on Small Satellites*, 2018.

Tethers Unlimited, I. Hydros-c - water propulsion system. Online. URL https://www.tethers.com/wp-content/uploads/2020/07/TUI-DATA-SHEETS-1-compressed.pdf. Retrieved September 16th, 2020.

ThrustMe. Npt30 - stand-alone propulsion system. Online, 2019. URL https://satsearch.co/products/thrustme-npt30. Retrieved September 17th, 2020.

Tribble, A. *The Space Environment - Implications for Spacecraft Design*. Princeton University Press, 41 William Street, Princeton, New Jersey 08540, UK, October 2003. ISBN 0-691-10299-6.

Tsuda, Y., Mori, O., Funase, R., Sawada, H., Yamamoto, T., Saiki, T., Endo, T., and Kawaguchi, J. Flight status of ikaros deep space solar sail demonstrator. *Acta Astronautica*, 69(9):833 – 840, 2011. ISSN 0094-5765. doi: https://doi.org/10.1016/j.actaastro.2011.06.005. URL http://www.sciencedirect.com/science/article/pii/S0094576511001822.

VACCO Industries. Jpl marco - micro cubesat propulsion system, a. URL https://cubesat-propulsion.com/wp-content/uploads/2015/11/X14102000-01_2019update.pdf. Retrieved September 16th, 2020.

VACCO Industries. Argomoon propulsion system. Online, b. URL https://cubesat-propulsion.com/argomoon-propulsion-system/. Retrieved September 24th, 2020.

Vallado, D. and Cefola, P. Two-line element sets - practice and use. *Proceedings of the 63rd International Astronautical Congress, IAC*, 7:5812–5825, October 2012.

Voronka, N., Hoyt, R., Newton, T., Barnes, I., Shepherd, J., Frank, S., Slostad, J., jaroux, B., and Twiggs, R. Early results of the multi-application survivable tether (mast) experiment. *21st Annual AIAA/USU Conference on Small Satellites*, 2007.

Williams, M. Spacex's starlink constellation construction begins. 2,200 satellites will go up over the next 5 years. *Universe Today*, April 2019. URL https://www.universetoday.com/141980/spacexs-starlink-constellation-construction-begins-2200-satellites-will-go-up-over-the-next-5-years/.

Williams, T. W., Ottenstein, N., Farahmand, M., and Palmer, E. *Initial Satellite Formation Flight Results from the Magnetospheric Multiscale Mission*. American Institute of Aeronautics and Astronautics, Inc., September 2016. doi: 10.2514/6.2016-5505. URL https://arc.aiaa.org/doi/abs/10.2514/6.2016-5505.

Witze, A. How satellite 'megaconstellations' will photobomb astronomy images. *Nature*, August 2020. doi: 10.1038/d41586-020-02480-5. URL https://www.nature.com/articles/d41586-020-02480-5. Retrieved September 25th, 2020.

Wu, S., Chen, W., and Chao, C. The stu-2 cubesat mission and in-orbit test results. *30th Annual AIAA/USU Conference on Small Satellites*, 2016.

Zanoni, C., Alfauwaz, A., Aljadaan, A., Althubiti, S., Balakrishnan, K., Buchman, S., Byer, R. L., Conklin, J. W., Cutler, G. D., DeBra, D., Hultgren, E., Lipa, J. A., Saraf, S., and Zoellner, A. The design of a drag-free cubesat and the housing for its gravitational reference sensor. In *Proceedings of 2nd IAA conference on University Satellites*, 2013.

The author appreciated the support for UWE–4 by the German national space agency DLR (Raumfahrt-Agentur des Deutschen Zentrums für Luft- und Raumfahrt e.V.) by funding from the Federal Ministry of Economic Affairs and Energy by approval from German Parliament with reference 50 RU 1501.

Lehrstuhl Informatik VII
Robotik und Telematik
Am Hubland
D-97074 Wuerzburg

Tel.: +49 (0) 931 - 31 - 86678
Fax: +49 (0) 931 - 31 - 86679

schi@informatik.uni-wuerzburg.de
http://www7.informatik.uni-wuerzburg.de

ISSN: 1868-7474 (online)
ISSN: 1868-7466 (print)
ISBN: 978-3-945459-34-8 (online)

Die Schriftenreihe

wird vom Lehrstuhl für Informatik VII: Robotik und Telematik der Universität Würzburg herausgegeben und präsentiert innovative Forschung aus den Bereichen der Robotik und der Telematik.

Die Kombination fortgeschrittener Informationsverarbeitungsmethoden mit Verfahren der Regelungstechnik eröffnet hier interessante Forschungs- und Anwendungsperspektiven. Es werden dabei folgende interdisziplinäre Aufgabenschwerpunkte bearbeitet:

- Robotik und Mechatronik: Kombination von Informatik, Elektronik, Mechanik, Sensorik, Regelungs- und Steuerungstechnik, um Roboter adaptiv und flexibel ihrer Arbeitsumgebung anzupassen.

- Telematik: Integration von Telekommunikation, Informatik und Steuerungstechnik, um Dienstleistungen an entfernten Standorten zu erbringen.

Anwendungsschwerpunkte sind u.a. mobile Roboter, Tele-Robotik, Raumfahrtsysteme und Medizin-Robotik.

Zitation dieser Publikation

KRAMER, A. (2021). Orbit Control of a Very Small Satellite using Electric Propulsion. Schriftenreihe Würzburger Forschungsberichte in Robotik und Telematik, Band 22. Würzburg: Universität Würzburg. DOI: 10.25972/OPUS-24155

Dissertation an der Universität Würzburg im Rahmen der Graduate School of Science and Technology